Experimental Investigation on Turbulent Droplet Breakup in Orifice-type High-pressure Homogenizers

M.Sc Martin Benedikt Schumm

Vollständiger Abdruck der von der
Fakultät für Luft- und Raumfahrttechnik
der Universität der Bundeswehr München
zur Erlangung des akademischen Grades eines

Doktor-Ingenieurs (Dr.-Ing)

genehmigten Dissertation

Gutachter:
1. Prof. Dr. C. J. Kähler
2. Prof. Dr. M. Schlüter

Diese Dissertation wurde am 25.05.2022 bei der Universität der Bundeswehr München eingereicht und durch die Fakultät für Luft- und Raumfahrttechnik am 5.11.2022 angenommen. Die mündliche Prüfung fand am 30.11.2022 statt.

Abstract

Droplet breakup in turbulent flow fields such as those occurring during high-pressure homogenization is not yet fully understood and the existing models for describing the process are not adequate for process design. Therefore, in this work the droplet breakup in transitional flows and in particular in the turbulent flow field of the decaying free jet behind an orifice is investigated in more detail using optical measurement techniques. On the one hand, the flow fields behind the homogenizing orifice used are characterized by means of particle image velocimetry (PIV) and, on the other hand, the droplet breakup process is resolved spatially and temporally very closely by means of high-speed cameras. The investigations take place in a test facility geometrically scaled up by a scale factor of 50 and with material combinations adapted according to a scaling concept based on six dimensionless ratios at two Reynolds numbers (Re = 2000 and Re = 5700).

The droplet deformation and breakup process is analyzed starting with the deformation as the droplet passes through the orifice unit, continuing with the deformation process behind the orifice, and ending with the high turbulent deformation and breakup process in the turbulent free jet region behind the orifice.

Comparison of the velocity field measurements with the droplet deformation and breakup studies shows that the droplet breakup is significantly influenced by the interaction of the droplet with the vortex field in the turbulent decaying free jet region. The droplets are deformed to filaments or, in some cases, to sheet-like droplet films and break up into many secondary droplets under locally very strong deformation. This finding is confirmed by investigations in which undeformed droplets are injected into the free-jet region behind the orifice. Depending on the viscosity ratio of the two phases, there are clear differences, especially in the deformation process in the orifice. The deformation of the primary droplets to droplet filaments is much more pronounced at lower viscosity ratios. Increasing the Reynolds number has a similar effect. In addition, the Reynolds number increase shifts the laminar-turbulent transition point of the free jet towards the orifice, which also shifts the drop breakup in this direction. In addition to the shift, the droplet breakup occurs much faster at the higher Reynolds number because the velocity fluctuations and vortices are much more intense.

The use of passive flow control structures at the trailing edge of the orifice can significantly influence the velocity field behind the orifice, but the structures must be designed to prevent flow separation.

Kurzzusammenfassung

Der Tropfenaufbruch in turbulenten Strömungen wie er beim Hochdruckhomogenisieren stattfindet ist bisher nicht systematisch verstanden. Folglich sind die existierenden Modelle zur Beschreibung des Vorgangs zu ungenau für Auslegungsprozesse, sodass empirische Modelle verwendet werden. Daher wird in dieser Arbeit der Tropfenaufbruch in transitionellen Strömungen und insbesondere im turbulenten Strömungsfeld des zerfallenden Freistrahls hinter einer Blende mittels optischer Messverfahren genauer untersucht. Einerseits werden die Strömungsfelder hinter der verwendeten Homogensierblende mittels Particle Image Velocimetry (PIV) charakterisiert, andererseits wird der Tropfenaufbruchsvorgang mittels Hochgeschwindigkeitskameras räumlich und zeitlich sehr fein aufgelöst. Die Untersuchungen finden in einer mit dem Maßstabsfaktor 50 geometrisch vergrößerten Versuchsanlage und mit, entsprechend einem Skalierungskonzept, basierend auf sechs dimensionslosen Kennzahlen, angepassten Stoffkombinationen bei zwei Reynoldszahlen (Re = 2000 und Re = 5700) statt.

Der Deformations- und Aufbruchsvorgang der Tropfen wird beginnend mit der Tropfendehnung beim Durchlaufen der Blendeneinheit über den Deformationsprozess hinter der Blende bis zum hochturbulenten Deformations- und Zerfallsprozess im turbulenten Freistrahlbereich hinter der Blende analysiert.

Der Vergleich der Geschwindigkeitsfeldmessungen mit den Deformations und Aufbruchsuntersuchungen der Tropfen zeigt, dass der Tropfenaufbruch maßgeblich durch die Interaktion des Tropfens mit dem Wirbelfeld im Bereich des turbulenten Freistrahls beeinflusst wird. Die Tropfen werden zu Filamenten bzw. teilweise zu flächigen Tropfenfilmen deformiert und zerfallen bei lokal sehr starker Dehnung in viele Sekundärtropfen. Diese Erkenntnis wird durch Untersuchungen, bei denen undeformierte Tropfen in den Freistrahlbereich hinter der Blende injeziert werden, bestätigt. In Abhängigkeit des Viskositätsverhältnisses der beiden Phasen zeigen sich deutliche Unterschiede insbesondere beim Deformationsprozess in der Blende. Die Deformation der Primärtropfen zu Tropfenfilamenten ist bei niedrigeren Viskositätsverhältnissen deutlich stärker ausgeprägt. Eine Erhöhung der Reynoldszahl hat einen ähnlichen Effekt. Zudem verschiebt sich durch die Reynoldszahlerhöhung der laminar-turbulente Umschlagsbereich des Freistrahls hin zur Blende, wodurch auch der Tropfenaufbruch in diese Richtung verschoben wird. Neben der Verschiebung findet der Tropfenaufbruch bei der höheren Reynoldszahl deutlich schneller statt, da die Geschwindigkeitsschwankungen und die Wirbel deutlich stärker sind.

Die Verwendung von passiven Strömungsbeeinflussungsstrukturen an der Blendenhinterkante kann das Geschwindigkeitsfeld hinter der Blende deutlich beeinflussen, allerdings müssen die Strukturen so angelegt sein, dass das Ablösen der Strömung verhindert wird.

Contents

List of Figures

1

Introduction

Emulsions, i.e. mixtures of at least two non-soluble phases such as oil in water or vice versa, play an important role in many areas of daily life such as cosmetics, food or medical preparations. In addition to the production of consumer ready end products (especially in the pharmaceutical and food industries), emulsions are also used in the chemical industry in intermediate products, which is why they are also very relevant economically.

Depending on the area of application, different properties like droplet size distribution, disperse phase fraction or emulsion viscosity, of an emulsion are required. In addition, depending on the material properties, such as unstable biological products or stable components, different requirements are specified for the production process, so that there is a broad production spectrum. An essential property of the emulsion is the droplet size or droplet size distribution. It can determine the shelf life of the product in that the creaming time, i.e. the time until separation due to the possibly different density of the product phases, depends quadratically on the droplet size (see Stokes Equation Walstra (1983)). High pressure homogenization is an important process for the production of low to medium viscosity emulsions with small droplet sizes.

In this process a raw emulsion, i.e. a mixture of the continuous and disperse phases, is passed under high pressure through a homogenization unit with a small channel cross-section. Due to the high pressure and the resulting high velocities, the disperse phase is broken up into fine droplets and distributed within the continuous phase.

The individual processes and the conditions that lead to a particularly effective drop size reduction under laminar flow conditions are well understood but turbulent flow conditions are more complex. Despite decades of application of the process in industry, new products and disintegration units are developed by evolutionary improvements. This approach has led to a variety of different designs that co-exists. Empirical and above all plant-specific correlations between the essential parameter pressure or the specific energy and the resulting particle size exist and are used for new product lines in industry (Köhler and Schuchmann, 2015).

Detailed and fundamental investigations on droplet breakup have so far almost exclusively been carried out for laminar flow conditions. In this flow regime different mechanisms depending on the flow field and the viscosity ratio of the two phases have

been found ((Taylor, 1934) (Grace, 1982) (Zhao, 2007)). In turbulent flows, which is the most common flow in industrial homogenizers, especially in high-pressure homogenizers, thorough understanding of the breakup process would be beneficial for the design process of new plants or products. The description of droplet breakup in turbulent flows has so far been based on semi-empirical models (Kolmogorov, 1949) (Hinze, 1955) or empirical correlations between the energy input and the secondary droplet size (Karbstein and Schubert, 1995). Due to improved measurement techniques, recent optical measurement methods in particular have been able to disprove some of the underlying assumptions. At the same time, these methods open up the possibility of performing more precise investigations than was previously possible. Therefore this work focuses on gaining deeper knowledge of the processes happening during droplet vortex interactions in turbulent flow fields and the resulting breakup through experimental investigations using optical measurement techniques.

In this thesis the drop breakup in a homogenizer unit at transient flow conditions is investigated in detail. In order to improve the spatial and temporal resolution of the investigations compared to other investigations or to enable temporal measurements at all, a strictly geometric scaled homogenizer unit was used. The material properties of the investigated components are also selected in such a way that the scaling parameters are maintained. As disintegration unit a concentric orifice is used, because this geometry represents the simplest homogenization flow field possible. The work is part of a cooperation in which, in order to validate the experiments on a scaled up scale, investigations are also carried out on the original scale and in a just slightly scaled experimental unit. The aim of this work is to better understand the individual processes that integrally lead to the breakup of the primary droplets into the broken-up secondary droplets in detail and thus to gain system-independent and transferable knowledge about droplet breakup.

Questions to be clarified include:

- What is the influence of the elongation and shear flow in the area of the orifice inlet?
- What processes occur during drop breakup in turbulent flow regimes?
- Do capillary or surface waves lead to Plateau-Rayleigh instability driven breakup?
- Do velocity fluctuations lead to tearing off of individual secondary droplets?

2

Emulsification

Emulsions are mixtures of several liquids that are insoluble in each other, which is why several phases are formed. In the case of two immiscible liquids, one phase is present in the form of droplets dispersed in the continuous second phase. Thermodynamically, these mixtures are unstable, which is why phase separation can occur through drop coalescence and creaming (Binks, 1998). Emulsions are used in many areas of industry. Particularly in the food, pharmaceutical and chemical industries, emulsions are produced and processed either as a product or as an intermediate (Rähse and Dicoi, 2009) (Raikar et al., 2009) (Umbanhowar et al., 2000). In addition to the phase ratio, the droplet size or droplet size distribution is one of the most important properties of an emulsion (Schultz et al., 2004). Therefore manufacturing processes must be specially adapted to the requirements in the specific area of particle size and particle distribution (Tesch et al., 2003). In the food industry, for example, mouthfeel and shelf life are strongly influenced by particle size (Floury et al., 2000) (Stang et al., 2001). In the pharmaceutical industry, particle size is of particular importance, as bioavailability is increased by smaller particle sizes and the associated larger surface to volume ratio promotes a better transfer of the active ingredients (Velmula et al., 2015).

2.1. Homogenizers

Several processes are available for the production of emulsions, e.g. production in stirred vessels with rotor and stator that can be run continuous or batchwise, continuously running high-pressure homogenizers or the production of disperse droplets using a membrane.

The production of desired particle size distributions can be adjusted in stirred vessels by varying the internals (rotor and stator) or the stirring intensity. In high-pressure homogenisation (HPH), the specific energy input is lower compared to the use of a stirring vessel (Schultz et al., 2002). Moreover they function without rotating parts. The droplet breakup occurs because the raw emulsion, which consists of the continuous phase and coarse, disperse primary droplets, is forced through a homogenisation unit, sometimes under very high pressure (50 – 3500 bar (Floury et al., 2000) (Kelemen et al., 2014b)). As homogenisation unit different variants are available, which are characterised by small channel cross-sections. Compared to valves, orifices as the simplest homogenization unit, have the disadvantage that the volume flow is coupled to the pressure loss and is not variable at the same pressure difference. This is possible in valves because the gap width can be adjusted.

The droplets obtained after passing through this homogenization unit have droplet sizes in the sub-micrometer range up to several micrometers, depending on the homogenization pressure. In most technical processes such as HPH with various homogenizing units or rotor-stator based homogenizers, an immense excess of energy is required compared to the theoretically required energy. The theoretical surface energy required to produce a certain amount of droplets with a certain droplet size is several orders of magnitude lower than the energy required in practice. Only the production of fine droplets by means of membrane processes comes close to these regions, although a massive energy surplus is still required and this process is not suitable for the high volume throughputs of the other processes.

Apart from the membrane processes, in which the stresses leading to drop breakup are transferred to the droplets through the wall, but which will not be considered in detail below, the stresses are transferred to the disperse phase droplets through the continuous phase. That is why in addition to the energy requirement, the viscosity or viscosity ratio of the phases is also important for the selection of the homogenization method. High-pressure homogenization can be economically operated up to a viscosity of approx. 200 mPas. Higher viscous media of up to 10000 mPas can be processed in stirred systems (Urban et al., 2006).

2.2. Droplet breakup

Although the actual drop breakup process was investigated by Taylor (1934) under generic conditions, the real process could not be explained in all its complexity until today, so that various methods and equations were partly determined empirically to enable the description of the drop breakup when designing new experimental plants. Experimental knowledge of drop breakup can be obtained by correlating the operating parameters and the change in drop size distribution with the loading caused by the operating parameters (Karbstein and Schubert, 1995). On the other hand, it is possible to observe the breakup process itself and to draw conclusions about the process and the relevant forces (Swartz and Kessler, 1970). In addition to the breakup process, coalescence processes also play an important role in the homogenization, especially when droplet collectives are examined rather than individual droplets as in the detailed investigation of the breakup process. Droplet coalescence can be prevented or reduced, for example, by using a stabilizer, but these processes are not considered in this work.

For a droplet to be broken up, the Laplace pressure (see equation 2.1) caused by the interfacial tension γ and the radii of curvature (R_1 and R_2) must be overcome (Schubert and Armbruster, 1989). It is important to note that the Laplace pressure increases significantly due to the deformation of the droplet. The increasing Laplace pressure can also be used to explain the increasing difficulty of crushing smaller droplets.

$$p_{\mathrm{La}} = \gamma\left(\frac{1}{R_1} + \frac{1}{R_2}\right) \tag{2.1}$$

In addition to the, at least local, exceeding of the restoring forces, in particular the surface stress driven Laplace pressure, by the external, attacking stresses, these must also be present long enough to lead to rupture of the droplet. Walstra (1983) defined a critical deformation time (t_{def}), based on the disperse phase viscosity (η_{d}) the primary drop radius (r) and the interfacial tension (γ), for this, which must be exceeded for breakup to happen (see equation 2.2).

$$t_{\mathrm{def}} = \frac{\eta_{\mathrm{d}} \cdot r}{\gamma} \tag{2.2}$$

Taylor (1934) developed two experimental apparatuses for single droplet tests to determine the critical stresses above which breakup occurs when the droplets are subjected to well-defined, two-dimensional stresses. The flow patterns investigated are, on the one hand, pure two-dimensional shear flow in the “parallel band apparatus” (Taylor, 1934) and two-dimensional hyperbolic flow in the “four roller apparatus” (Taylor, 1934) on the other hand. It became clear that the different flow patterns cause the droplets to be deformed to different degrees and also to break down into small secondary droplets at different stress intensities. The two-dimenstional hyperbolic flow like in the “four roller apparatus” appears to be more effective than the pure two-dimenstional shear

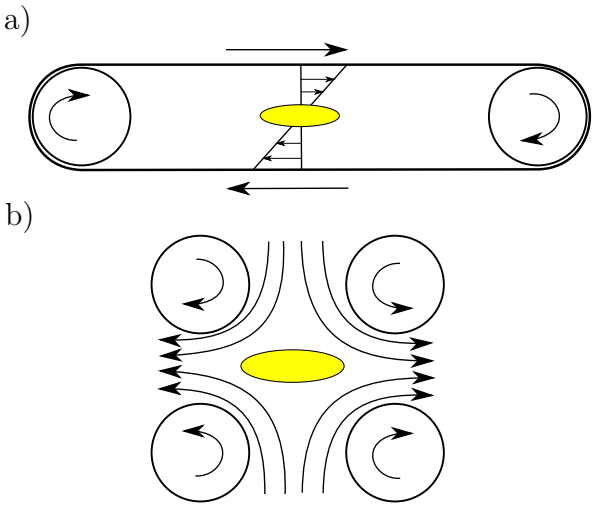

Figure 2.1: Schematic of the flow profiles in the "parallel band apparatus" with pure shear flow (a)) and the "four roller apparatus" with elongational or hyperbolic flow patterns (b)) investigated by Taylor (1934).

flow, i.e. the disintegration occurs at lower critical stresses. This decrease can be associated with the elongational flow pattern. Moreover, it is possible to disintegrate droplets with a very large viscosity ratio, i.e. much higher viscosities of the droplets than those of the continuous phase in the hyperbolic flow, whereas this is impossible in the shear flow. The shear flow around these high viscosity droplets only causes the droplet to align along an axis inclined by 45° to the velocity gradient with a small elliptical deformation and to be excited to rotate whereas the same flow conditions can lead to breakup in low viscosity droplets (see figure 2.2). Many other investigations, and in particular Grace (1982) investigations, also concluded that breakup of droplets with a viscosity ratio of $\eta^* = \eta_d/\eta_c > 4$ is not possible under pure shear flow. No limit in terms of viscosity ratio was found for pure extensional flow (Håkansson, 2015). The aim of all these investigations is to determine the minimum stress necessary to break up the primary droplet. As a measure of the viscous stress related to the interfacial tension forces, i.e. the Laplace pressure, the capillary number Ca has been established as a dimensionless ratio. It is formed from the external viscous forces (σ) and the interfacial tension forces, which are calculated according to equation 2.1 for round drops with the primary drop radius (r) and the interfacial tension (γ) (see equation 2.3).

$$Ca = \frac{\text{viscous forces}}{\text{interfacial tension forces}} = \frac{\sigma \cdot r}{2\gamma} \tag{2.3}$$

The critical capillary number Ca_{crit} at which disintegration of the droplet of a given material system occurs can be accomplished by varying the primary droplet size or by varying the shear stress. Mixed flow patterns of pure shear and pure extensional flows have also been used in automated "four roller apparatus" or counterjet systems investigated (Bentley and Leal, 1986) (Janssen and Meijer, 1993) (Janssen et al., 1993). These studies of superimposed flow patterns show that this leads to a shift in the

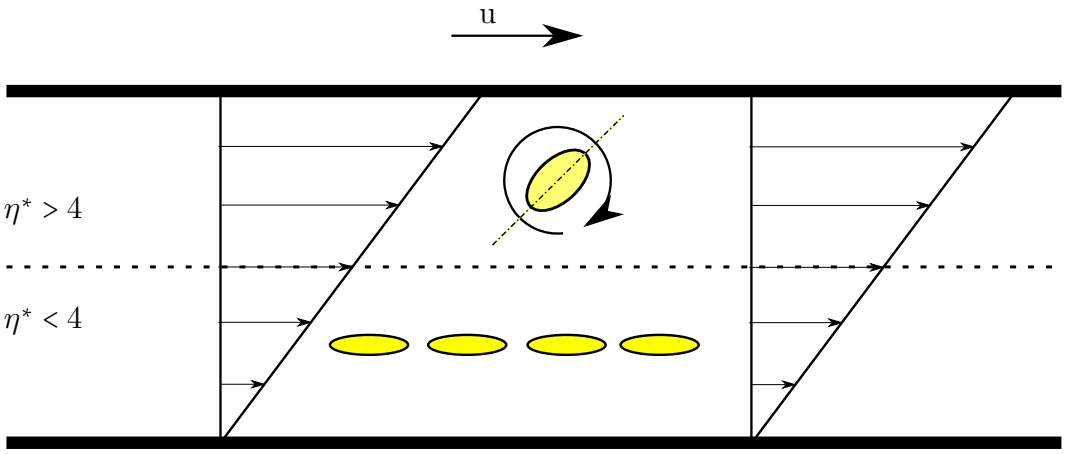

Figure 2.2: Schematic of the drop deformation of a high viscosity ratio droplet ($\eta^* > 4$) and a low viscosity ratio droplet ($\eta^* < 4$).

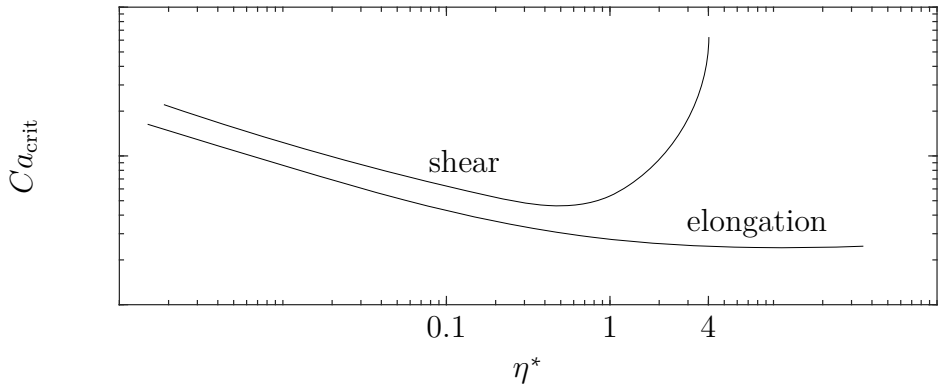

Figure 2.3: Schematic course of the critical capillary number Ca_{crit} and the influence of the flow profile.

breakup boundary and reduction in critical stress (Walstra and Smulders, 1998).

A very extensive study on droplet breakup under pure laminar shear was carried out by Zhao (2007). Thereby, the limit of breakup as a function of viscosity ratio was found at viscosity ratios of $\eta^* \approx 3.5$. Above this viscosity ratio breakup is only possible if there is elongational flow (= hyperbolic flow) or a mixture of shear and elongational flow present. For mixed flow patterns the critical stresses lie in between the extreme or pure cases. Furthermore, in these investigations as well as in the results presented by Grace (1982), an optimum or easiest possible breakup was found at viscosity ratios between 0.1 and 1. Figure 2.3 shows schematically the relationship between viscosity ratio and critical stress. In addition to determining the limiting stresses that lead to breakup, various breakup mechanisms have been identified by Zhao (2007) for pure shear and viscosity ratios lower than 3.5, as a function of stress or viscosity ratio.

At viscosity ratios greater than $\eta^* > 0.1$, a one-step breakup process takes place as a result of capillary instabilities. This means that the droplets are stretched into

very long filaments. These filaments tend to neck down into individual droplets as a result of capillary instabilities, which have different wavelengths depending on the viscosity ratio. The size of the primary drop plays a minor role in this break up mechanism, since the diameter of the resulting filament is constant for different primary drop diameters. This mechanism changes at higher viscosity ratios ($\eta^* > 1$) so that briefly existing filaments between the individual constricted droplets decay into one or more satelite droplets, resulting in a bimodal droplet size distribution. At viscosity ratios $\eta^* < 0.1$, the disintegration of the primary droplets or the resulting filaments also occurs by capillary instabilities, but in this case the process is multistage, so that already disintegrating filament pieces are further stretched and thus disintegrate into additional smaller droplets. This in itself already leads to a polydisperse droplet size distribution, which is reinforced by collisions and possibly coalescence taking place during the collisions. In addition to the three break up mechanisms described above ($\eta^* < 0.1$, $0.1 \leq \eta^* \leq 1$ and $\eta^* > 1$), there seems to be another break up mechanism at only slightly supercritical conditions ($Ca_{\mathrm{crit}} < Ca < 2\,Ca_{\mathrm{crit}}$), which occurs independently of the viscosity ratio of the phases. This breakup mechanism, called end pinching, means that the droplet becomes an elipsoid or filament stretched to different lengths depending on the viscosity ratio. The elongation of the droplets is significantly greater at low viscosity ratios, resulting in elongated droplet filaments, than at high viscosity ratios, where the droplets are more elliptical. The shear stress causes larger drops to form at the ends of the elipses or filaments, which are briefly joined by a much thinner filament. This filament disintegrates under further stressing. Two larger drops are thus formed from the primary drop and one or more smaller drops from the relaxing filament (Zhao, 2007).

While the previously described investigations always assumed equilibrium of forces and stationary flows, it was recognized by Stone et al. (1986) that, with sufficiently strong elongation, the restoring surface forces do not necessarily lead to the filament relaxing to the initial drop, but disintegrate into several smaller drops, even if the external attacking flow is abruptly switched off after a certain elongation is reached. In these studies, the disintegration occurred according to the end pinching mechanism. Similar transient processes were also studied by Elemans et al. (1993).

In addition to the laminar or viscous flow regime described above, in which viscous forces are responsible for the stresses, the turbulent flow regime is particularly relevant for technical applications. Turbulent flows contain vortices in various sizes, orientations and intensities which causes the velocities to fluctuate in time and space in a random fashion. Depending on the ratio of droplet size to vortex size, the turbulent flow regime is divided into the two regions turbulent inertia dominated and turbulent viscosity dominated regime (Walstra and Smulders, 1998). In the turbulent inertia dominated flow regime, the vortices are smaller than the droplets, so the droplets are stressed by velocity or pressure fluctuations perpendicular to the interface. In the turbulent viscosity dominated regime, the droplets are smaller than the vortices, so the droplets are stressed by velocity gradients along the interface, similar to laminar flows. In individual cases, droplet breakup can also be driven by interfacial tension, for example in membrane processes, or by cavitation, in addition to these three mainly responsible flow regimes. Cavitation induced drop breakup is mainly used in ultrasonic homog-

enization, but can also occur in high-pressure homogenizers when the static pressure falls locally below the vapor pressure of the fluid. The vapor cavitation bubbles cause a shock wave when they implode, which can lead to the breakup of the droplets in the vicinity. Some research exists specifically on cavitation in high-pressure homogenizers, as it is unclear whether this mechanism leads to an improvement in the homogenization process or, if so, is more disruptive and hinders breakup (Phipps, 1974) (Freudig et al., 2003) (Schlender et al., 2015a) (Schlender et al., 2015b) (Håkansson et al., 2010) (Mishra and Peles, 2005) (Gothsch et al., 2015) (Gothsch et al., 2016). In addition, cavitation during high-pressure homogenization should be viewed with caution, as it leads to increased wear of components or surfaces (Mohr, 1987). To avoid or suppress cavitation in high-pressure homogenizers, a backpressure is usually applied by a valve or a 2nd homogenizing stage. As a measure to describe cavitation, the Thoma number Th (see equation 2.4) (Kurzhals, 1977) (Schlender et al., 2015a) is used.

$$Th = \frac{p_2}{p_1} \tag{2.4}$$

This includes the pressure upstream (p_1) and downstream of the homogenizing unit (p_2). For complete cavitation suppression, a pressure ratio or Thoma number of about $0.35 < Th < 0.5$ is recommended (Jahnke, 1998). The optimal backpressure ratio may be somewhat lower (Finke et al., 2014). To investigate the influence of cavitation on droplet breakup in high-pressure homogenizers, recent studies have investigated the location and extent of cavitation using non-intrusive, optical and acoustic methods (Schlender et al., 2015a) (Schlender et al., 2015b) (Håkansson et al., 2010) (Håkansson et al., 2011b) (Mishra and Peles, 2005) (Gothsch et al., 2015) (Gothsch et al., 2016). It was found that the cavitation bubbles are already formed in the constriction and can reach far behind the constriction at high pressure differences, so that a large vapor bubble can be formed. When the vapor bubble is very large it dominates the flow downstream of the breakup unit and this is thought to impede the breakup of droplets due to turbulence, so the use of back pressure to suppress cavitation is beneficial. Without cavitation, drop breakup in homogenizing processes is mainly caused by turbulent flow processes, i.e. in the turbulent flow regime.

Based on his studies describing isotropic and homogeneous turbulence using turbulent kinetic energy (ϵ) (Kolmogorov, 1941) carried out a dimensional analysis of the quantities relevant for the breakup of droplets. This led to the definition of the capillary number for viscous stresses and the Weber number We (see equation 2.5) for inertia-domain stresses.

$$We = \frac{\text{inertial forces}}{\text{interfacial tension forces}} = \frac{\Delta u^2 \rho_c r}{4\gamma} \tag{2.5}$$

Since similar scaling approaches were established by Hinze (1955), this theory became known as the Kolmogorov-Hinze theory. In many cases, the Kolmogorov-Hinze theory has been viewed as a force balance between the external disintegrating forces and the internal stabilizing forces, with breakup occurring as soon as the external forces exceed

the internal ones. The critical Weber number, analogous to the critical capillary number, describes the maximum force ratio for a drop of a certain size that can withstand a continuous inert load without disintegrating. Based on this theory, the maximum droplet size in the respective flow regime can be estimated:

Turbulent inert regime (Rayner, 2015):

$$d_{\max} \propto \epsilon^{-2/3} \gamma^{3/5} \rho_{\mathrm{c}}^{-1/5} \tag{2.6}$$

Turbulent viscous regime (Rayner, 2015):

$$d_{\max} \propto \gamma \epsilon^{-1/2} \eta_{\mathrm{c}}^{-1/2} \tag{2.7}$$

The stabilizing forces are represented in the classical Kolmogorov-Hinze theory only by the Laplace pressure, i.e. by surface tension forces. By Davies (1985) a second resistance contribution due to viscous forces of the disperse phase was established (Håkansson, 2019):

$$\tau_{\mathrm{visc}} = \frac{\eta_{\mathrm{d}}}{d} \sqrt{\frac{\tau_{\mathrm{ext}}}{\rho_{\mathrm{d}}}} \tag{2.8}$$

Based on this, Calabrese et al. (1986) extended the Kolmogorov-Hinze theory, in that the stabilizing forces consist of a linear combination of the two stabilizing force components (p_{La} and τ_{visc}) and the inertia-dominated stresses (τ_{TI}) clearly outweigh the turbulent viscous stresses (τ_{visc}).

$$\tau_{\mathrm{TI}} = c_1 \left(p_{\mathrm{La}} + c_2 \tau_{\mathrm{visc}} \right) \tag{2.9}$$

The constants c_1 and c_2 have to be determined numerically (see e.g. (Vankova et al., 2007)). This simplification assumes that the droplets, depending on their size with respect to the Kolmogorov length (see equation 2.10 (Windhab et al., 2005)), i.e. the size of the smallest energy-bearing vortices, are either purely inertia-dominated turbulent stressed if they are larger than the Kolmogorov length l_{K} or they are purely turbulent-viscous stressed if they are smaller.

$$l_{\mathrm{K}} = \frac{\eta_{\mathrm{c}}^{3/4}}{\rho_{\mathrm{c}}^{3/4} \epsilon^{1/4}} \tag{2.10}$$

Measurements of the turbulence intensity or the turbulence spectrum show that the assumption of purely turbulent inert stress is not correct, so that a superposition of the two breakup mechanisms is more accurate (Håkansson, 2019):

$$\tau_{\mathrm{visc}} + \tau_{\mathrm{TI}} = c_1 \left(p_{\mathrm{La}} + c_2 \tau_{\mathrm{visc}} \right) \tag{2.11}$$

Håkansson (2019) also stated that the Kolmogorov-Hinze theory (Kolmogorov, 1949) (Hinze, 1955), even with the extension of Davies (1985) and Calabrese et al. (1986), has contributed to the understanding of turbulent droplet breakup, but still has several weaknesses, so that a new theory for droplet breakup in turbulent flows is needed. Weaknesses include the need for empirically determined constants, such as the critical Capillary and Weber numbers, as well as the constants c_1 and c_2, the neglect of the time scale or deformation time, and basically the assumption of isotropic and homogeneous turbulence, which is not present in the field of drop breakup in practical homogenizers (Håkansson et al., 2011a).

Due to the difficulty in determining the parameters of the Kolmogorov-Hinze theory for plants of relevance to industrial engineering, empirical approaches have also been developed to determine the droplet size on the basis of the operating parameters. Karbstein and Schubert (1995) therefore developed a correlation between the obtained mean droplet size or sauter diameter ($x_{3,2}$) and the volumetric energy density (E_V). The results could be represented very well by the equation 2.12 where the empirical constants b and c had to be determined.

$$x_{3,2} = c{E_V}^{-b} \tag{2.12}$$

This widely used approach (Stang et al., 2001) (Schlender et al., 2015a) was also applied by Schubert and Engel (2004), where membrane processes were included in addition to Karbstein and Schubert (1995). Kelemen et al. (2014a) investigated the influence of Reynolds number on the flow regime in homogenization units with pinholes. Experiments at different energy densities were able to show that the increase in droplet size with the decrease in specific energy density fits with the shift in the determined flow regimes from turbulent to transitional to laminar.

The foregoing discussion implies the necessety to investigate the flow fields in homogenizing units in more detail and to understand which flow conditions are present and can be responsible for drop breakup. With knowledge of the exact flow fields, the transition from integral correlations between droplet size and operating parameters to mechanistic understanding of droplet breakup is possible. Experimental measurements on the one hand and numerical simulations on the other hand can be performed to investigate the flow field in high pressure homogenizers. Since measurement in rotor-stator units is difficult due to the moving parts, more investigations are carried out with high-pressure homogenizers as the breakup unit. The high pressure required to generate the turbulent flow processes is a major reason for the complex measurements. Due to the high pressure, the units are mostly made of stainless steel, so that optical access can only be achieved by constructing model units. Since the dimensions of the homogenization units are so small, only optical measurement methods such as Particle Image Velocimetry (PIV) are suitable for determining the velocity fields.

Innings and Trägårdh (2007) used PIV to determine the velocity field upstream, inside, and especially downstream of the constriction in a special build two-dimensional flat valve model with two optical accesses (Innings and Trägårdh, 2005) instead of the axissymetric flat valve. Flow conditions in the scaled test facility were chosen with a

Reynolds number ($Re = uD\rho_c/\eta_c$) of $Re = 9400$ to be intermediate between those in a pilot facility and a production facility. It was shown that the flow in front of the orifice is accelerated relatively homogeneously across the cross-section and that a free jet is formed behind the constriction. This free jet behind the valve gap tends in the time average clearly towards the wall close to the outlet, so that the flow is guided along the wall towards the outlet of the valve. By adding a guide plate, it was possible to achieve a symmetrical free jet detached from the side walls.

Håkansson et al. (2011a) was able to increase the resolution of the measurement by stitching together several averaged fields. In these measurements at a Reynolds number of $Re = 27000$, no flow baffle was used, so the asymmetric wall jet was investigated. It was demonstrated by the analyzed measurements that the turbulence in the inlet region and in the constriction is very low and only increases significantly in the region of the free jet. The flow in the constriction is somewhat asymmetric due to the inflow geometry. The turbulence in the free jet could be characterized so that a real turbulence spectrum could be used for the calculation of the forces according to the Kolmogorov-Hinze theory.

Kelemen et al. (2014b) also performed PIV measurements, but in an optically accessible orifice. Instead of an concentric bore for the orifice a square channel at the top side of the channel below the optical access coverplate was used. The measurements behind the orifice show a free jet that does not tend to one side in the measurement plane, but the free jet flows along the optically accessible wall due to the geometry of the orifice. The velocity fields at two low Reynolds numbers in the transition region between laminar and turbulent flow ($Re = 330$ and $Re = 1280$, respectively), show that the free jet becomes shorter as the Reynolds number increases, i.e. it breaks up and decays more quickly. This faster decay can be influenced due to the friction losses at the wall. The investigations in the inlet region of the orifice and in the constriction show very high elongation stresses at the inlet and very high shear stresses at the wall inside the constriction (Kelemen, 2014). Kollhoff et al. (2015) was able to show in similar tests in the inlet area that the velocity fields are also similar in multiphase flows and that the second phase does not cause any fundamental changes to the flow profile.

Gothsch et al. (2015) also performed PIV measurements in microstructured homogenization units with Reynolds numbers of $Re > 10000$, i.e. turbulent flow conditions. Both behind an orifice and a microchannel with a T-mixer, he found a strong free jet with a very strong velocity gradient, similar to Kelemen et al. (2014b).

Blonski et al. (2007) investigated the droplet breakup in a microchannel with a turbulence element and performed PIV measurements upstream and downstream of the constriction. The Reynolds number in the region of the constriction is $Re \approx 8000$ so that the flow is in the transition region. The turbulence in the region behind the constriction is not very pronounced, but high shear forces could be identified in the region of the constriction. In addition to the PIV measurements to determine the flow field, CFD simulations of the flow field were performed, showing a recirculation region behind the homogenizing unit that matches the experimental measurements.

Numerical simulations on flows in flat valves have already been performed by Stevenson and Chen (1997). These simulations were performed for a very large pressure difference,

so that the Reynolds number of the flow at the inlet of the valve is already turbulent ($Re > 13000$), so that the Reynolds number in the constriction is significantly higher. The simulations performed refer to gap widths of 10 μm and 30 μm, respectively, where the velocity (u) in the gap (h) is about 3 times larger for smaller gap diameter and thus is about $u \propto 1/h$. The simulation results for the formation of a free jet behind the constriction and for the velocity or the flow field fit the measurements despite slightly different geometry and different Reynolds number than in Innings and Trägårdh (2007), but it seems that the free jet hits the impact ring due to the different geometry. This is not visible in the detailed measurements of Håkansson et al. (2011a) due to the limited field of view.

Wieth et al. (2016) performed numerical flow simulations and based on them simulations on the breakup behavior of single droplets and compared the data with PIV measurements. The simulations and measurements were performed in one of the modified orifices as in Kelemen et al. (2014b) at a Reynolds number of Re = 600 in the constriction. Similar to the experimental measurements, the elongation stress directly in front of the leading edge of the constriction is very high. In contrast to the experimental investigations (Kelemen et al., 2014b), no symmetric free jet is generated, but the free jet is deflected to a lateral wall. For the drop breakup studies, two different viscosity ratios and two trajectories of the drops were compared by different initial positions of the drops. At the lower viscosity ratio of $\eta^* \approx 2$, a more significant elongation of the droplet to a filament is achieved in the inlet region than at the higher viscosity ratio of $\eta^* \approx 14$. In both cases, the droplets are deformed significantly less when added on the axis of symmetry than when dispensed at the edge, since the droplets in this region are subjected to much stronger shear and elongation flows during entry. The droplets at the edge are further stressed in the orifice by the shear forces near the wall. As a result, they are deformed into very thin filaments, whereby individual droplet filaments disintegrate after a certain point. In and especially behind the orifice, the droplet filaments follow the flow profile and the free jet that is created, with the edge-dispersed droplets and broken filaments leaving the free jet core and being distributed over the entire wake. The droplets passing through the orifice on the symmetry axis follow the free jet and are irregularly deformed along the path of the free jet, however, no breakup was observed in the simulated region. The deformation in the turbulent region of the free jet is different for both viscosity ratios, which in addition to the viscosity difference can also be related to the different deformation or filament length generated in the inlet region and the associated different large expansion into different flow regions.

Maniero et al. (2012) simulated a pipe flow with concentric orifice at a Reynolds number in the laminar to transition range (Re = 1050 and Re = 2100, respectively) and could additionally simulate the drop breakup in the flow. The simulated results for the droplet breakup could be adapted to the experimental investigations of Galinat et al. (2006) by an adjustment at the simulation model.

In addition to these more facility-based simulations, generic simulations of droplet breakup in turbulent flow fields were performed by Cristini et al. (2003) and Komrakova (2019). Cristini et al. (2003) studied droplet breakup in the turbulent viscous flow regime, for droplets smaller than the Kolmogorv length. It was shown that the duration

of the stress due to the shear forces is also very significant, in addition to the elongation. Despite large elongation, drops can relax back to the initial state when the stress is reduced, if the stresses are of a short duration. Komrakova (2019) studied droplet breakup in isotropic turbulence. These studies show that the energy stored until the breakup of the droplet, in the form of surface energy, can vary. The observations of the breakup process could show different types. On the one hand, a simple disintegration or possibly a series of simple disintegration processes can occur, whereby secondary droplets relax after splitting from the initial droplet, or the secondary droplets can be further deformed after splitting from the primary droplet without relaxation and then disintegrate again, which would correspond to a direct disintegration cascade. In addition, there is the possibility that a stressed droplet breaks up quasi-explosively into many small droplets. With increasing droplet size and increasing turbulence intensity, the probability of a breakup cascade increases.

Eastwood et al. (2004) investigated the breakup of a dispersed phase free jet in a surrounding turbulent continuous free jet. The dispersed phase jet breaks up into individual segments very rapidly. Individual vortices similar in size to the droplet do not appear to be sufficiently strong to cause the breakup, but only lead to deformation of the droplet. When the stress is released, the drops relax. Drop breakup is only possible through interaction of multiple vortices and through the larger vortices. The droplets break up at the points where the filament is formed due to capillary forces. Accordingly, individual drops are formed at the ends and in turns or nodes. These investigations show, in comparison with those carried out in the same plant on the breakup of gas bubbles (Martínez-Bazán et al., 1999b) (Martínez-Bazán et al., 1999a), that the droplet breakup is not easily transferable to the breakup of gas bubbles.

The differences in breakup between drops and bubbles were also evident in the studies of Hesketh et al. (1991) and R. Andersson and B. Andersson (2006). Hesketh et al. (1991) studied the breakup of droplets and bubbles in horizontal pipe flow. He found that there is an active drop breakup zone at the edge region, which he determined from the edge to half the radius, and a passive core zone. Due to the significant density differences between the continuous phase and the lighter gas phase, the bubbles migrate very quickly to the active zone at the upper edge of the pipe and break up. The dispersed-phase droplets studied have a much smaller density difference, so they are distributed over the entire cross-section of the pipe by the turbulent flow motions and thus break up less strongly in the shear layer near the wall. R. Andersson and B. Andersson (2006) studied droplet and bubble breakup per se in a multiphase flow reactor in more detail and were able to see that the size distributions produced by the breakup of droplets or bubbles are significantly different. This is because gas bubbles break up into two secondary bubbles of different sizes in most cases studied. Droplets breakup into secondary droplets of mostly the same size, but the filament connecting the droplets often gives rise to one or more satelite droplets. Angeli and Hewitt (2000), similarly to Hesketh et al. (1991), investigates the breakup of droplets in a horizontal turbulent pipe flow. Droplet size was determined inline using a camera with an endoscope and an image evaluation algorithm. The resulting droplet size distribution and maximum droplet size were compared with Kolmogorv-Hinze theory, which underestimated the droplet size.

Blonski et al. (2007), in addition to his flow measurements with PIV and the numerical investigations, also carried out experiments on drop breakup with two material systems of different viscosity ratios. The comparison of the measured droplet size with those calculated according to the model of Taylor (1934) or Davies (1985) showed partly significant deviations. This illustrates the difficulties in applying the empirically determined models.

Tjahjadi and Ottino (1991) studied the breakup of droplets in a chaotic flow field. The droplets were deformed in a gap between rotating inner and outer cylinders. Since the cylinders are not concentric, but the inner one is eccentric to the outer one and the rotation direction of the cylinders is varied in time, chaotic droplet deformations could be generated. The examined droplets were stretched in the viscous flow field to very long filaments, which are wound several times around the inner cylinder. The coiled filaments break up in particularly stretched regions due to capillary instabilities, while other less stretched regions remain and are only further stretched by the flow. It is clear that the elongation and compression during the change of direction leave individual nodes or loops of the filament with significantly larger cross-sections. These spots form particularly large secondary drops. In addition, breakup of the filament in the area of the ends can occur due to the end pinching process. The experimental results could be compared with numerical simulations carried out specifically for this purpose, and good agreement was found. Overall, it was found that very large elongation ratios could be obtained due to the chaotic flow field and that several disintegration mechanisms can be responsible for drop breakup in different areas at the same time.

In technically relevant homogenizing plants, different flow regimes exist simultaneously in different areas, as shown by velocity field measurements (Håkansson et al., 2011a) (Kelemen et al., 2014b), which can lead to different breakup processes. Innings and Trägårdh (2005) performed measurements on droplet breakup in flat valves or in a flat valve model and were able to visualize the deformation and breakup processes using camera images in the different areas of the flat valve. In the inlet region, the droplets appear to be deformed into elipses by the shear and elongational flows due to the continuous narrowing of the cross-section. In the constriction, the droplets are further linearly deformed by the shear forces. Behind the constriction, the strongest deformation of the droplets occurs due to turbulent eddies. This outlet region or the droplet breakup behind the constriction is studied in more detail by Innings and Trägårdh (2007) in a slightly different geometry using double images. The double images allow to observe the very fast motion of the droplets in the free jet behind the constriction at least at two very short successive times. It becomes clear that the drops in the free jet are significantly deformed and stretched by turbulent eddies and finally disintegrate. In the backflow region surrounding the free jet, disintegrated round secondary droplets can be seen. The images of individual droplets, which can be related to each other on two successive images, show that the droplets are stressed and deformed by vortices of different sizes. Compared to the droplet, both small-scale and large-scale deformations of the droplet can be observed, indicating small-scale and large-scale vortices, respectively. Images taken slightly further downstream of the constriction show the decay of deformed droplets into fine secondary droplets.

This observation that the droplets disintegrate in the area behind the constriction also

fits the investigations of Galinat et al. (2005) in which the droplet breakup behind a concentric orifice in a tube was investigated by high speed recordings of single droplet experiments and experiments with multiple droplets. Drop breakup occurs in the region behind the constriction or orifice in more detail in the shear layer with both investigated surface stresses. In contrast to the investigations of Innings and Trägårdh (2005) or Innings and Trägårdh (2007), time-resolved high-speed recordings were performed, so that an evolution of the deformation of the droplet and the droplet breakup that may occur can be observed. In particular, the superpositions of the flow field or the local Weber number calculated from it and the drop breakup locations presented by Galinat et al. (2007) show that the drop breakup occurs in the region of the shear layer with the locally highest stresses. Maniero et al. (2012) also showed this by experimental measurements of the velocity field for drop breakup in a similar test facility, which he compared with numerically calculated stress fields.

Time-resolved breakup investigations were also performed by Kolb (2001) and Budde et al. (2002) in scaled experimental systems for high-pressure homogenization with orifices. The investigations of Kolb (2001) show again that droplet breakup occurs only in the turbulent region of the free jet. Moreover, at small Weber and Reynolds numbers, the breakup of the droplets does not seem to be as intense as at high Weber and Reynolds numbers. This is reflected in a breakup of the primary droplets that are stretched into filaments and break up into a few secondary droplets or the explosive breakup of the stretched droplet filament into very many small secondary droplets. The investigations of Budde et al. (2002) could not confirm this distinction into different breakup mechanisms. The experimental setup of Budde et al. (2002) had a 5-fold larger orifice diameter compared to that of Kolb (2001) (D_{Kolb} = 10 mm, D_{Budde} = 50 mm). In addition, the scaling in Budde et al. (2002) was done according to six defined dimensionless ratios, so that the results are transferable to other experimental plants of the same scaling principle if the ratios are the same. The experimental plant could also be used to investigate the influence of the droplet trajectory or the dosing point on the disintegration process. It was found that droplets at the edge disintegrate significantly earlier behind the orifice which fits to the earlier interaction with the shear layer. This also applies to droplets that are only slightly offset from the axis of symmetry. The influence of the viscosity ratio on the drop breakup is shown by the significantly later disintegration that occurs in drops with a high viscosity ratio. This may be due to the fact that the droplets are deformed less strongly or less easily.

Kelemen et al. (2015) complemented the velocity field measurements carried out in the optically accessible original-scale orifice with extensive studies on droplet breakup (Kelemen et al., 2014b). The results of the droplet deformation investigations show a clear influence of the viscosity ratio on the droplet deformation in the inlet region under otherwise identical conditions, where the droplets of the material system with lower viscosity ratio are significantly more deformed. In the wake region downstream of the orifice, both the influence of the viscosity ratio (η^* = 2 and η^* = 14, respectively) and the influence of the Reynolds number were studied, with Reynolds numbers in the laminar and transition region (Re = 285 and Re = 1280) (Kelemen et al., 2014b).

The data show that with the low Reynolds number and the comparatively low viscosity ratio, the droplet leaves the orifice as a long stretched filament. Due to the low

turbulence, the free jet remains stable over a wide range and expands only very slowly. As a result, the droplets hardly experience any turbulent stresses. Therefore it is possible for the droplets or filaments to break up very far downstream as a result of the Plateau-Rayleigh instability mechanism into fine droplets of approximately the same size. This disintegration mechanism is shown by the straight lined up fine secondary droplets which are visible downstream from a length of 40 orifice diameters of the free jet. It is also clear that not all drops have disintegrated at this point, as filaments are partially visible. In the case of the higher viscosity ratio, the elongation of the droplets at the outlet of the orifice is significantly lower because the shear and elongation flow, which are sufficiently large to achieve a large elongation at the lower viscosity ratio, are not large enough to achieve a comparable elongation. In the other observation areas behind the orifice, no drop breakup is seen at these conditions. Nevertheless, it is clear from the visual comparison and from the drop size distribution measurements performed that the droplets are significantly larger than at the lower viscosity ratio, but smaller than the primary droplets, i.e. breakup must have occurred. In the experiments with the higher Reynolds number, the low-viscosity droplets are stretched before and in the orifice to form very long filaments, which can be seen at the outlet of the orifice. Already at this measuring position, it is clear that individual filaments are deformed by vortices, which can be recognized by droplets deformed transversely to the main flow direction. In the downstream measuring position, a chaotic deformation of the drop filaments due to the turbulent eddies can be seen. At the higher viscosity ratio, the elongation of most of the droplets flowing centrally through the orifice is again significantly lower. Only individual droplets at the edges are very strongly elongated. In the further course of the free jet, the droplets are deformed and stretched by the turbulently decaying free jet, i.e. the interaction with vortices. In the comparison of the droplet size distribution at the higher Reynolds number, the difference in the droplet size distribution is also visible with significantly larger droplets at the high viscosity ratio.

2.3. Improvements in the homogenizing process with orifices

Orifice type homogenizers were first discribed by Stang et al. (2001). Since then this homogenization unit has been widely used in research.

2.3.1. Geometric improvements

As described previously, when orifices are used as disintegration units, the flow rate is directly coupled to the pressure drop across the orifice. In contrast, with flat valves as disintegration units, the gap width can be changed and thus the flow rate can be adjusted with the same pressure loss. On the one hand, this means greater flexibility; on the other hand, the flow regime may change due to the variation of the gap width. This can mean that the achieved droplet size is also changed as a side effect by changing the throughput at the same pressure drop. In order to increase the throughput of orifices, many different approaches exist, such as numbering up, where the distance between the orifice holes is important for the size reduction result (Aguilar et al., 2004) (Aguilar et al., 2008) (Karasch and Kulozik, 2008).

Aguilar et al. (2004) investigated the influence of the orifice diameter on the droplet size distribution. These investigations, which were also carried out as a function of the energy density, show a trend towards poorer homogenization efficiencies with larger orifice diameters. They also carried out various investigations with other orifice geometries in order to increase the homogenization efficiency. At low energy densities, rounded leading edges led to a deterioration in efficiency. Only at high energy densities do the results of the orifice with rounded inlet edge and sharp-edged orifice equalize. In addition, the effect of two or more inclined orifices on the resulting droplet size distribution was investigated. The orifices were oriented in such a way that the free jets generated at the outlet of the orifices collide downstream. In addition to the influence of the number of boreholes, the influence of the borehole angle and thus the angle or the location where the free jets collide was also investigated. Both an increase in the bore angle and thus an earlier impingement of the free jets and an increase in the number of bores lead to an improvement in homogenization efficiency at the same pressure loss. Karasch and Kulozik (2008) also investigated the influence of inclined orifices. It could be shown that regardless of the disperse phase fraction at constant pressure drop, four converging jets from round orifices are more efficient than two round orifices, but no geometry parameter apart from the orifice angle was kept constant in this comparison. An orifice variant using two slotted holes at the same orifice angle proved to be even more efficient. This variant produced the smallest droplet size distribution with the same orifice circumference to orifice cross-sectional area ratio as the variant with four round orifices.

2.3.2. Process changes

A fundamentally improved concept for homogenizing milk, for example, was presented by Köhler et al. (2007). In this new process, instead of a low-concentration raw ma-

terial stream, a high-concentration disperse-phase stream is to be passed through the homogenizing unit. Downstream of the orifice, the free jet is diluted to the original composition by a feed line containing the continuous phase. The new process method is called "simultaneous homogenization and mixing" (SHM) according to the substeps. This process approach significantly reduces energy requirements, since only a partial stream needs to be pressurized to high pressure. Various modes of operation have been presented for this process approach (Köhler et al., 2010) (Köhler and Schuchmann, 2012), which basically differ in whether the disperse phase is added as a pure stream or as a pre-emulsion. In addition, the line routing can be varied. Thus, the continuous phase or the disperse phase can be fed through the orifice or through the entrainment point. A flow simulation was carried out for this approach (Köhler et al., 2007). The distance of the mixing point to the orifice and the influence on the velocity field or the turbulence distribution was investigated. Supplementary, experimental tests were carried out in a test facility. The advantage of using the SHM process was demonstrated. In a further series of tests, the distance between the mixing point and the orifice was varied experimentally and the influence on the droplet size distribution or the droplet size was investigated. The optimum dosing point was found to be approximately 35 hydraulic orifice diameters downstream of the orifice (Köhler et al., 2007). In the further investigation (Köhler et al., 2009) a rectangular and a round orifice were compared. Especially at higher pressure differences, the rectangular orifice proved to be slightly more effective. However, direct comparison is difficult because the orifices differ not only in shape but also have different dimensions.

The distance of the mixing point to the orifice was also investigated by Kempa et al. (2006). In these investigations, the stabilizer was dosed into the free jet only after the orifice. It was shown that in the area directly behind the orifice, dosing leads to similar droplet size distributions as in the standard process, in which the emulsifier is also passed through the orifice. This shows that the emulsifier does not necessarily contribute to the breakup of the droplets, but mainly to the stabilization of the broken up droplets.

Hecht et al. (2013) was able to show by experiments that the concept of separate routing more accurately dosing the disperse phase behind the orifice into the free jet, has a similarly good homogenization efficiency at higher pressure differences than the original homogenization process. This is particularly important since wear is thus reduced by the use of nanoparticle solids, which are used for stabilization and do not have to be passed through the orifice in this process design. In addition, this shows that pre-elongation of the droplets by the shear and elongational flow is not essential for droplet breakup. The reduced material wear as well as the reduced energy consumption, make this process very interesting.

Sauter and Schuchmann (2008) investigated the applicability of this process to the deagglomeration or breakup of nanoparticle aggregates i.e solid particles. It could be shown that the process is very well suited to break up the aggregates and agglomerates, whereby the energy efficiency is higher than with the standard process.

2.3.3. Double stage orifices

Kolb (2001) developed a very efficient disintegration unit by connecting two eccentrically installed orifices in the flow channel where the orifices were not on one axis, but offset from each other. This multi-stage disintegration process has since been widely used and scientifically investigated. Kolb (2001) varied the size of the orifice bore, the distance between the orifices, and the number of orifices (1–3) in the investigations. It became clear that the bore diameter of the second stage should be larger than that of the first stage and a third stage does not lead to further improvement. Similar results were also obtained by Finke et al. (2014) in microchannels. In the investigations carried out by Kolb (2001), it was shown that two-stage process operation is more efficient than single-stage process operation, regardless of the differential pressure. This was also shown in the investigations of Schlender et al. (2015a) where even at a very high backpressure, i.e. a Thoma number of $Th = 0.75$ and accordingly a pressure drop in the first orifice of only 25 % smaller droplet sizes were achieved compared to the single stage process without backpressure. The orifice bore ratio and thus the generated backpressure was systematically investigated by Freudig et al. (2003). It was also shown that a conical outlet of the first orifice increases the throughput. Without conical expansion, a free jet of about 5–8 orifice diameters in length is formed behind the first orifice and the intermediate space between the orifices corresponds to a mixing chamber, with high collision probability of droplets, but at the same time only very short collision time, so that coalescence is unlikely (Finke et al., 2014). The influence of the turbulent mixing chamber was also studied by Kolb (2001). The distance between the stages was very short but due to the eccentric and also non-axial arrangement of the orifices, there was no simple flow through the 2nd orifice as in the case of Finke et al. (2014). It was shown that a residence time increase in the mixing chamber leads to a smaller droplet size distribution. In addition, the advantage of the multistage process is independent of the speed of the emulsifier used. Köhler et al. (2009) were able to show through their experiments on SHM orifices that the addition of emulsifier is also very efficient downstream of a two-stage orifice unit and that, in particular with short feed point distances to the second orifice, smaller droplet sizes are achieved than with single-stage process designs.

In a test facility with two orifices connected in series or a pressure tank behind the first orifice to generate the backpressure, Schlender et al. (2015a) were able to show that the second orifice is not relevant for drop breakup up to Thoma numbers of $Th > 0.5$, i.e. this takes place almost exclusively in or behind the first orifice, and the second orifice has the purpose of cavitation suppression by the backpressure obtained.

Karasch and Kulozik (2008) used a two-stage orifice consisting of two orifice stages with two orifice bores inclined at 60° so the free jets collide and was able to practically prove the advantages of the two-stage process design for milk and cream homogenization, respectively. The orifice diameters were selected in such a way that a Thoma number of $Th = 0.15$ was achieved.

2.3.4. Passive flow control

Most research on passive flow controll is done on air flows. In the following a brief literature overview is given.

There are various applications where a flow is to be influenced by certain measures in order to achieve a preferred flow shape. For this purpose, both active measures such as blowing jets or passive measures such as tripping devices are suitable. Seiferth (1946) was one of the first to investigate the influence of passive flow control devices on the free jet. For this purpose he mounted a metal ring on the outlet of the nozzle. The ring is cut in the direction of flow, so that segments can be bent alternately inwards and outwards. This structure significantly reduced the vibrations of the free jet.

The variation of the contraction angle at the end of the nozzles was investigated by Bradbury and Khadem (1975). They found that a contraction angle of 45° resulted in a shortened free jet compared to a contraction angle of 10°. Compared to the undisturbed case, the smaller contraction angle also led to a slight improvement. They also investigated the influence of tabs on the length and velocity distribution of the free jet. Investigations with different numbers of tabs on the circumference showed that the number of tabs has a clear influence on the free jet. The smallest effect compared to the original free jet was observed when using eight tabs. The reduction of the number of tabs to four or to only two tabs led to a significant improvement, i.e. reduction of the free jet core length from six orifice diameters to only two orifice diameters.

Samimy et al. (1993) as well as Mi et al. (2007) could confirm these results, i.e. the influence of the number of tabs, by visualizing the free jet cross section. Zaman et al. (1994) could show by visualizations of the free jet that tabs angled in flow direction work much better than tabs perpendicular to the flow direction. The tabs create a pair of counterrotating vortices turning from the bottom of the tab up to the tip of the tab. Furthermore, the structural height of the tabs in relation to the shear layer thickness was identified as a very important feature. If the tabs rise above the shear layer, this leads to the formation of finger-like structures of the shear layer, thus increasing the shear layer volume.

In accordance with these studies, Island et al. (1998) identified that triangular tabs have the greatest influence on the flow. Isomoto and Honami (1989) investigated the influence of the turbulence intensity of the flow in connection with the reattachement length behind backward facing steps (BFS) and found that higher turbulence leads to increased mixing and a shorter reattachement length. Foss and Zaman (1999) investigated various passive flow control devices and confirmed the findings that tabs are most effective. In addition, the spacing (sp = center to center) of the tabs was investigated, which is particularly important for 2D geometries. They found that with a spacing of $3sp$ or more, the tabs act as individual tabs and a spacing of $1.5sp$ causes the greatest effects. The effect of the tabs is based on the fact that the tabs break up large structures and increasingly create smaller structures.

Park et al. (2007) investigated the mixing behavior and the influence of tab size and spacing and confirmed the special efficiency of the tabs in terms of mixing and improved entrainment. McCormick and Bennett (1994) also investigated the mixing behaviour,

especially of two parallel flowing fluids and identified the Lobed Mixer, which was also investigated by Mengle (2005) on jet engines, as particularly efficient. On rocket stages Schrijer et al. (2010) investigated chevrons, and Bolgar et al. (2019) and Kim and Samimy (1999) investigated different passive flow control devices in high speed air jets. The aim of these investigations is to keep the reattachement length as short as possible due to a fast expansion of the free stream or the fast expansion of the shear layer. In addition to these rotation-symmetric BFS investigations, Kang and Choi (2002) for example conducted experimental and Neumann and Wengle (2004) numerical investigations on 2D BFS.

Lemenand et al. (2005) investigated the effect of tabs on the mixing performance in a straigth pipe flow. Inside the pipe four arrays of four trapezoidal shaped tabs arranged evenly each 90° of the pipe circumference improved the mixing. As in airflows the tabs seem to create vorticies that transport low momentum fluid from the wall inward and vice versa which increases turbulence downstream of the tab. The mixing performance was shown by single phase flow profile visualisations after several tab arrays, PIV measurements at the wake region of the last tab and droplet breakup investigations. The droplet breakup investigations showed that the Sauter diameter is proportional to the maximum turbulent kinetic energy and not the mean turbulent kinetic energy. Lemenand et al. (2017) connected the findings on the turbulent homogenisation process in this setup to the Kolmogorov-Hinze (Kolmogorov, 1949) (Hinze, 1955) framework.

The investigations presented here show that it is possible to modify an existing flow field even by making small changes to the flow control, so that, for example, higher turbulence or better mixing behavior can be achieved. With regard to drop breakup, however, it has not been conclusively clarified what an optimum flow field for efficient breakup must comprise. Therefore, the aim of the work presented in the following is to investigate the drop breakup in detail in an optically very accessible test facility using high-resolution spatial and temporal measurement methods. For this purpose, individual parameters such as the Reynolds number and the viscosity ratio are varied in the standard homogenization setup, but modifications are also made to the standard setup in which the drops flow through the orifice plate, so that individual aspects of the drop breakup can be systematically investigated in a focused manner.

3

Measurement techniques

3.1. Flow field characterization

The determination of the velocity fields along the main flow direction was performed using Particle Image Velocity (PIV) (Raffel et al., 2018). The evaluation of the particle image zpairs was performed with the commercial software Davis 8 from Lavision GmbH and a standard evaluation algorithm with adaptive interrogation window size. The final interrogation window size for all evaluations was 16 pixel × 16 pixel with a interrogation window overlap of 50 %.

The determination of the velocity fields transverse to the main flow direction was performed by means of Particle Tracking Velocity (PTV). The evaluation of these particle image pairs was performed with a combination of a Davis 8 algorithm for particle position determination and the calculation of the velocity fields based on these particle positions with a Matlab algorithm based on the nearest neighbor principle.

The post-processing of all vector fields, and if necessary the combination of vector fields from several cameras, was performed using custom Matlab algorithms.

3.2. Drop visualization

The basic shadowgraphy method uses a strong light source to archive a homogeneous volumetric illumination and a camera to visualize objects in the measurement volume. The light source is precisely aligned with the camera, so any objects between the camera and the light source cause shadowing on the camera sensor. Figure 3.1 illustrates the basic shadowgraphy setup.

This process is particularly suitable if the particles to be imaged are solid, as they completely block the light. For gas bubbles, this method is also suitable because reflections occur on the surface – especialy close to the edges of the structure – which prevent light from passing through the bubble and thereby lead to shading. In contrast, oil droplets in an aqueous continuous phase can be optically denser than the ambient phase, which is why total reflection of light at the phase interface does not occur in convex droplet cross-sections. Figure 3.2 illustrates the refraction processes at the phase interface of droplets or bubbles for different phase constellations.

As the oil is also transparent, the shadow produced is not particularly strong. This results in a very low signal to noise ratio so the oil drop is hardly visible in comparison to its surroundings. Therefore binarization of images for automated image evaluation becomes complicated.

By colouring the disperse phase with a dye it would be possible to make the drops less transparent and thus intensify the shadow. This could be problematic because the addition of a dye might influence the surface tension and especially not completely dissolved dye particles could promote drop breakup. This would make the measurements obsolete. However, in order to improve the visualization of the oil droplets in the aqueous phase, a new method was developed which exploits the existing refraction of the light at the phase interface and functions without additives. This method uses a spatially periodic background gradient instead of a homogeneous background light. This background is distorted by the refraction of light at the drop interface, making the edges of the drop more visible.

Figure 3.3 shows an example of the improvement in visualization. Image a) shows an

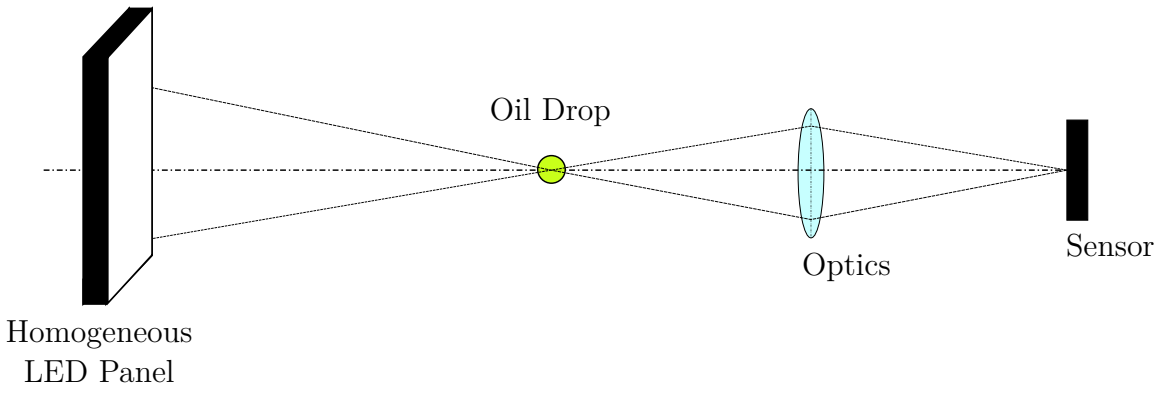

Figure 3.1: Scematic representation of the basic shadowgraphy setup.

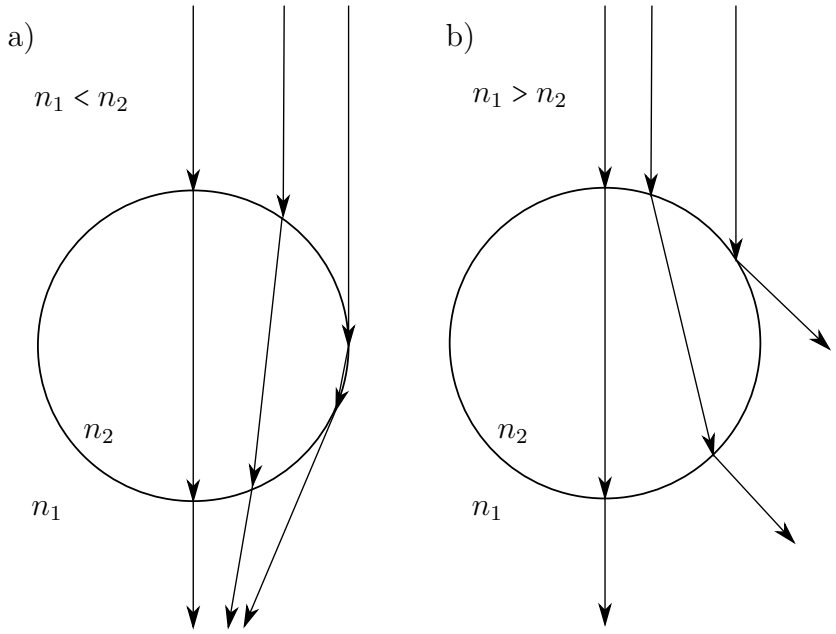

Figure 3.2: Refractive scheme for two different combinations; a) refraction on optically denser droplets, b) refraction on optically thinner droplets or bubbles.

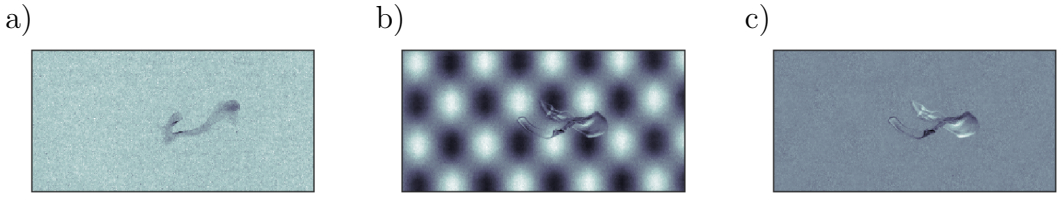

Figure 3.3: Comparison of the two visualization methods; a) basic shadowgraphy image, b) shadowgraphy image with background pattern, c) shadowgraphy image with background pattern subtracted.

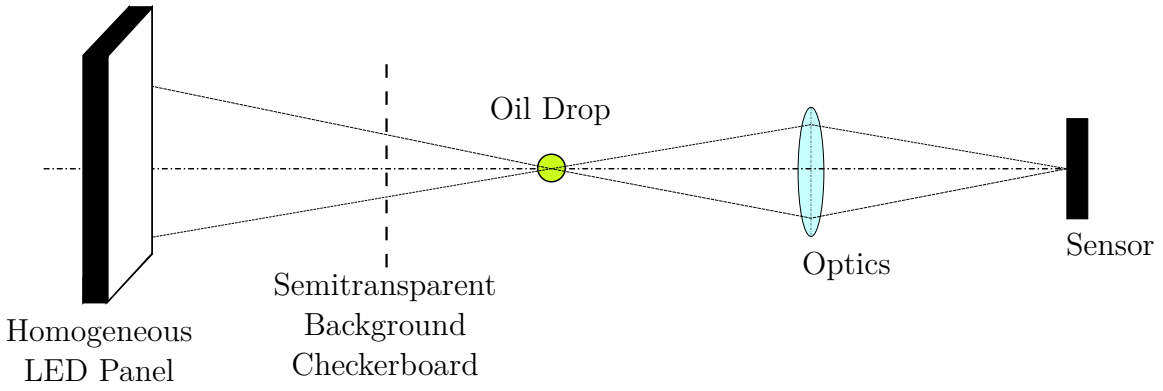

Figure 3.4: Scematic representation of the novel shadowgraphy setup.

oil drop against a homogeneously illuminated background. The twisted drop filament, especially the thinner part, is hardly recognizable, because the shadow is not very pronounced and the signal to noise ratio is high. In image b) a much more twisted drop is recognizable and especially the edges are clearly distinguishable. In the edges of the drop filament, the effect of light refraction is particularly pronounced and therefore leads to the clearest distortion of the background. The spatial periodicity of the background is also clearly visible. In image c), the background is subtracted, so that only the drop is visible. This image can be binarized for further evaluation steps.

Figure 3.4 schematically shows the experimental setup for the new, modified shadowgraphy method. A semitransparent checkerboard pattern is placed between the homogeneous light source and the measurement volume.

As can be seen in Figure 3.3 b), the background pattern appears as a periodic gray value distribution. This is generated by inserting the regular semitransparent checkerboard pattern into the light path. Since the depth of field of the camera system does not reach the position of the background pattern, it automatically appears defocused with blurred edges. If the background pattern would not already appear defocused due to the positioning, a pattern without edges but with transitions would have to be used. Besides the transitions, the size of the checkerboard pattern is also crucial for an optimal visualization. The goal is to achieve a constant periodic gray value distribution. Patterns that are too large cause a pattern with constant light and dark areas separated by a transition area. Within the constant bright or dark areas, visualization is only possible using the standard shadowgraphy method. Too small areas compared to the object to be visualized lead to a kind of noise of the background pattern so that visualization is difficult.

Figure 3.5 shows a schematic intensity profile through a background pattern with too large, too small and optimal size ratio of the checkerboard pattern.

In addition to the size of the checkerboard pattern, it is found that the orientation of the pattern is also important for the visualization of the oil droplets in the high pressure homogenizer. Along the axes of the regular checkerboard pattern, there are areas where defocusing creates a blurred region where the intensities of the background

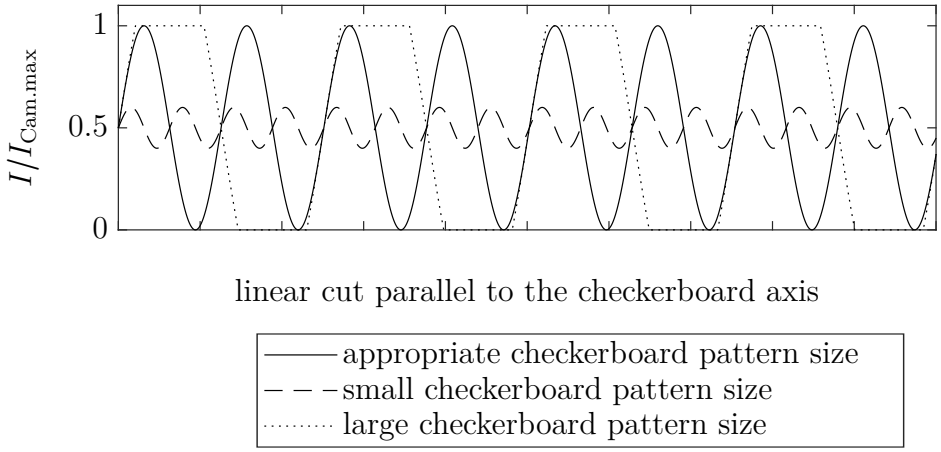

Figure 3.5: Scematic representation of a grey-value distribution of the background pattern.

pattern fluctuate periodically in the middle intensity range. On average, the drops move along with the free jet mainly parallel to the axis of symmetry of the orifice. If the axis of symmetry of the orifice and one axis of the checkerboard pattern are parallel to each other, drops can enter the range of low background contrasts and remain largely invisible for long distances. This effect is further enhanced by the fact that the elongation flow in the orifice stretches the drops into straight filaments, which are also aligned parallel to the axis of symmetry without further influence. By rotating the background pattern by 45°, the axes of the background pattern and the symmetry axis of the orifice, and thus the main direction of motion of the drops, are no longer parallel, so that the drops can be visualized much better. The zones of poor contrast are passed by the drops only for a short time, so that the gaps in the drop detection can be filled by a temporal interpolation. Figure 3.6 shows the differences in the background pattern caused by the changed orientation. The green lines mark the orientation of the main axes of the checkerboard pattern. The line plots below the checkerboard patterns represent the gray value profiles along the lines shown above. In case a) the amplitudes along line 1 and line 3 are very large, because the maximum contrast of the camera illumination system can be used. However, line 2 shows that the contrast in the intermediate area between the maxima disappears completely and therefore visualization along this axis is not possible in this area. In case b) all profiles along the drawn lines have the same amplitude. Only the average intensity changes. Compared to case a), only half the maximum amplitude can be used, but this disadvantage is clearly outweighed by the better visualization.

Since a printed film is inserted into the beam path for this measurement method, reflections occur on another surface and the light arriving at the camera is attenuated. Particularly in the case of high-speed images with short exposure times, the light intensity is a decisive factor in addition to the homogeneity.

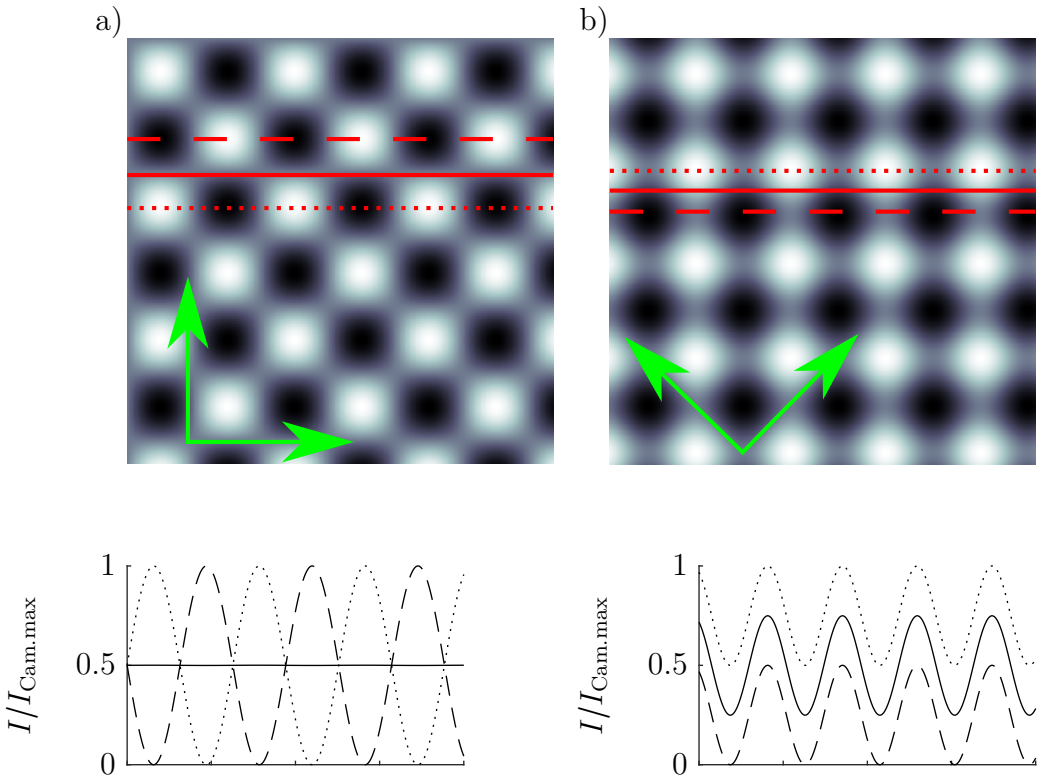

Figure 3.6: Comparison of the different orientation of the checkerboard pattern and the resulting low-contrast axes. The green lines mark the axes with low contrast. a) horizontally aligned checkerboard pattern; b) checkerboard pattern rotated by 45°.

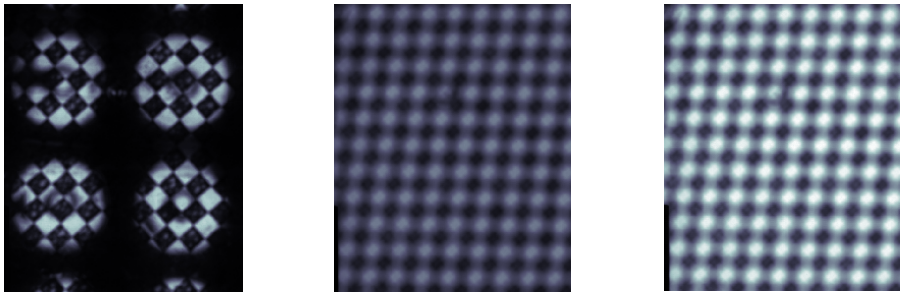

Figure 3.7: Comparison of LED illumination for the shadowgraphy method. a): LED-array; b) high-luminance panel; c) high-directivity panel.

A high power LED (ILM-501CG, Hardsoft) with an LED array of 5 × 15 LEDs on an area of about 0.15 m × 0.45 m, and green light color, with a constant, i.e. unpulsed total electrical power of up to 2000 W (approx. 3 W/cm^2) proved to be unsuitable despite very high light output because no homogeneous light was emitted, and no suitable diffuser was found or the light output was no longer sufficient when diffuser plates were used. As an alternative to these LED arrays, very homogeneous LED panels (TH2 Series, Vision Light Tech) with white light color can be used. These have an area of 0.14 m × 0.105 m and an electrical power consumption of 28 W. Despite significantly lower theoretical power density, these LED panels are much more suitable for shadowgraphs due to their homogeneity and the resulting elimination of losses in the diffuser. The LED panels are available in a "high-luminance" and a "high-directivity" version. The "high-directivity" variant proved to be more suitable, since fine structures in particular are better resolved and, in addition, the light intensity measured by the camera sensor is greater. It should also be noted that with the shadowgraphy method, the images are taken directly against the light source, so that volumetric illumination is not necessary.

Figure 3.7 shows images of the background pattern for direct comparison of the light sources. It is very clear from the image of the background pattern illuminated with the LED array that the light is distributed very inhomogeneously, so that a continuous image of the drop is not possible. In comparison, the two images with the LED panels are very homogeneously illuminated over the entire recorded area. However, the comparison of the intensities based on the displayed background images is not directly possible without restrictions. The LED array is many times brighter, so that the exposure time at the minimum LED illumination level is so intense that the exposure time has to be shortened to the minimum possible intensity compared to the other two LEDs. In addition, in the comparison shown, the aperture of the camera lenses is almost completely closed when recording with the LED array. At the lowest intensity level of the LED array, the intensity in the exposure peaks is greater by a factor of approx. 175 than at the brightest LED panel level. The two images with LED panels

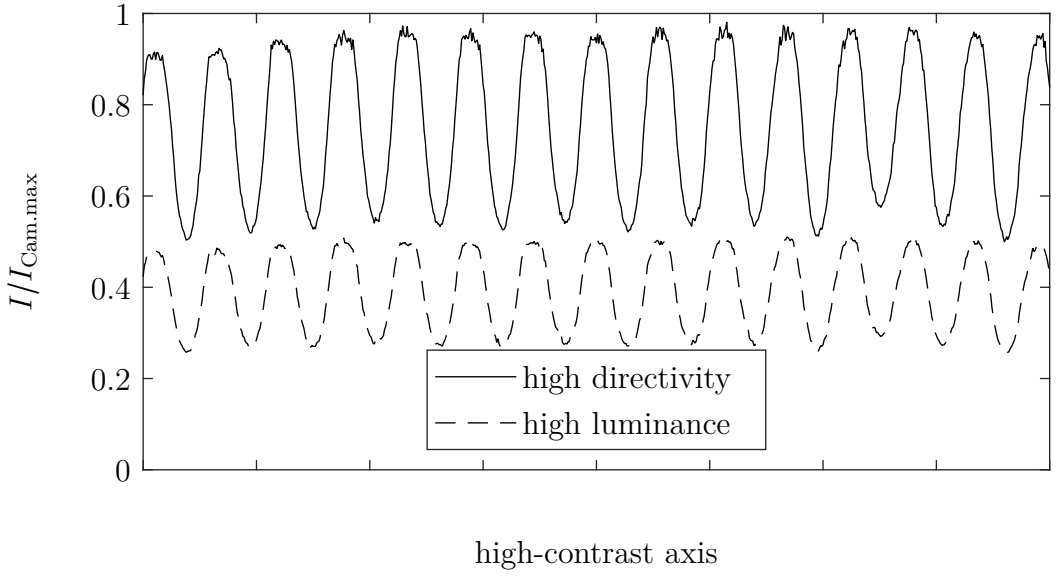

Figure 3.8: Comparison of light intensity and amplitude of the two LED panels.

are taken at the same illumination settings so that the intensity can be compared. For this purpose, Figure 3.8 shows the intensity distribution along the most illuminated axis.

The comparison clearly shows that the "high-directivity" variant of the LED panel is significantly brighter and therefore better suited for shadowgraphy imaging. In addition to the absolute intensity, which is greater with this LED, the amplitude between the area shadowed by the background pattern and the unshadowed area is also greater, so that a stronger background gradient is present for drop visualization.

For the detection of the drops on the images taken by this method, an evaluation algorithm was developed in Matlab, which can detect and mark the drops. As shown in the illustration of the measurement procedure (see Figure 3.3), the background is subtracted from the single image to visualize the changes and thus the extent of the drop. As a background image, a mean image is calculated from about 1500 successive recorded undisturbed images. In this way, vibrations of the camera and the illumination are covered at least once for all recording rates used. In the next step, this background image is subtracted from all droplet images and the absolute value of the resulting droplet images is formed. Depending on the areal extent of the droplets on the camera images, a threshold value is determined. This threshold is adaptively adjusted to the images and is typically in a range that falls below 98 % – 99.8 % of the gray values present in the image. With this threshold, the droplet images are binarized. These binarized images (with the dimensions $W \times H$) are further processed to reduce the existing noise and to highlight the drops more clearly. The binarized images contain on the one hand pixels marked as drops, which actually only exceed the threshold due to camera noise, and on the other hand not all areas of the drops are marked, because on the one hand they are also below the threshold due to camera noise and on the other hand they are in the area with too low background contrast. To correct these errors,

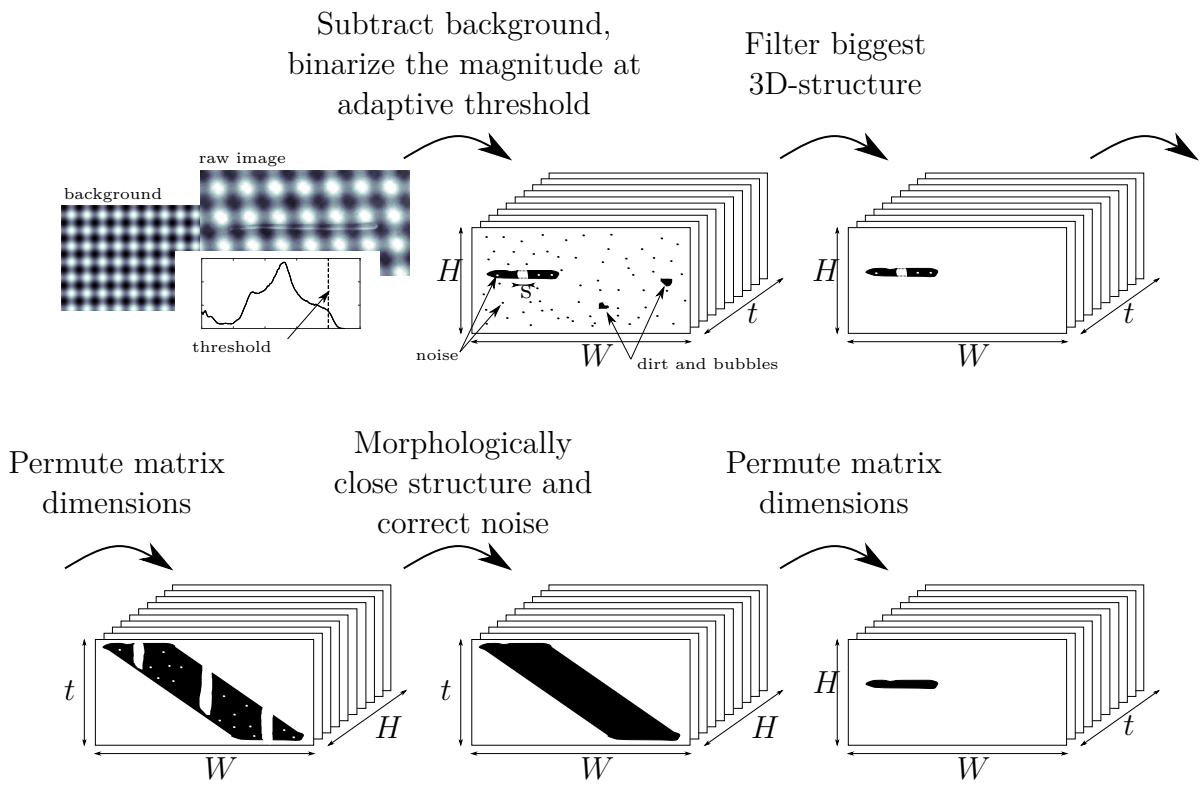

Figure 3.9: Scematic representation of the image evaluation algorithm.

the time series of the images is taken as a third dimension ($W \times H \times t$). A 3D filter detects connected structures in the binary data. Since the temporally continuous and possibly breaking droplet is the largest 3D object, this object could be extracted and the remaining structures discarded as noise or dirt particles or air bubbles contained in the flow. The resulting structure still does not represent the drop correctly, since pixels not marked by noise are missing and drop segments without background contrast have not been binarized. These two sources of error can be partially eliminated by a morphological filter. For this purpose, the 3D dataset is restructured so that the two-dimensional morphological filters obtain many two-dimensional matrices with a spatial axis (W or H) and the temporal axis (t) as dimensions ($t \times W \times H$).

The length or size of the morphological filters can be calculated from the theoretical flow velocity of the acquisition frequency and the scaling of the images as well as the size of the poorly contrasted areas (s). After this processing step, the datasets can be transformed back to the initial form ($W \times H \times t$). The algorithm is shown schematically in Figure 3.9. Figure 3.10 shows an example of the application of the algorithm.

It can be seen that the subtraction of the background pattern leads to the drop structures becoming clearly visible. However, the problem with very fine structures, which are created during the drop breakup, also becomes visible. Larger structures can be detected and masked very well by the masking algorithm. Smaller structures of only a few pixels in diameter are difficult to mask, partly because of the size itself, but also because of the poorer shading caused by the small size.

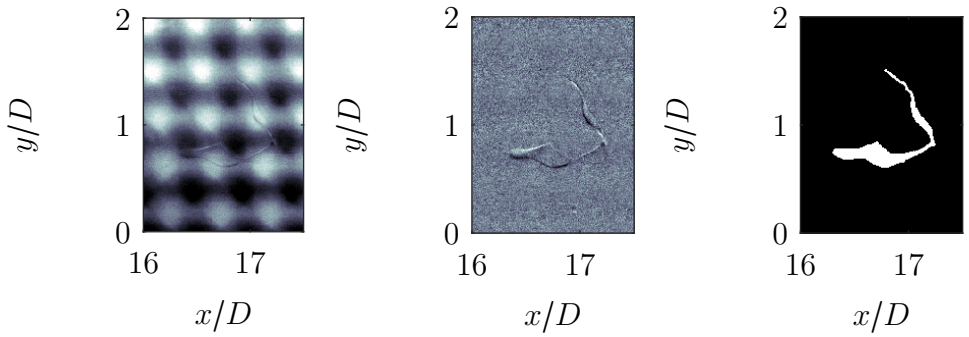

Figure 3.10: Example of the application of the masking algorithm.

For the 3D reconstruction of the drop, when using multiple cameras focused on the same volume (e.g. viewing from the side and from the bottom), the drop masks created from the shadow images are used. With the help of pinhole calibration, it is possible to project the drop mask into space according to the linear light beam propagation. This is done for the two corresponding cameras. The three-dimensional measurement space is mapped by a voxel space. The edge length of the voxels is given by the resolution of the cameras in the measurement volume, which was determined based on the callibration. According to this principle, the droplet position in space corresponds to the area of ray overlap of the two projected droplet mask rays. Figure 3.11 illustrates the method of calculation. The figures on the left represent the individual camera images of the side view and the bottom view. The Figure on the right shows the three-dimensional measurement space, with only the rays calculated from the two images. The colors of the rays correspond to those in the two-dimensional individual images and are only used for the purpose of clarification. The area where the rays overlap, the calculated drop position, is marked in black. Since the droplets are very small compared to the experimental setup and the measuring distance of the cameras, only the central area of the beam overlap is shown. Due to the simultaneous callibration of the two camera positions, the coordinate system is rotated by 45° around the x-axis.

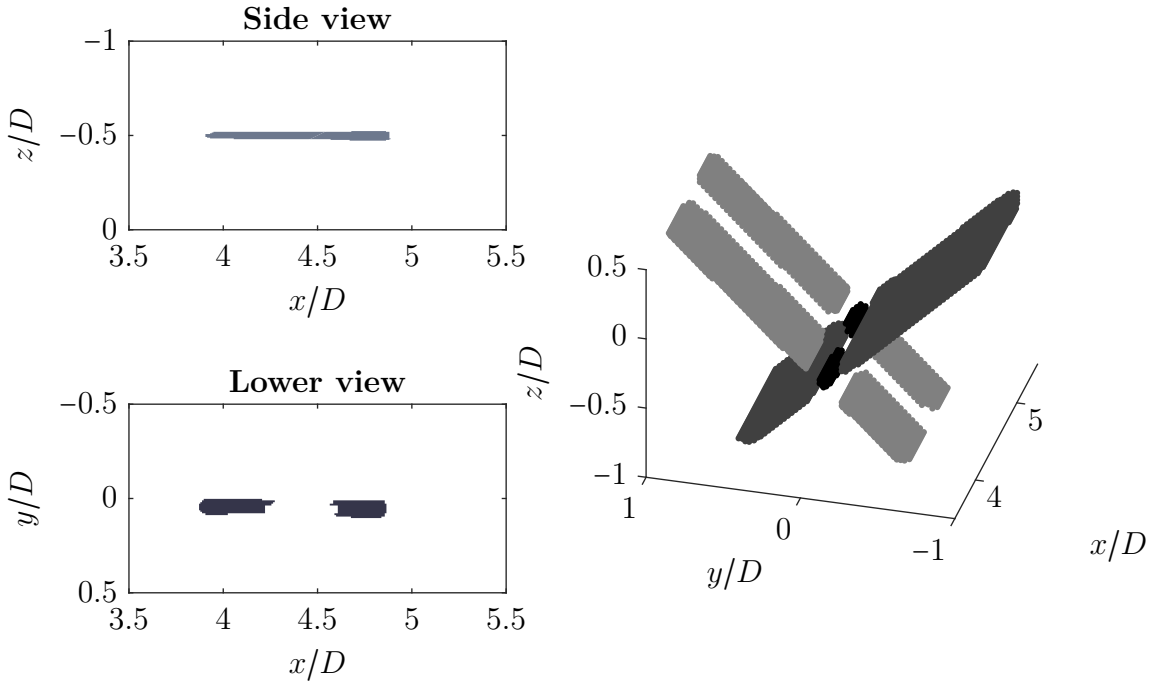

Figure 3.11: Illustration of the 3D reconstruction mechanism. Left side: 2D single-camera views of the drop filament; right side: 3D-reconstruction with two Projections (grey) and the intersecting 3D reconstructed drop filament (black).

4

Experiments

4.1. Test plant

Since the aim of this work is to understand the mechanisms relevant for droplet breakup in the emulsification process, measurements were done in a homogenization apparatus. The homogenizer used was a scaled up version of an original size homogenization unit with an orifice as disintegration unit used in industry or laboratories. The scale up factor was 50, thus the geometric length dimensions were 50 times larger than the original. This was done because in the original scale breakup processes happen on a very small spatial scale with orifice dimensions on a micrometer scale and are extremly fast (up to several hundred meters per second). By enlarging the homogenization unit ongoing processes could be analyzed by means of optical high-speed measurements and a higher spatial resolution. Figure 4.1 shows a schematic sketch of an orifice. The relevant length dimensions and the origin of the coordinate system are indicated. The orifice diameter (D) and the diameter of the inlet channel (D_i) were constant for all investigations done. The diameter of the low pressure channel after the orifice (D_o) could be changed. The length of the cylindrical orifice part was always $2D$ long. The radius of curvature at the orifice leading edge was also $2D$ if present. The conical inlet angle α was 60° or 120° if present.

In addition to the geometric enlargement, an attempt was made to keep relevant process parameters constant. This was possible by changing the material properties viscosity η and density ρ of the two phases (disperse phase d and continuous phase c) and also adjusting the materials interfacial tension γ. The process parameters like the pressure difference across the orifice Δp and the size of the primary droplets d_P were adjusted too. These changes enable to keep a set of six dimensionless numbers constant when comparing the original process and the scaled up process: The Reynolds number Re (see equation 4.1), the viscosity ratio η^* (see equation 4.2), the density ratio ρ^* (see equation 4.3), the pressure ratio Δp (see equation 4.4), the drop size ratio d_P^* (see equation 4.5) and the outlet channel size ratio D_O^* (see equation 4.6).

$$Re = \frac{D\sqrt{2\Delta p \rho_\mathrm{c}}}{\eta_\mathrm{c}} \tag{4.1}$$

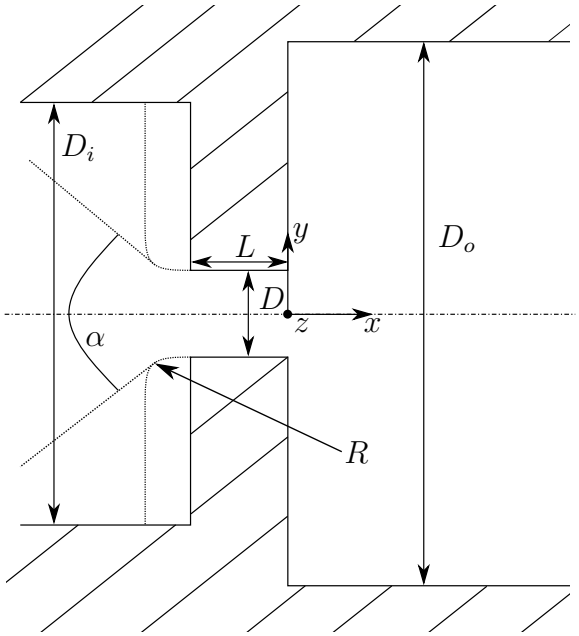

Figure 4.1: Sketch of an orifice with definition of the length dimensions.

$$\eta^* = \frac{\eta_\mathrm{d}}{\eta_\mathrm{c}} \tag{4.2}$$

$$\rho^* = \frac{\rho_d}{\rho_\mathrm{c}} \tag{4.3}$$

$$\Delta p^* = \frac{2\Delta p D}{\gamma} \tag{4.4}$$

$$d_\mathrm{P}^* = \frac{d_\mathrm{P}}{D} \tag{4.5}$$

$$D_\mathrm{o}^* = \frac{D_\mathrm{o}}{D} \tag{4.6}$$

The characteristic times could not be kept constant during scale up. That's why drop-drop-collisions and coalescence phenomena could not be investigated in this project, thus the disperse phase ratio was extremely low. The objective in the development of the measuring section and the test stand was to achieve the broadest possible optical accessibility. The test section is therefore made out of glass and acrylic glass. All other parts are constructed of stainless steel and the flexible pipes consist of plastic.

The test plant of the scaled up high-pressure-homogenizer is designed as a closed circuit in which the continuous phase is circulated. The primary drops of the disperse phase are

injected into the circuit just before the homogenization unit or right after. The plant is driven by a frequency controlled centrifugal pump (CME10, Grundfos, Bjerringbro, Denmark). Compared to displacement pumps, this has the advantage that the flow is virtually pulsation-free. A one-way valve is connected to the pump to dampen any pressure fluctuations that may occur. The use of the centrifugal pump, which is actually designed for high volume flow and low pressures, is possible because the operating pressures are not very high due to the scale up of the system. The pressurized continuous phase is forced through a filter to remove dirt and particles larger 30 μm before entering the measurement section. The filter can be switched on or off by a bypass. An inductive volume flow sensor for monitoring the pump is integrated in the supply pipe to the measuring section. The inflow to the measuring section should be as homogeneous as possible, therefore the cross-section of the supply pipe to the measuring section, which is circular and 100 mm in diameter, widens conically from the pipe diameter.

The first version of the inlet channel had a step-shaped diameter extension from the pipe diameter of 25 mm to the inlet channel diameter of 100 mm. Due to the fact that this variant leads to an inhomogeneous inlet flow profile, a new inlet pipe was designed and manufactured. This is conically widened with an opening angle of 9°. After the widening a flow straightener with an length to diameter ratio of 87.5 is integrated into the supply line. The feed line of the disperse phase is also integrated into the supply line.

In order to avoid turbulence and to ensure a smooth flow, the disperse phase feed line is shaped like a NACA 0012 airfoil. This feed line can be shifted radially so that the disperse phase feed capillary can be placed at different radial positions. This shifting mechanism makes it possible to systematically examine the drop breakup on different trajectories through the orifice. At the rear edge of the profile, a capillary is guided right up to the homogenization unit which is placed about 450 mm downstream. The pressure transducer for the high pressure side of the homogenizer is installed next to the disperse phase feed inlet. In order to investigate the inflow of the homogenizing unit with optical measuring methods, this last piece of the supply tube consists of a pressure-resistant glass tube. In order to avoid distortions caused by the round glass surface, a glass jacket with a square cross-section can be placed around this tube. If this sheathing is filled with the continuous phase or generally with a fluid of the same refractive index, the flow in the supply line can be measured through the flat glass wall of the sheathing. From the large number of possible homogenizing units, the simplest shape, namely the orifice, was selected as the homogenization unit for the investigations. This has the advantage that it is structurally simple and generates a comparatively simple flow field. This orifice is also optically accessible as it consists mainly of acrylic glass. Four different inlet geometries of the orifice were manufactured. The aim of the investigations with these different shapes is to investigate which shape leads to the most effective droplet breakup. Possible influencing parameters are the occurrence of cavitation or its suppression and the efficient conversion of pressure energy into velocity. The simplest of these orifices consists of a simple concentric borehole with a sharp-edged leading edge. In the second orifice, this edge was rounded (R) off with a radius of two times the orifice diameter. The other two orifice also had a concentric bore

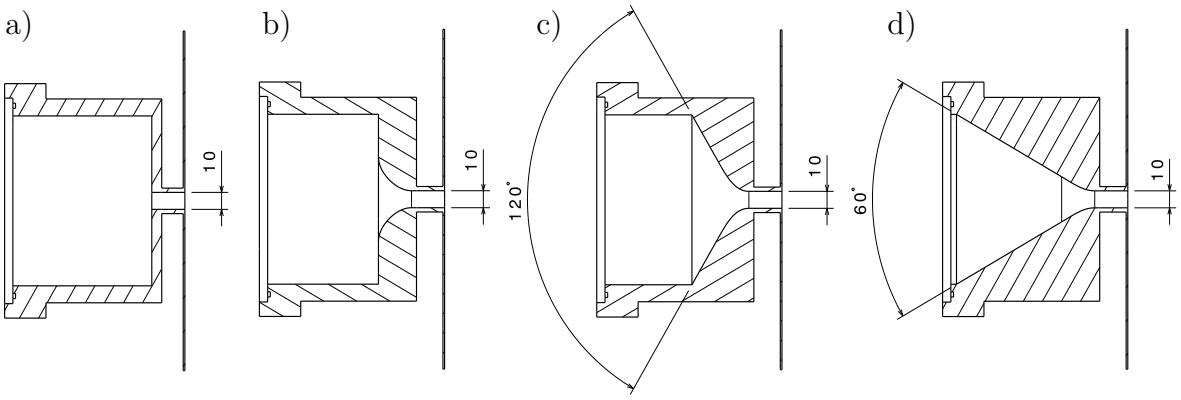

Figure 4.2: Sketches of the different orifice geometries. a) sharp edge orifice; b) orifice with rounded inlet; c) orifice with conical 120° inlet and d) orifice with conical 60° inlet.

with a rounded inlet edge, but the inlet was conical with an inlet angle of 60° and 120° respectively. The orifice diameter (D) was in all cases 10 mm and the length (L) of this smallest cross section was 20 mm. These dimensions correspond to a 50 times enlarged original orifice with 0.2 mm diameter, which is a typical laboratory sized homogenizer. Figure 4.2 shows sketches of the orifices used. Behind the orifice the flow is guided into a 1 m long glass channel with a square cross-section. The edge length is 200 mm. The ratio of the outlet channel diameter to the orifice diameter (D_o^*) can be flexibly adjusted by means of various inserts.

At the end of this outlet channel there is another pressure sensor to determine the pressure loss at the orifice. After the outlet channel, the fluid is led back to the pump via pipes. These pipes also lead to an expansion tank and a vent so that the low-pressure side is virtually pressureless.

The centrifugal pump has a maximum drive power of 3 kW. This input energy leads to a temperature rise in the measuring fluid during longer operating times. Since the material values are defined by the scale-up to the temperature of 20 °C, the system must be cooled. For this purpose, a bypass is installed parallel to the measuring section. Via this bypass, a partial flow is led to a heat exchanger and subcooled with cooling water. The volume flow rate of the bypass is controlled by regulating valves.

Since single drops are to be studied in the investigations and the drop-drop interaction is to be prevented, the drops must be injected into the system individualy. To ensure that these primary droplets have a reproducible droplet size and can be produced independently of the flow conditions in the test plant, a small partial flow of the continuous phase is removed from the plant and fed into the primary droplet production unit. Figure 4.3 shows this device.

A syringe pump (PHD Ultra, Harvard Apparatus, Holliston, United States) is used to introduce the disperse phase through a capillary into the center of the chamber. At the tip of the capillary, oil droplets are formed which are sheared off by the drag of the surrounding continuous phase flowing around the droplet. The wedge-shaped

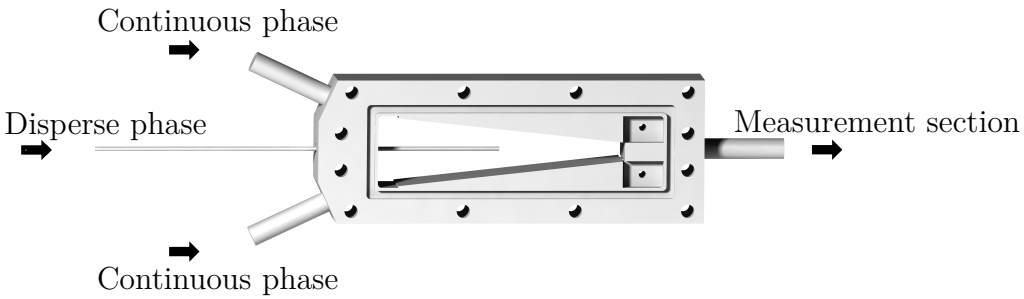

Figure 4.3: External drop production plant.

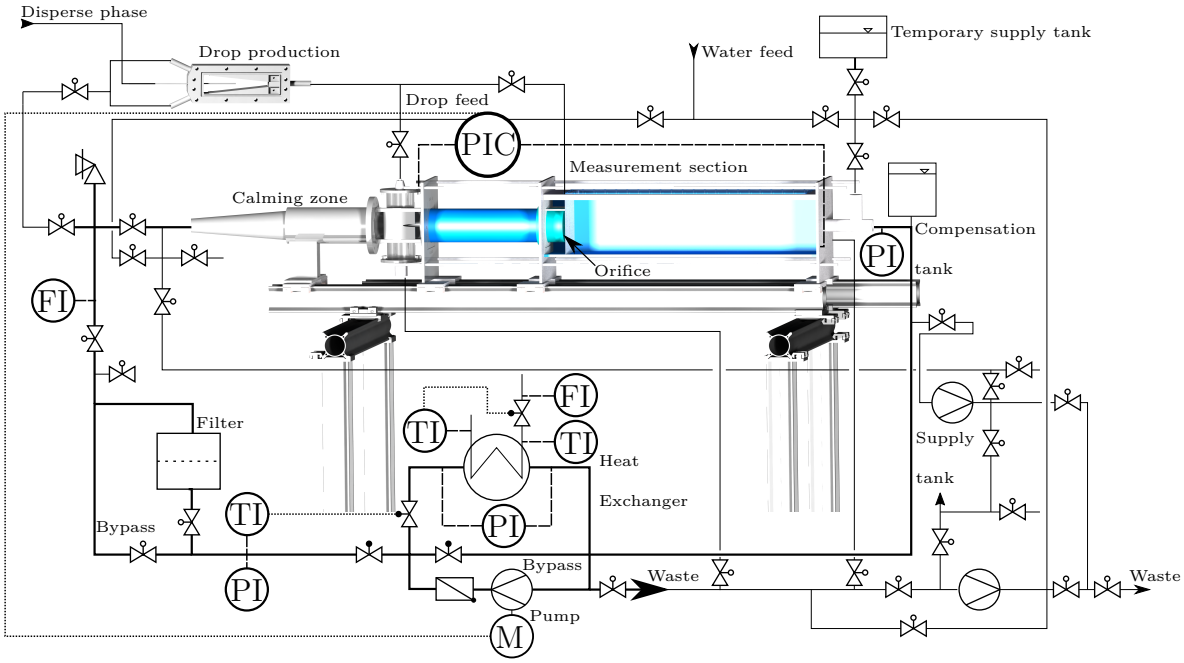

Figure 4.4: Process flow diagram of the test plant.

constriction leads to a constant velocity increase of the surrounding continuous phase. By moving the capillary deeper into the constriction, the droplet size can be adjusted, since the shear acting on the droplets is increasing due to the higher continuous phase velocity. The front and back of the chamber is made of acrylic glass, so that shadow images of the drops and the capillary can be taken. This makes it easy to adjust the droplet size to different flow conditions. These single drops can be guided by capillaries either directly to the front of the orifice or via a line system to different positions downstream of the orifice. The guidance of the disperse drops behind the orifice is used to expose the drops to the turbulent velocity field behind the orifice without passing through the orifice. Since this flow field is spatially very different, feeding points are provided in the axial direction every $2.5D$. The radial position of the feeding point can be adapted to the flow conditions or the objective of the investigation using capillaries of different lengths. Figure 4.4 shows a process flow diagram of the test plant.

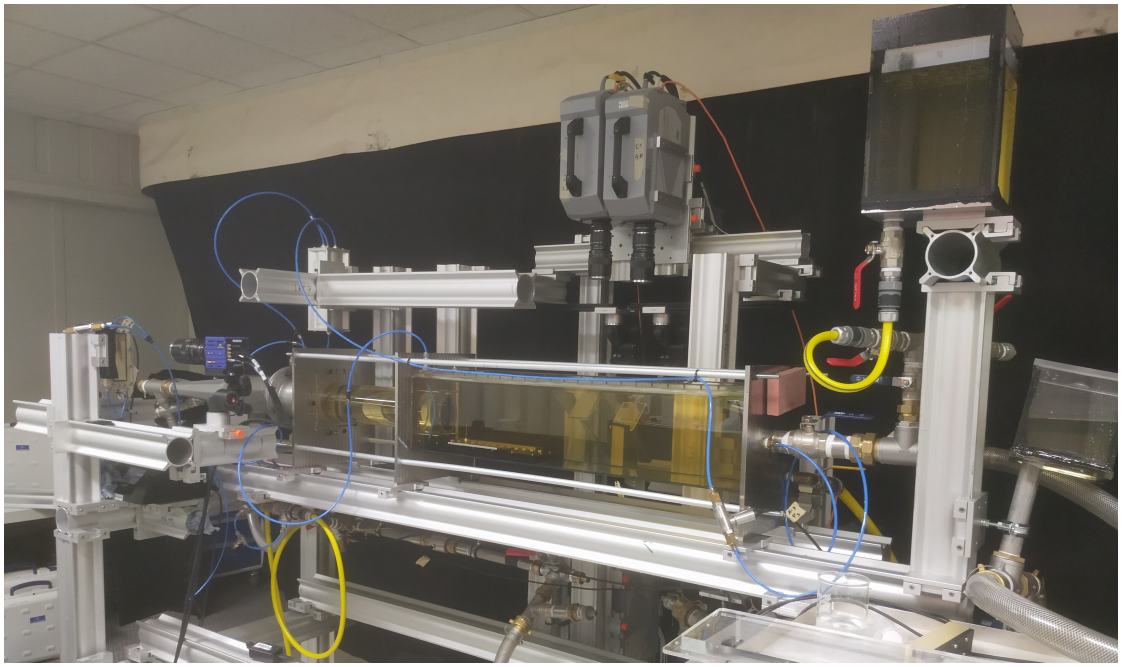

Figure 4.5: The final measurement setup.

The measurements are done at different Reynolds numbers inside the orifice, therefore the velocity of the continuous phase fluid had to be controlled. This was done by means of a Labview-program. Since the velocity could not be measured online so easily due to the special density and viscosity, the pressure drop across the orifice was used as the controlled variable. Assuming that the total static pressure difference between the pressure measurement position in front of the orifice (p_1) and the one at the end of the measurement section (p_2) is converted into velocity according to the Bernoulli equation (equation 4.7), the flow velocity in the orifice could be determined.

$$u = \sqrt{\frac{2\Delta p}{\rho_c}} = \sqrt{\frac{2(p_1 - p_2)}{\rho_c}} \tag{4.7}$$

The required pressure difference could be entered in the control software. This set-point was approached by a Labview PID controller which sends a control signal to the frequency-controlled pump. The pressure is adjusted by this controller to an accuracy of less than 1 mbar and kept stable. The maximum error caused by any deviation from the setpoint value is 1.4 %. The bypass ratio for temperature regulation with the heat exchanger (EWT-BE 14-20, EWT, Hannover, Germany) is controlled manually because the system's warm-up process is very slow. The other valves, e.g. bypass to the drop production unit, filter or cooling water etc. are also operated manually.

In order to better understand the influence of droplet elongation in the orifice on the breakup process of the droplets behind the orifice, an improvement of the experimental setup was developed, by which droplets could be directed into the free jet only behind the orifice. This makes it possible to compare breakup studies with droplets that flow through the orifice and thus experience a pre-elongation, and those that do not flow

through the orifice, but only come into contact with the turbulent flow behind the orifice.

Furthermore, the aim of these experiments is to systematically establish the relationship between the velocity field and the injection point or the breakup process when the droplets are introduced into the free jet behind the orifice, so that the SHM process can be better understood. In particular, the influence of the injection point on the drop breakup process can be investigated in more detail by the experimental setup. In addition, it is possible to investigate the influence of the viscosity ratio or the Reynolds number.

For this series of experiments, as for the other experiments, the pre-emulsion, i.e. the dispersed primary droplets were produced during the ongoing experiments with the droplet production unit. The primary droplets have a diameter of approximately $d_P = 2\,\text{mm}$. This pre-emulsion was fed into the sealed glass channel via an inlet point in the lid of the measurement section. A channel plate could be installed at the bottom of the measurement section, through which the pre-emulsion could be directed via fine channels to different dosing positions at intervals of 25 mm, i.e. every $2.5D$ in the flow direction. The actual injection of the droplets into the main flow within the measurement section is done via 4 interchangeable capillaries of different lengths. The different lengths of the capillaries cause ejection positions of the droplets from the capillaries in y-direction (distance capillary end to symmetry axis of the orifice or free jet behind the orifice) of: $y/D = -1$, $y/D = -2$, $y/D = -2.2$ and $y/D = -3.0$

This line system allows investigations in the range $0 < x/D < 30$ as well as $-3 < y/D < -1$. Figure 4.6 shows the injection device installed in the experimental set-up, with the line system made visible by a semitransparent injection plate.

The introduction of the droplets via the capillaries causes a small bypass flow to the main flow, which is directed through the orifice. However, the quantity and velocity of the bypass flow is negligible compared to the main flow, and only causes the droplets of the pre-emulsion to be transported and, eventually, directed towards the free jet, i.e. the main flow.

For the investigations on improving the flow field behind the orifice due to passive flow control a special orifice was built. Like the other orifices this was mainly made out of acrylic glass to be optically accessible. In contrast to the regular orifice the rear edge of the orifice could be changed. This enables to investigate different rear edges. Six different orifices were investigated. The first orifice has a cylindrical shape and is designed as the reference case. One orifice has a conical opening with a cone angle of approx. 17.7° starting 2.5 mm upstream of the trailing edge as for all investigated orifices with conical opening in this study. The orifice with the trailing edge that has the complete opening is an extreme form of the other orifices. Three further orifices have a conical opening on 50 % of the circumference which is divided equally into three, four or eight segments and have an opening angle of approx. 17.7°. The last orifice has also four notches which cover 50 % of the circumference but the opening angle ist smaller with approx. 9.1°. Figure 4.7 shows a comparison of the trailing edges.

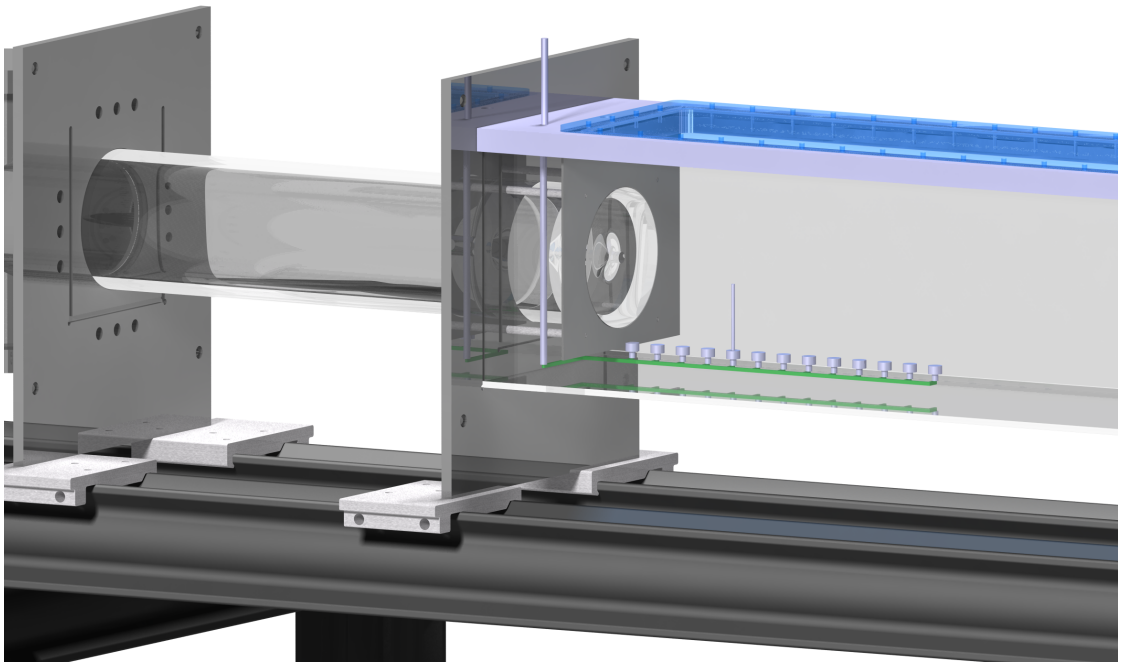

Figure 4.6: Illustration of the feed line at the bottom of the measuring section for the injection of primary droplets behind the orifice.

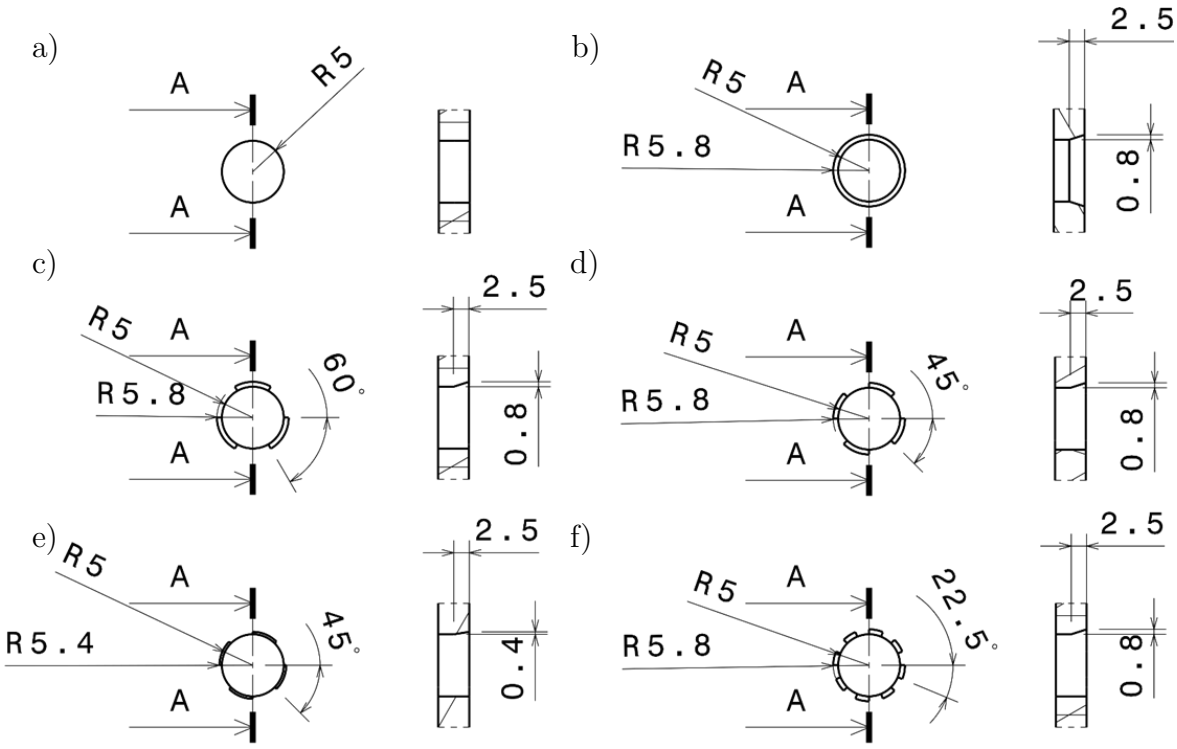

Figure 4.7: Comparison of the different orifice trailing edge designs. a) standard orifice; b) orifice with circumferential conical expansion; c) orifice with three notches; d) orifice with 4 large angle notches; e) orifice with 4 small angle notches; f) orifice with 8 notches.

4.2. Materials

Due to the scaling of the homogenization unit, the material properties had to be adapted in order to keep the process physically as well as geometrically similar to the original process.

4.2.1. Continuous phase

The continuous phase is the aqueous phase of the two-phase material system and consists mainly of water. The scaling increases the density and viscosity of the model fluid compared to the original fluid. To increase the viscosity, 10.5 $w/w\%$ PVP K30 is used. This is the polymer polyvinylpyrrolidone, where the degree of polymerization is also indicated (K30). In addition, 27.5 $w/w\%$ sucrose is mixed into the aqueous phase. This not only increases the viscosity but also the density. The model fluid can in principle be produced by these two additives. In order to ensure a certain protection against spoilage of the solution, a preservative (potassium sorbate) and an acid (citric acid) are added in small quantities. Table 4.1 shows the mixing ratio. Table 4.2 shows the calculated material values of the original, the theoretical model system and the realized model system. The continuous phase was freshly prepared for the various test series, since it had to be replaced after a certain time due to seeding deposition, the homogenization tests and other processes. Aging of the continuous phase degrades the visualization quality of the droplets using shadowgraphy techniques as the fluid becomes opaque. The viscosity and density were checked for compliance before the experiments.

4.2.2. Disperse phase

Three silicone oils are used as the disperse phase. The oils differ mainly in their viscosity. When using the medium viscous silicone oil (AK100) with a dynamic viscosity of approx. η_d = 96 mPas, the viscosity ratio of the material system is η^* = 3.0 and directly scaled to the original process. To investigate the influence of the viscosity ratio on the drop break up also a low viscosity silicone oil (AK10) with a dynamic viscosity of approx. η_d = 9.3 mPas and the viscosity ratio of about η^* = 0.3 or a high

Table 4.1: Composition of the continuous phase

Component	mass percent
Water	61.5
PVP K30	10.5
Sucrose	27.5
Potassium sorbate	0.26
Citric acid	0.24

Table 4.2: Material properties

		Scaling factor -	Density kg/m³	Dynamic viscosity mPas	Viscosity ratio -	Interfacial tension mN/m
Continuous phase	Original	1	1146.5	46		
	Target value	50	1146.5	32.5		
	Actual value	50	1145.7	32.4		
Disperse phase	AK 10	50	930	9.3	0.3	16.9
	AK 100	50	960	96	3.0	20.1
	AK 350	50	970	339.5	10.5	18.0

viscosity silicone oil (AK350) with a dynamic viscosity of approx. $\eta_d = 339.5\,\text{mPas}$ and the viscosity ratio of about $\eta^* = 10.5$ was used. The density and the interfacial tension of the material systems is listed in Table 4.2 with the viscosity parameter. Since no emulsifier is used in the experiments the interfacial tension is taken as constant.

4.3. Experimental setup

The optical measurements investigating the droplet breakup in high-pressure homogenizers with orifices as disintegration units are done at different positions. Figure 4.8 shows the overview of the measurement positions for all performed measurements. The measurements are divided into three categories: Velocity field measurements using PIV (black), droplet visualizations using shadowgraph techniques (blue) and velocity field measurements using PTV (green).

The PIV measurements at position A) and B) are used to characterize the experimental system with respect to the incoming flow and the effect of the different orifices, respectively. The PIV measurements at position C) were performed to analyze with high spatial resolution the flow phenomena during high pressure homogenization using orifices. The PIV measurements in the orifice at position D) are used as a comparison of the drop elongation measurements in the orifice performed at the same position (2)). The main series of measurements on droplet deformation and breakup during high-pressure homogenization with orifices was carried out at measurement position 1) using a modified shadowgraph method. Based on the findings from measurement series 1), the drop breakup of non pre-stretched drops was investigated at measurement position 3) using a modified shadowgraph method to characterize turbulent drop breakup more precisely. In the visualization of the drop breakup, the difficulty in all test series is that the drop moves very fast with the main velocity even in the scaled experimental setup, so that, in order to observe the entire breakup, a FOV with a large aspect ratio at simultaneously high spatial resolution is necessary, since the drop and especially the filaments formed during the breakup are very small. At the same time, the disintegration takes place within a very short time, so high temporal resolution measurements are necessary. The investigations on the modification of the turbulence behind orifices were carried out by means of PIV recordings at measuring position 1) but also by the 3D-PTV measurements at the positions designated as measuring position a).

The individual measurement positions and setups are presented below.

4.3.1. Flow field characterization

For the characterization of the four orifice geometries as well as for the characterization of the inflow condition and the velocity field inside the orifice a planar 2D2C PIV test setup with a single camera was chosen (setup A), B) and D)). The light sheet was set up radial along the symmetry axis. This experimental setup could be used in front of, inside and behind the orifices to determine velocity profiles. For the measurements a PCO.edge 5.5 sCMOS camera with a sensor of 2560 pixel × 2160 pixel was used. The laser used was a Litron Nano S 65-15 PIV Nd:YAG laser with 65 mJ pulse energy. The measurements were run at 10 Hz. As seeding of the flow hollow glass speres with a medium particle size of about 16 μm and a density matched to water of about 1000 kg/m^3 were used. To meassure velocities in the round inflow glass tube without distortions a second glass channel with a square cross section was placed arround the glass tube. This outer channel was filled with the same fluid as the inner one.

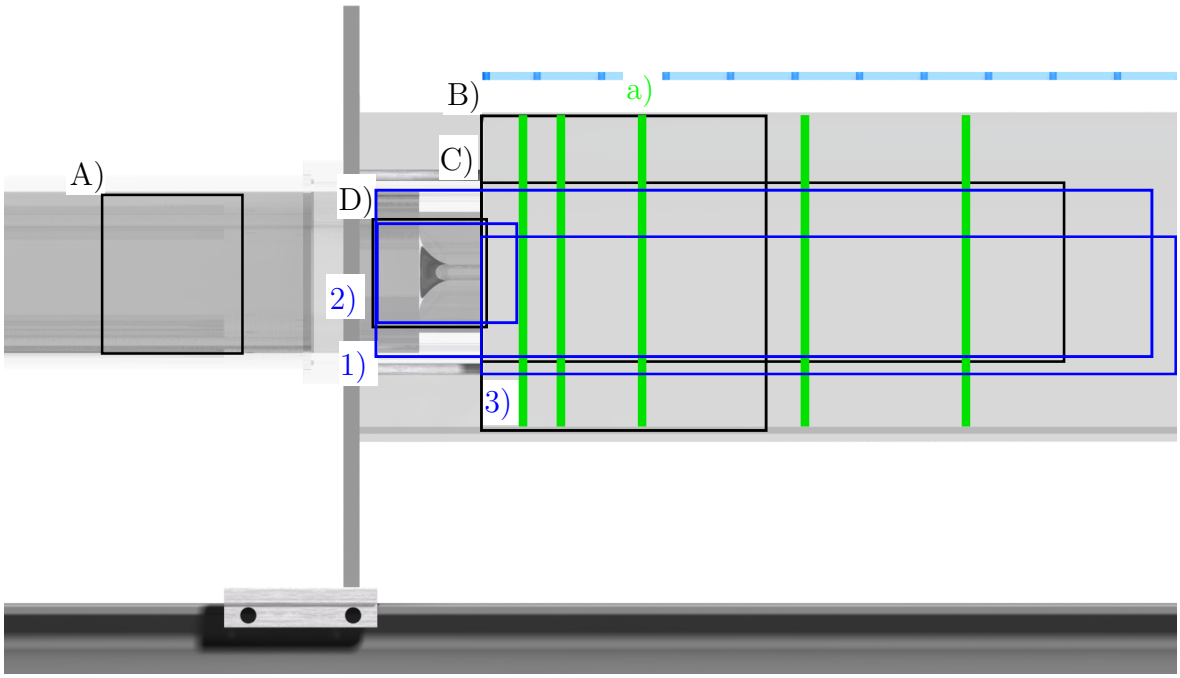

Figure 4.8: Overview of the measurements. PIV velocity measurements: A) inflow velocity field, B) orifice characterization, C) velocity field measurements behind the orifice, D) velocity measurements inside the orifice; droplet visualization: 1) droplet breakup visualiszation (drop through orifice), 2) droplet deformation measurements 3) droplet breakup visualizations (high-pressure post feed homogenization); a) passive flow controll measurements with PTV.

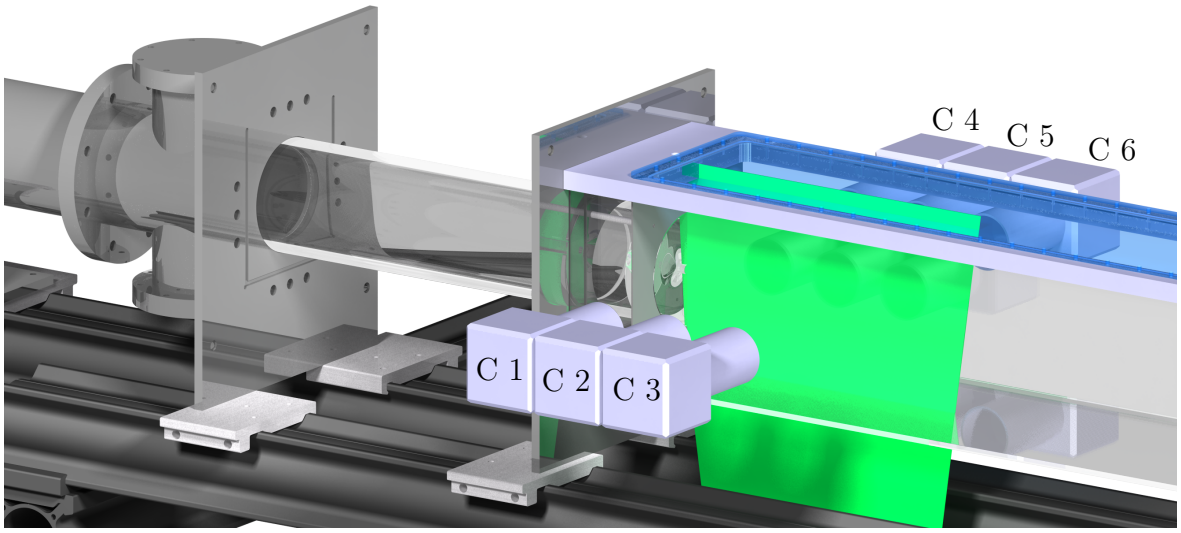

Figure 4.9: Setup for the single phase PIV-measurement with six sCMOS-cameras simultaneously.

Due to this method the interphase betwen air and glass or the measurement fluid is perpendicular to the line of sight.

The field of view in front of the orifice to characterize the inflow was about 100 mm × 84 mm, with a resolution of 25.6 px/mm which results in a vector spacing of 0.32 mm/vector respectively. To obtain a flow profile the calculated streamwise vectors were averaged.

The field of view behind the orifice to characterize the jet exiting the orifice was 225 mm×190 mm so the resolution was about 11.3 px/mm resulting in 0.32 mm/vector.

In order to investigate the rotational symmetry of the experimental setup, especially the orifices, the orifice was rotated relative to the light sheet in steps of 30° and measured again. The geometric reference point for all measurements was the trailing edge of the orifice respectively the corresponding point on the symmetry axis. The axis of symmetry in the direction of flow corresponds to the positive x-direction. The y- and z-axes are perpendicular to each other and are parallel to the trailing channel side walls. Positive y-axis is directed to the top and z-axis coming out of the plane.

For more detailed images of the velocity field and the jet behind the orifice and thus a more precise analysis of the flow processes (setup C)), six of the cameras were focused on small areas of the free jet. When aligning the cameras, care was taken to ensure that the fields of view overlapped slightly. This made it possible to combine the individual images to form a large area image with high resolution. This experimental arrangement was implemented in such a way that all six cameras recorded simultaneously, so that the instantaneous velocity measurements could also be combined. For the illumination in this measurements a Quantel Evergreen laser with 200 mJ pulse energy was used. The field of view investigated was 340 mm × 69 mm in size. The resulting vector-field after

stitching had a vector spacing of 0.245 mm/vector. Figure 4.9 shows the experimental setup schematically.

A similar setup was used for the measurement of the flow field inside the orifice with a Photron Fastcam SA-Z high-speed camera and a high-speed laser (two Innolas Blizz high-speed laser units with a combined output power of 60 W running simultaneously). The field of view in this case was 23.4 mm × 47.6 mm with a resolution of 21.5 px/mm resulting in a vector field resolution of 0.37 mm/vector.

4.3.2. Drop deformation visualization

The characterization of the deformation of the disperse phase single drops passing through the orifice (setup 2)) was performed with two Photron Fastcam SA-Z high-speed cameras using the modified shadowgraphy method outlined in section 3.2. The cameras can record up to 20 kHz with a Megapixel sensor (1024 pixel × 1024 pixel). The oil droplets were captured at higher frame rates, so the sensor had to be trimmed. Since the measuring volume has a high aspect ratio, the sensor could be cut perpendicular to the flow direction without having to accept resolution losses in the flow direction. One camera was oriented towards the orifice itself, i.e. the inlet and the constriction. The second camera was oriented to the free jet directly behind the orifice. Figure 4.10 shows the experimental setup schematically. The second camera was used to determine the final drop filament length in case the drop filament was too long for the field of view of camera 1. The recordings were made with a recording frequency of 40 kHz. The camera sensors were reduced to 504 pixel × 1024 pixel to enable recording at the high recording frequency. The field of views were 23.4 mm × 47.6 mm and 36.8 mm × 74.7 mm respectively. This leads to a resolution of 21.5 px/mm for camera 1 and 13.7 px/mm for camera 2. Due to the strong rounding of the inlet area of the orifice, distortion occurs when the drop is recorded inside the orifice. These distortions can be corrected by callibration. In addition, the curvature of the orifice in the inlet area leads to the fact that an area of the orifice ($-4.2 < x/D < -3.7$) cannot be observed due to total reflection.

4.3.3. Drop breakup visualization

Four high-speed Photron Fastcam SA-Z cameras were used for the multiphase measurements to visualize the drop breakup using the modified shadowgraphy method. Recording frequencies were 40 kHz or 72 kHz. The exposure time was set to 3.5 μs. The resolution was about 13 px/mm with a total field of view of about 295 mm × 35 mm. To ensure that the initial drop size of the measured drops could be determined accurately, a fifth high-speed camera was used, which was aimed to the inlet area of the orifice. The incoming droplets could be visualized there as round primary droplets. At this point a Phantom V12 camera was used. As the velocity in the inflow of the orifice is comparatively slow, it was possible to measure with a recording frequency of 2 kHz. The resolution of these camera recordings is about 30 px/mm. Figure 4.11 visualizes the measurement setup (setup 1)).

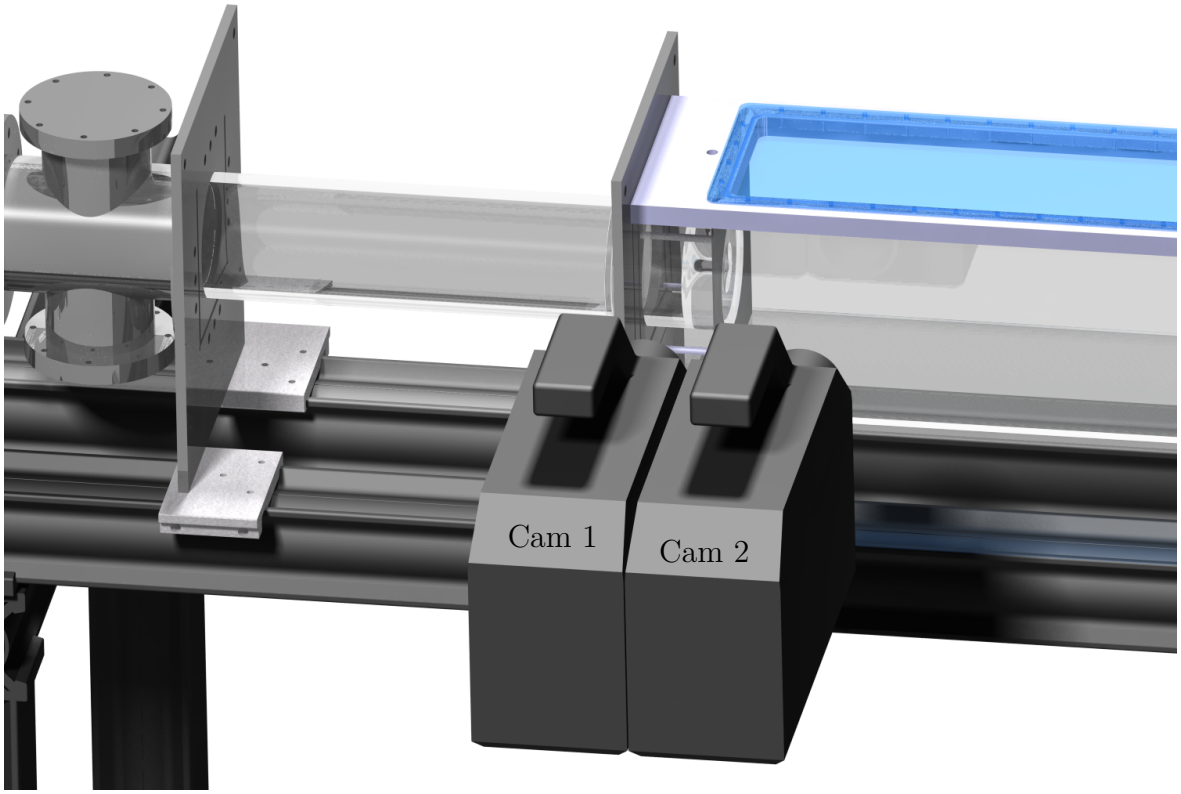

Figure 4.10: Setup for the multiphase measurement with two high-speed cameras to determine the drop deformation inside the orifice.

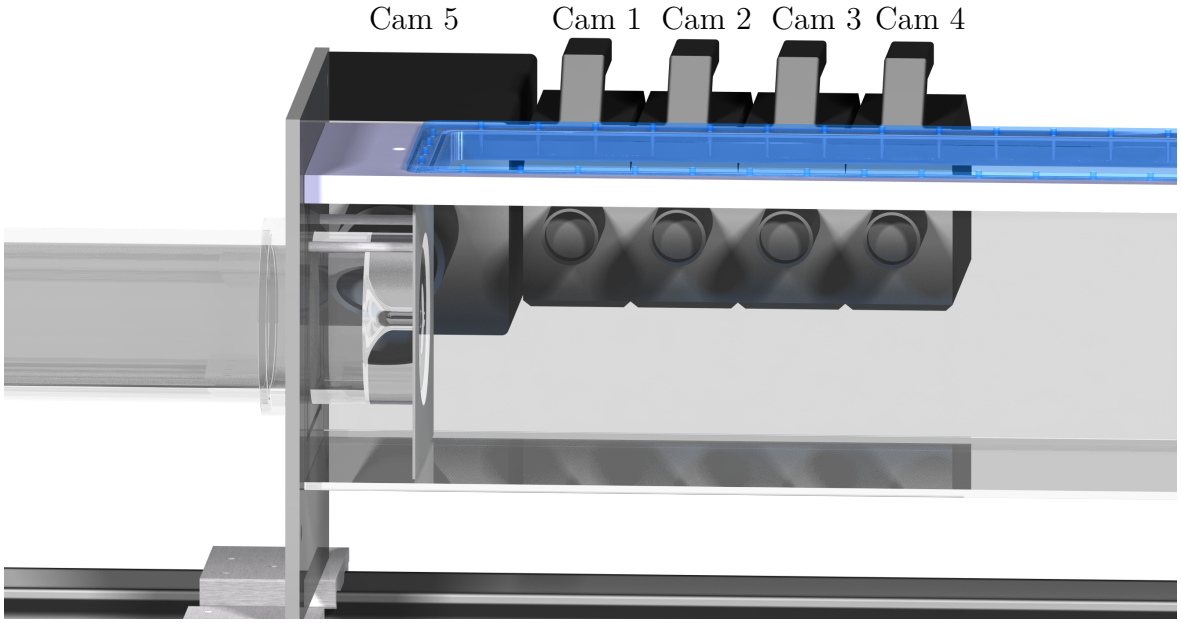

Figure 4.11: Setup for the multiphase measurement for the breakup visualization with four high-speed cameras downstream of the orifice and one high-speed camera upstream.

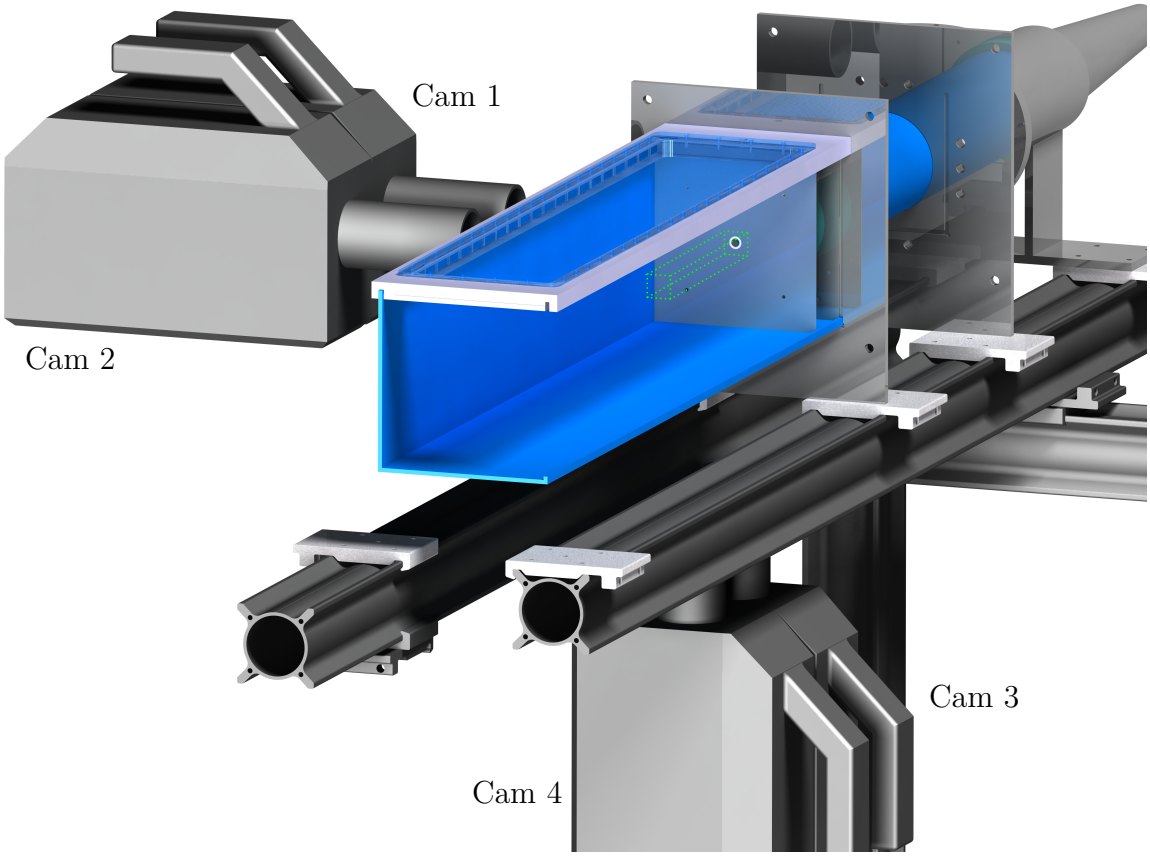

Figure 4.12: Setup for the multiphase measurement with four high-speed cameras to determine the drop trajectory and the breakup location.

4.3.4. Drop trajectory measurement

Figure 4.12 shows schematically the setup for the simple two angle view multiphase measurement. During these measurements, two high-speed cameras were placed on the side (cameras 1 and 2) and two cameras (cameras 3 and 4) below the measuring section. All cameras were Photron Fastcam SA-Z high-speed cameras. The phase boundary (air-aqueous phase) or the glass wall was always perpendicular to the viewing direction in order to avoid distortions.

Cameras 1 and 3 or 2 and 4 were aligned to the same volume from their respective viewing angles. Thus droplets in these areas were recorded simultaneously from 2 viewing angles at 90° to each other, which enabled position determination and coarse 3D reconstruction of the droplet volume.

In addition to the shadow images for the 3D reconstruction it is also possible to simultaneously record the velocity field via PIV measurements. For the PIV recording, a light sheet is inserted vertically into the measuring volume. Thus, with camera 1 and 2 planar PIV images can be taken. Camera 3 and 4 cannot be used for the PIV images because reflections on the lower channel wall occur. In order to get a 3D reconstruction of the droplet from shadow images and the PIV images, camera pairs 1 to 2 or 3 to

Table 4.3: Camera FOV for the two meassurement positions.

Position	FOV / x/D	FOV / y/D
Position 1	-0.50 - 32.95	-3.22 - 1.78
Position 2	14.50 - 46.40	-3.24 - 1.76

4 are triggered differently. Cameras 1 and 2 are operated at twice the frequency of cameras 3 and 4, so that every second shot of cameras 1 and 2 is taken simultaneously with cameras 3 and 4. In the intervals where only cameras 1 and 2 take images, the high-speed laser (two Innolas Blizz high-speed Laser units with a combined output power of 60 W running simultaneously) is triggered for the PIV images.

4.3.5. Drop-vortex interaction

In order to investigate the drop-vortex interactions more precisely and separately from the effect of drop deformation by the inlet flow in the orifice, the drops were injected into the free jet or the turbulent flow behind the orifice directly after the orifice or at several downstream positions. This method is simmilar to the simultaneous homogenization and mixing process or the high-pressure post feeding method first proposed by Köhler et al. (2007). Figure 4.13 shows the dosing device submerged in the measurement section behind the orifice and the theoretical camera positions. To investigate the deformation and breakup of the injected drops four Photron Fastcam SA-Z high-speed cameras were used. The camera field of views were set up in line. To archive a high spatial resolution and to have the field of views overlap for each camera.

In these experiments, the images were captured at a recording rate of 32 kHz, so the sensors of the cameras had to be reduced to a size of 600 px × 1024 px. The exposure time was set to 7.5 μs. The spatial resolution was approximately 12 px/mm. Due to the large extension of the investigation area in the main flow direction, the investigations were divided into 2 parts where in the first part dosing points in the range $0 < x/D \leq 15$ were investigated, and in the second part dosing points in the range $15 \leq x/D \leq 30$. However, the cameras or the observation area had to be able to simultaneously observe an area downstream of the possible dosing site, since the droplets are transported downstream with the main flow after exiting the injection capillary and break up at the same time. Table 4.3 summarizes the FOV extent and recorded area of the two measurement positions.

Since the droplets initially moved much slower in these experiments than in the experiments with droplets passing through the orifice, the recording could be triggered manually, with the recording sequence timed so that approximately 1 s was acquired after the trigger signal was received and approximately 1.3 s were acquired before the trigger signal was received to compensate for the reaction time.

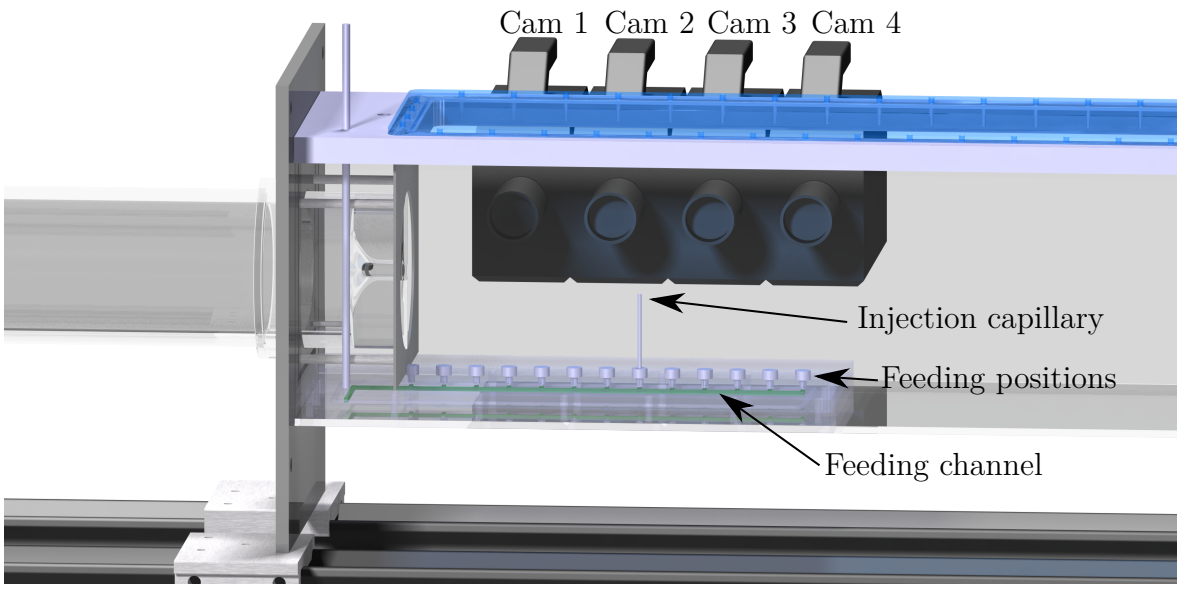

Figure 4.13: Setup for the multiphase measurement for the breakup visualization of droplets interacting with vortices downstream of the orifice with four high-speed cameras.

4.3.6. Flow control orifice characterization

Special orifices were developed to increase the turbulence or modulate the turbulence behind orifices. To characterize the flow behind the orifices, flow field measurements were carried out in the wake of the orifice. 2D2C-PIV measurements were done in streamwise direction along the xy-plane. The measurement setup was the same as for the flow field characterization with six cameras simultaneously from the sides of the channel and a laser light sheet coming from the bottom (see Figure 4.9 (setup 1)). To characterize the velocity field perpendicular to the main flow direction measurements in the yz-plane were made. Since the velocity gradients at the edge of the free jet behind the orifice are very large, no interrogation window based measurement technique could be used for the measurement, because the spatial resolution of the boundary layer would be too low. By using a 3D-PTV measurement setup the velocity field in the free jet and the boundary layer could be resolved very well. Figure 4.14 shows the experimental setup. For the 3D-PTV measurements three sCMOS cameras were used. The cameras were aligned to the measuring plane from three spatial directions at an angle of 45° or 55°. To ensure that the interface air - continuous aqueous phase is perpendicular to the line of sight of the cameras, prisms were attached to the side walls and the channel bottom (see Figure 4.14). The prisms could be filled with the continuous phase so that the distortions were minimized. To ensure that the focal plane of the cameras is parallel to the measuring plane, Scheimpflug adapters were installed between the camera sensor and the lens system. To improve the image quality and supress reflections due to air bubbles flourescent seeding particles were used. The seeding particles were spiked with Rhodamine B so that they are excited by laser light of the wavelength 532 nm. The cameras were equipped with a filter that blocked the laser light so that only the fluorescent light was recorded. The medium particle size of

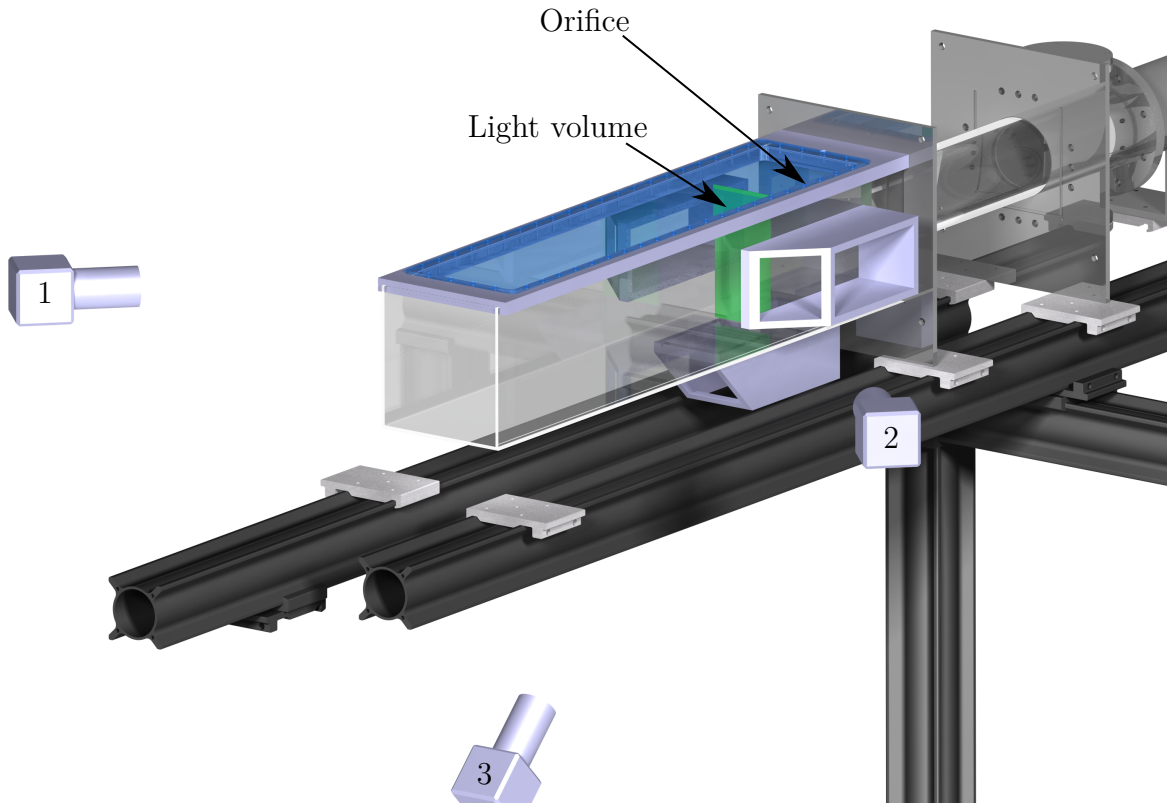

Figure 4.14: Setup for the 3D-PTV measurements with three sCMOS cameras. Parts of the test facility were not shown for the sake of clarity.

the seeding particles was about 15 μm.

5

Results and discussion

5.1. Test plant characterization

5.1.1. Inflow characterization

For the investigation of droplet breakup in the test facility to be possible, the inflow must be laminar so that the droplet trajectory in front of and in the orifice can be reproducibly adjusted. Figure 5.1 shows the measured velocity profile in the round 100 mm in diameter wide supply line to the orifice unit. The flow profile shown is normalized by the theoretical velocity $u_{\mathrm{Re,in}}$ (see equation 5.1) in the feed line. The theoretical velocity is calculated from the Reynolds number Re, the viscosity η_{c} and the density ρ_{c} of the continuous phase, and the orifice diameter $D = 10\,\mathrm{mm}$. For the inlet region, this theoretical velocity is converted to the larger channel cross section using the continuity equation (see equation 5.2).

$$u_{\mathrm{Re}} = \frac{\eta_{\mathrm{c}} Re}{D \rho_{\mathrm{c}}} \tag{5.1}$$

$$u_{\mathrm{Re,in}} = u_{\mathrm{Re}} \frac{A_{\mathrm{orifice}}}{A_{\mathrm{inlet}}} = u_{\mathrm{Re}} \frac{\frac{\pi D^2}{4}}{\frac{\pi D_i^2}{4}} = u_{\mathrm{Re}} \frac{D^2}{{D_i}^2} \tag{5.2}$$

As can be seen the flow is very homogeneous over the entire channel cross-section with a narrow boundary layer area. This homogeneous inflow to the orifice is achieved by the conical widening of the channel cross-section, a flow straightener at the beginning of the cylindrical inlet area and an overall extended cylindrical inlet area. This inlet channel is much more suitable for measurements of drop breakup and for checking the flow conditions than the inlet channel used initially, which had a sudden widening of the channel and a shorter overall length and did not produce a homogeneous inlet flow.

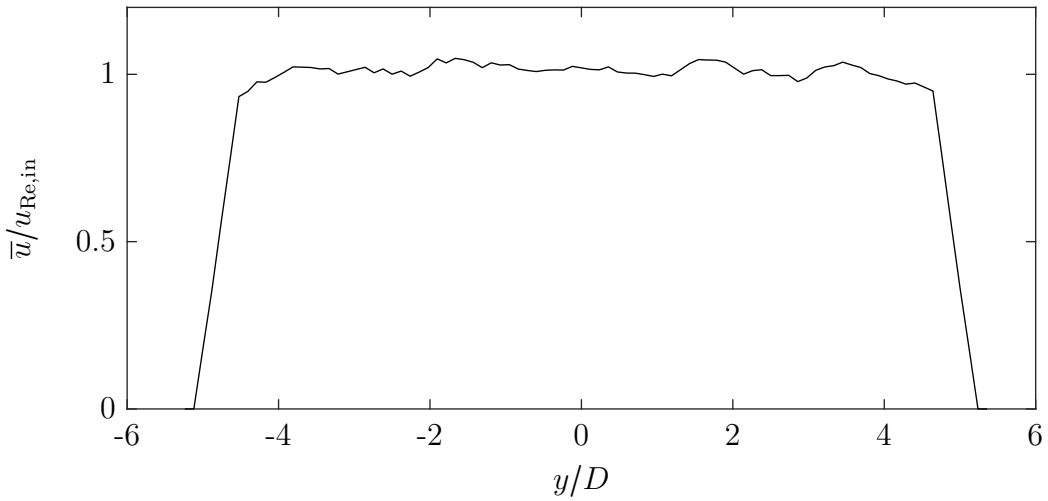

Figure 5.1: Normalized, ensemble-averaged velocity profile of the incoming flow in front of the orifice.

5.1.2. Orifice characterization

To compare the four different orifice geometries (see Figure 4.2), the orifices were measured one after the other at the same pressure loss (2 bar), i.e. same theoretical Reynolds number. A planar PIV setup was chosen to investigate the free jet behind the orifice as the reference area. The measured velocity fields were then analyzed to compare the orifices. Figure 5.2 shows the velocity profiles of the free jet behind the four different orifices at three positions.

It becomes clear that the orifices type b) to d) have very similar free jet profiles regardless of the running length, while the flow profile of the orifice type a) with the sharp edged inlet differs significantly from these. On the one hand the profile is clearly flatter, i.e. the flow velocity is lower than with the other three orifices and on the other hand the profile is wider from the beginning. In addition, clear cavitation occurs at the orifice of type a), which is clearly perceptible both acoustically and optically. With the remaining orifices no such distinct cavitation can be detected. Figure 5.3 shows both the velocity profile of the four types on the symmetry axis of the free jet and the dimensionless free jet diameter for comparison of the orifices. The differences and similarity of the orifices are again evident in these illustrations. Based on the results shown, only a minimal dependence of the flow conditions of the free jet on the orifice geometry of type b) to d) can be determined. In contrast, the orifice of type a) produces significantly different flow conditions with cavitation and must be investigated separately.

Due to the results of the orifice characterization and the very similar flow profiles behind the type b), c) and d) orifices, an orifice with an inlet of type b) was used for all further investigations on the test facility. This orifice has the advantage over the other inlet designs that no cavitation (in the investigated Reynolds number range) occurs (compare with orifice type a)) and furthermore the optical accessibility is better

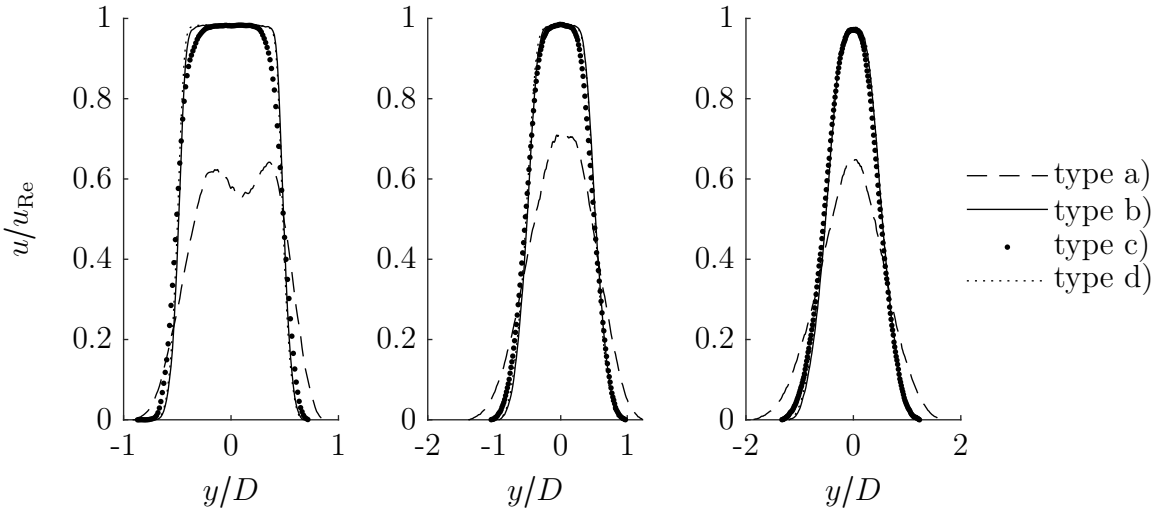

Figure 5.2: Comparison of the radial normalized, ensemble-averaged velocity profiles of the four orifice geometries at different streamwise positions; left: x/D = 5, middle: x/D = 10, right: x/D = 15.

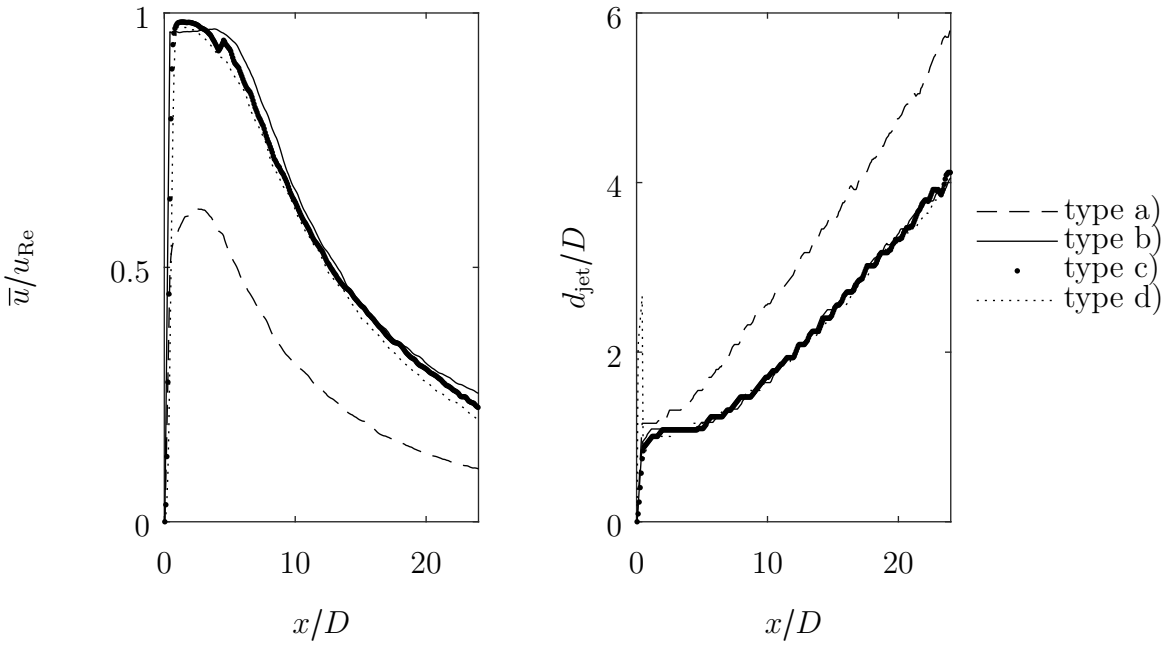

Figure 5.3: Comparison of the normalized, ensemble-averaged velocity profile along the axis of symmetry on the left side and the normalized jet width on the right side for the four orifice geometries.

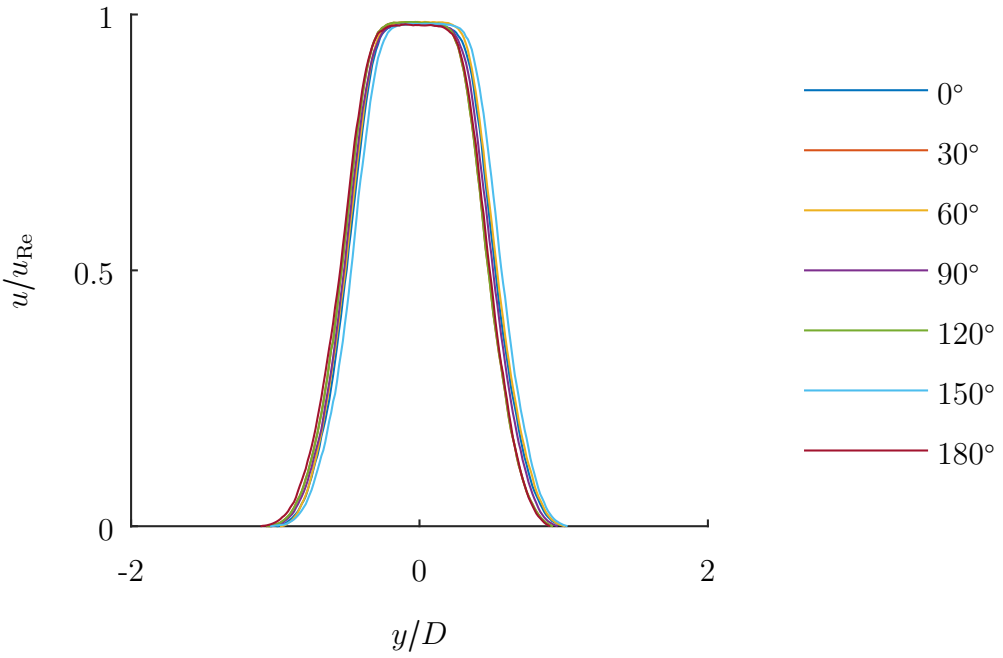

Figure 5.4: Comparison of the normalized, ensemble-averaged velocity profiles of the free jet with rotation of the orifice in 30° steps at the flow position $x/D = 3$.

compared to the orifices with conical inlet (type c) and d)). In addition, the capillary for injecting the drops can be moved to the same length in front of the orifice in all radial positions for the investigations with drops. This simplifies the test procedure and leads to more precise results, since the distance to the orifice can be kept very small as well, so that the drops are hardly influenced by the buoyancy of the drops before they pass through the orifice.

Figure 5.4 shows the investigation of the orifice for rotational symmetry. It can be seen very clearly that the free jet profile is very symmetrical regardless of the orientation of the orifice and the measured velocities are also identical. Only the vertical alignment of the orifice in the duct seems to be subject to minor fluctuations. This may be due to the given tolerance when installing the orifice, but it does not influence the further measurements, since the symmetry axis does not change within a series of measurements and thus only has to be determined once.

5.2. Flowfield characterization

5.2.1. Inside the orifice

The flow field characterization in the orifice was performed using a 2D2C-PIV measurement method. Figure 5.5 shows the normalized, ensemble-averaged flow field in front of and inside the orifice at a Reynolds number of $Re = 2000$ normalized with the theoretical orifice velocity u_{Re} (see equation 5.1). It becomes clear that due to the mentioned reflections no values in the range $-4.2 < x/D < -3.7$ can be determined. However, this range is also rather small and the rest of the measurement is very clear, so the absence of this range is not very important. In the remaining area the flow is symmetrical and there is a steady acceleration due to the constriction in the nozzle. Figure 5.6 shows the velocity profile on the symmetry axis of the orifice. In the non-visible area the velocity curve is fitted. Again the continuous acceleration of the fluid inside the inlet of the orifice is visible. The theoretical orifice velocity is almost reached. The velocity deficit of the measured velocity to the theoretical velocity can be explained by the position of the pressure measuring position, which does not directly measure the pressure loss through the orifice, but also the loss over a distance of approx. 1.3 m, whereby the velocity is very low for most of the distance and the channel is very wide and therefore has little influence on the measured pressure loss.

5.2.2. Behind the orifice

Knowledge of the velocity fields behind the orifice is essential for the investigation of drop breakup during hightpressure homogenization with orifices. Figure 5.7 shows three different plots of the measured velocity field behind the orifice at a Reynolds number of $Re = 2000$ and a channel diameter ratio of $D_{\mathrm{o}}^{*} = 20$, the velocities are normalized with the theoretical orifice exit velocity (u_{Re}). The upper plot shows the ensemble-averaged velocity field, the central plot shows the ensemble-averaged velocity fluctuations and the lower plot shows an instantaneous velocity field. It becomes clear that the free jet is very symmetrical in the ensemble-averaged plot. The free jet core, which is characterized by a laminar flow without major velocity fluctuations, is very long at this Reynolds number and extends to a length of about $10 < x/D < 12$ downstream. From this point on, the free jet diverges radially so that the velocity decreases rapidly. In the representation of the velocity fluctuations, the zone of highest velocity fluctuations begins at this point and continues until about $20 < x/D < 22$. The plot of the instantaneous velocity field shows that the described zones exist in an instantaneous field as well. The free jet starts to meander very slightly and then more and more until the free jet breaks up into individual structures at $x/D = 15$. From a length of approx. $25D$ the velocity in the instantaneous flow field is reduced to a fraction of the initial velocity and the velocity fluctuations are minimal. Figure 5.8 shows the same plots as figure 5.7 but for a higher Reynolds number ($Re = 5700$). As shown in Figure 5.7 and figure 5.8, the flow field of the free jet changes significantly depending on the Reynolds number.

At the high Reynolds number the individual zones in the free jet described above can be recognized as in the case of the low Reynolds number, but the jet core region is compressed in the flow direction. The free jet is symmetrical again in the mean and

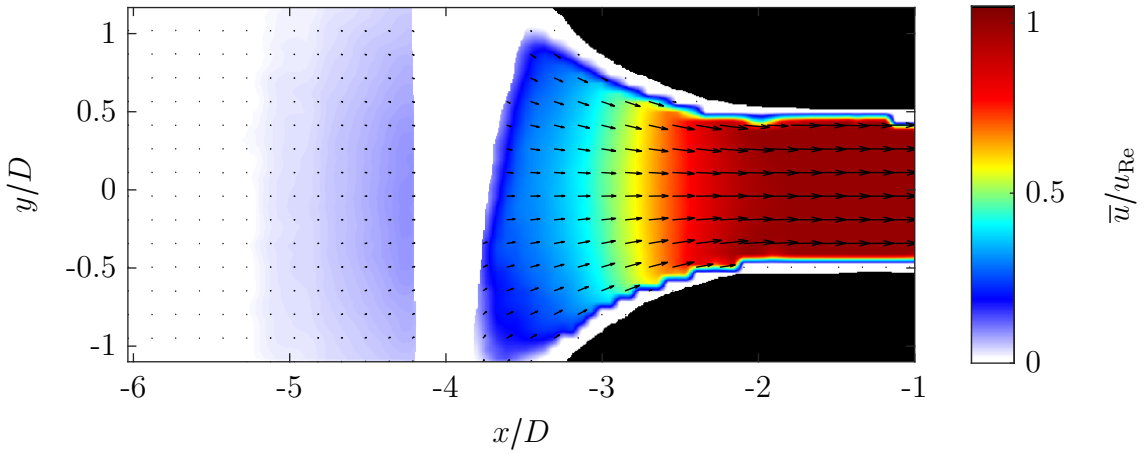

Figure 5.5: Ensemble-averaged velocity field inside the orifice at a Reynolds number of Re = 2000 normalized with the theoretical orifice velocity.

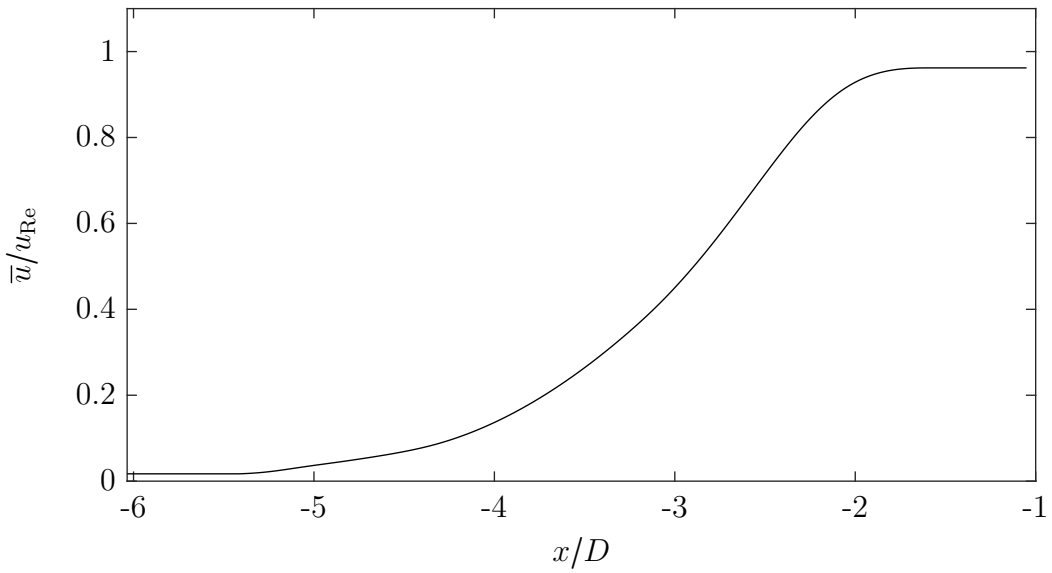

Figure 5.6: Normalized, ensemble-averaged velocity profile at the inlet of the orifice on the axis of symmetry.

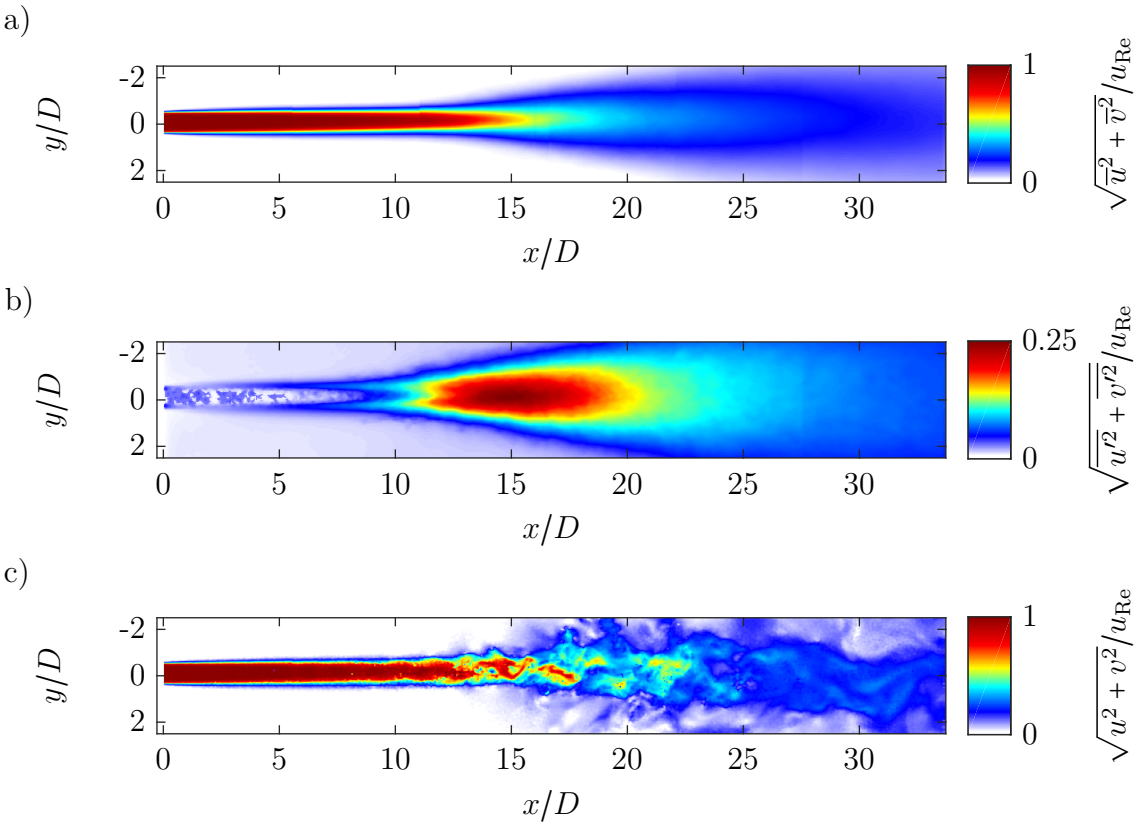

Figure 5.7: Normalized velocity fields at a Reynolds number of Re = 2000. a) Ensemble-averaged velocity field; b) ensemble-averaged velocity fluctuations; c) instantaneous velocity field.

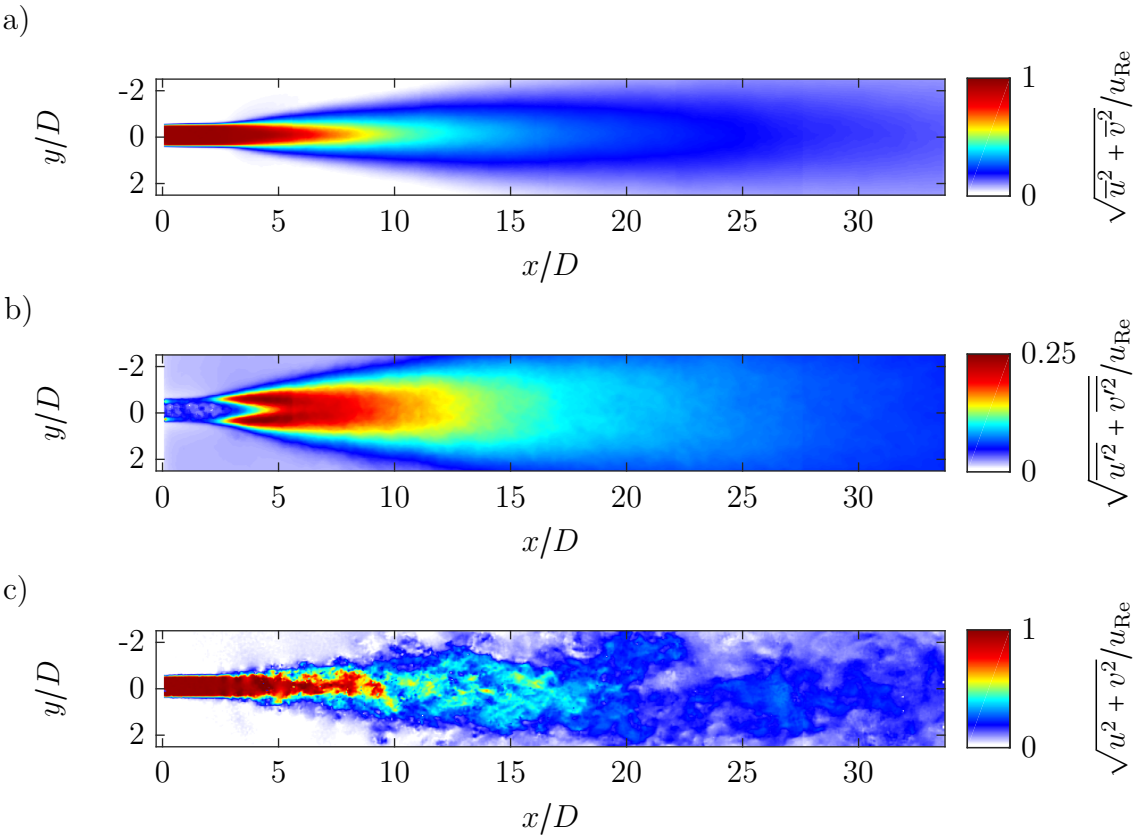

Figure 5.8: Normalized velocity fields at a Reynolds number of Re = 5700. a) Ensemble-averaged velocity field; b) ensemble-averaged velocity fluctuations; c) instantaneous velocity field.

has a core area without significant fluctuations, but this area is only about $5D$ long. In the instantaneous velocity field it is visible that the free jet starts to meander already at a length of about $3D$ and disintegrates into individual structures at about $10D$. The highly turbulent zone with a length of approx. $15D$ is similar in length to the low Reynolds number, but it starts earlier, in the edge area of the free jet at approx. $3D$ behind the orifice. The relative intensity of the velocity fluctuations is also comparable to that of the lower Reynolds number.

As the Figures 5.7 and 5.8 show, the initially stable, symmetrical free jet breaks down after a certain length. This instability is caused by the fact that the fluid in the free jet moves much faster than the surrounding fluid. The velocity gradient in the area of the stable free jet is very large. As a result of this very large velocity gradient, Kelvin-Helmholtz vortices are formed, which form rings around the free jet. Due to instabilities the vortices spread asynchronously. This causes the free jet to meander and the shear layer to increase or the velocity gradient to decrease. The vortices thus lose their energy source. In the further course of the process, the large vortices disintegrate into smaller ones, whereby the energy is transferred and dissipated. Figure

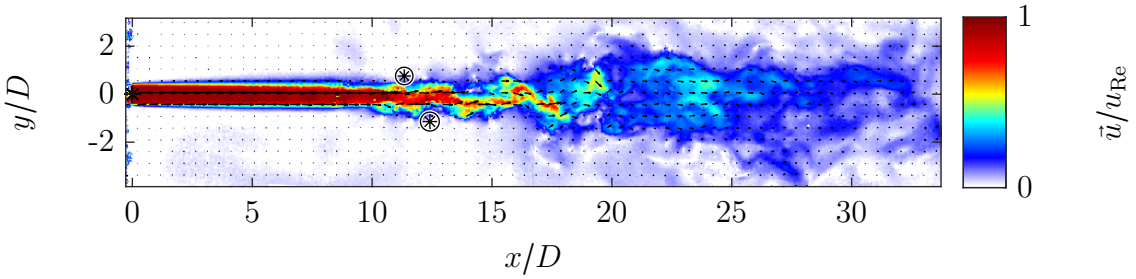

Figure 5.9: Exemplary visualization of detected vortices in an instantaneous velocity field. The vector length is color coded in the background, with vectors ploted on top. Two exemplary vortices are marked by circles.

5.9 shows an example of a instantaneous velocity field with two detected, exemplary visualized vortices. For the detection of the vortices visible in the measurement plane an algorithm according to Graftieaux et al. (2001) was used. The two vortices which are connected by a vortex ring fit very well to the clearly visible meandering shape of the free jet. Figure 5.10 shows a spatial number distribution of the vortices at the Reynolds number Re = 2000 based on 1000 statistically independent vector fields. It is clearly visible that the vortices are located in the shear layer and not in the core or recirculation area. The number is highest in the highly turbulent area. Figure 5.11 shows the spatial number distribution of the vortices for the high Reynolds number case (Re = 5700).

The size distribution and size development of the vortices are shown for two investigated Reynolds numbers Re = 2000 and Re = 5700 in figure 5.12. In both cases the vortex size increases very strongly with x, whereby this increase starts earlier with the higher Reynolds number. The increase occurs up to the beginning of the high turbulent range of the Reynolds number Re = 2000 at approx. x/D = 11 and at Re = 5700 at approx. x/D = 3 the vortex size increases. In the further course, the size of the vortices decreases slightly. In the area of decreasing turbulence intensity, the vortex size increases again. This increase is slower than in the initial area. It should be noted that the vortex size is larger at the lower Reynolds number Re = 2000 than at the higher Reynolds number Re = 5700.

Figure 5.13 shows the comparison of the normalized, ensemble-averaged fields at a Reynolds number of Re = 2000 and variation of the low pressure channel ratios of D_o^* = 5, D_o^* = 10, D_o^* = 15 and D_o^* = 20. It should be noted that when measuring with a low pressure channel ratio of D_o^* = 5, the range of approximately $0 < D_o^* < 1$ is not visible due to a seal. In addition, a distortion of the free jet is visible in the range $7 < D_o^* < 9$ in the same measurement, which is caused due to the mounting of the very small inner channel. Apart from these restrictions, the flow fields shown are very similar. The free jets are all symmetrical, and have a distinct core area that reaches up to about x/D = 12 behind the orifice, as shown above. The subsequent expansion of the free jet is also similar in all cases, but in the more distant range of $x/D > 20$,

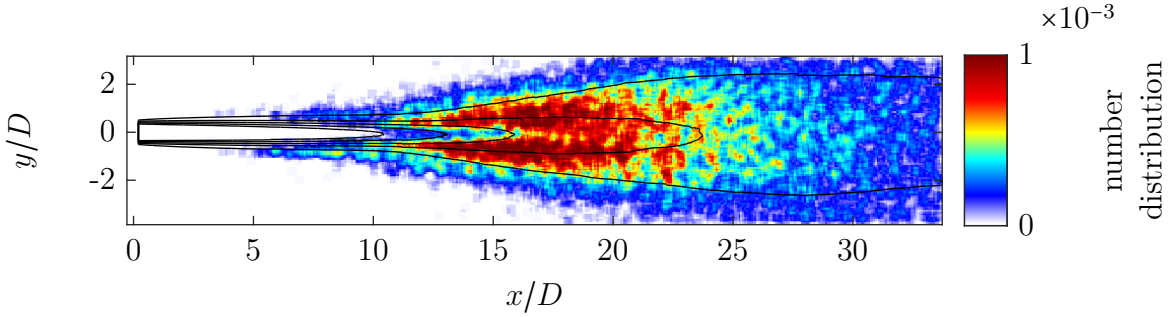

Figure 5.10: Spatial distribution of the detected vorticies at a Reynolds number of Re = 2000.

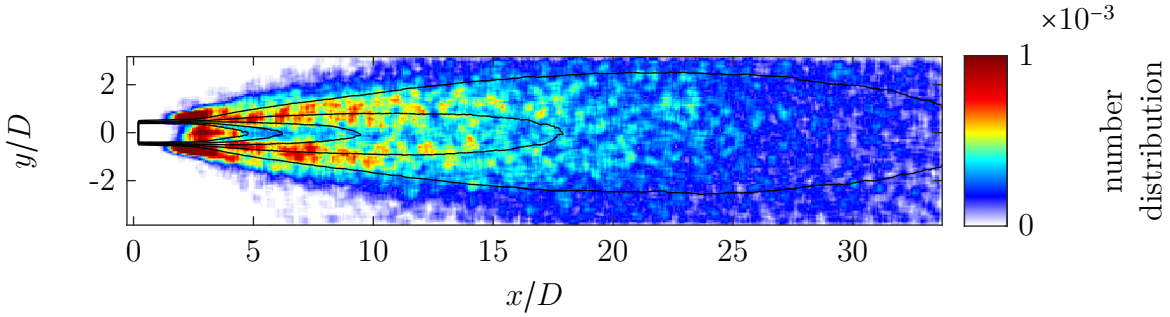

Figure 5.11: Spatial distribution of the detected vorticies at a Reynolds number of Re = 5700.

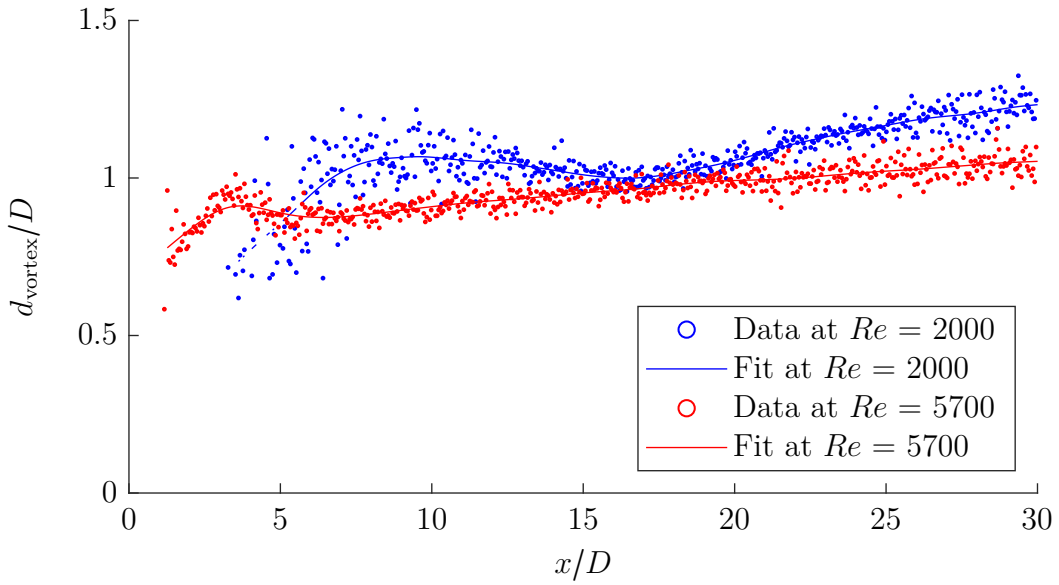

Figure 5.12: Development of the vortex diameter over the length of the free jet for both Reynolds numbers investigated.

a more pronounced decrease in velocity is observed the smaller the channel diameter ratio is. Accordingly, with a channel ratio of $D_{\mathrm{o}}^{*} = 5$ and a length of $x/D = 30$, the free jet is decayed almost completely and the energy is dissipated. In comparison to the diameter ratios of $D_{\mathrm{o}}^{*} = 15$ and $D_{\mathrm{o}}^{*} = 20$, a reduced velocity in the rear velocity field can also be observed in the case of the diameter ratio of $D_{\mathrm{o}}^{*} = 10$.

The measured velocity fields fit very well with the original scale results, where also the influence of the wake flow channel diameter D_{o} on the free jet as well as the influence of the Reynolds number were investigated (Preiss et al., 2021).

Based on the measured velocity fields, the Kolmogorov length l_{K}, i.e. the diameter of the smallest energy-carrying vortices as well as the size of the largest energy-carrying vortices l_0 can be calculated to characterize the turbulence similar to the calculations of Innings and Trägårdh (2007). In the estimation performed by Innings and Trägårdh (2007) for flat valves with a gap of the height h, the calculation of the turbulent energy dissipation rate is based on a roughly determined dissipation volume of 20 gap widths in the flow direction, two gap widths in the perpendicular to the flow and the model depth. In this region the jet has lost more than 50% of the velocity so most of the energy is dissipated. The turbulent kinetic energy based on the dissipated power P_{diss} in the defined dissipation volume V_{diss} is calculated based on equation 5.3. The dissipated power is calculated with equation 5.4. Due to the simplifications concerning the dissipation volume the turbulent kinetic energy is calculated with equation 5.5. The Kolmogorov length and the length of the largest vortices are calculated based on equation 5.6 and 5.7.

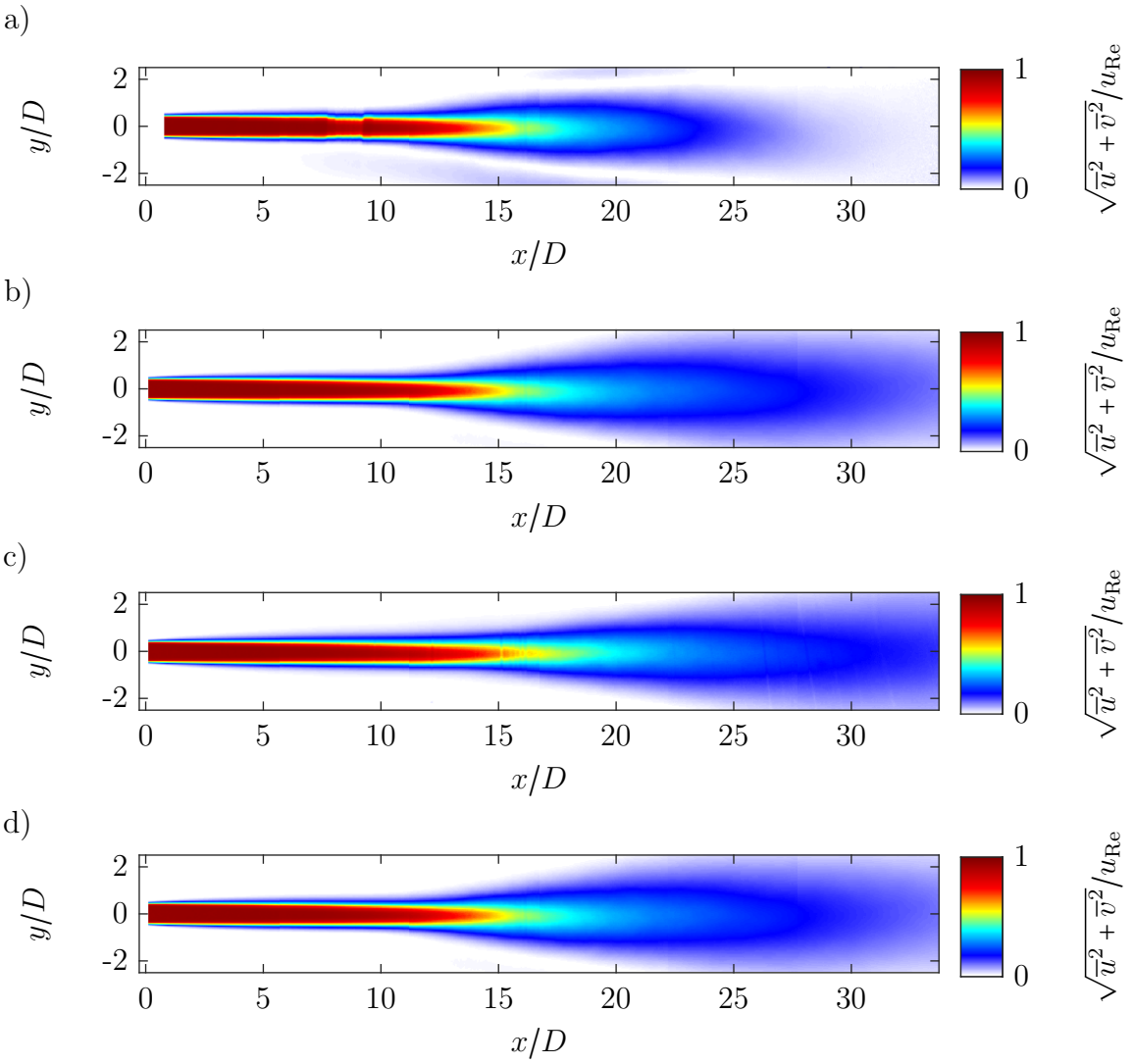

Figure 5.13: Comparison of the normalized, ensemble-averaged free jet velocity fields at four different low pressure channel diameters. a) D_{o}^{*} = 5; b) D_{o}^{*} = 10; c) D_{o}^{*} = 15; d) D_{o}^{*} = 20.

$$\epsilon = \frac{P_{\mathrm{diss}}}{V_{\mathrm{diss}} \cdot \rho_{\mathrm{c}}} \tag{5.3}$$

$$P_{\mathrm{diss}} = \frac{\rho_{\mathrm{c}} \cdot u_{\mathrm{Re}}^2}{2} \cdot \dot{V} \tag{5.4}$$

$$\epsilon = \frac{u_{\mathrm{Re}}}{80h} \tag{5.5}$$

$$l_{\mathrm{K}} = \left(\frac{(\eta_{\mathrm{c}}/\rho_{\mathrm{c}})^3}{\epsilon} \right)^{1/4} \tag{5.6}$$

$$l_0 = l_{\mathrm{K}} \cdot Re^{3/4} \tag{5.7}$$

In the present model of the concentric orifice, with exact knowledge of the symmetrical velocity fields, the range of turbulent flow and thus the turbulent dissipation volume can be estimated more accurately as a body of revolution. The free jet core region can be excluded from the calculation of the turbulent dissipation volume on the basis of the velocity field measurements, since laminar flow is present there. Based on the detailed knowledge of the velocity field, this calculation approach can be modified and the dissipated velocity fraction f and the corresponding dissipation volume can be varied systematically. Corresponding to the dissipated velocity fraction, the dissipation volume can be calculated from the ensemble-averaged velocity field, omitting the free jet core region, more precisely the region where the velocity is greater than 99% of the theoretical free jet velocity u_{Re} ($u > 0.99u_{\mathrm{Re}}$). Figure 5.14 shows the color coded velocity field corresponding to the dissipated velocity fraction at Reynolds number $Re = 2000$ for the calculation of the dissipation volume. For larger dissipation fractions, the specified smaller volumes must be included. The evaluation was done up to a dissipated velocity fraction of $f = 0.8$. Larger fractions could not be investigated because of the limitations of the investigated FOV of the velocity field measurements.

Table 5.1 shows the dissipation volume calculated based on the velocity fields for the two Reynolds numbers as a function of the dissipated velocity fraction f. In addition, the volume calculated according to Innings and Trägårdh (2007) is shown.

The dissipated power is also calculated according to the velocity fraction (see equation 5.8).

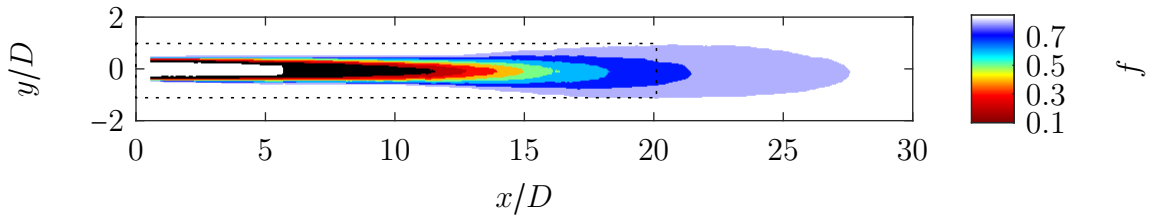

Figure 5.14: Representation of the dissipation area as a function of the dissipated velocity fraction f. The dissipation volume estimated according to the assumptions by Innings and Trägårdh (2007) is indicated by a dashed frame.

Table 5.1: Dissipation volumes as a function of Reynolds number and dissipated velocity fraction f compared to the dissipation volume based on Innings and Trägårdh (2007) in cm^3.

f	0.1	0.2	0.3	0.4	0.5	0.6	0.7	0.8
Re = 2000	1.0	1.5	2.2	3.3	5.3	9.5	21.3	58.6
Re = 5700	2.5	4.0	5.6	7.2	9.4	13.8	23.8	58.6
Innings and Trägårdh (2007)					62.8			

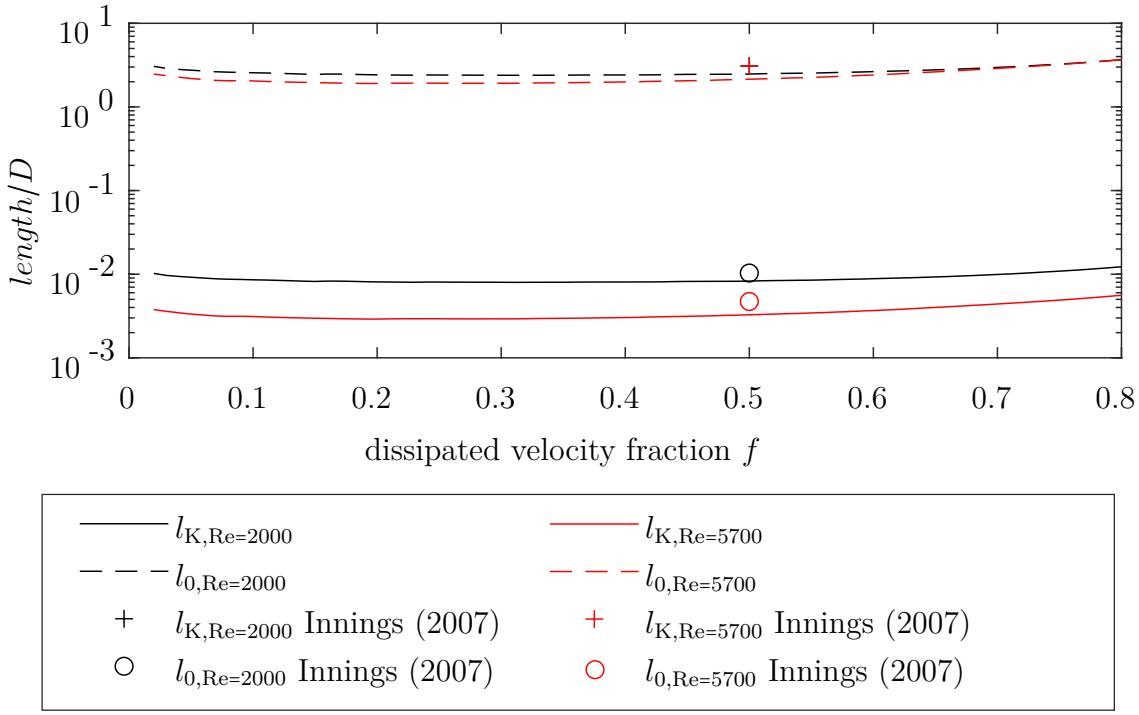

Figure 5.15: Comparison of the Kolmogorov length and the diameter of the largest vortices according to the modified method of Innings and Trägårdh (2007). For comparison, the sizes calculated according to the assumptions of Innings and Trägårdh (2007) are plotted.

$$P_{\text{diss}} = \frac{\rho_c \cdot ((0.99 u_{\text{Re}})^2 - (f \cdot u_{\text{Re}})^2)}{2} \cdot \dot{V} \tag{5.8}$$

From this dissipation power and the dissipation volume determined from the velocity fields, the turbulent kinetic energy and from this the Kolmogorov length and the length of the largest vortices are calculated according to equations 5.3, 5.6 and 5.7. Figure 5.15 shows the Kolmogorov length and diameter of the largest vortices as a function of dissipated power and Reynolds number for the two Reynolds numbers Re = 2000 and Re = 5700.

For reference, the calculation according to Innings and Trägårdh (2007) is also shown, using the orifice diameter D instead of the gap width h. It can be seen that the calculation according to Innings and Trägårdh (2007) somewhat overestimates the sizes. It is to be noted that in the calculation not only a velocity or energy fraction is included, but the total energy. This is overcompensated by the overestimated dissipation volume. The influence of the dissipated velocity fraction f on the vorticity scales seems to be rather small for both Reynolds numbers investigated for the Kolmogrov length and the length of the largest vortices in the range $0.1 < f < 0.6$. In this range, the expansion of the dissipation volume seems to be proportional to the dissipated power. For larger dissipation velocity fractions, the dissipation volume increases more than the dissipated

power, so that the calculated sizes of the Kolmogorov length and correspondingly the derived size of the largest vortices increase. In total, the Kolmogorov length is in the range of $l_{\mathrm{K,Re=2000}} \approx 100\,\mu$m or $l_{\mathrm{K,Re=2000}} \approx 40\,\mu$m. This means that according to the Kolmogorov-Hinze theory droplets larger than the Kolmogorov length, i.e. $40\,\mu$m or $100\,\mu$m respectively are mainly stressed by turbulent inertia dominated forces, i.e. velocity fluctuations due to vortices. This size range is in the region of the visualization limit due to the measurement resolution and the shadowgraphy method. The size of the largest vortices is in the range of $2D < l_0 < 3D$ which would overestimate the observed vortex size of $d_{\mathrm{vortex}} \approx D$.

5.3. Drop breakup

5.3.1. Deformation in the orifice

In studies, the importance of the elongation in the orifice has been described as particularly important for drop breakup (e.g. Windhab et al. (2005)). To verify the influence of the inlet flow into the orifice on drop breakup, high temporal and spatial resolution measurements were performed in this region. The investigations show that the round primary droplets are all stretched in the inlet region of the orifice due to the shear and elongational flow, regardless of the viscosity ratio. However, the strength of the elongation is very clearly dependent on the viscosity ratio and the flow conditions, i.e. the Reynolds number. Figure 5.16 shows the comparison of three time series for droplet deformation in the orifice.

The images on the left show the deformation process in the inlet area of the orifice and the images on the right show the drops at two points in time after leaving the orifice, so that the final elongation of the drops is clear. The orifice contour is drawn in gray in both images. The drops are drawn in black. All drops are injected into the channel at the same point and move through the orifice almost on the axis of symmetry. The output droplet size is nearly the same for all three cases shown, with a primary droplet size of approximately d_P = 2 mm, so the only difference between the cases shown is the viscosity ratio. The case a) shows the deformation of a drop with a viscosity ratio of η^* = 0.3. The first drop shown is still almost completely round when viewed in detail. However, the second drop shown is already slightly elliptically deformed. When passing the inlet zone, i.e. the area in the flow direction of $-4 < x/D < -2$, the droplet is accelerated with the flow and experiences a very strong elongation. The very large linear elongation of the drop can be seen in the images on the right. The two droplet images after the orifice show that initially no further deformation occurs behind the orifice. Comparison of the two imaged drops shows a slight decrease in drop elongation. This relaxation is much slower compared to the rate of elongation. With increasing viscosity ratio (b): η^* = 3.0, c) η^* = 10.5) the elongation occurs more slowly and is thus lower overall.

Figure 5.17 shows the influence of the Reynolds number on the deformation process in the orifice at three different Reynolds numbers: a) Re = 2000, b) Re = 4000 and c) Re = 5700. The droplets shown all have a primary droplet diameter of d_P = 2 mm. The viscosity ratio of the compared droplets is η^* = 10.5. The comparison shows that as the Reynolds number increases, the elongation of the droplets increases to an elongated drop filament.

From the time-resolved measurements shown in parts in Figure 5.16 and 5.17, the course of the elongation can be calculated. For this purpose, Figure 5.18 and Figure 5.19 show the course of the drop or filament length l, respectively, as they pass through the orifice for different viscosity ratios at Re = 2000 and for the high viscous system (η^* = 10.5) at the Reynolds numbers Re = 2000 and Re = 4000. For the highest Reynolds number Re = 5700 the filament length was to long to be measured precisely. The droplet or filament length is normalized by the diameter of the primary droplets d_P. As was already clear in Figure 5.16 and Figure 5.17, the elongation or aspect ratio

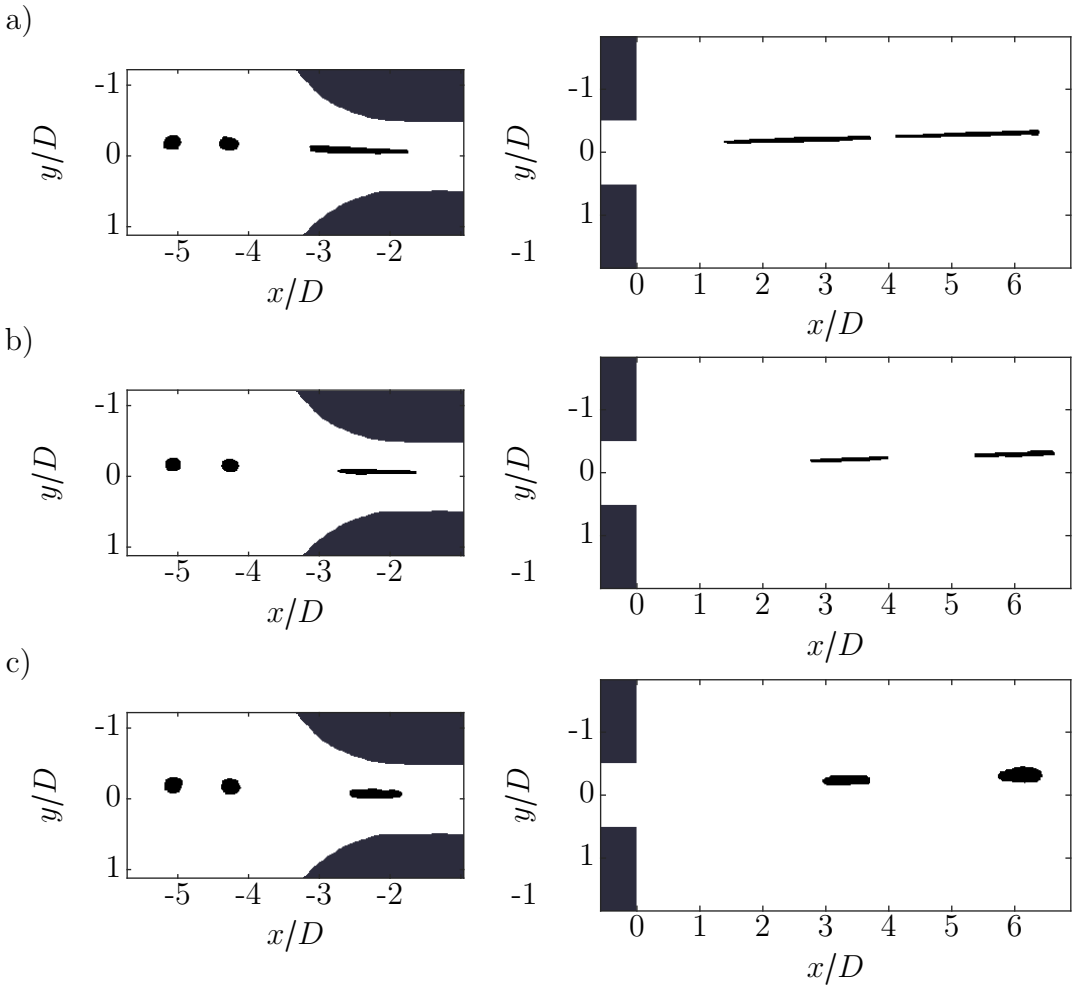

Figure 5.16: Ilustration of the influence of the viscosity ratio on the droplet deformation at the orifice inlet at a Reynolds number of $Re = 2000$ and a primary droplet size of about $d_P = 2\,\text{mm}$. a) $\eta^* = 0.3$, b) $\eta^* = 3.0$ and c) $\eta^* = 10.5$.

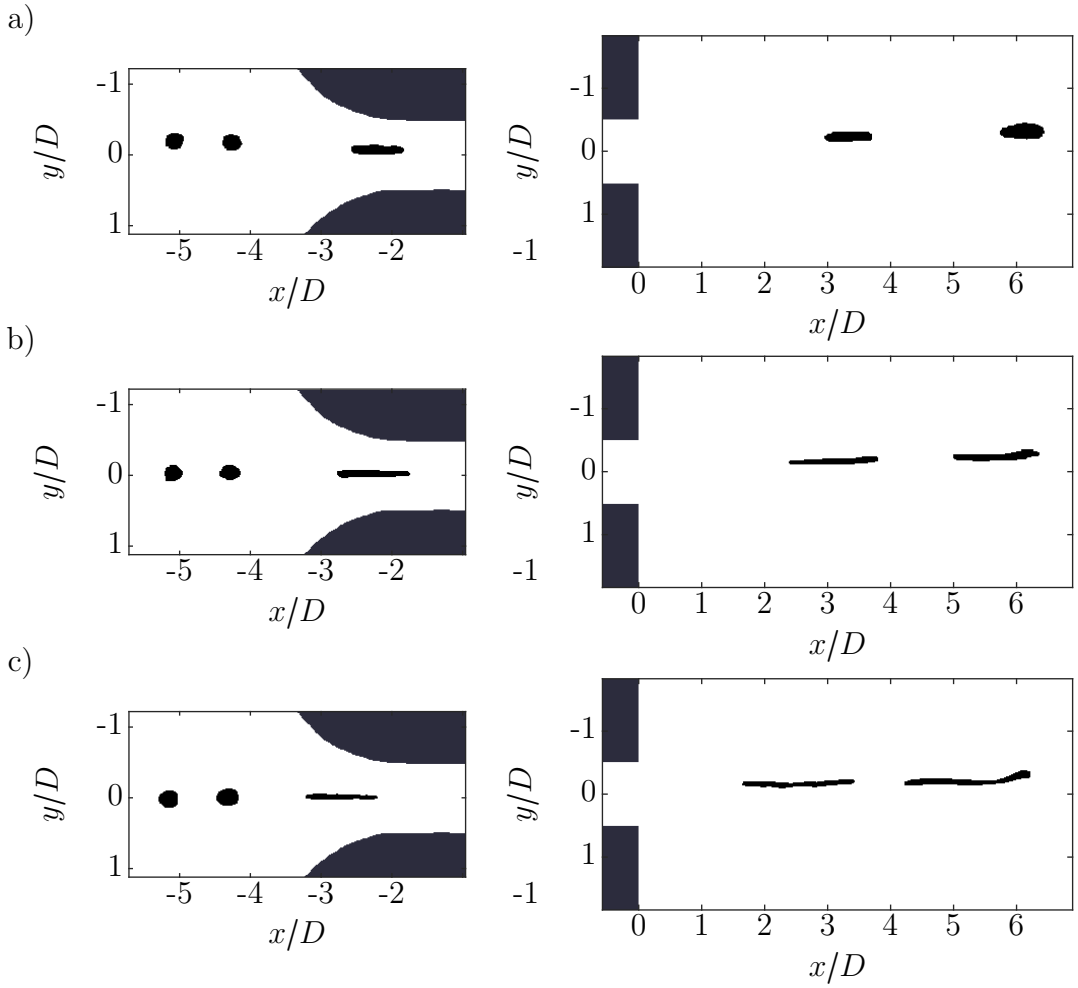

Figure 5.17: Ilustration of the influence of the Reynolds number on the droplet deformation at the orifice inlet at a viscosity ratio of $\eta^* = 10.5$ and a primary droplet size of about $d_P = 2\,\text{mm}$. a) $Re = 2000$, b) $Re = 4000$ and c) $Re = 5700$.

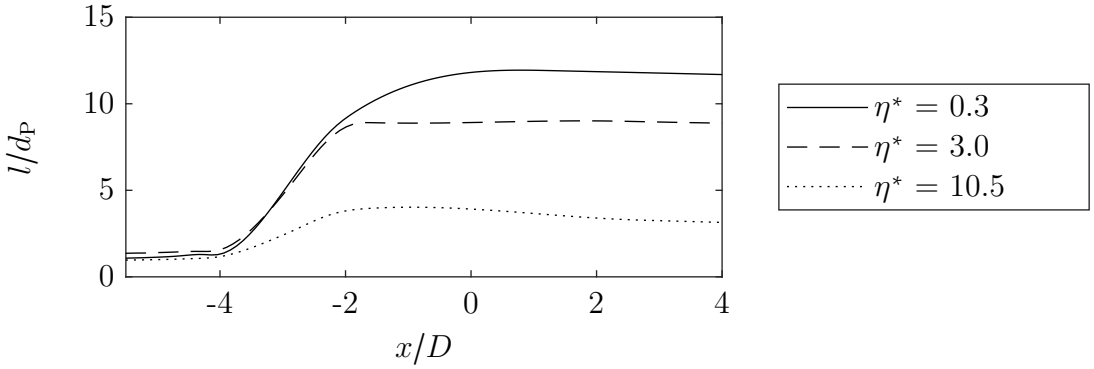

Figure 5.18: Course of the drop or filament length when passing through the orifice for three different viscosity ratios at the Reynolds number $Re = 2000$.

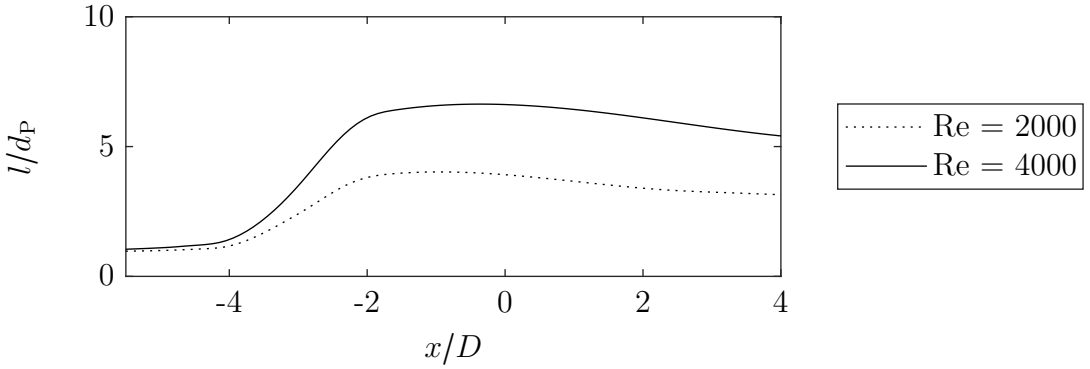

Figure 5.19: Course of the drop or filament length when passing through the orifice for two different Reynolds numbers at a viscosity ratio of $\eta^* = 10.5$.

of the droplets decreases with increasing viscosity ratio and increases with increasing Reynolds number. The length is shown above the drop position, i.e. the position of the drop center of gravity. It is clear from the drop images that the deformation only occurs in the range between approx. $-4 < x/D < -2$. The problem with the representation of the length profile over the drop position in the orifice is the non-uniform deformation of the drop. At one point in time, the drop is subjected to completely different stresses depending on its position and extent, so that the deformation is not uniform along the stretched droplet. While the front part of the drop is already in the cylindrical region of the orifice, where hardly any stresses act on the drop, the rear part of the drop is still in the region of contraction and experiences strong stresses. The same applies to the beginning of the contraction, where the drop front experiences different stresses than the rear area, which still experiences hardly any stresses, although the differences are smaller there due to the smaller elongation. Due to this problem, a positive length change is also shown in the range between approx. $-2 < x/D < 0$.

As shown in chapter 5.2.1, not all of the inlet region due to reflections is optically accessible. This concerns both the $-4.3 < x/D < -3.7$ and $-1.2 < x/D < 0$ regions, the latter not being so important due to the small change in stress. In both cases, the

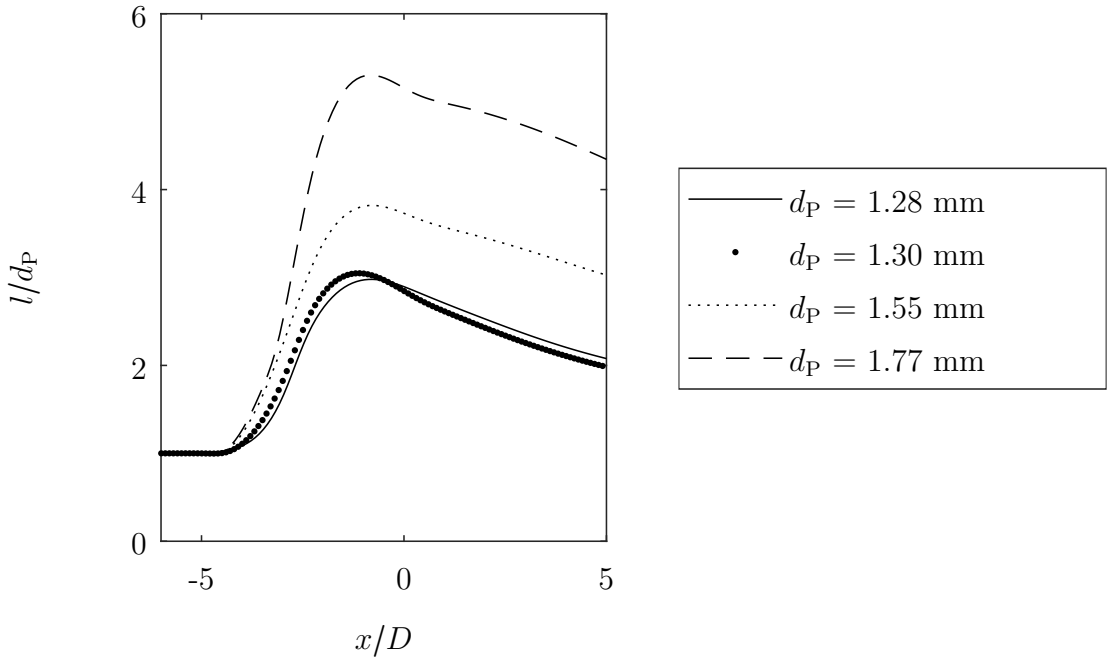

Figure 5.20: Comparison of the drop or filament length for different primary drop diameters.

curve is obtained by a fit of the drop leading edge position and the drop trailing edge position.

All droplet trajectories through the orifice shown so far were performed with droplets of a primary droplet diameter of approximately $d_P = 2\,\text{mm}$. To determine the influence of the droplet diameter, experiments were performed with different primary droplet diameters at the same viscosity ratio ($\eta^* = 3.0$) and the same Reynolds number ($Re = 2000$). Figure 5.20 shows the course for four different sized droplets.

It can be seen that even small droplets are significantly deformed and elongated to a multiple primary length, but the maximum elongation achieved increases significantly with increasing initial diameter. These results further show that the measurement method is very well suited to measure the course of the deformation independent of the drop size or the deformation ratio. Due to the very good temporal and spatial resolution of the measurement data, transient deformation calculation models can be adapted to these data or validated with these data (see Mutsch et al. (2021b)).

5.3.2. Deformation and breakup after passing the orifice

Visualization of drop breakup during high-pressure homogenization was achieved by high-speed imaging using the modified shadowgraphy technique. To visualize the drop breakup and the previous deformation in the free jet behind the orifice, four high-speed cameras were set up so that the fields of view were aligned in a row along the axis of symmetry in the main flow direction and overlapped slightly. In order to know

exactly the initial state, i.e. the primary droplet size and the trajectory of each droplet investigated, a fith high-speed camera was directed at the area of the orifice or just before the orifice.

The observations show that the droplets follow the fluid and therefore are mainly transported downstream along the main flow direction. As the free jet decays, the droplets in the free jet begin to meander with the jet, becoming slightly deformed. In the region of the decaying free jet, i.e. the shear layer, the droplets, which have already been deformed depending on the flow conditions and the viscosity ratio by the inlet flow into the orifice, are deformed turbulently and finally break up if the deformation is sufficiently large. Figure 5.21 shows an overlay of the normalized, ensemble-averaged velocity field in the region in front of and in the orifice and the free jet behind the orifice with individual droplet images or respectivly masks of the droplets (black structures) from a time series. For a better overview, the area behind the orifice was divided into two parts, so that the individual details are better visible.

Since the influence of the trajectory on the droplet breakup could be investigated by the movable injection capillary, the dimensionless dosing position parameter r^* is defined from the dosing position r_{in} and the inlet diameter D_{i}.

$$r^* = \frac{r_{\mathrm{in}}}{D_{\mathrm{i}}/2} \tag{5.9}$$

The droplet time series shown belongs to a test series at a viscosity ratio of $\eta^* = 0.3$ and a droplet dosing position or droplet trajectory close to the axis of symmetry ($r^* \approx 0$). The Reynolds number of the drop breakup time series, as well as the background flow field, is $Re = 2000$.

Starting at a length of about $x/D = 7$, an up and down motion of the drop can be seen, which is superimposed by a turbulent three-dimensional deformation starting at a length of about $x/D = 15$. In this region, the droplet is stretched, twisted, or compressed by the interaction with multiple vortices in individual regions. The turbulent droplet-vortex interactions lead to an increasingly severe deformation of the filament, which is accompanied by further elongation. This elongation causes a reduction of the filament diameter, so that a clear identification of the filament structure becomes more and more difficult without the drop necessarily being broken. In particular, automated masking of the drop fails at this stage, so that only individual clearly identifiable filament segments are masked as drops.

Figure 5.22 and 5.23 show the corresponding superpositions for the two viscosity ratios $\eta^* = 3.0$ and $\eta^* = 10.5$ for comparison of the influence of the viscosity ratio on the drop breakup in the turbulent region behind the orifice during high pressure homogenization. The droplet injection position and the Reynolds number as well as the primary droplet diameter are similar for all three test series ($r^* \approx 0$, $Re = 2000$ and $d_{\mathrm{P}} = 2\,\mathrm{mm}$).

The comparison shows that, independent of the viscosity ratio, a turbulent droplet deformation and the subsequent droplet breakup takes place in the region of the turbulently decaying free jet, i.e. in the range of approx. $x/D > 15$. Up to this region, a

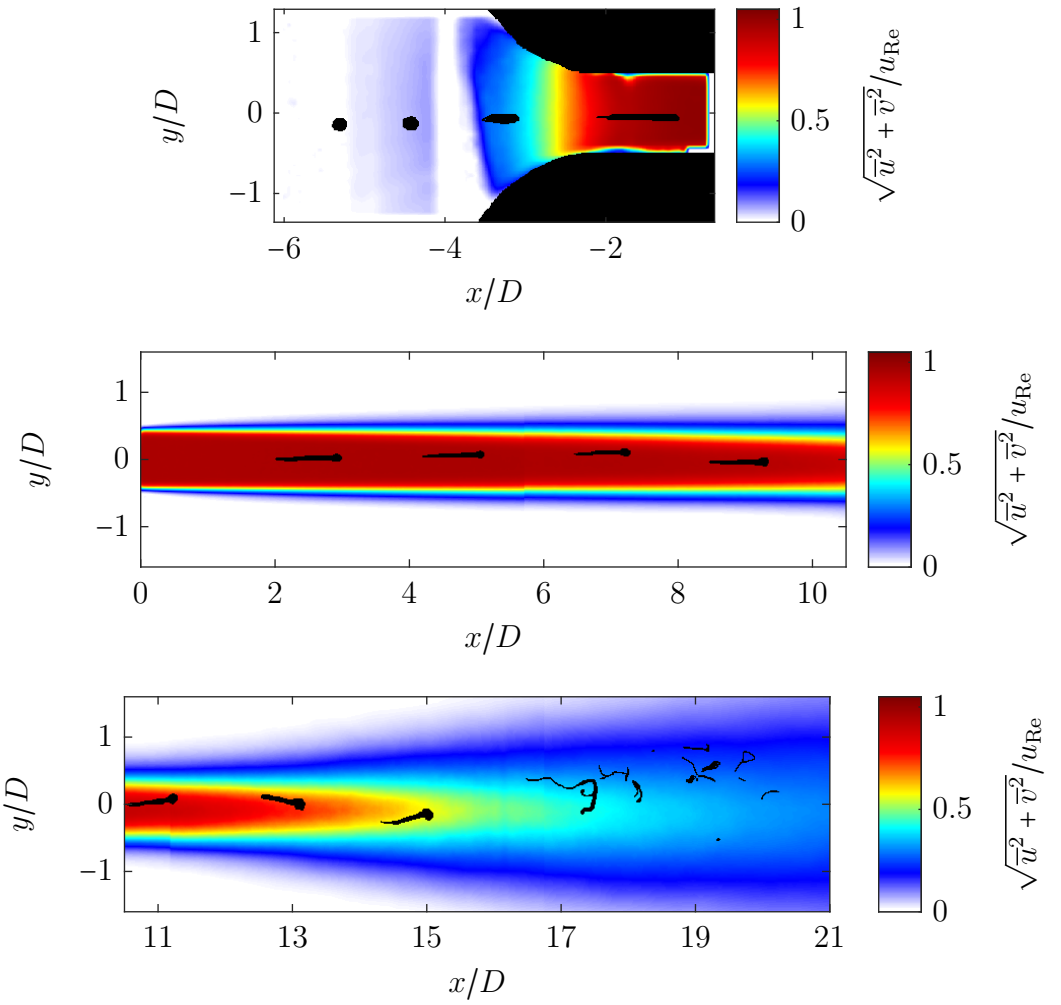

Figure 5.21: Representation of the temporal and spatial drop breakup in the free jet behind the orifice for a drop with viscosity ratio $\eta^* = 0.3$ at a Reynolds number of $Re = 2000$. The normalized, ensemble-averaged velocity field is shown in the background. The dimensionless dosing point of the primary drop is $r^* \approx 0$ which corresponds to the axis of symmetry.

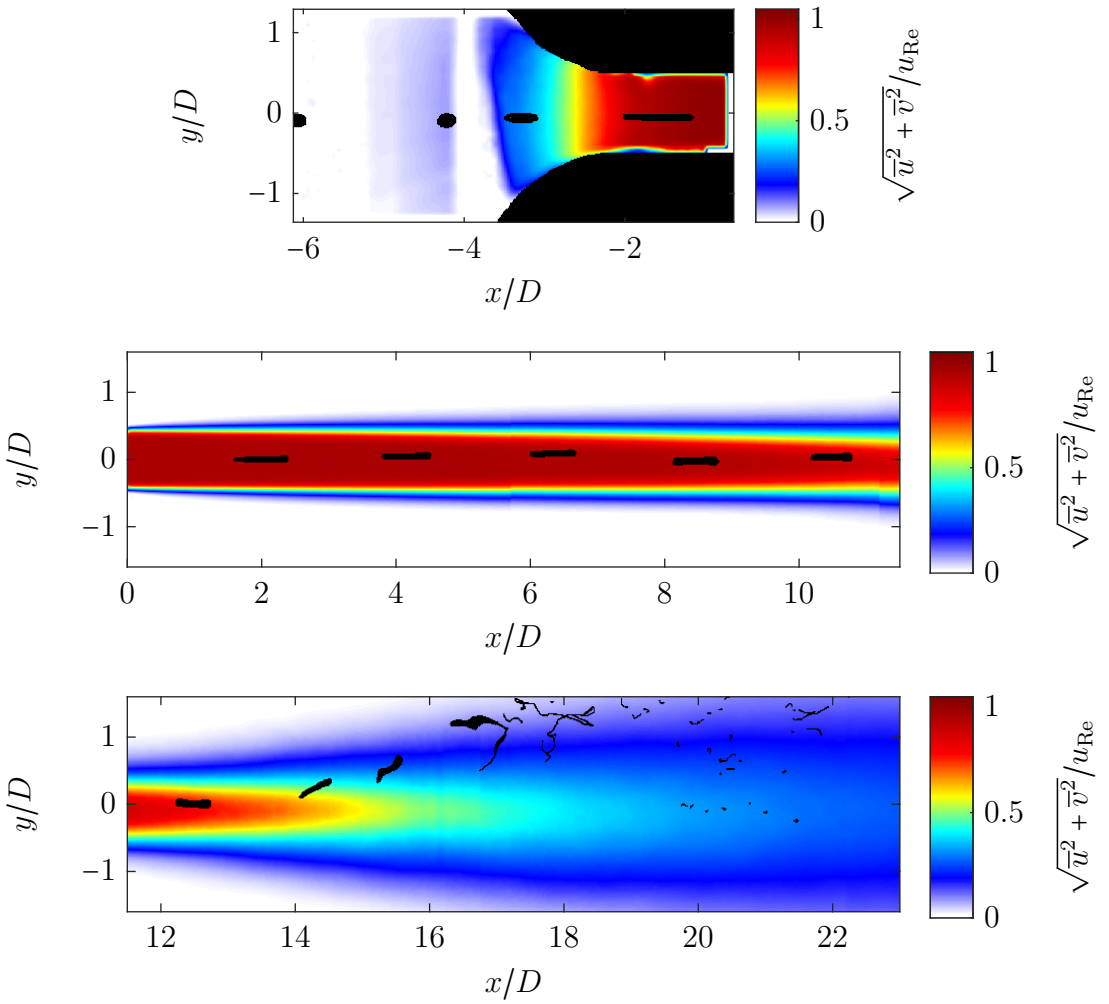

Figure 5.22: Representation of the temporal and spatial drop breakup in the free jet behind the orifice for a drop with viscosity ratio $\eta^* = 3.0$ at a Reynolds number of $Re = 2000$. The normalized, ensemble-averaged velocity field is shown in the background. The dimensionless dosing point of the primary drop is $r^* \approx 0$ which corresponds to the axis of symmetry.

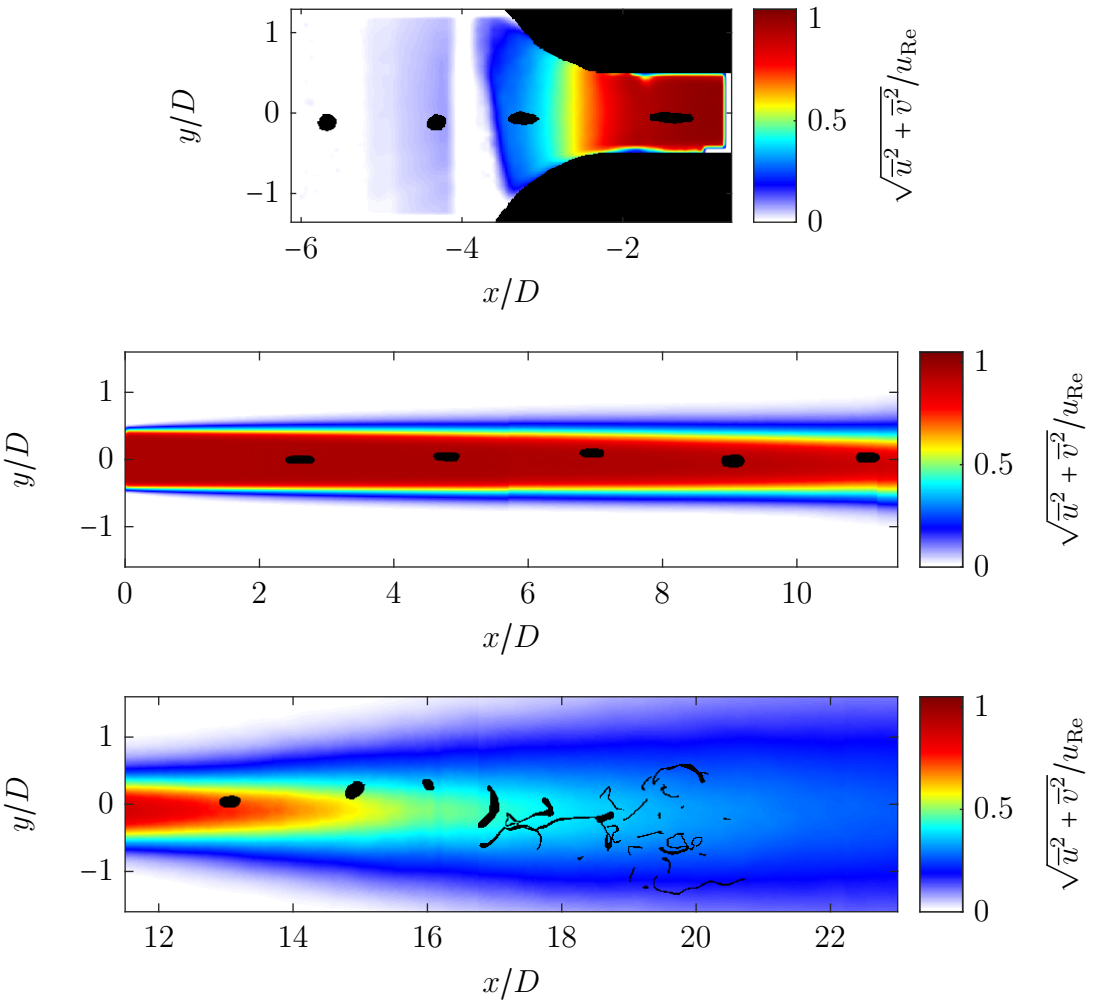

Figure 5.23: Representation of the temporal and spatial drop breakup in the free jet behind the orifice for a drop with viscosity ratio $\eta^* = 10.5$ at a Reynolds number of $Re = 2000$. The normalized, ensemble-averaged velocity field is shown in the background. The dimensionless dosing point of the primary drop is $r^* \approx 0$ which corresponds to the axis of symmetry.

meandering of the droplet in the free jet core can be observed, which clearly increases from a length of about $x/D = 13$ and is superimposed by first vortices.

However, it is clearly noticeable that the relaxation of the droplets in the free jet core occurs at different rates. The droplet of the test series with the viscosity ratio of $\eta^* = 10.5$, which was hardly elongated by the elongation and shear flow in the inlet region of the orifice, almost reaches its undeformed round initial state again by the time it leaves the free jet core, whereas the two lower-viscosity droplets are still clearly elongated. Figure 5.24 shows the direct comparison of the droplet deformation in the free jet core region.

In addition to the different relaxation, the comparative images also show differences in the droplet shape for the different test series, which mainly differ in the viscosity ratio. The surface tension as well as the density of the three different material systems is only slightly different. The differences in the drop shape in the free jet are shown in the enlarged representation in Figure 5.25. The droplets shown are exemplary for all experiments with the three different droplet viscosities, and the droplet shape is very reproducible for the different viscosity ratios.

It can be clearly seen that the two higher viscosity ratio droplets form a more cylindrical droplet filament with round ends, while the lower viscosity ratio droplet tapers to a pointed shape at the end and assumes a round shape in the front region with a diameter that is larger than the filament diameter.

The influence of the drop trajectory, i.e. the droplet dosing position r^* on the drop breakup could be investigated. For this purpose, series of tests were carried out with both the system with viscosity ratio $\eta^* = 3.0$ and $\eta^* = 10.5$ at different dosing positions. The experiments with the viscosity ratio $\eta^* = 3.0$ are shown below. The experimental results with the viscosity ratio $\eta^* = 10.5$ are shown in the appendix A.1.

Figure 5.26 shows the time course of a droplet with viscosity ratio $\eta^* = 3.0$ at Reynolds number $Re = 2000$. The dosing point is located at the dimensionless radius $r^* \approx 0.8$. The images show the droplet deformation in the orifice, with the droplet passing through the orifice near the orifice wall due to radial dosing. The radial droplet position causes the droplet to be sheared in the free jet region immediately after exiting the orifice. This leads to a visible shear deformation, which can be observed in the drop images up to a length of about $x/D = 13$. The region closer to the free jet core or the axis of symmetry shifts in the direction of flow relative to the outer region of the droplet. At the transition of the drop into the shear layer region, the drop is three-dimensionally deformed by vortices and disintegrates in the further course.

Figure 5.27 shows the course of a droplet with the same Reynolds number and viscosity ratio ($Re = 2000$, $\eta^* = 3.0$) but with the droplet dosed even further out ($r^* \approx 1$). In the orifice region, the images show that the drop is stretched along the orifice wall for a very long length. Behind the orifice, the drop is directly inside the shear layer. In addition, the drop is stretched very long due to the elongation in the inlet region of the orifice. Due to the radial position, the droplets reach the outermost region of the free jet in which Kelvin-Helmholtz instabilities develop due to the large velocity difference. The elongated droplet filament is wound up by the vortices in the vortex cores and thus

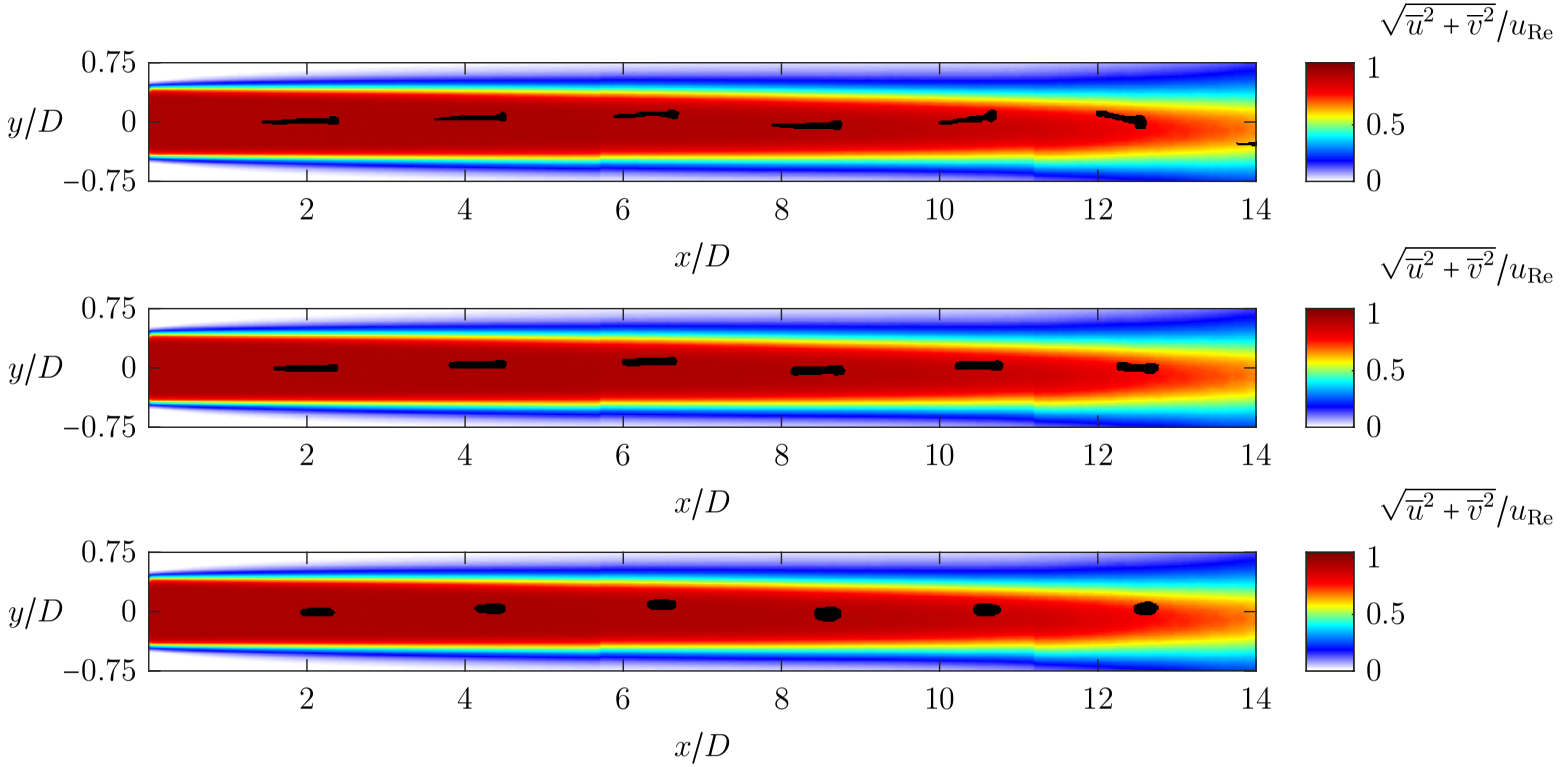

Figure 5.24: Temporal and spatial comparison of the relaxation process of the droplets in the core region of the free jet behind the orifice at three different viscosity ratios: top: η^* = 0.3; middle: η^* = 3.0; bottom: η^* = 10.5. In the background the normalized, ensemble-averaged velocity field is shown.

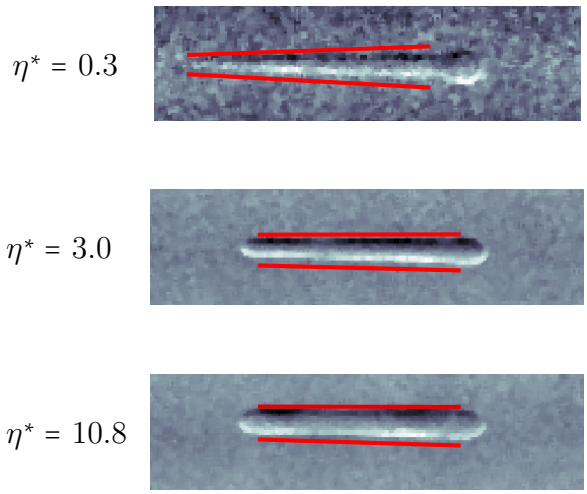

Figure 5.25: Illustration highlighting the different droplet-filament shapes after passing through the orifice for the different material systems with different viscosity ratios. The FOV shown is the same in all three images and the primary droplet size is comparable as well as the Reynolds number.

strongly deformed and further stretched. Due to the extreme length, the front region of the droplet is deformed in the vortices while the back region is still in the orifice. The drop filaments are stretched by the vortices to such an extent that at a certain point they break down into individual segments, or the part of the drop filament becomes so thin that it can no longer be resolved optically by the measurement technique. Due to the interaction with the vortices, the front filament segment is swirled and finally broken up into fine secondary droplets.

For better visualization, individual images are combined in enlarged form in Figure 5.28.

The images show that from a length of approx. $x/D = 3$ the drop filament is twisted by vortices. They also show that several of these vortices attack the filament at different points, as the filament continues to move in the direction of flow after passing through the vortex region. After 2–4 vortex interactions, the filament is so thin that it can no longer be imaged or disintegrates into individual secondary droplets. The spacing of the vortices varies, but is about $2D$ in the front area behind the orifice. When the filament disintegrates into individual, easily identifiable segments, larger drops form near vortex cores, which may disintegrate into finer drops downstream.

The comparison of the three dosing points investigated and the different droplet trajectories achieved shows that the droplet is turbulently stressed more quickly with increasing radial dosing/trajectory, i.e. earlier in the free jet, and thus apparently breaks up more quickly. The filament, of the droplet passing through the orifice on the axis of symmetry ($r^* \approx 0$), is only slightly turbulent deformed until far into the shear

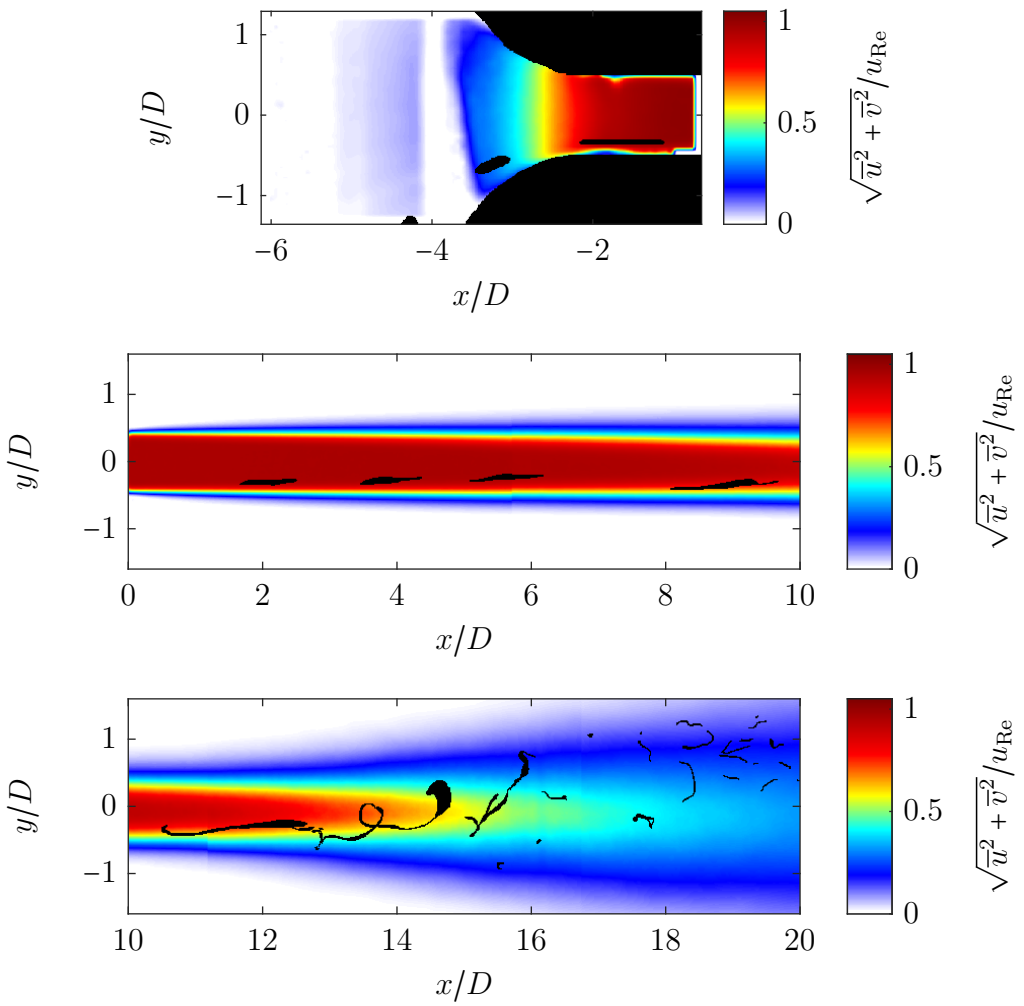

Figure 5.26: Representation of the temporal and spatial drop breakup in the free jet behind the orifice for a drop with viscosity ratio $\eta^* = 3.0$ at a Reynolds number of $Re = 2000$. The normalized, ensemble-averaged velocity field is shown in the background. The dimensionless dosing point of the primary drop is $r^* \approx 0.8$.

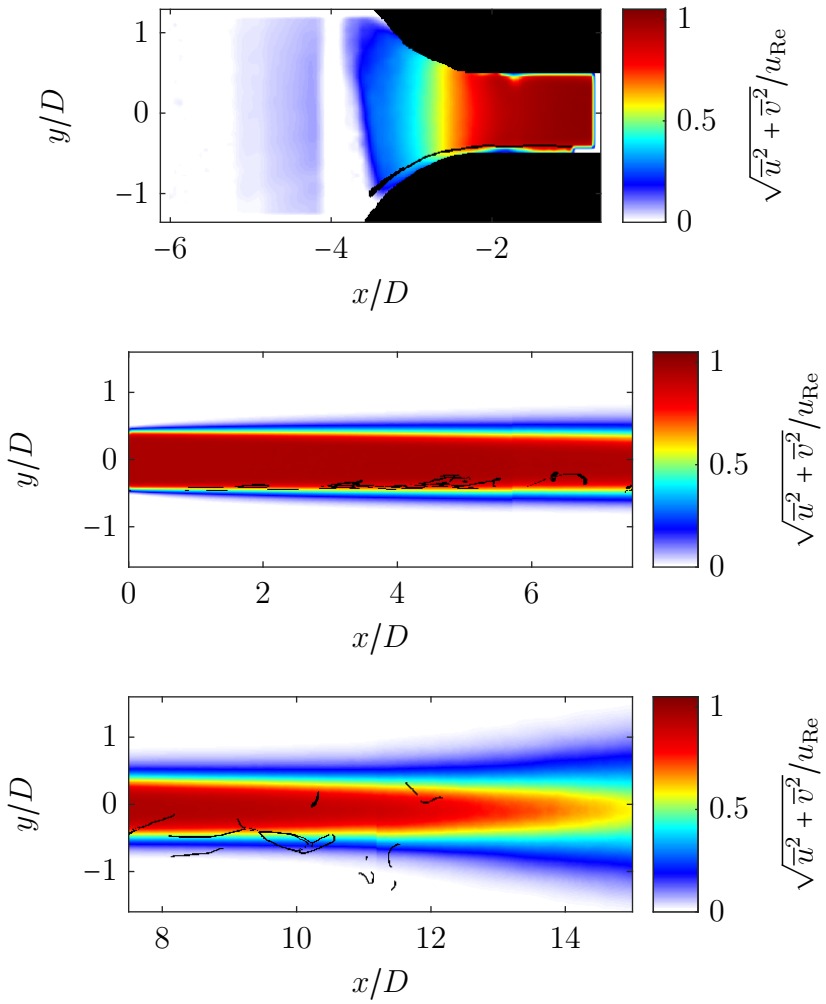

Figure 5.27: Representation of the temporal and spatial drop breakup in the free jet behind the orifice for a drop with viscosity ratio $\eta^* = 3.0$ at a Reynolds number of $Re = 2000$. The normalized, ensemble-averaged velocity field is shown in the background. The dimensionless dosing point of the primary drop is $r^* \approx 1$.

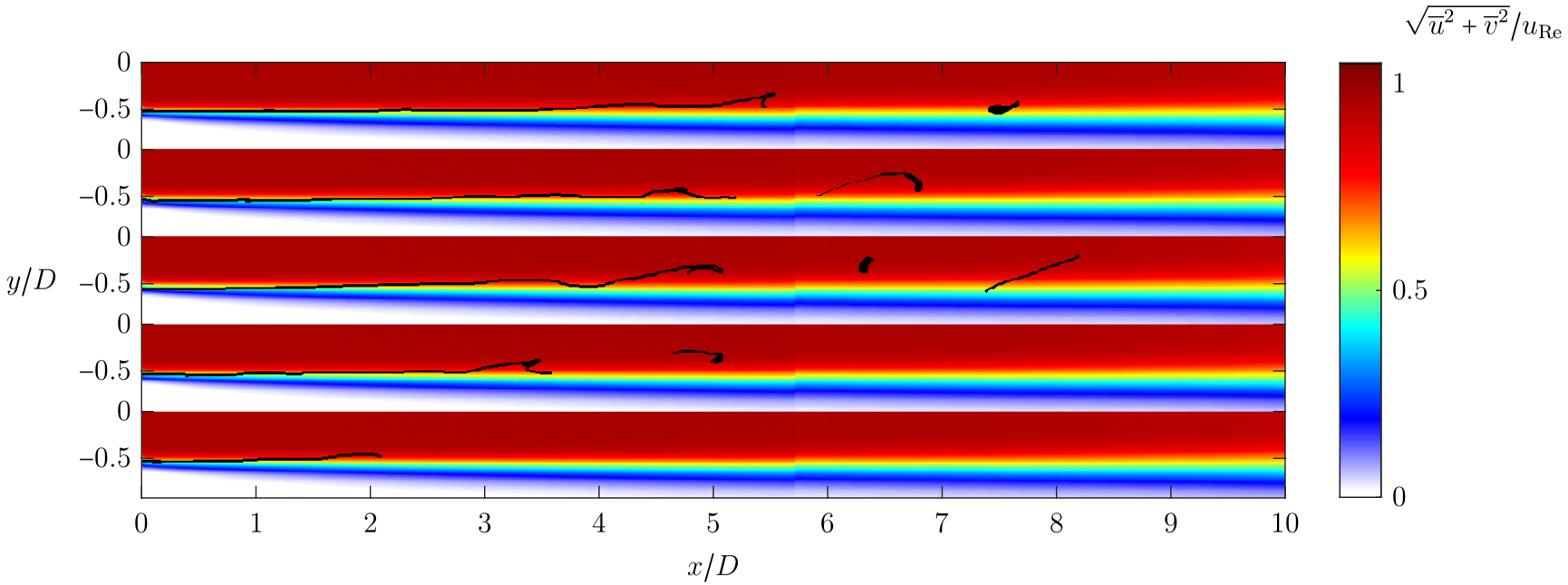

Figure 5.28: Temporal course of droplet deformation and breakup by Kelvin-Helmholtz vortices in the shear layer for droplets passing through the orifice at the wall ($r^* \approx 1$) and a Reynolds number of Re = 2000. In the background the normalized, ensemble-averaged velocity field is shown.

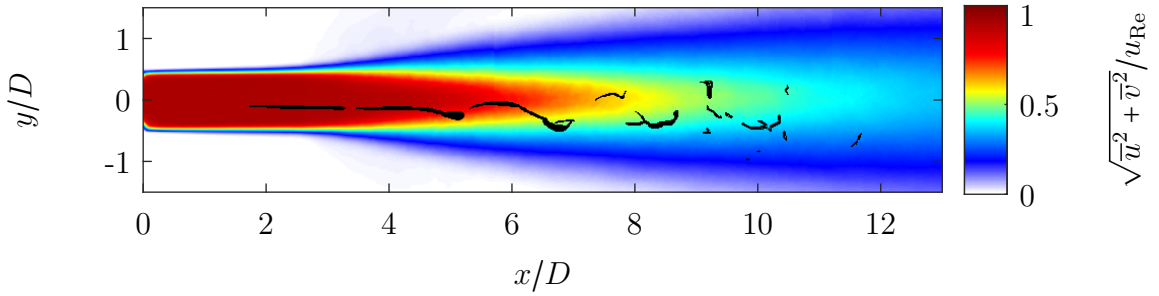

Figure 5.29: Representation of the temporal and spatial drop breakup in the free jet behind the orifice for a drop with viscosity ratio $\eta^* = 3.0$ at a Reynolds number of $Re = 5700$. The normalized, ensemble-averaged velocity field is shown in the background. The dimensionless dosing point of the primary drop is $r^* \approx 0$ which corresponds to the axis of symmetry.

layer, starting at a length of approx. $x/D > 15$ and breaks up into individual secondary droplets or filament segments (see Figure 5.22). When dosing at a radial position of $r^* \approx 0.8$ the resulting droplet filament is turbulently deformed starting at a length of approx. $x/D > 13$ (see 5.26). For dosing close to the wall ($r^* \approx 1$), this deformation and break up process may already start at $x/D > 3$ (see 5.27). These results agree very well with the described findings in the literature ((Budde et al., 2002) (Wieth et al., 2016)).

Experiments at higher Reynolds numbers were also carried out in the test facility. Here, the visualization problems caused by small filament size or the chaotic three-dimensional superposition of filaments or filament fragments in the turbulent region, which only occur in some cases at the low Reynolds number, are intensified by the fact that the stresses are significantly greater. These increased stresses already lead to thin filaments due to the elongation in the inlet area of the orifice. In addition, the breakup is much faster and the deformation due to interactions of the droplet with vortices are much more intense, resulting in finer and much more tightly swirled filaments that can only be diffusely seen. Figure 5.29 shows the course of droplet breakup at a viscosity ratio $\eta^* = 3.0$, a Reynolds number of $Re = 5700$ and a dosing on the symmetry axis ($r^* \approx 0$).

As already shown, the free jet is significantly shorter and decays faster. Compared to the images taken at the lower Reynolds number, the filament in the free jet core region downstream of the orifice is elongated significantly longer with the same viscosity ratio of the droplet. As with the lower Reynolds number, a three-dimensional defor-

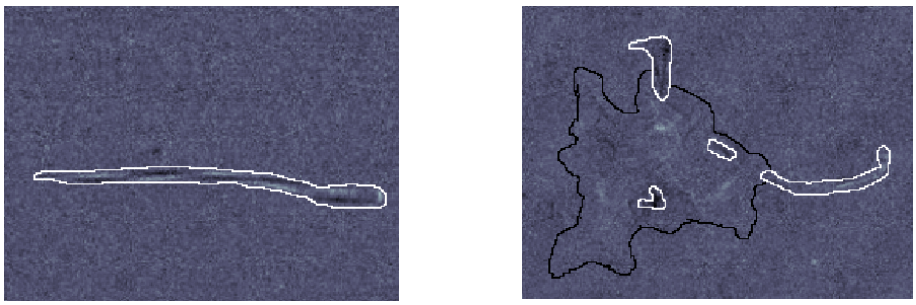

Figure 5.30: Image illustrating the difficulties in studying drop breakup at the higher Reynolds number (Re = 5700). The white line shows the border of the drop detected by the algorithm. The black line shows the difuse area in which the droplet is turbulently deformed.

mation of the previously linearly stretched droplet filament occurs when the droplet passes from the free jet core region into the turbulent free jet region. In the shear layer region, the droplet disintegrates very rapidly. In this description, however, it must be noted that visualization of the disintegrating, three-dimensionally deformed droplet filament is very difficult at the high Reynolds number. In contrast to the lower Reynolds number, the vortices are so intense that the filament is strongly deformed and twisted very quickly or in a narrow spatial range, resulting in overlapping of individual filament regions. This is much less the case with the lower Reynolds number, due to the slower breakup and because the deformation of the filament by small-scale vortices is usually superimposed by large-scale vortices, which ensure that the twisted filament is distributed over a larger area. To illustrate the problem, Figure 5.30 shows a filament in the free jet core region and a diffusely swirled, disintegrating droplet in the shear layer region in an experiment with the high Reynolds number (Re = 5700) as a gray scale image. Background correction has been performed on the raw images for improved visualization. While the filament inside the core region is detected by the evaluation algorithm, identification of the diffuse deformed droplet is not easily accomplished. Furthermore, no significant information about the interaction of the droplet with the turbulence and thus about the droplet breakup can be obtained from the diffuse overlapping of filament segments.

Although the experiments at a Reynolds number of Re = 2000 are further away from the Reynolds numbers relevant in industrial practice, these series of experiments are nevertheless suitable for achieving a mechanistic understanding of droplet breakup in turbulent flows through the interaction of vortices and droplets. As previously recognized, droplet breakup essentially begins in the region of the decaying free jet. Although the deformation of the droplets in the inlet region, i.e. the elongation to droplet filaments of greater length leads to a simplified subsequent deformation in the further course, since the droplets thus have a larger spatial extent and are thus more

likely to interact with several vortices simultaneously or are simply exposed to a larger shear, the recordings show that this pre-elongation is not necessarily required and also non-deformed droplets or relaxed droplets are deformed and disintegrated in the turbulent free jet region. Whether the pre-elongation has an influence on the resulting secondary droplet size could not be clarified, since the final droplet size could not be recorded optically in the given experimental setup, and moreover the disperse phase or droplet concentration and the number of single droplet experiments performed are too low to make a statistically valid statement about the final droplet size distribution.

In Figure 5.31, 5.32 and 5.33 three breakup series are shown as examples to describe the breakup mechanism of droplets when interacting with vortices in a turbulent flow field, as occurs during high-pressure homogenization. In the first two cases, a nearly undeformed or relaxed primary droplet is present that has passed through the orifice on the axis of symmetry and enters the shear layer of the decaying free jet near the axis of symmetry. In the third case a still elongated filament, that also passed the orifice on the axis of symmetry, is breaking up in consequence of the droplet vortex interactions.

The droplet of the experimental series from Figure 5.31 is first caught by a large-scale vortex and thus moved in the direction of the negative y-axis in addition to the movement in the main flow direction along the x-axis. At the same time, the droplet is stretched, which may be caused by interaction with at least one second vortex. The movement and direction of the deformation is marked by red arrows. Due to this stretching, the droplet is stretched within a very short time (about $5 - 7.5\,\mathrm{ms}$) to an elongated filament with a length many times longer than the previously existing diameter of the round, relaxed primary droplet. The ends of the filament are thicker than the filament diameter, which is relatively constant over a large area. These two ends are each further deformed three-dimensionally by small-scale vortices and simultaneously stretched, while the central filament region is temporarily left undisturbed. In the further course, this filament segment is also stressed and deformed by small-scale vortices. The overlapping of the filament segments makes it difficult to identify the individual deformations, but the droplet eventually disintegrates into a large number of small secondary droplets. By this time, the elongation becomes very large, so that the filament diameter is smaller than the resolution size, and thus only individual segments that are not so strongly elongated can be identified.

In comparison to this deformation process, the droplet shown in Figure 5.32 is initially not deformed linearly, but stretched two-dimensionally to form a two-dimensional droplet film. The relaxed, round primary droplet is also initially moved in the shear layer region by a large-scale vortex transverse to the main flow direction. However, this movement results in a two-dimensional stretching of the droplet to form a two-dimensional droplet film. The visualization of the film is difficult, because the two-dimensional deformation hardly leads to a distortion of the background pattern and thus only the edges of the film are recognized. For better visualization, the sheet-like deformed drop is outlined in red and the drop film is marked by dashed red lines. Within a few ms, the droplet film is affected by many small-scale vortices and deformed three-dimensionally. Due to the small thickness and the large extent of the film, the

Figure 5.31: Time series for linear deformation of an almost completely relaxed droplet behind the orifice. The motion and deformation due to large-scale vortices is illustrated by red arrows. The linear elongation is followed by a three-dimensional deformation of the filament by small-scale vortices.

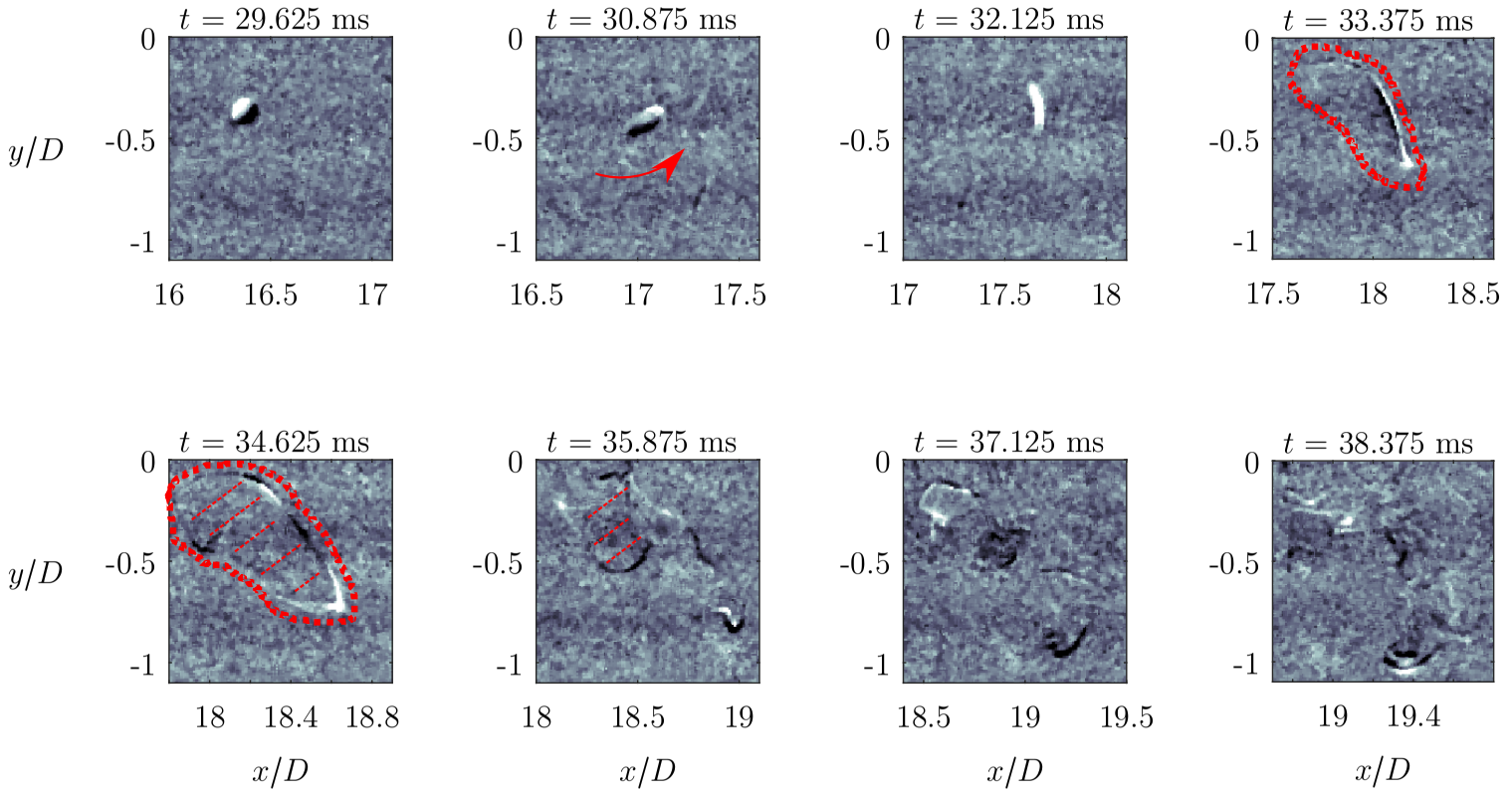

Figure 5.32: Time series for the deformation of an almost completely relaxed droplet behind the orifice to a two-dimensionally stretched droplet film and the further deformation of this film. The film structure, which is difficult to recognize, is outlined in dashed lines and the flat stretched area is marked by dashed straight lines.

interaction with the small-scale vortices is very fast and leads to a small-scale, diffuse deformation of the drop within a very short time.

The droplet breakup series shown in Figure 5.33 shows a droplet passing through the orifice on the axis of symmetry, being deformed by vortices in the shear layer region and breaking up. Compared to the previously shown breakup series, in this case there is a drop filament that is not completely relaxed. The interaction of the filament with the first larger vortex causes a rotation of the filament and simultaneous lateral movement. The front end of the filament at the beginning of the movement becomes the rear end due to the rotation and is deformed two-dimensionally at the same time as the rotation. The other end of the filament is deformed linearly. The movement of the filament is again marked by arrows. The two-dimensional deformation is indicated by a dashed border and hatching of the film. The two different deformation processes lead in the further course to the fact that the droplet is deformed to a three-dimensional twisted "T"-shaped filament. The shape is marked by red dashed lines. Due to the large deformation of the T-shaped filament, many small-scale deformations occur in the further course, and lead to a strong turbulent deformation.

Independently of the previously described breakup mechanism, it can be seen that the drop breakup takes place within an active zone. This zone is characterized by the presence of vortices, which cause deformation of the entering droplets or filaments. As a result of the strong deformation, i.e. the elongation towards long or branched filament structures, the droplets break up into a large number of secondary droplets. As soon as the forces transmitted to the droplets by the turbulence are no longer sufficient for further deformation, the droplets or filaments are only moved along with the flow and swirled. Figure 5.34 shows an example of the relaxation of a filament segment with the large viscosity ratio ($\eta^* = 10.5$) that was only subjected to low stress by the turbulence in the decaying free jet to a secondary droplet when leaving the active zone.

The first image shows one of the filament segments (outlined in red) and an already relaxed secondary droplet. The vortex structure indicated by the red arrow leads to a separation of the two drops and rotation of the filament. Due to the reduced external stresses, the filament relaxes in the course of the exposure series to a large secondary drop visible in the last image. This process can be observed if the size of the secondary drop is above the resolution limit. Figure 5.35 shows the difference in the coarse secondary droplet size due to the viscosity ratio by showing images of the larger, discernible secondary droplets visible after the breakup of the individual primary droplet. The droplets are distributed over a wide area in the x-y-plane and also in the depth position there can be a distribution detected since not all secondary droplets are in the focus plane. Only the very coarse drops are visible and no statement about the further drop size distribution is possible on the basis of these images. The comparative images are representative of a large number of observations and were taken under the same flow conditions (Reynolds number $Re = 2000$), primary droplet diameter ($d_\mathrm{P} = 2\,\mathrm{mm}$) and potentially similar trajectory ($r^* \approx 0$).

It is clear that the secondary droplets in the case of the lower viscosity ratio ($\eta^* = 3.0$) are much smaller and there are no very coarse droplets with diameters in the range of about 1 mm, as is the case in the experiments of the system with the viscosity ratio of

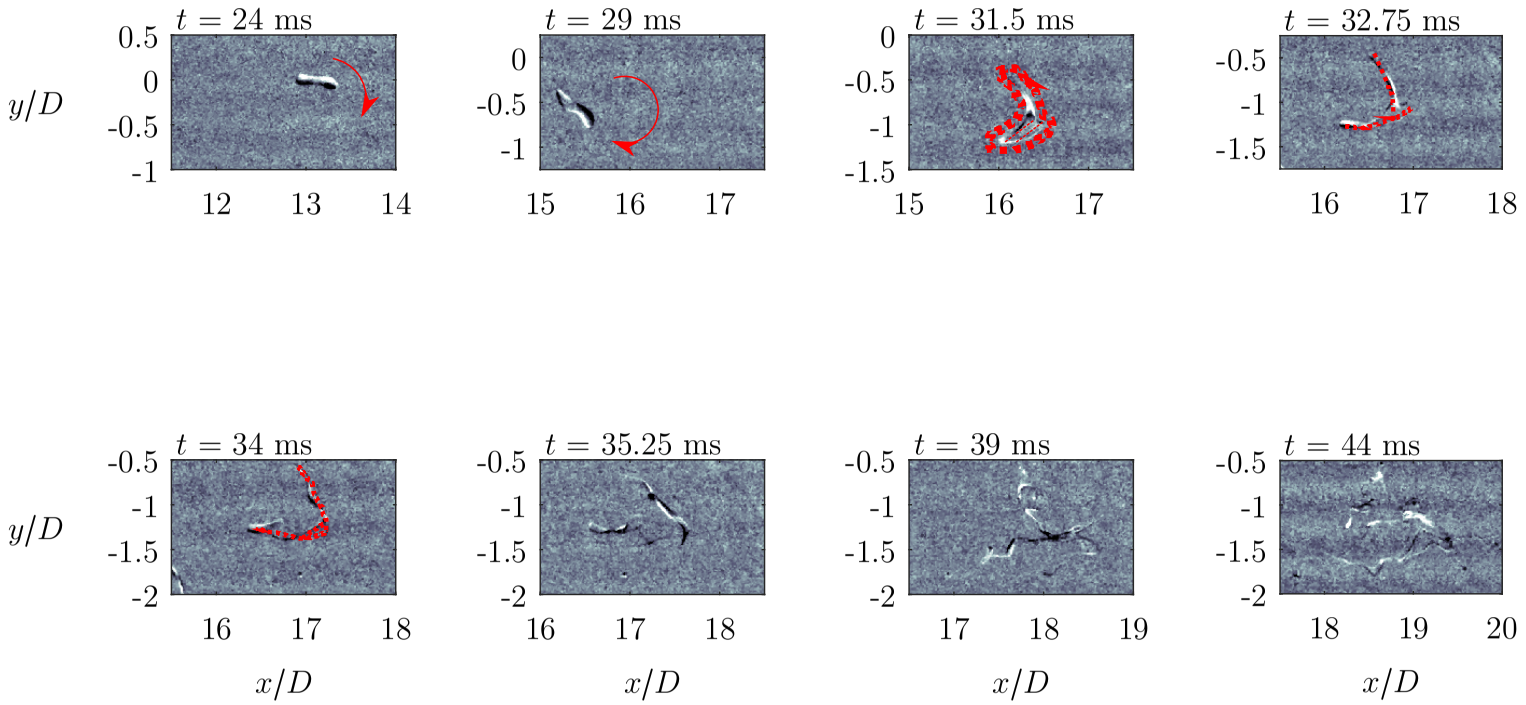

Figure 5.33: Time series for the deformation of a pre-elongated droplet behind the orifice to a partially two-dimensionally stretched droplet film and a linear elongated filament. The further deformation in shape of a "T" is marked and breakup is shown. The film structure, which is difficult to recognize, is outlined in dashed lines and the flat stretched area is marked by dashed straight lines.

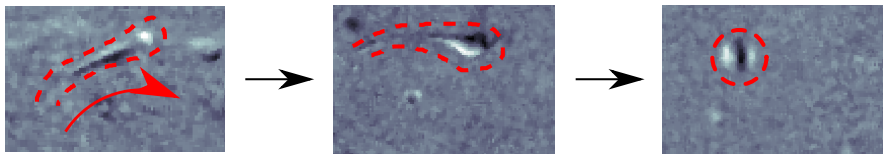

Figure 5.34: Illustration of the relaxation of broken up filament segments into large secondary droplets. The filament or droplet contour is marked by a dashed red line. The movement of the filament is marked by a red arrow.

η^* = 10.5 and the corresponding pictures. In the case of the material system with the low viscosity ratio of η^* = 0.3, no droplets are discernible, so that it must be assumed that the breakup at lower viscosity ratios but the same stress intensity leads to finer secondary droplets (Kelemen et al., 2015). The depicted drops are possibly swirled in the further course by the flow field of the decaying free jet, but no further deformation occurs, only a transport away from the active zone.

The extent of the active zone coincides spatially with the area of the shear layer, although only the inlet side is determined by the tests. The exit area of the droplets from the active zone can hardly be determined with the conducted experiments, since the primary droplet size and shape of the droplets at this point cannot be set freely, but is determined by the deformation and possibly breakup processes that the droplet has experienced up to this area.

To gain a better understanding of the forces and stresses that lead to drop breakup during high-pressure homogenization, quasi-simultaneous PIV and shadowgraphs were taken. This allows the velocity field to be determined and compared with the resulting droplet deformation.

Figure 5.36 shows an example of a time series for the droplet course and the velocity fields recorded at the same time. It can be seen that the droplet follows the velocity field and is moved along with the free jet. In the core region, the straight drop filament follows the stable free jet core. Further downstream, the stable free jet begins to decay and the drop is deflected.

Unfortunately, no exact determination of the forces near the drop is possible, because on the one hand the resolution is not large enough despite the scaled system. This is due to the fact that the convective motion clearly outweighs the drop elongation or deformation velocity. Therefore, a certain FOV size is necessary so that the drop trajectory can be observed at least in sections, which is why the spatial resolution cannot be increased indefinitely. Even when using several cameras in the main flow direction, the spatial resolution for determining high-resolution velocity fields next to the droplet surface is not high enough. In particular, small-scale vortices, which

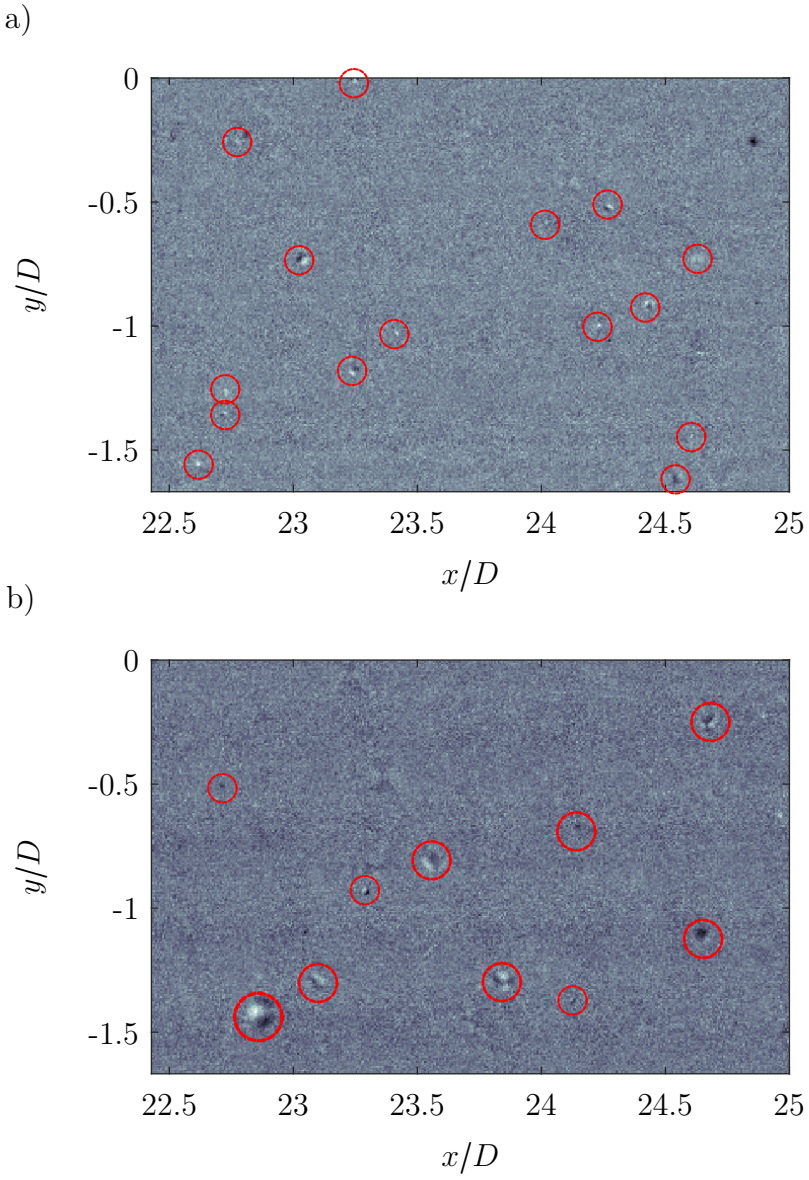

Figure 5.35: Comparison of secondary droplets still visible after droplet breakup with two different viscosity ratios. a) $\eta^* = 3.0$; b) $\eta^* = 10.5$.

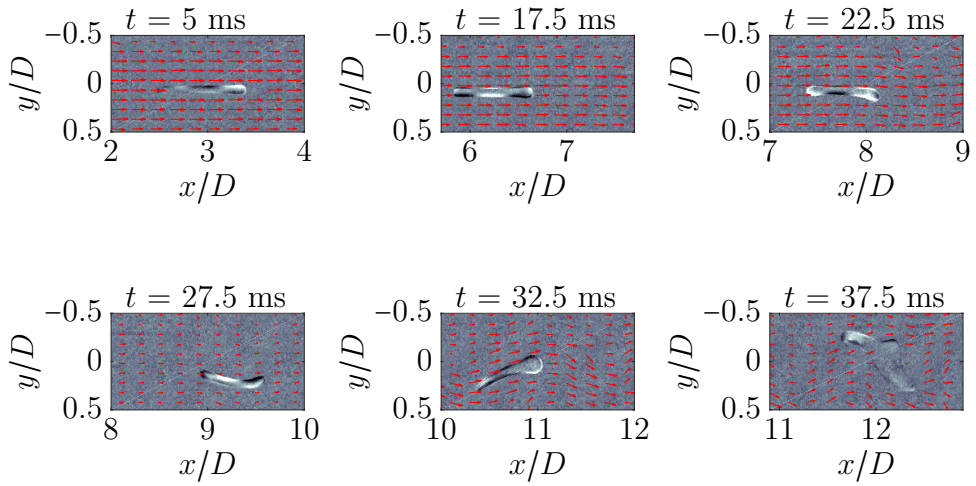

Figure 5.36: Time series for drop breakup with superposition of the velocity field determined by 2D2C-PIV along the $x-y$-plane.

contribute significantly to the deformation of the droplet as shown above, can hardly be imaged. This is aggravated by the fact that due to the large velocities high-speed cameras have to be used, which have often a reduced sensor size compared to low-speed cameras. On the other hand, the determination of the external forces acting on the droplet during deformation is not possible in this test setup, since no volumetric velocity measurement could be performed, but only the velocities along a plane were determined. In some cases, the droplet has a significantly higher extension transverse to the plane or moves completely out of the plane. For a volumetric velocity measurement, a much higher illumination power would be necessary, which is hardly achievable in the high-speed measurement range. A volumetric or tomographic velocity measurement would also require a much more complex camera setup, which is possible in the present test facility, but only allows measurements in a small region.

However, the use of the volumetric shadowgraphy experimental setup still allows the droplet trajectory to be determined in three dimensions. Figure 5.37 shows the trajectory of the droplet for this purpose. To simplify the three-dimensional representation, the radial position is color-coded.

It can be clearly seen that the droplet dosed on the axis of symmetry remains in the center of the free jet even when viewed in three dimensions. Only in the area of the shear layer does the droplet begin to meander with the surrounding flow. Due to the limited field of view in the axial direction and the special problem of reconstructing the breaking drop or the overlapping drop in the individual projection views in three-dimensional reconstruction, this method is not suitable for investigating the breakup process in detail at the given resolution and the possible directions of observation.

Due to the already described problem of the exact determination of the breakup process by the resolution limitation and the not simultaneously or uniformly occurring drop

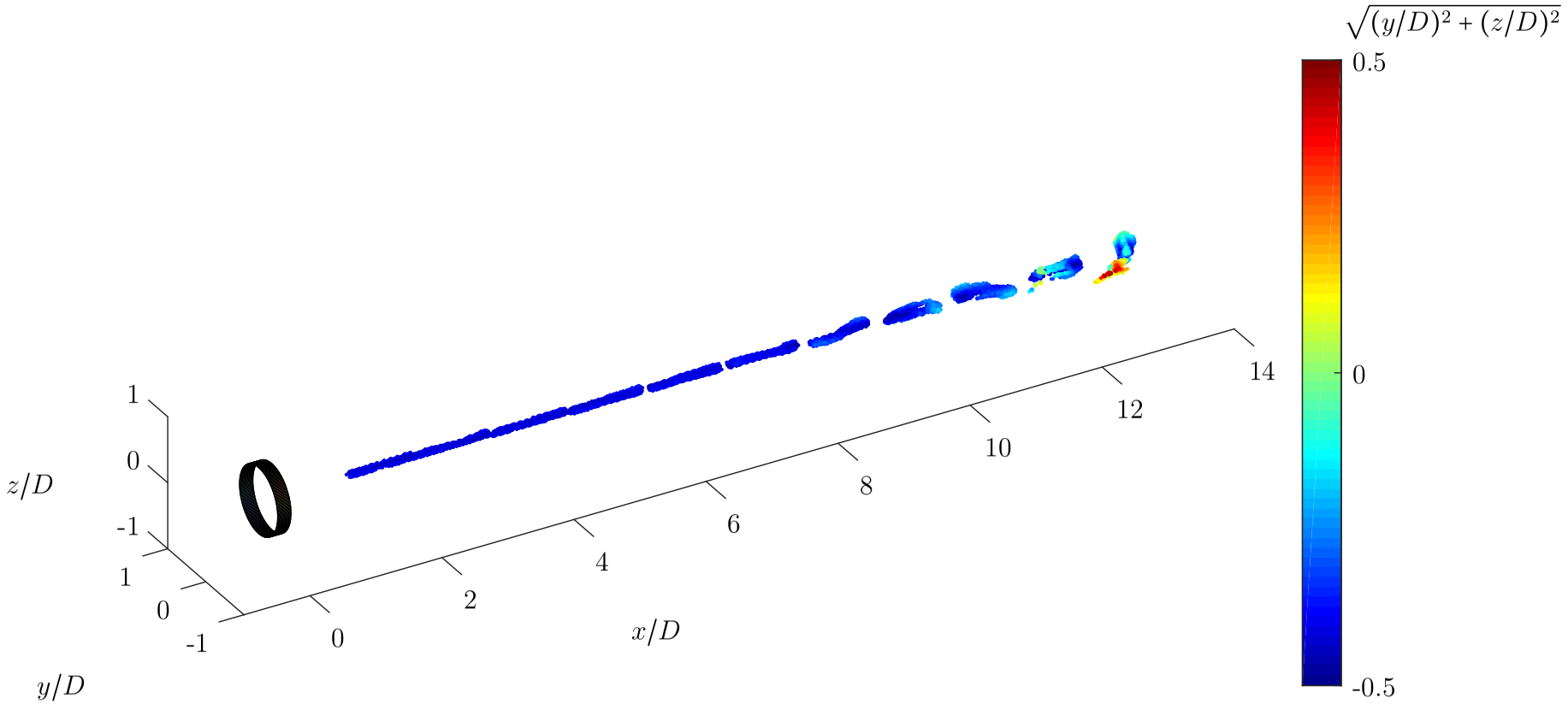

Figure 5.37: Time evolution of the drop path in the free jet behind the orifice. The radial position is color-coded. The time increment between the depicted droplets is 2 ms.

breakup, it is not possible to make more exact statements about the conditions and location for breakup to happen. However, it is possible to compare more precisely the initial stage of drop breakup, namely the drop deformation due to the interaction of the drops with the vortices. For this purpose, a breakup or, more precisely, a deformation criterion is defined. By means of this criterion, the different observed droplet breakups can be compared with each other, and the time or location of the criterion reached can be analyzed more precisely as a function of different investigation parameters.

As breakup criterion a combination of the area ratio A^* of the deformed drop image A_i compared to the deformed drop after leaving the orifice A_o and the shape factor of the drop determined by the Matlab function "Solidity" S was used. The drop is considered as disintegrated or deformed, as soon as the droplet size A_i is 50% bigger than the original size A_o and simultaneously the solidity S is only 60%, the drop is marked as "disintegrated" ($A_i^* > 1.5$ and $S_i < 0.6$).

Figure 5.38 shows an example of the course of the droplet in the free jet until the breakup criterion is reached (image a)), the course of the area ratio A^* and the solidity S for a recording sequence (image b)) and an example of the recording of the droplet at the time of the fulfilled criterion is shown (image c)).

The image of the spatial course of the drop in image a) shows the center of gravity of the drop represented by black dots. When the drop path is recorded by several cameras, the center of gravity of the drop may not be displayed correctly in the overlapping area of the camera fields, since individual parts of the drop can only be seen in the other camera image. However, this error is small and only slightly disturbs the evaluation. The location of the reached breakup criterion is marked by a red cross. In the background, the normalized, ensemble-averaged free jet velocity field is shown. It is clear that the droplet passes through the free jet core region close to the symmetry axis. The drop center begins to meander in the decaying free jet region. The breakup criterion is reached in the shear layer region when the free jet decays turbulently. Image b) shows the course of the two parameters which are decisive for the breakup criterion. It becomes clear that the progression is by no means continuous. By combining the two criteria, the statement about the achievement of the criterion becomes more stable against outliers. The drop shown in image c) when reaching the criterion is clearly linearly stretched and twisted by the interaction with large-scale vortices. The observation of many droplet courses shows that such strongly twisted and stretched droplet filaments do not relax again to the initial droplet, but may be further deformed and finely broken up in the further course or at least disintegrate into coarse secondary droplets when leaving the high-intensity zone.

With the aid of this breakup criterion, the droplet trajectories shown above as examples can be systematically compared as a function of the viscosity ratio η^* of the droplet trajectory through the orifice or of the dimensionless dosing point r^* and the Reynolds number Re. Figure 5.39 shows for this purpose the droplet trajectory and breakup location as a function of the viscosity ratio η^* for a Reynolds number of $Re = 2000$ and a droplet feed position close to the axis of symmetry ($r^* \approx 0$).

The droplet trajectories are very similar in all cases up to a length of $x/D = 15$, i.e. in the free jet core region, and lie almost on the axis of symmetry corresponding to the

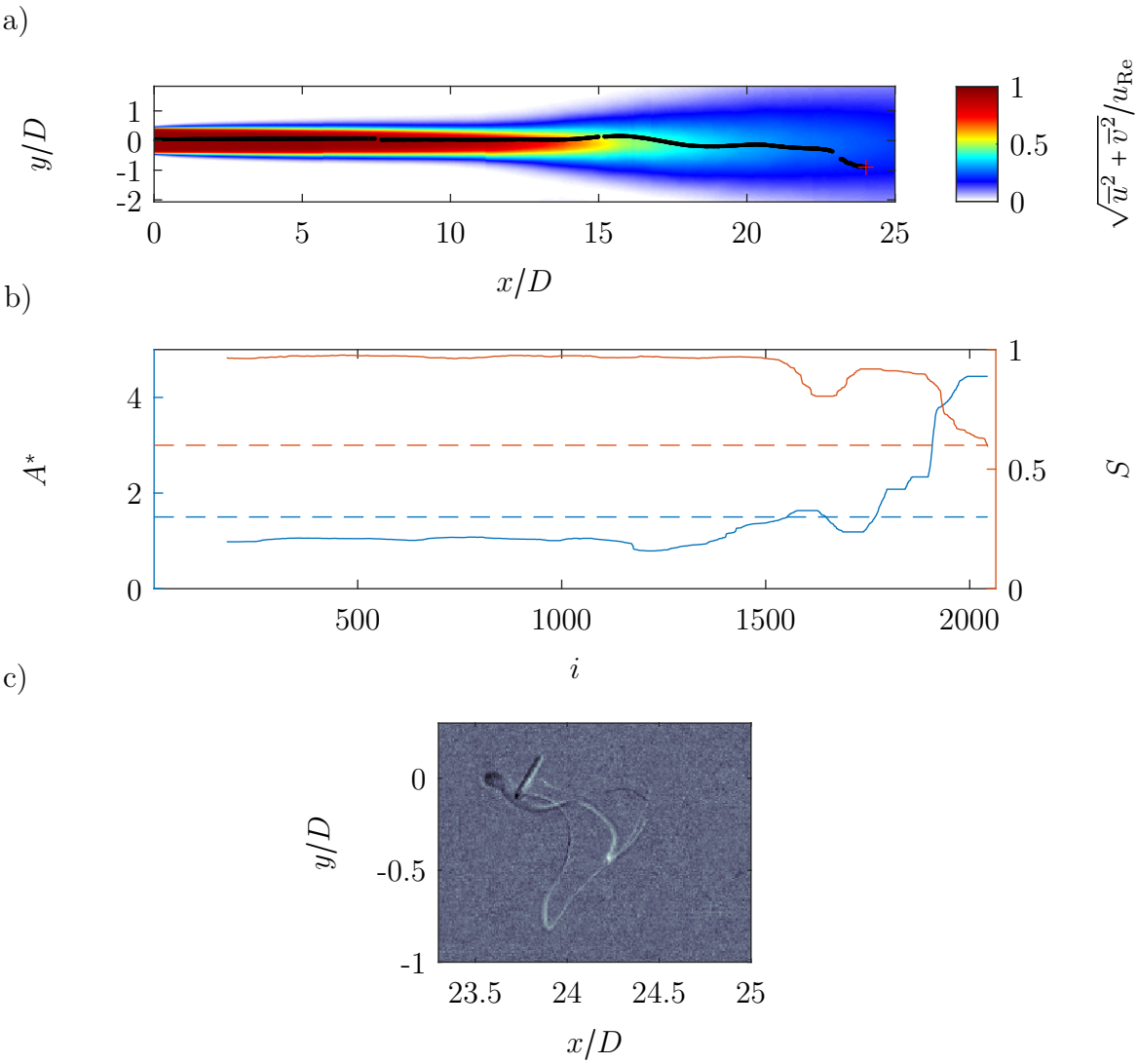

Figure 5.38: Illustration to explain the breakup criterion. a) Course of the drop path of a drop that has passed through the orifice in the free jet area behind the orifice. The drop center is shown as a black dot for each image. When the breakup criterion is reached, the drop center is marked by a red cross. The normalized, ensemble-averaged velocity field of the free jet is shown in the background. b) shows the course of the two individual criteria, the area ratio A^* and the solidity S until the breakup criterion is reached. c) shows the droplet deformed to an elongated and twisted filament when the breakup criterion is reached.

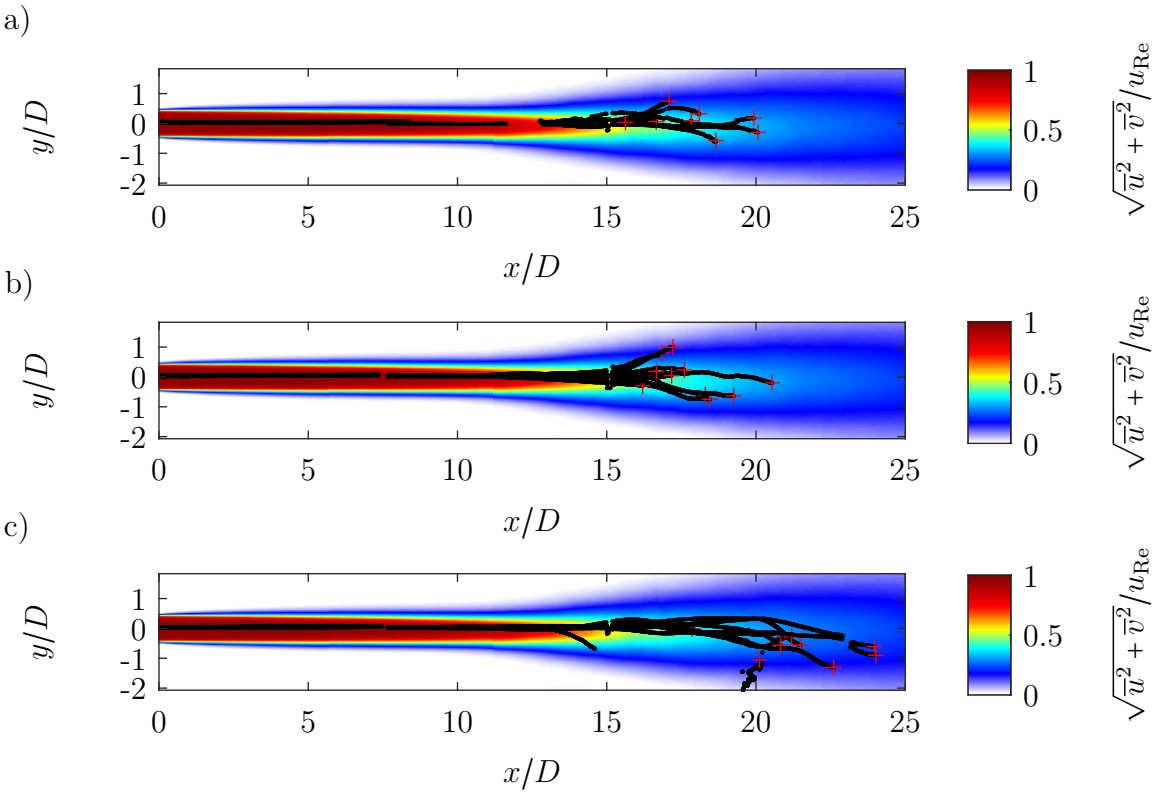

Figure 5.39: Course of the drop trajectories and position of the drop breakup location as a function of the viscosity ratio at a Reynolds number of Re = 2000 and a droplet injecton location of r^* ≈ 0. In the background the normalized, ensemble-averaged velocity field of the free jet is shown. a) η^* = 0.3; b) η^* = 3.0 and c) η^* = 10.5.

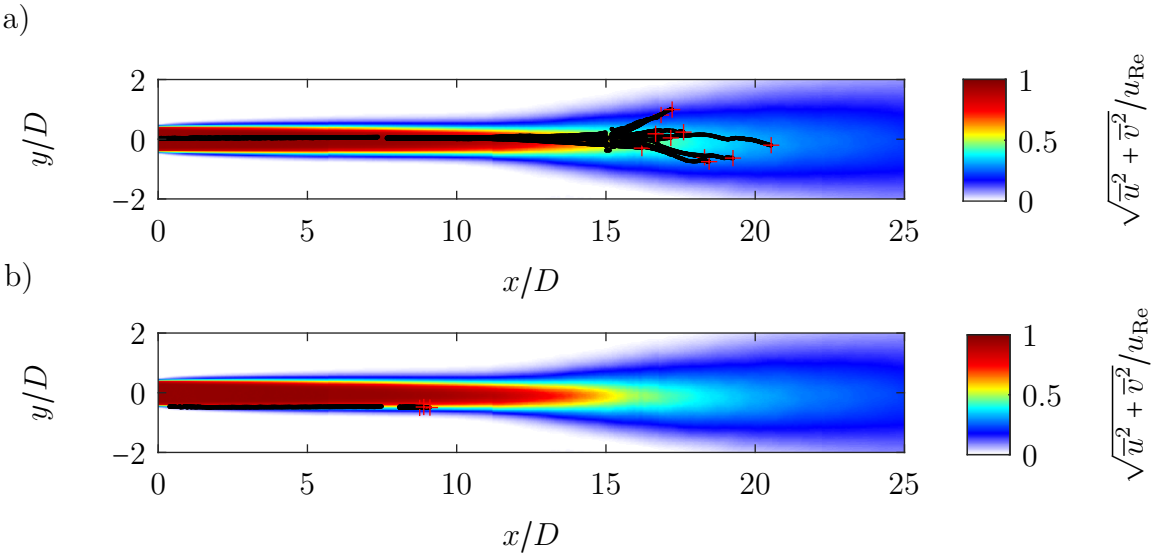

Figure 5.40: Course of the droplet trajectories and position of the droplet breakup location as a function of the dosing position of the droplets in front of the orifice at a Reynolds number of Re = 2000 and a viscosity ratio of η^* = 3.0. The normalized, ensemble-averaged velocity field of the free jet is shown in the background. a) $r^* \approx 0$; b) $r^* > 0.8$.

droplet dosing point. The location of the droplet breakup site differs for the viscosity ratios shown in that the droplets with viscosity ratios η^* = 0.3 and η^* = 3.0 break up in the range between $15 < x/D < 21$, and the high viscosity droplets with viscosity ratio η^* = 10.5 break up only from a length of $x/D > 20$. This difference may be due to the fact that the droplets with the viscosity ratio η^* = 10.5 relax almost completely in the core region of the free jet due to the comparatively low elongation beforehand and are therefore deformed and stretched by the interaction with vortices only when they reach the shear layer and thus break up or fulfill the breakup criterion at a later stage.

The influence of the droplet trajectory through the orifice, which can be achieved by the different dosing points is shown in Figure 5.40 for droplets of viscosity ratio η^* = 3.0 at Reynolds number Re = 2000. Image a) shows the trajectory of the droplet center of mass and the location when the breakup criterion is reached when the droplets are dosed on the axis of symmetry ($r^* \approx 0$), whereas image b) shows the droplet trajectory and the breakup location when the droplets are dosed near the edge ($r^* > 0.8$). The difference in the shift of the location of the breakup criterion reached can be clearly seen. In the case of dosing close to the edge, the droplets break up almost at the same point in the range $x/D \approx 9$, whereas in the case of dosing on the axis of symmetry, the breakup occurs further downstream at $x/D > 15$ and there is also a greater dispersion.

Figure 5.41 normalized, ensemble-averaged of the Reynolds number on the droplet breakup location or the reaching of the breakup criterion. Shown in image a) is the droplet trajectory and breakup location for droplets of viscosity ratio η^* = 10.5 when dosed close to the axis of symmetry ($r^* \approx 0$). As shown before, the breakup in this case takes place comparatively far downstream. Image b) shows for comparison the droplet trajectory or breakup location at the high Reynolds number Re = 5700. It is clear that

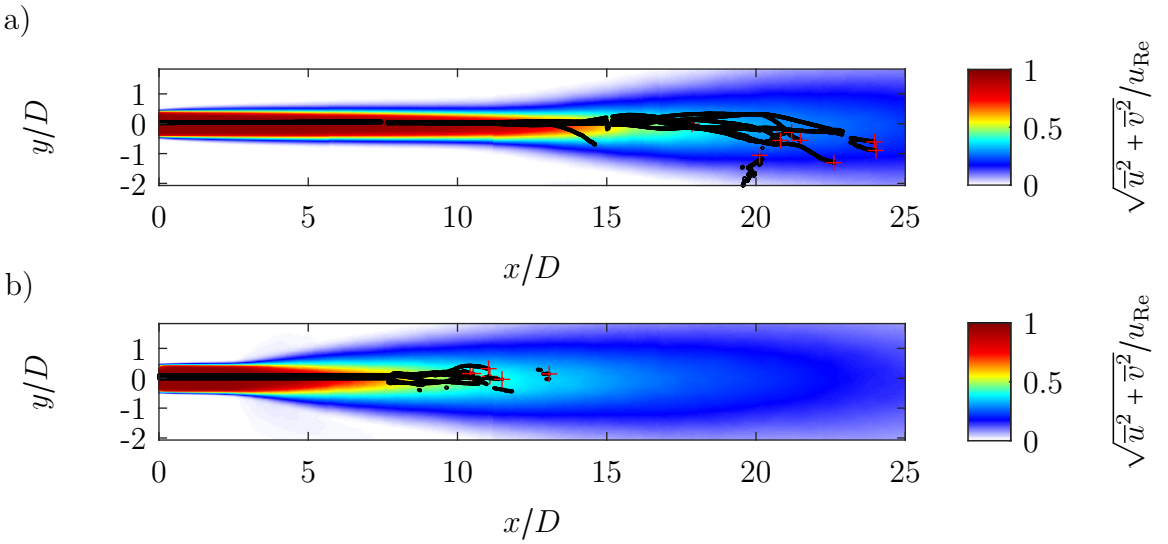

Figure 5.41: Course of the droplet trajectories and position of the droplet breakup location as a function of the Reynolds number for a droplet dosing close to the symmetry axis $r^* \approx 0$ and a viscosity ratio of $\eta^* = 3.0$. The normalized, ensemble-averaged velocity field of the free jet is shown in the background. a) $Re = 2000$; b) $Re = 5700$.

the droplet breakup takes place much earlier. However, the comparison with the mean velocity field behind the orifice shows that even at the higher Reynolds number the droplet breakup takes place in the shear layer region, i.e. the turbulently decaying free jet region.

In summary, the studies on droplet breakup after passing through the orifice show that the droplets break up in the shear layer region and are significantly stretched, deformed and broken up by interaction with vortices within the shear layer. The elongation in the orifice due to the inlet flow can play a role in the resulting droplet size, since the droplets are already elongated at the first contact with the vortices and thus a larger elongation can be achieved if necessary. Drop filaments or segments that have passed through the intensive turbulent region are not broken up further, but are simply carried along with the main flow. This may well result in swirling of the droplets transverse to the main flow direction, but no further strong deformation or secondary breakup of the droplets was observed.

The results on droplet breakup in turbulent flows carried out in the larger scaled experimental plant and presented here fit very well with results carried out in a original scale experimental plant and also with those from an experimental plant scaled only with the scaling factor 5 (see Mutsch et al. (2021a)). Through the agreements, it can be shown that the principle breakup process can be transferred to different size scales with strict scaling and with neglect of the surface dynamics due to emulsifiers and of coalescence processes. This makes it possible to carry out further investigations in larger-scale experimental plants and to obtain fundamental findings on drop breakup with higher temporal and spatial resolution.

5.3.3. Deformation and breakup without passing the orifice

The initial design of the plant does not enable any specific investigations of drop breakup of drops that have not passed through the orifice. Recordings showing a relatively large secondary droplet entering the free jet from the outside through the backflow area surrounding the free jet directly at the orifice outlet were taken by chance, but they show the possibility of further breakup of secondary droplets without targeted recirculation of the process stream with multiple breakup processes, as was investigated by Vankova et al. (2007), for example. Figure 5.42 shows a time series for this droplet breakup.

The droplet is superimposed as a black mask over the normalized, ensemble-averaged velocity field. The Reynolds number is Re = 2000. The approx. 1 mm large drop approaches the orifice from the backflow region and is drawn into the free jet or the surrounding shear layer at a length of the free jet of approx. x/D = 0.2. The droplet is deformed by the shear, since the area first touching the shear layer is already accelerated by the flow, while the rear area is unaffected. In the shear layer, the droplet is accelerated and linearly stretched very strongly by the shear. The length of the droplet filament reaches values well above $7D$. Due to the very large extension, it can be observed how the front region is swirled with the decaying free jet, while the rear region is still moved linearly with the free jet. It can be seen that the breakup of this droplet, which is fed from the outside, is similar to the droplet dosed through the orifice at a high radial trajectory $r^* > 0.8$. Based on these findings, an experimental set-up was developed by which this type of droplet breakup can be systematically investigated.

With the aid of a developed pipeline system, drops can be directed from below through capillaries of different lengths in the direction of the free jet. The distance of the capillary or the injection position to the orifice can be adjusted in steps of about $2.5D$ in the range of $0 < x/D < 30$. The distance of the injection position to the symmetry axis can be varied between $-3 < y/D < -1$ due to the different lengths of the capillaries. The experiments carried out with the help of this experimental set-up show different breakup phenomena which are presented in the following. First, the investigations at the low Reynolds number Re = 2000 are presented. The viscosity ratio in these experiments is always η^* = 10.5 unless otherwise stated.

Figure 5.43 shows the breakup process of a drop injected in the near field behind the orifice at a position of x/D = 1 and y/D = −2.2. The outlet capillary and the droplet mask at different times are shown. The normalized, ensemble-averaged velocity field is shown in the background. The droplet, which leaves the capillary slightly stretched because the droplet diameter is slightly larger than the capillary inner diameter, relaxes after exiting the capillary and moves towards the free jet. Upon reaching the free jet edge region, i.e. the shear layer, the droplet is linearly stretched very rapidly. This elongation starts at the top of the droplet, which reaches the shear layer first. As the drop continues to move toward the axis of symmetry, a larger and larger portion of the drop is sheared. The droplet is stretched by the shear into a long droplet filament and breaks downstream in the region of $x/D > 8$ into very fine secondary droplets, which cannot be well imaged during masking due to overlaping of multiple filament segments.

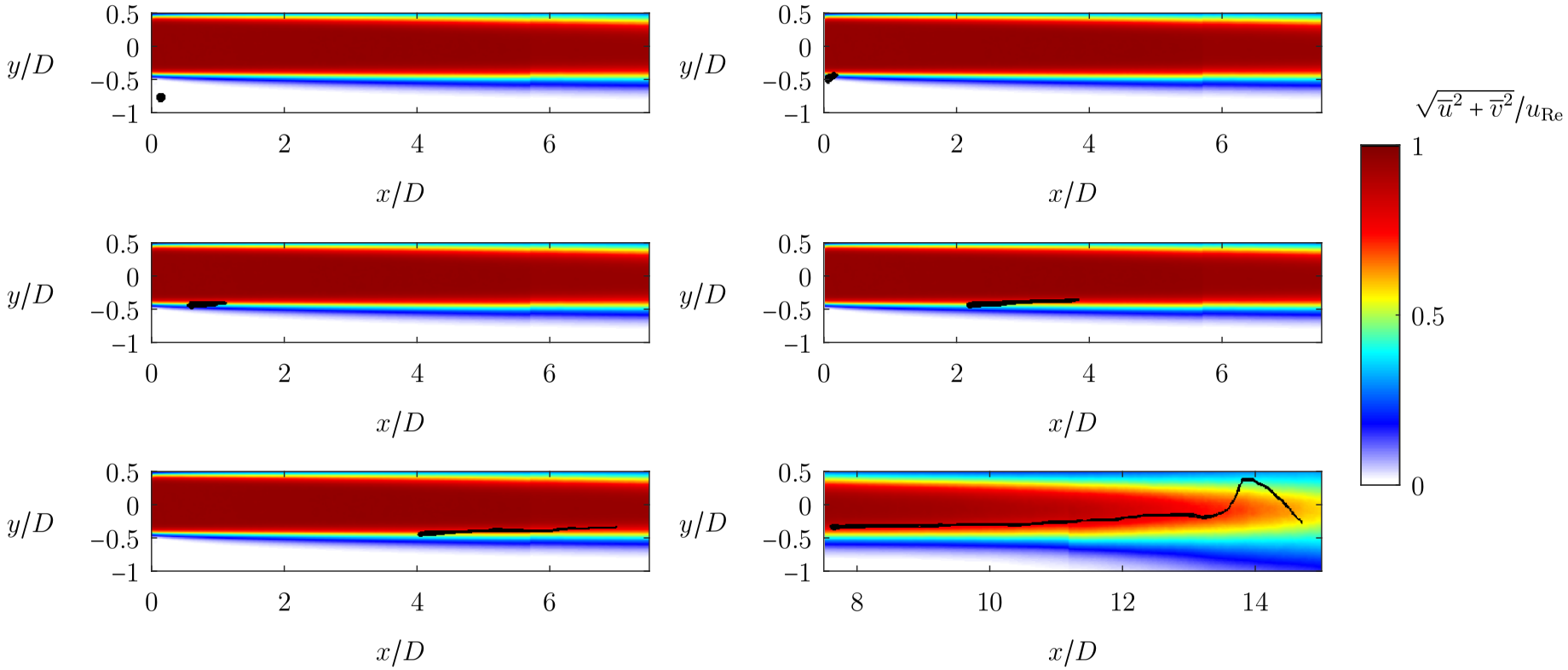

Figure 5.42: Example of a coarse secondary droplet, displayed as black mask as an overlay with the normalized, ensemble-averaged velocity field of the jet behind the orifice, entering the free jet near the orifice due to the recirculation flow surrounding the free jet and breaking up due to interaction with the shear flow and the vortex in the turbulent free jet region.

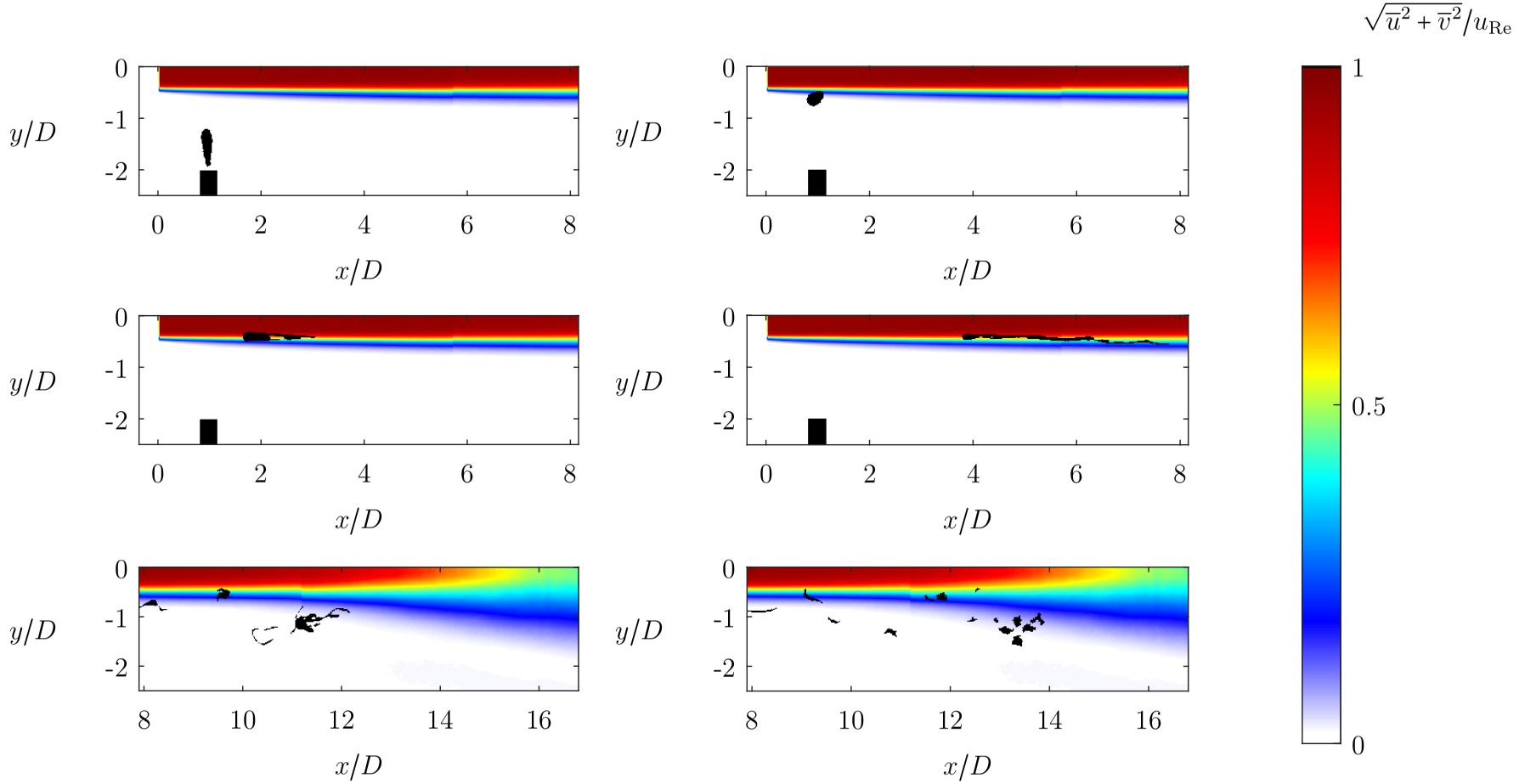

Figure 5.43: Example of a droplet, shown as a black mask with the free jet normalized, ensemble-averaged velocity field as background, which is introduced in the near region of the jet into the measurement section at the dosing position $x/D = 1$ and $y/D = -2.2$ (marked in black) without flowing through the orifice. Until the interaction of the droplet with the free jet, the droplet passed through the capillary relaxes to a round primary droplet, which then breaks up when interacting with the free jet, namely the shear layer and the turbulent region.

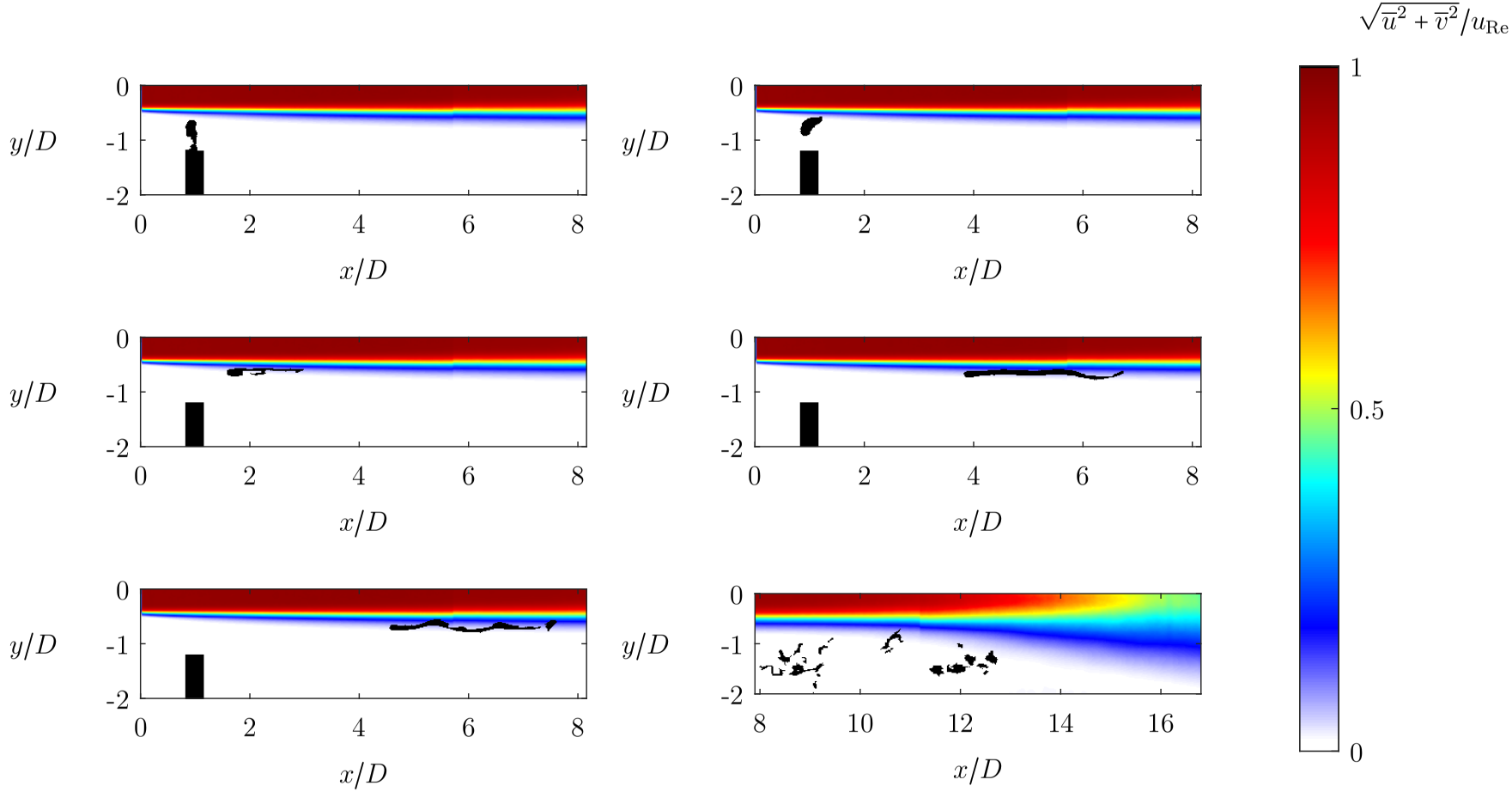

Figure 5.44: Example of a droplet, shown as a black mask with the free jet normalized, ensemble-averaged velocity field as background, which is introduced in the near region of the jet into the measurement section at the injection position $x/D = 1$ and $y/D = -1$ (marked in black) without flowing through the orifice. The shortened distance of the injection point to the free jet prevents the relaxation of the primary droplet, which is very quickly stretched in the shear flow and disintegrates downstream due to the interaction with vortices.

When dosing a comparable droplet via a longer capillary, i.e. a smaller distance between the injection position and the symmetry axis of the free jet, the longer capillary or the shorter distance means that the time required for the droplet to relax after leaving the capillary is not quite sufficient. The droplet is thereby slowed down within a short time or over a short distance on its movement in the direction of the free jet and strongly deformed transversely to the original direction of movement by the shear. In the further course, the droplet is deformed exactly as in the case described above, i.e. linearly stretched by the shear in the shear layer. The breakup of the drop takes place in a similar area. The process described is shown in Figure 5.44.

In individual experiments in the near field of the jet at $0 < x/D < 7.5$, whereby these limits cannot be determined exactly due to the small number of experiments, it can be observed that the drops do not penetrate the free jet or the shear layer after leaving the capillary or interact with it, but are deflected. In extreme cases, the drops are virtually reflected by the free jet and change the direction of motion by nearly 180°. In many cases, the deflection occurs in such a way that the droplet does not interact with the free jet in the area of the dosing point, but flows sideways past the free jet. In addition to the deflection by the free jet, it is possible that the vortices in the recirculation area of the free jet, which are generally very slow compared to the free jet, are sometimes fast enough to deflect and swirl the droplet. However, droplet breakup was only ever observed in the region of the free jet due to interactions with the free jet. Figure 5.45 shows a droplet flowing from the capillary up to the shear layer, but then being reflected and flowing back towards the capillary. The path of the drop is indicated by a red arrow. In addition to the drop, the normalized, ensemble-averaged flow field of the free jet is shown. The initial relaxation of the drop after leaving the capillary can be observed particularly well in this time series. Figure 5.46 shows analogously to Figure 5.45 a droplet which, after leaving the capillary, flows in the direction of the orifice in the opposite direction to the free jet due to the reverse flow.

The two cases of droplet deflection shown represent exemplary individual cases, since for most droplets injected from the two points, droplet breakup occurs according to the principle shown previously in Figure 5.43. It can be seen that as the distance between the injection point and the free jet or the axis of symmetry decreases, the probability of droplet deflection decreases and was not observed for the longest capillary or the shortest distance. However, it must be pointed out once again that the number of investigations is limited by the observation of single drops and that the transitions are fluid.

When dosing the droplets slightly further downstream in the range $7.5 < x/D < 17.5$, droplet disintegration occurs in all observed cases. In addition, it can be observed that especially in the range $12.5 < x/D < 17.5$ the droplet interacts directly with the free jet when leaving the orifice and is immediately entrained and deformed. Figure 5.47 shows an example of the detected droplet and capillary at different times, with the normalized, ensemble-averaged flow field shown in the background.

It can be clearly seen that as soon as the droplet has partially emerged from the capillary, it is carried along with the free jet flow and the droplet is thus immediately drawn into length. In addition, it becomes clear that the flow is by no means uniform,

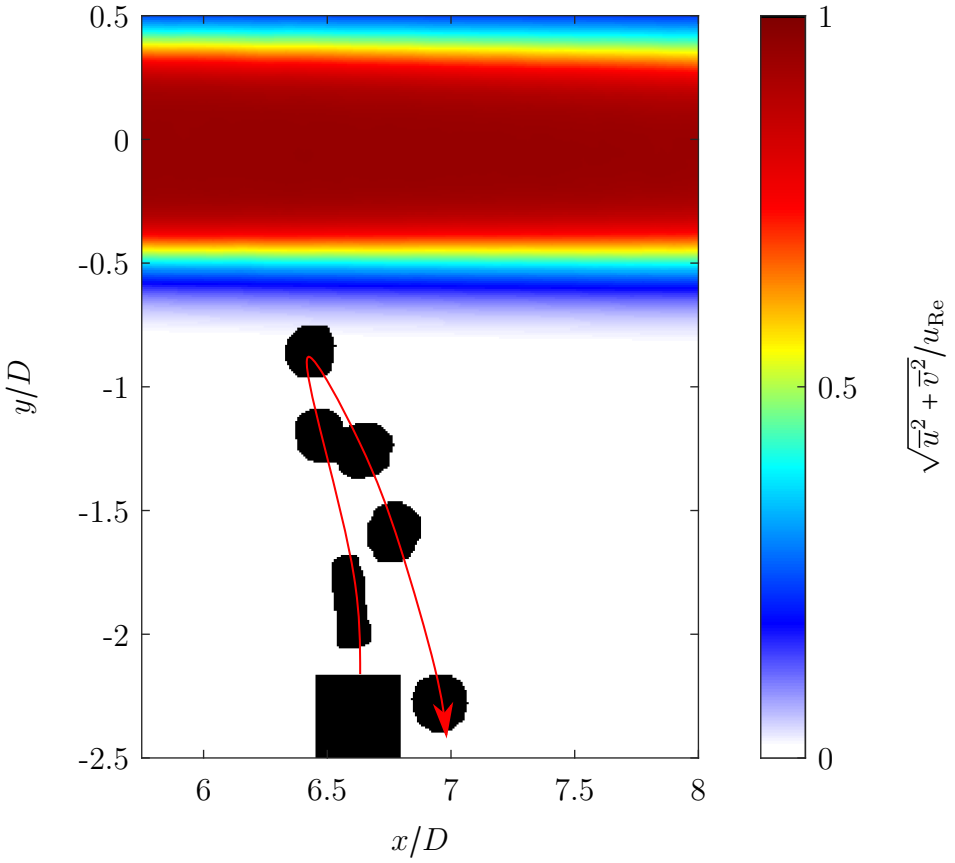

Figure 5.45: Example of a droplet injected in the near region of th jet that is deflected by the recirculation flow or reflected by the free jet, shown as a black mask with the normalized, ensemble-averaged velocity field of the free jet as background. The drop path is marked by a red arrow.

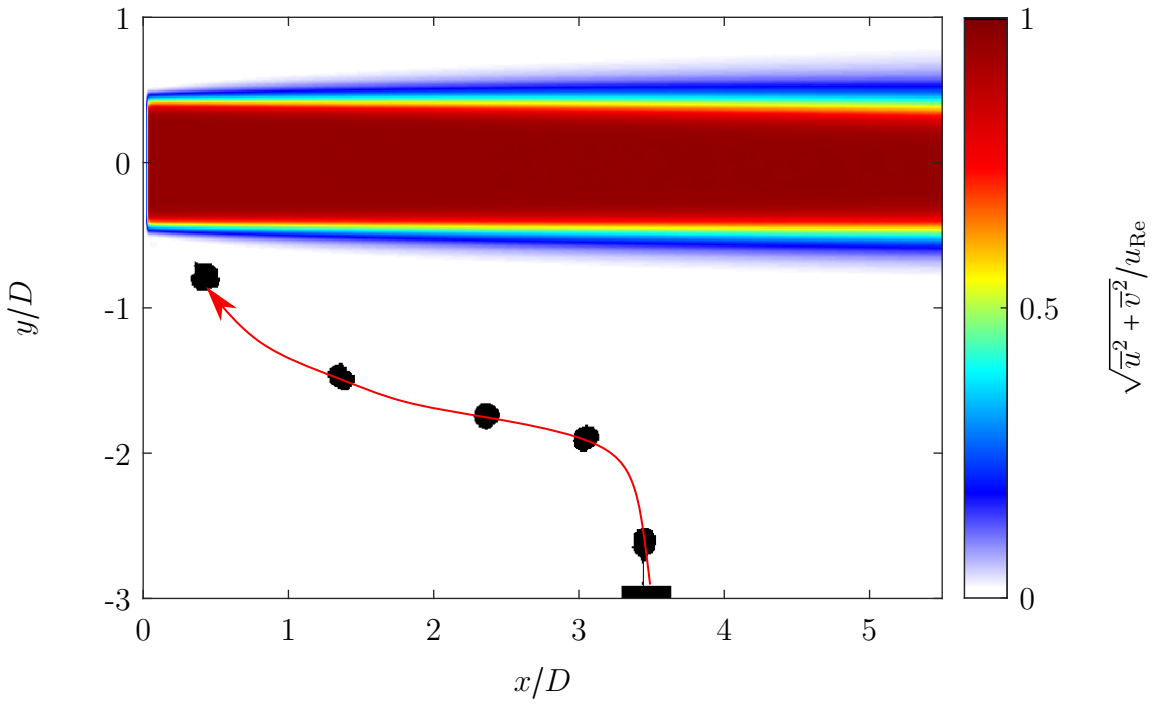

Figure 5.46: Example of a droplet injected in the near region of the jet that is deflected by the recirculation flow, shown as a black mask with the normalized, ensemble-averaged velocity field of the free jet as background. The drop path is marked by a red arrow.

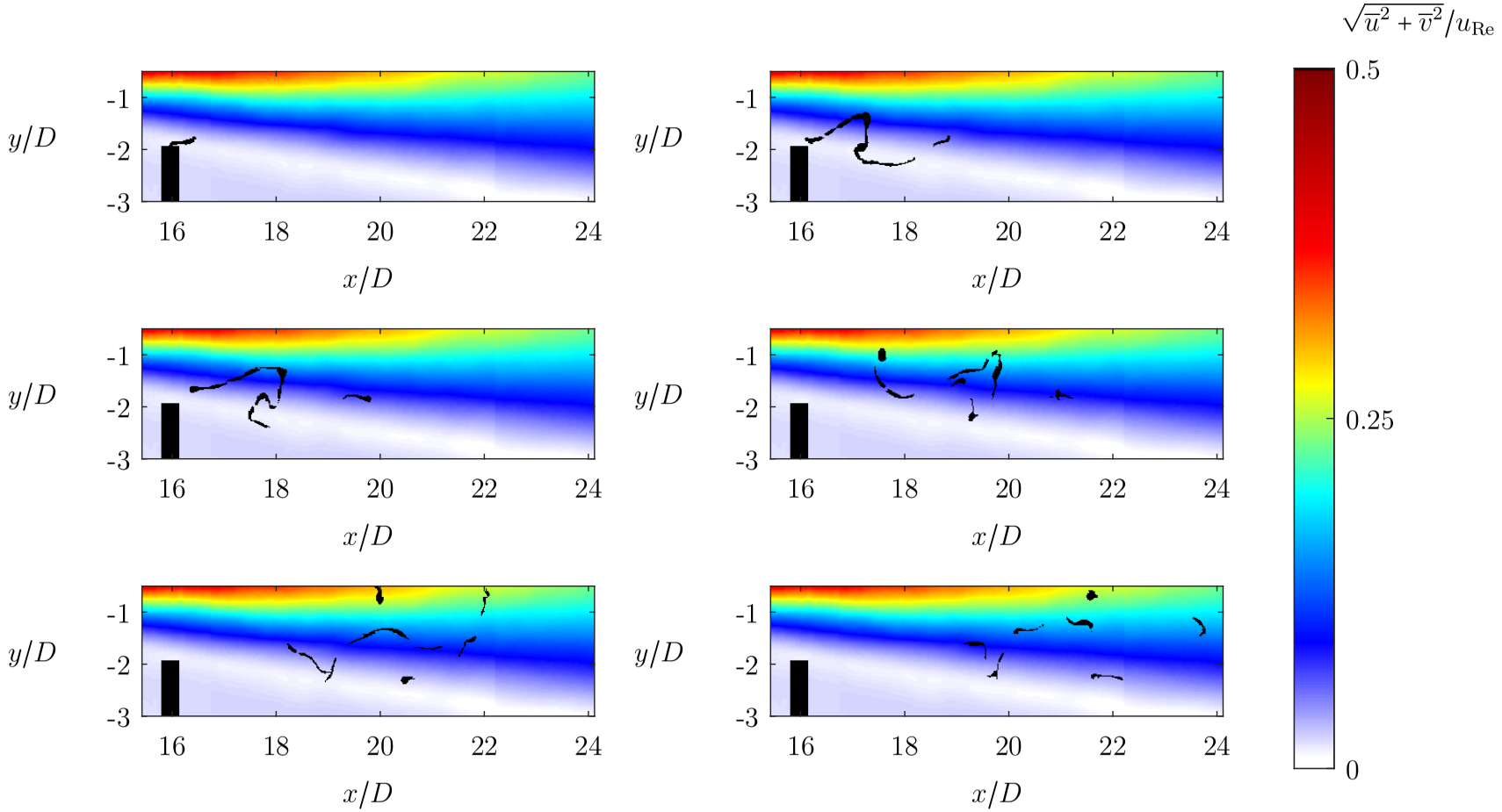

Figure 5.47: Example of a droplet breakup time series of a droplet injected in the transitional region at $x/D = 16$ and $y/D = -2$, shown as a black mask with the normalized, ensemble-averaged velocity field of the free jet behind the orifice as background. The droplet which is caught by the free jet flow directly as it partially leaves the capillary and is deformed and stretched. Further interactions with vortices lead to increased deformations and the disintegration of the droplet filament.

but that the drop is directly deformed irregularly by eddies. The segmented appearance in the first 5 figures is not due to the breakup of the drop, but to the masking algorithm and the low filament thickness. Only in the last image the droplet seems to disintegrate into single filament segments. The direct breakup shown, or rather the direct deformation of the droplet, occurs in this dosage range ($7.5 < x/D < 17.5$) for all capillary lengths investigated. The degree and speed of the deformation differs from case to case due to the turbulent decaying free jet and cannot be directly attributed to the capillary length or the dosing distance.

Figure 5.48 shows a droplet that was introduced into the free jet in an area even further downstream. Again, the deformation occurs immediately as the droplet exits the capillary. In contrast to the previously shown case, however, the droplet moves in a region of the free jet velocity field in which the velocity fluctuations are significantly smaller. Overall, they are still so large that the droplet is not deformed by the entrainment at the capillary alone, but clear turbulent deformations of the droplet filament can still be observed in the further course. However, the stressing forces are no longer so large that the droplet is deformed to a very fine, twisted filament and then breaks up, but it can be seen that in some cases very large secondary droplets are formed from the stretched filament by relaxation (see the last image in Figure 5.48).

Independent of the three breakup mechanisms described above depending on the location where the droplets are introduced into the free jet, the droplet trajectories can be compared. In doing so, the "breakup location" can be investigated, as in the studies of droplet breakup for droplets flowing through the orifice. The breakup location again does not represent the actual location of the drop breakup, but the location where a drop is deformed to such an extent that it is very likely that it no longer relaxes to the primary drop, but disintegrates into several secondary drops. As before, the ratio of the drop area of the primary drop with the drop area in the individual images and the solidity of the drop image was used as the breakup criterion.

Figure 5.49 shows the course of the droplets with viscosity ratio $\eta^* = 10.5$ in experiments with Reynolds number $Re = 2000$. The droplet injection sites shown are in the range $0 < x/D < 30$ and $-1 < y/D < -3$. Shown are the droplet trajectories, i.e. the positions of the droplet centroids at the acquisition times as black dots and the location of the achieved breakup criterion shown as a red cross. To classify the drop trajectories, the normalized, ensemble-averaged velocity field is shown in the background.

It can be clearly seen that the droplets dosed in the vicinity of the free jet ($0 < x/D < 7.5$) initially move with the bypass injection flow in the direction of the free jet and are then entrained by the free jet. The breakup of these droplets is marked in the area of the shear layer after a certain length or duration. Droplets that are strongly deflected or reflected by the free jet are not shown.

In the transition region ($7.5 < x/D < 17.5$), it can be seen that the droplet trajectories are deflected almost as soon as the droplets exit the capillary and are transported downstream. During this motion, the droplets are deformed as shown previously and eventually disintegrate. The trajectories shown are very short due to the immediate onset of deformation, as the breakup criterion is reached very quickly. The marked breakup location in these studies is almost always in or near the region of the decaying

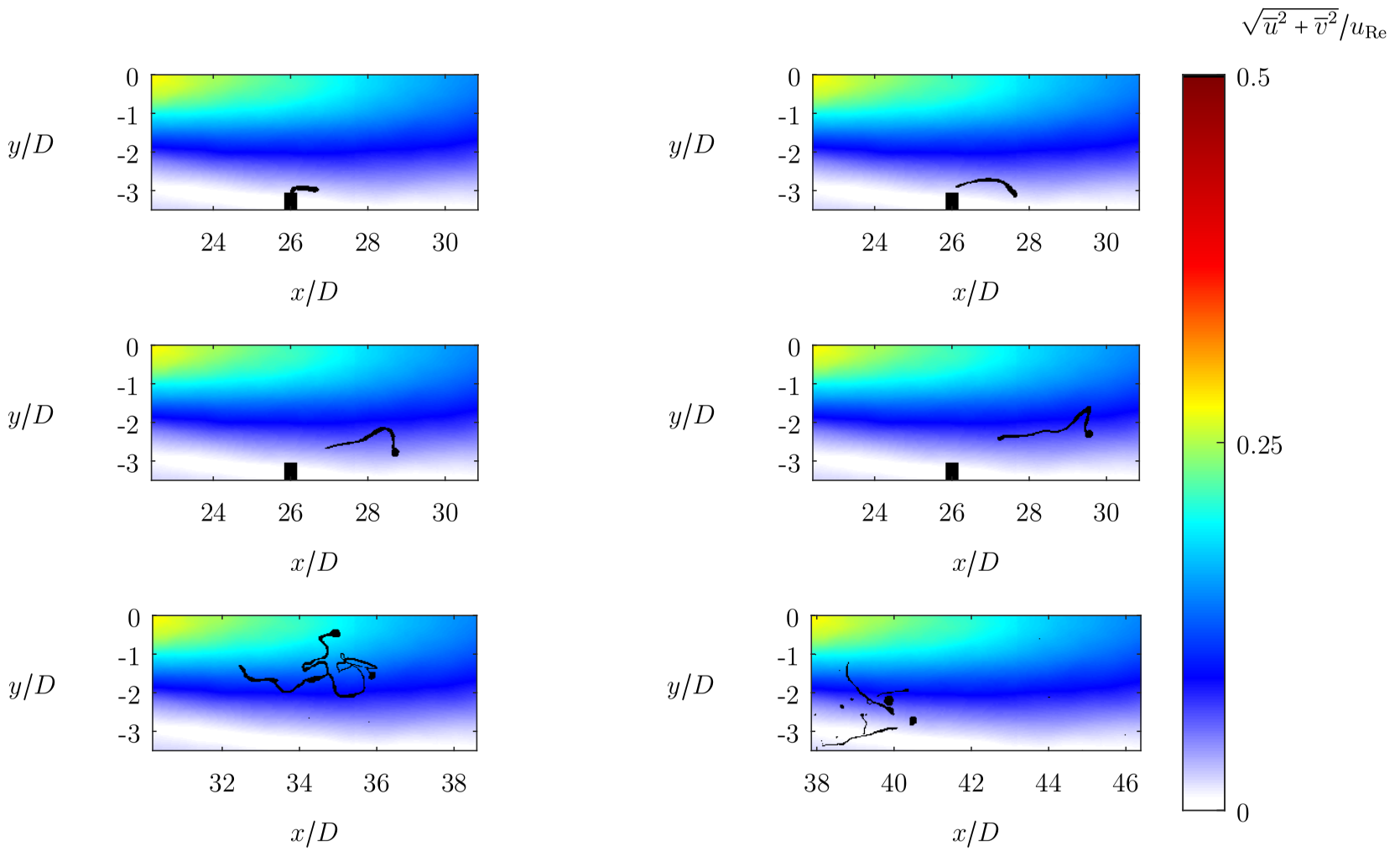

Figure 5.48: Example of a droplet breakup time series of a droplet injected in the far region at x/D = 26 and y/D = −3, shown as a black mask with the normalized, ensemble-averaged velocity field of the free jet behind the orifice as background, which is caught by the free jet flow directly as it partially leaves the capillary and is deformed and stretched. Due to the downstream position of the droplet, the deformations are not so fast and pronounced, so that the droplet or the stretched droplet filament breaks up into several coarse secondary droplets.

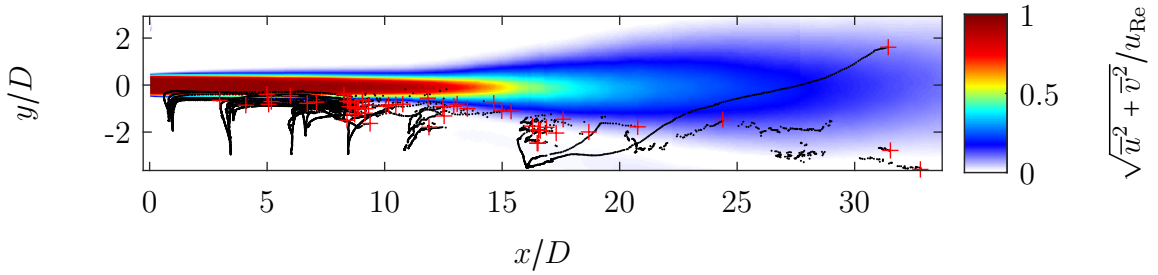

Figure 5.49: Illustration of the droplet trajectories as a black row of dots and the location of the reached droplet breakup criterion as red crosses. In the background the normalized, ensemble-averaged velocity field is shown to enable the data to be interpreted.

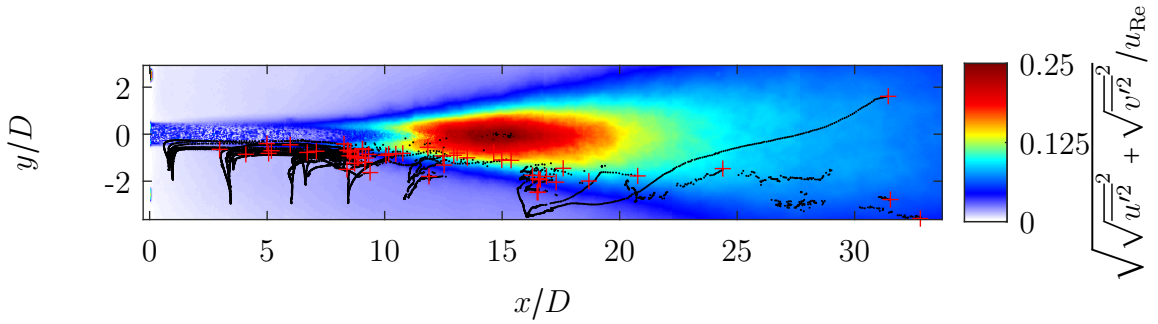

Figure 5.50: Illustration of the droplet trajectories as a black row of dots and the location of the reached droplet breakup criterion as red crosses. In the background the nomalized, average velocity fluctuations are shown to enable the data to be interpreted.

free jet core where the largest velocity fluctuations are present. For clarity, the normalized, averaged velocity fluctuation field is shown as background in Figure 5.50 instead of the normalized, ensemble-averaged velocity field. Individual droplets injected at position $x/D = 16$, i.e. in the transition region with a very short capillary, i.e. $y/D = -3$ show a significantly longer trajectory, which suggests that they are not deformed as much and therefore the breakup occurs later, i.e. further downstream. This may be due to the fact that the droplets are injected in a comparatively low-velocity zone or a zone with low velocity fluctuations and are transported by low-intensity vortices. Possibly, there is also a significant displacement of the droplets in z-direction, so that the droplets bypass the highly turbulent core region.

Droplets dosed in the far field of the free jet also exhibit a longer trajectory in some cases. As already described, this is due to the fact that the droplets do not pass through the highly turbulent free jet region and are therefore only deformed by less powerful vortices and finally break up into coarse secondary droplets.

In order to investigate the influence of the viscosity ratio on the drop breakup of drops which do not flow through the orifice but are injected into the free jet behind the orifice, experiments with drops of viscosity ratios $\eta^* = 0.3$ and $\eta^* = 3.0$ were carried out in addition to the previously shown experiments, where the viscosity ratio was $\eta^* = 10.5$. Figure 5.51 shows the comparison of the droplet trajectories and the breakup location for the three different viscosity ratios. Image a) shows the trajectories at viscosity ratio $\eta^* = 0.3$, image b) shows the trajectories at $\eta^* = 3.0$, and image c) shows the data previously shown at $\eta^* = 10.5$.

Comparison of the complete droplet trajectories or droplet breakup location in respect to the viscosity ratio shows no significant difference in the length of the trajectories or in the position of the detected droplet breakup location. This might be due to the fact, that despite the different viscosity ratio all droplets begin the interaction with the jet as more or less round droplets.

The observation of the individual initial deformation processes at the beginning of the droplet-free jet interaction shows that droplets injected in the vicinity of the free jet are excited to oscillations or surface waves become visible due to the interaction with the free jet or the shear layer that builds up. This phenomenon can be observed at all viscosity ratios as shown in Figure 5.53, 5.54 and 5.55. The three drops shown were injected at a time preceding the time series at position $x/D = 5$, $y/D = -2$. Figure 5.52 schematically shows the measurement position compared to the free jet and the capillary.

The time series of the different drops are shown to illustrate the oscillations. The time stamp is used to classify the deformation velocity or oscillation frequencies and refers to the first image shown.

Despite different degrees of deformation and different deformation rates, no dependence of the droplet deformation phenomenon and the viscosity ratio can be detected on the basis of the measurements, and the time series shown as examples. This may be due to the limited sample size in single droplet studies, or because the shear layer is not stationary, but fluctuates in time, albeit to a lesser extent, than in the turbulent free jet region. These fluctuations are the reason why the examined drops are exposed to completely different stresses and thus a comparison is not possible. This explanation would again show that investigations in turbulent flows are clearly more difficult to analyze than investigations to determine critical stress conditions in laminar flows. For a better understanding of the deformation processes, it would be necessary to simultaneously determine the droplet deformation and, at best, the volumetric velocity field. It would also be possible to create a generic turbulence field independent of a free jet and investigate the droplet interactions with the turbulent field.

The phenomenon that primary drops are deflected by the free jet or the recirculation flow is also independent of the viscosity ratio. Figure A.4 in the appendix A.2 shows an example with a drop of viscosity ratio $\eta^* = 0.3$.

In the further course of the interaction of the droplets with the free jet, the droplets of all investigated viscosity ratios are strongly deformed and twisted by vortices and very strongly stretched. In the high turbulent zone of the decaying free jet, the droplets

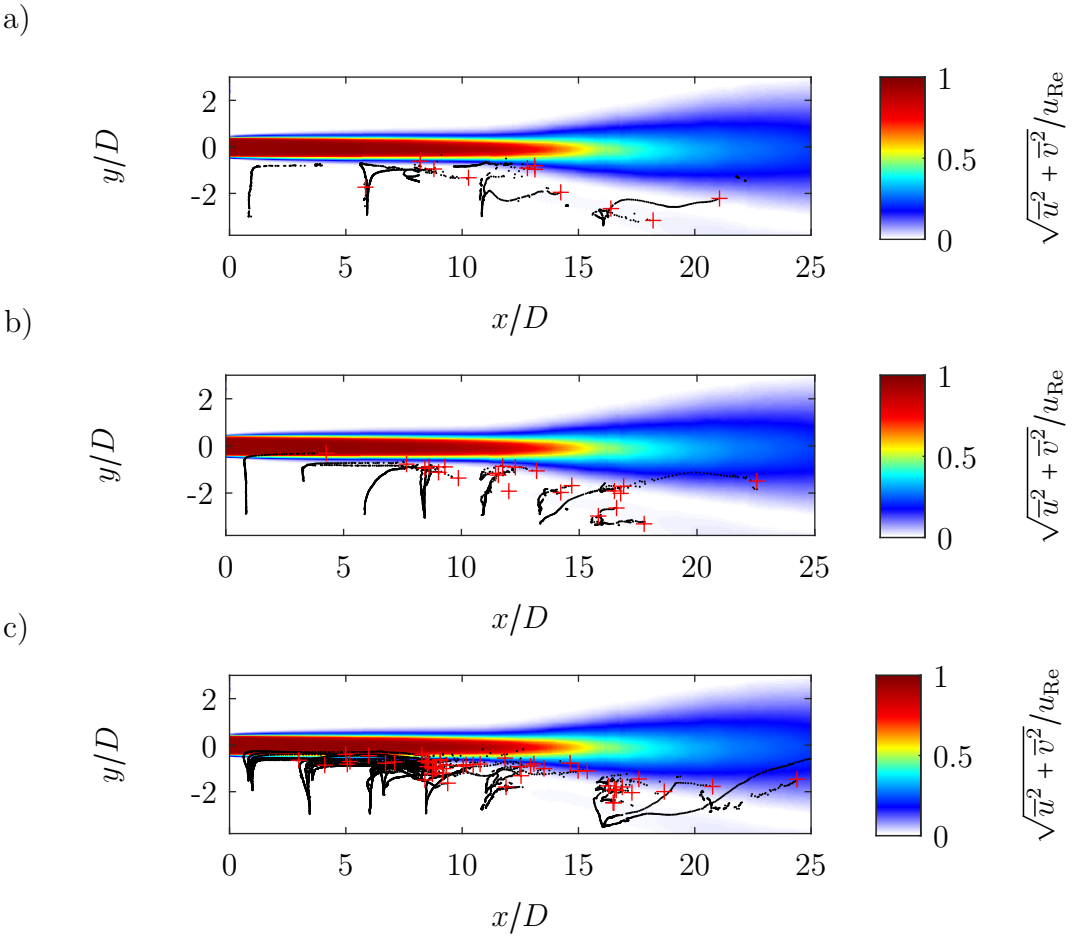

Figure 5.51: Comparison of droplet trajectories and breakup locations at different viscosity ratios. The droplet trajectory or the position of the droplet center of mass is shown as a black dot, the location where the breakup criterion is reached as a red cross. In the background the normalized, ensemble-averaged velocity field at the corresponding Reynolds number (Re = 2000) is shown for comparison. The viscosity ratios are: a) η^* = 0.3; b) η^* = 3.0; c) η^* = 10.5.

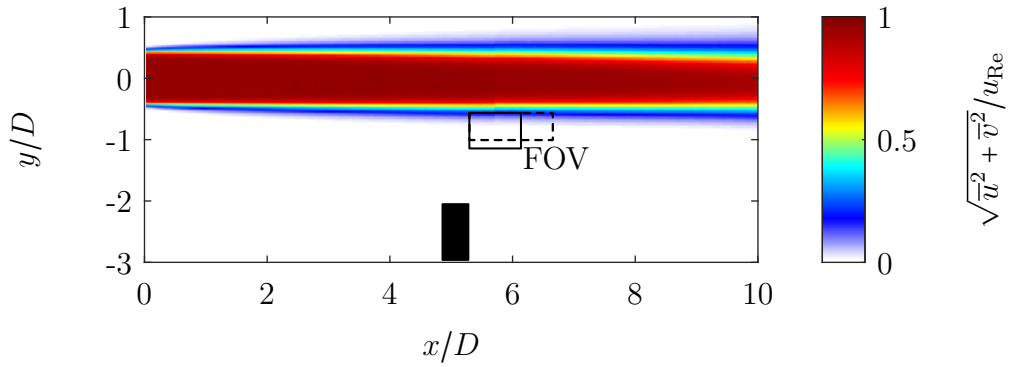

Figure 5.52: Graphic illustrating the measurement position for the droplet oscillation or surface wave investigations.

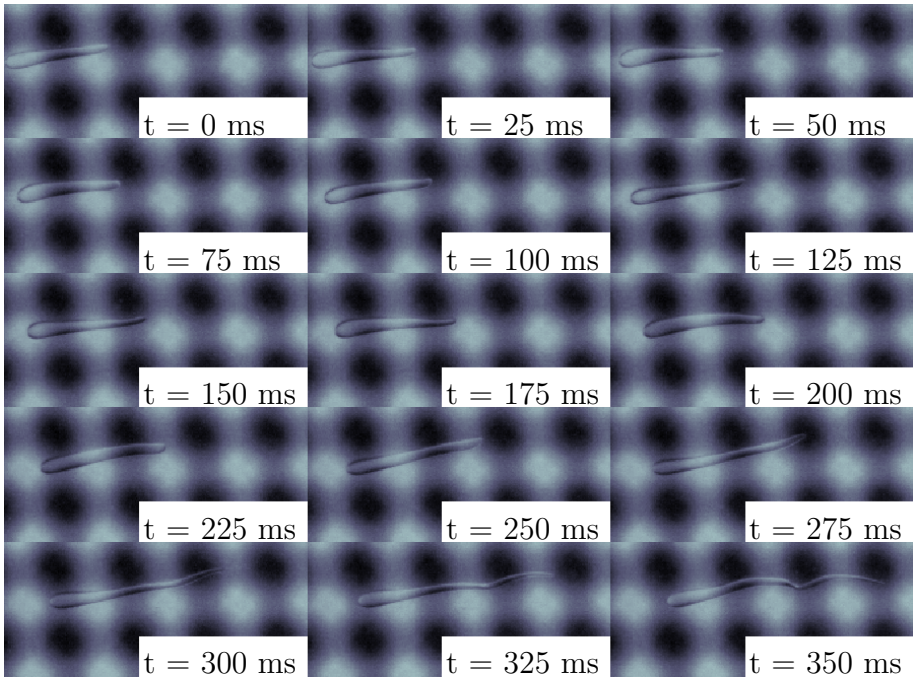

Figure 5.53: Time series of the droplet to illustrate the droplet oscillations and surface waves at viscosity ratio $\eta^* = 0.3$.

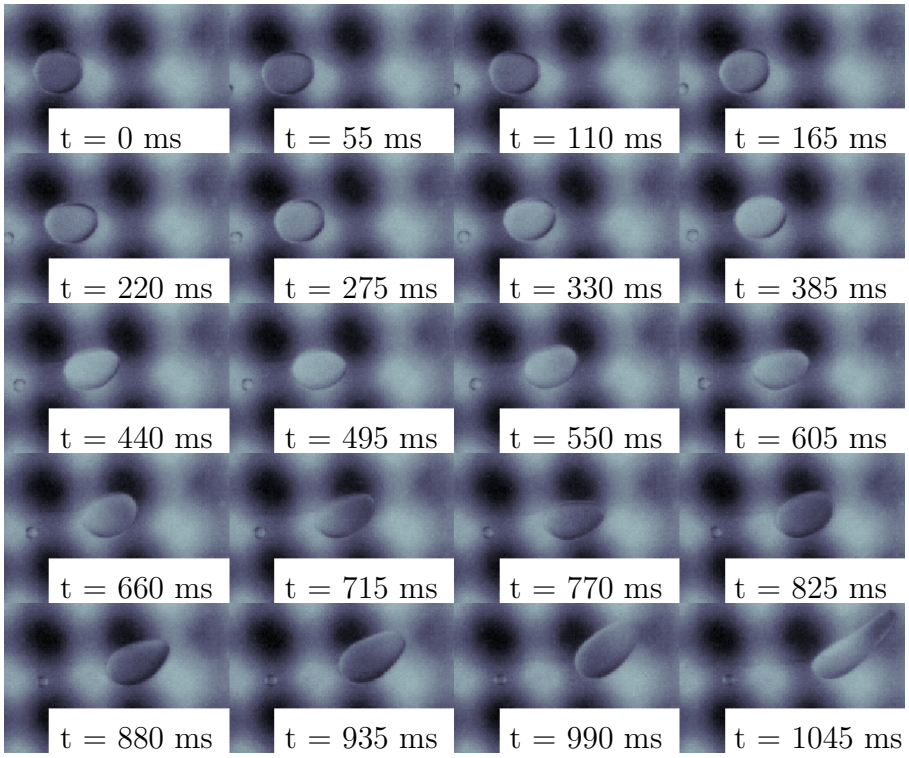

Figure 5.54: Time series of the droplet to illustrate the droplet oscillations and surface waves at viscosity ratio $\eta^* = 3.0$.

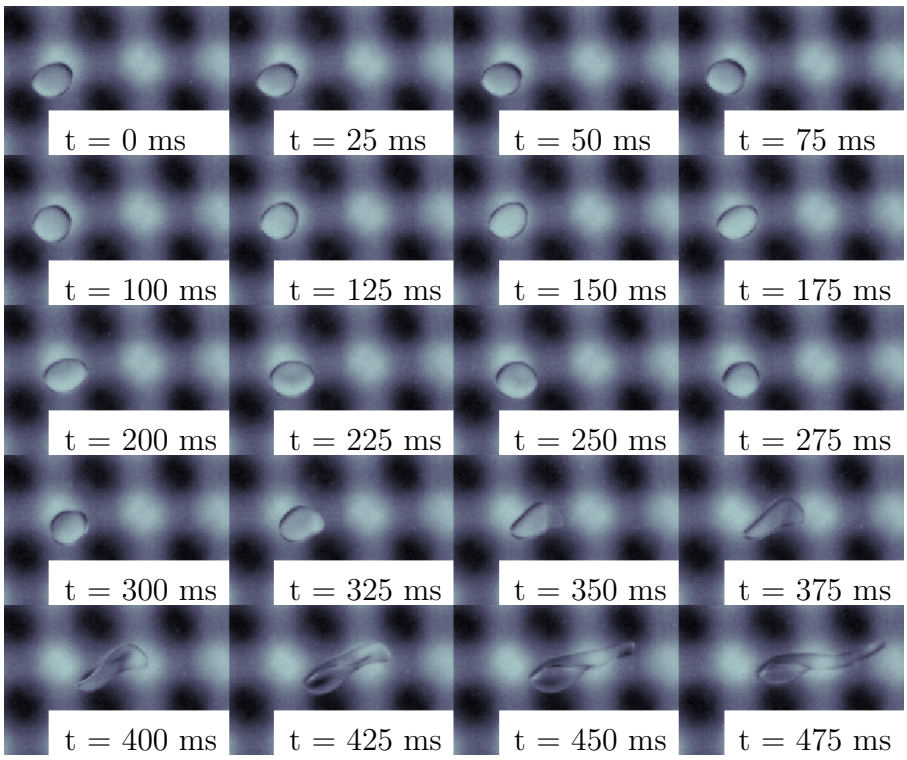

Figure 5.55: Time series of the droplet to illustrate the droplet oscillations and surface waves at viscosity ratio $\eta^* = 10.5$.

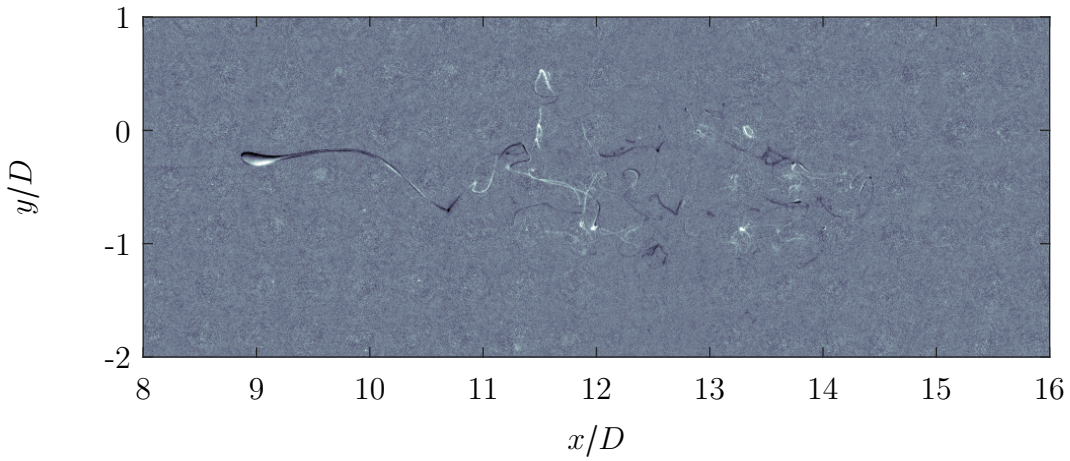

Figure 5.56: Image of the disintegrating droplet with viscosity ratio $\eta^* = 0.3$. The droplet injection point is at position $x/D = 5$, $y/D = -2$. The droplet is deformed to a strongly stretched and twisted long droplet filament due to the interaction with the free jet.

are extremely deformed and the twisted droplet filaments extend over a large area. Figure 5.56, 5.57 and 5.58 show strongly deformed droplets in the region of the highly turbulent zone for the three viscosity ratios studied.

The images show that the droplets are deformed into extremely long and networked droplet filaments regardless of the viscosity ratio. The filaments extend in the main flow direction over a length of up to $7D$ and also extend transversely to the main flow direction very widely. The individual filament segments overlap several times, so that the complete filament structure can hardly be identified. The drop filament of the drop with the lowest viscosity ratio appears to be slightly less deformed, but the difference is small, so this difference is not necessarily a consequence of the viscosity ratio. Droplets with higher viscosity ratios can also be similarly, mainly linearly stretched and deformed. This effect can also be caused by the temporally inhomogeneous turbulent structure due to the first interaction step.

In addition to the investigations on drop breakup of drops introduced into the free jet behind the orifice at the Reynolds number of $Re = 2000$, investigations at the higher Reynolds number $Re = 5700$ were also carried out. Similar to the investigations shown in chapter 5.3.2, it is also difficult to achieve a similarly good imaging quality for these investigations as for the low Reynolds number, since the processes are significantly faster, the resulting filaments are finer and significantly more interlinked or overlap more frequently, and dirt particles and air bubbles are swirled up to a significantly greater extent and thus impair the measurement. Therefore, it is not possible to determine droplet trajectories or the breakup location based on the previously defined breakup criterion. However, the measurements show that the previously observed breakup zone, i.e. shear layer region exists even at the higher Reynolds number. However, due to the higher Reynolds number, the breakup zone shifts towards the orifice as shown in the characterization of the flow fields (see chapter 5.3.2). Figure 5.59 shows

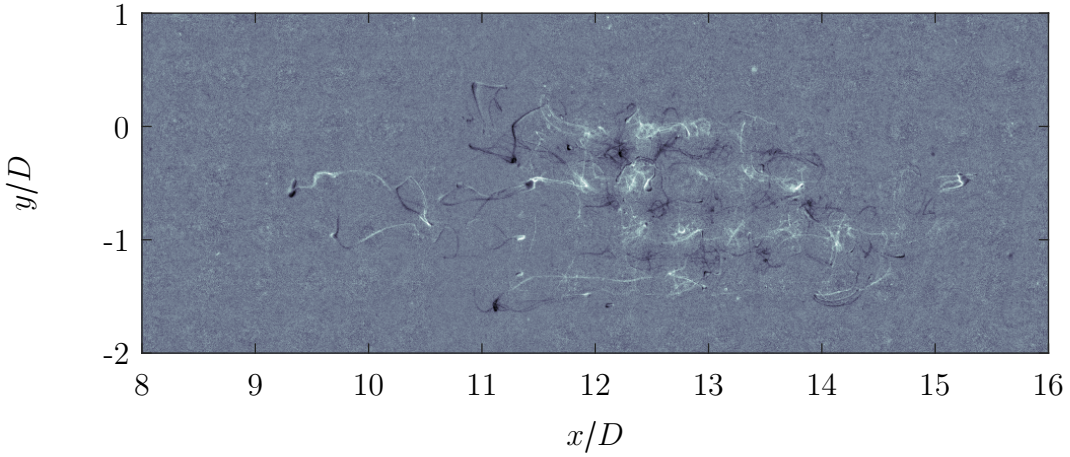

Figure 5.57: Image of the disintegrating droplet with viscosity ratio η^* = 3.0. The droplet injection point is at position x/D = 5, y/D = −2. The droplet is deformed to a strongly stretched and twisted long droplet filament due to the interaction with the free jet.

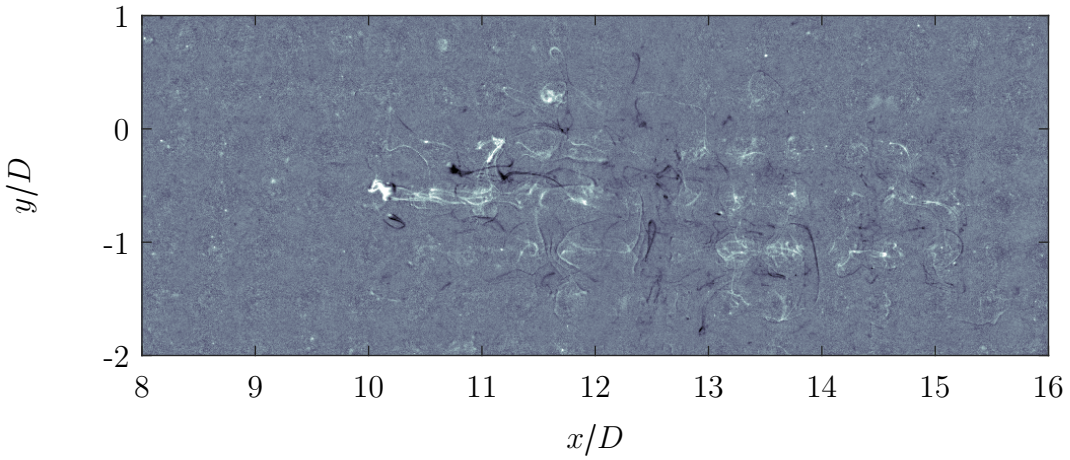

Figure 5.58: Image of the disintegrating droplet with viscosity ratio η^* = 10.5. The droplet injection point is at position x/D = 5, y/D = −2. The droplet is deformed to a strongly stretched and twisted long droplet filament due to the interaction with the free jet.

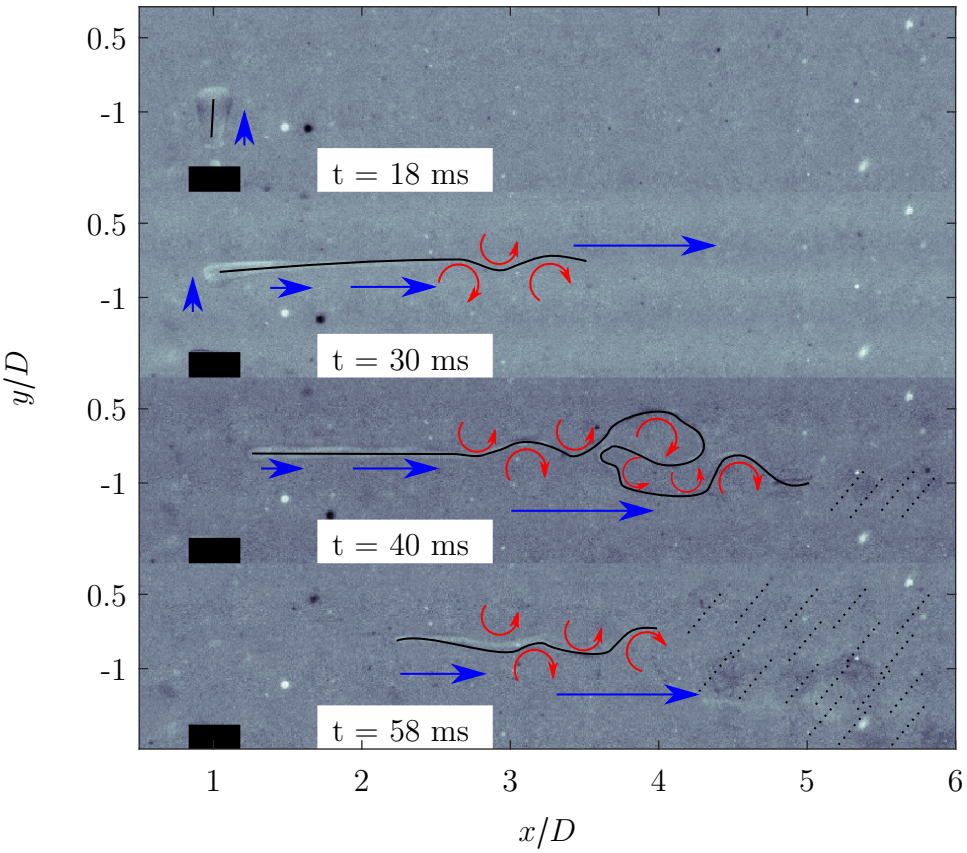

Figure 5.59: Plot of droplet breakup at Reynolds number $Re = 5700$ and a dosing of the droplet at $x/D = 1$, $y/D = -1.5$ at different times. The time $t = 0$ denotes the exit of the droplet front from the capillary. The capillary is marked in black. The drop is symbolized as a black line. The region that has already begun to break up or can no longer be precisely identified is marked by black dashed lines. The droplet velocity is marked by blue arrows and the vortices by red arrows.

schematically the droplet breakup process at the high Reynolds number $Re = 5700$ and an injection of the droplet near the orifice.

Shown is a time series of four images after the droplet exits the capillary. The dosing point is at the position $x/D = 1$, $y/D = -1.5$. The drop, which is illustrated by a black line, exits the capillary marked in black at time $t = 0$ and initially moves comparatively slowly in the direction of the free jet. The droplet velocity is illustrated by blue arrows. The shear layer causes the droplet to shear and stretch transversely to the original direction of motion, which also occurs slowly at first. The front of the resulting droplet filament is stretched faster and faster, so that the filament becomes longer and longer. As a result, the droplet extends into the region of the unstable shear layer, where Kelvin-Helmholtz vortices cause the filament to deform transversely to the main flow direction in addition to the axial elongation. The vortices are symbolized by red arrows. In the further course, these vortices cause the filament to be deformed more and more

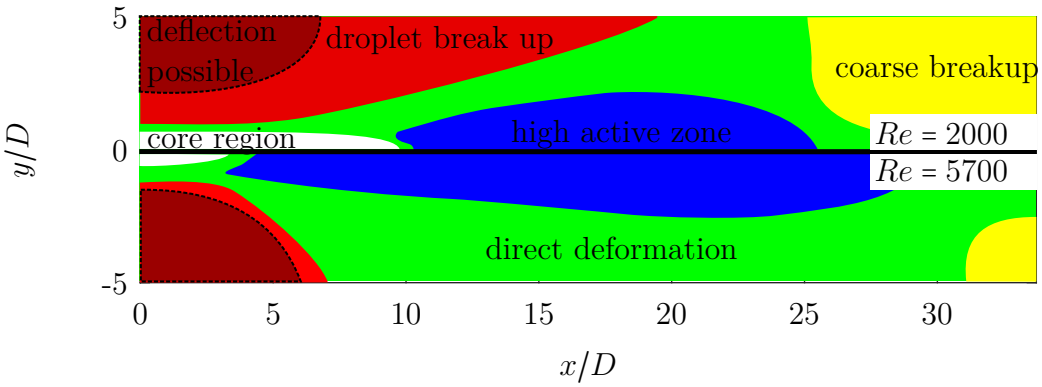

Figure 5.60: Representation of the drop breakup map for the two investigated Reynolds numbers Re = 2000 and Re = 5700. Color coded are the different droplet injection areas leading to different breakup mechanisms.

turbulently and to be stretched in length, so that the strongly deformed or elongated segments at the drop front can no longer be clearly identified. These segments or the area is marked by black dashed lines. The rear part of the drop is still present as an only slightly elongated drop and moves only slowly downstream. The rear droplet area is sucked out more and more by this mechanism until it finally also reaches the faster flowing zone and is also strongly deformed and swirled.

Based on the studies of droplet breakup of droplets injected behind the orifice into the free jet of the continuous phase, a map can be made relating the different observed breakup mechanisms to the injection site. These results can be used in the application of the SHM method to determine the optimal injection point of the dispersed phase with respect to the orifice. Figure 5.60 shows the breakup map.

Shown are the different zones, which lead to different breakup mechanisms or possibly to deflection of the droplets, for the two Reynolds numbers investigated (Re = 2000 top, Re = 5700 bottom). Shown are the zones explained below. The free jet core zone, where no breakup takes place, however no droplets could be introduced directly into this zone from the outside. The zone of normal droplet disintegration, which is characterized by the fact that the droplets are more or less relaxed into round droplets after leaving the capillary and then break up due to the shear stresses in the shear layer and the turbulent stresses in the highly active zone of the disintegrating free jet core area. Within this dosing region, especially due to larger distances of the dosing point from the free jet, the droplets may be deflected by the flow in the recirculation region and not break up according to the intended disintegration mechanism. Downstream, the zone of direct drop breakup follows, in which drops are already caught by the flow as they leave the capillary and are deformed as a result. In this area, it is possible that the droplets are carried along by the flow and, due to the inhomogeneous velocity field in the turbulent area, are deformed to a greater or lesser extent and thus pass through the highly active zone or not. Droplets injected even further downstream do not enter the high-intensity zone. The flow velocity in this area is also high enough to deform the droplets by shearing as they leave the capillary, but the turbulent stresses decrease with increasing distance from the orifice, so that the droplets are no longer

deformed and stretched as extremely as within the active zone and are therefore no longer effectively broken up, but only disintegrate into coarse secondary droplets.

In addition to the application of the investigated drop breakup of primary droplets which are introduced into the free jet behind the orifice deliberately (SHM process), these investigations can also show why homogenizing processes with two orifices or, as it were, a chamber of limited length behind the first orifice can lead to an improved drop breakup. The investigations suggested that the particularly good breakup efficiency in this multistage breakup process, which was investigated for example by Kolb (2001), is due to the fact that broken droplets within the turbulence chamber enter the free jet or shear layer several times and thus any coarser secondary droplets present after the first step are broken up again. In order to investigate this phenomenon in more detail, an experimental setup as in the investigations by Schlender et al. (2015a) would be well suited. In these investigations, the 2nd orifice could be simulated by a counterpressure tank. Using this back pressure tank instead of the 2nd orifice would not change the back pressure, but the flow conditions would be different and the turbulent mixing chamber, in which multiple disintegration could take place, would not be present without the 2nd orifice. Due to the dimensions used with a very large distance between the orifices compared to the channel diameter or the orifice diameter ((Karasch and Kulozik, 2008) (Freudig et al., 2003) (Finke et al., 2014)), this influence has not been investigated so far except for Kolb (2001) where the distance was in the range of 3–9 orifice diameters. However, when two conentric orifices follow each other very closely, there is the problem that the free jet generated by the first orifice flows straight through the second orifice, so that no distinct mixing zone is created or the droplets hardly enter this mixing zone (see Finke et al. (2014) with orifice distance to diameter ratio of 3.75). By using two offset, excentrically mounted orifices, this problem was overcome by Kolb (2001). The use of inclined orifice holes as in Karasch and Kulozik (2008) would also circumvent this problem.

5.4. Comparison of turbulent drop breakup of drops with and without predeformation in the orifice

The investigations on the breakup of droplets flowing through the orifice and breaking up in the free jet behind the orifice and droplets injected into the free jet behind the orifice allow the comparison of the results and can thus provide information on the influence of the orifice on the breakup. The measurements show that droplets flowing through the orifice are linearly stretched depending on the Reynolds number or the flow conditions and the viscosity ratio. High stresses, i.e. high Reynolds numbers or trajectories near the wall as well as low viscosity ratios lead to high elongations of the primary droplets. The large elongation leads to a rapid breakup, since the droplets are already stretched when they reach the shear layer or the high-intensity zone, and this elongation is further increased until the droplets break up, although this last step cannot be investigated as shown before. Highly viscous droplets have a low elongation due to the pre-stretching and partially due to the following relaxation, which occurs in droplet trajectories along the axis of symmetry through the orifice and the free jet core region, so that the breakup criterion investigated is reached somewhat later. Since the droplet trajectory through the orifice in industrial plants is not adjustable, but the droplet collective flows through the orifice distributed over the entire cross-section, this effect is advantageous for the size reduction of the individual droplets in the case of droplet trajectories at the edge, but it is not readily adjustable. It may be possible to exploit this effect in orifices with a high perimeter-to-passage area ratio, i.e. orifices with a rectangular bore with a large rectangular aspect ratio, but no detailed studies are available on this besides Karasch and Kulozik (2008).

When dosing the drops behind the orifice into the free jet, it is to a certain extent inevitable that the drops do not exhibit any pre-elongation, irrespective of the viscosity ratio, provided that the injection point is far enough away from the free jet. Moreover, this effect is only relevant for droplets individually dosed by capillaries and not for technically used dosing of pre-emulsions. The most important parameter determining the drop breakup at a given Reynolds number is the choice of the dosing point. Depending on this, droplets can break up according to different breakup mechanisms. The investigations carried out show that dosing the droplets as close to the orifice as possible, at least in front of the high-turbulence active zone, seems to lead to the most effective droplet breakup. However, when dosing the droplets, care must be taken to ensure that the individual droplets or the droplets of the pre-emulsion are not deflected by the flow in the recirculation region, which can occur if the droplets are dosed radially far away from the free jet. If this is prevented, the droplets enter the shear layer directly and are stretched very quickly and for a long time by the strong velocity gradient before they are further deformed turbulently in the further course by vortices created by the decay of the free jet core area.

Droplet dosing directly in the high active turbulent zone would disregard the deformation potential of the shear layer. The turbulent forces acting on the droplets due to the interaction of the droplets with the vortices also lead to deformation and disintegration of the droplets in this case. However, the investigations also show that too late

dosing of the droplets can lead to deteriorated droplet breakup, i.e. large secondary droplets.

Irrespective of the dosing point and the viscosity ratio, drop breakup occurs in the case of undeflected or reflected drops, as in the case of drops flowing through the orifice, due to the strong deformation of the drop. The droplets, if not already stretched by shear elongation, are deformed by interaction with vortices into very stretched and twisted droplet filaments with extreme length to diameter ratios. The exact mechanism in the tearing of the filament cannot be accurately observed due to the resolution or visualization limitations of overlapping and extremely thin filaments. However, the images show that the drop filaments relax when leaving the high-intensity zone or when the external forces fade, splitting into individual secondary droplets, with the droplet size depending on the elongation, i.e. the filament diameter or the diameter of the least elongated sites. These droplets are mainly formed at the points which, due to the non-uniform elongation of the filament by the vortices, have a larger filament diameter, i.e. the filament bridges between filament nodes or less deformed filament bends break.

The Reynolds number increase from $Re = 2000$ to $Re = 5700$ seems to lead mainly to a shift of the breakup zones according to the measured velocity fields. A change in the observed breakup mechanism does not seem to take place. Rather, it seems that the intensity of the droplet-vortex interaction, which leads to the elongation of the droplet towards twisted filaments, is significantly more intense due to the higher Reynolds number. While at the lower Reynolds number single droplets or filament segments are transported through seemingly less intensive free jet regions due to the inhomogeneous turbulence at the particular point in time, at the higher Reynolds number it appears that these regions do not exist or rather that even these comparatively less intensive regions are smaller or intensive enough compared to the lower Reynolds number so that the droplet is strongly deformed.

Due to the very low dispers phase concentration and the avoidance of emulsifier molecules, which would stabilize secondary droplets, but at the same time would greatly reduce the measurement time with an experimental batch of the measurement fluid, no statements can be made about the resulting secondary droplet size. Therefore, it is not possible to conclusively assess from these measurements the influence of the drop elongation, which is generated when passing through the orifice, on the secondary drop size distribution. However, it can be shown that pre-stretching is not necessarily required for droplets to be broken up during high-pressure homogenization. This is especially true for highly viscous droplets, which are hardly deformed even when flowing through the orifice and are still broken up. The main cause of drop breakup during high-pressure homogenization appears to be the turbulent stressing of drops by a large number of large- and small-scale vortices.

5.5. Influence of passive flow control at the orifice trailing edge on the velocity field and turbulence intensity distribution

The investigations of the velocity field behind the orifice show that the high-turbulence zone moves significantly closer to the orifice by increasing the Reynolds number. At the same time, it is known that the droplet breakup is more efficient at a higher Reynolds number or the larger pressure difference ((Karbstein and Schubert, 1995) (Kelemen et al., 2015)). The inhomogeneous distribution of turbulence intensity could be considered as an explanation. Although the relative turbulence intensity is similar for the higher Reynolds number as for the lower one, the absolute turbulence intensity is higher. This is accompanied by the fact that the relatively low turbulent regions are more turbulent in absolute terms than at the low Reynolds number. The studies on droplet breakup show that the turbulence intensity is sufficient to stretch and break up the droplet even at the low Reynolds number, but this happens more slowly. On the one hand, more time is available for the droplet to relax, since the turbulent region is only further downstream, but on the other hand, the intensities are at least partially lower, so that stretching and deformation occur more slowly.

By using passive flow control, the spatial distribution of the turbulence intensity, as well as the height of the local turbulence intensity, should be influenced in such a way that the droplet breakup takes place more efficiently at lower Reynolds numbers.

The orifice trailing edges developed for turbulence manipulation can be incorporated into the same orifice main body, so that any differences obtained are generated only by the different trailing edges with the passive flow control structures. In the following, the results of the velocity field measurements behind the different orifice trailing edges at a Reynolds number of $Re = 2000$ are presented.

Figure 5.61 shows the comparison of the normalized, ensemble-averaged velocity fields behind the different orifices. Case a) shows the velocity field behind the standard orifice without turbulence influence. Compared to this case, most velocity fields with passive flow control deviate in individual aspects. In case b) with the circumferential conical expansion of the orifice bore, the free jet is very symmetrical as in the reference case, but the expansion of the flow profile, i.e. the decay of the free jet, occurs somewhat faster, but essentially with a comparable run length of the free jet, so that no significant shift of the breakup zone is to be expected. The free jet core in case c) is somewhat shorter and the course of the free jet is also not completely symmetrical. The shear layer on the top of the free jet shown expands somewhat faster. This is also the case with the free jet shown in case d), although the free jet is similar in length or even minimally longer compared to the reference case. The free jet in case e) with 4 smaller recesses appears to be symmetrical and the region of free jet decay is elongated, while in case f) it is also symmetrical and is significantly shorter or starts earlier. Figure 5.62 appropriately shows the normalized, ensemble-averaged velocity fluctuations. In this plot, the shear layer region can be seen particularly well. The asymmetry in case c) of the orifice trailing edge with 3 recesses is clearly visible, as well as the resulting earlier emergent high-intensity zone. Cases d) and e) with orifice trailing edges with 4 recesses

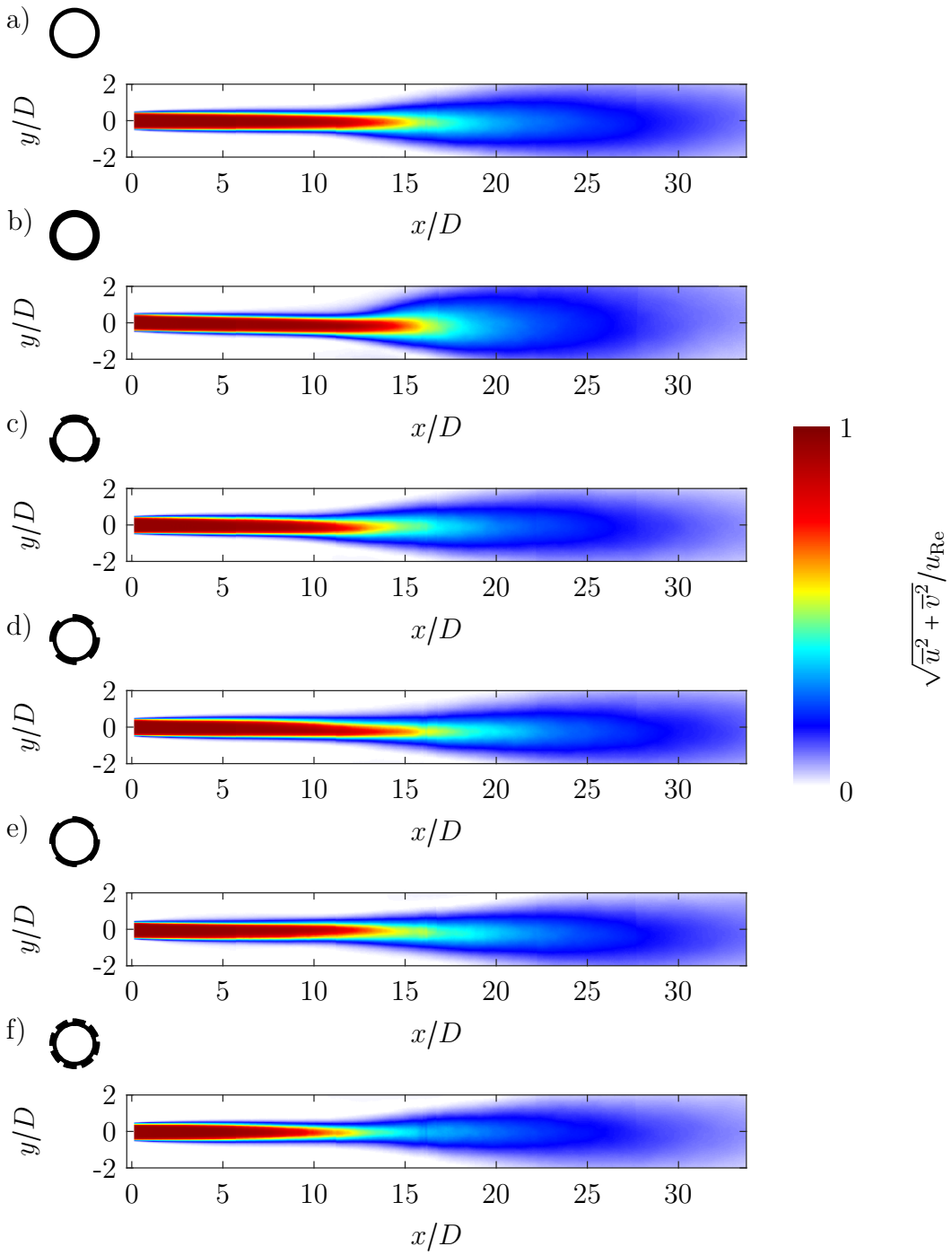

Figure 5.61: Comparison of the normalized, ensemble-averaged velocity fields in the free jet behind the different trailing edges with passive flow control structures. a) standard orifice; b) orifice with circumferential conical expansion; c) orifice with three notches; d) orifice with four large angle notches; e) orifice with four small angle notches; f) orifice with eight notches.

but different cone opening angles are also asymmetrical. Case f) is symmetrical and has a very large high-intensity mixed zone.

The asymmetry may be caused by the fact that, at least in the case of the orifice with 3 conical recesses, the measuring plane intersects the recess on one side and no recess on the opposite side. In the case with 4 recesses, the measuring plane exactly intersects the edge of two opposite recesses, but due to the propagation or possibly existing twists of the free jet, a displacement may occur, so that the free jet is measured asymmetrically. Another explanation could be a slightly shifted measuring plane to the symmetry axis.

For a more detailed analysis of the generated free jets and the velocity fields, the velocity field of the free jet is measured transversely to the main flow direction by means of a further measurement setup, so that the shape of the free jet becomes clear. For this purpose, a 3D-PTV measurement method is used in order to be able to map the strong velocity gradients well. Using this method, it is possible to measure the ensemble-averaged velocity fields and free jet cross sections at different lengths. Figure 5.63 shows the normalized, ensemble-averaged velocity fields of the original free jet at four length positions (x/D = 2.5; x/D = 5; x/D = 10 and x/D = 20).

The free jet cross section is round at the first three measuring positions. The increase of the shear layer thickness is clearly visible. In the last image, no free jet core can be seen, but only a diffuse round velocity field of the decaying free jet.

In comparison to this case, the figure 5.64 shows the free jet behind the rear edge of the orifice with three recesses and 60° extent each at the corresponding run lengths. It is clearly visible that the free jet has a triangular cross-sectional shape. The orientation of the triangle corresponds to the orientation of the trailing edge of the orifice, i.e. the openings of the orifice correspond to the triangular tips in the free jet profile. While the triangular free jet profile is very symmetrical in the first image, an asymmetry develops in the second and third measurement positions, in that the free jet core appears to be displaced in the direction of the lower right triangle tip. In the fourth image at the run length x/D = 20, as with the original free jet, no free jet core can be seen any more, but only a diffuse velocity field with a velocity maximum in the center, but without a triangular cross-section.

To compare the different trailing edges of the orifice, the free jet cross-sections of the six trailing edges are shown in Figure 5.65 for the run length x/D = 5. As already shown, the free jet cross section for the original orifice is round. In the lower region shown, a slight velocity increase is visible in the region of low flow velocities. This may be due to an increase in velocity in the backflow region, i.e. a vortex lasting longer. A similar phenomenon can be seen in the free jet profile of the free jet behind the orifice trailing edge with a circumferential conical opening. This free jet profile is also essentially round. In the case of the orifice trailing edge with three recesses, a triangular free jet profile can be seen, as already shown. The two orifice rear edges with four recesses produce a quadrangular free jet cross-section regardless of the opening angle, although the extent of the corners is greater at the larger opening angle. As with the triangular free jet cross section, the alignment of the corners of the square free jet cross section also matches the alignment of the orifice trailing edge or the recesses.

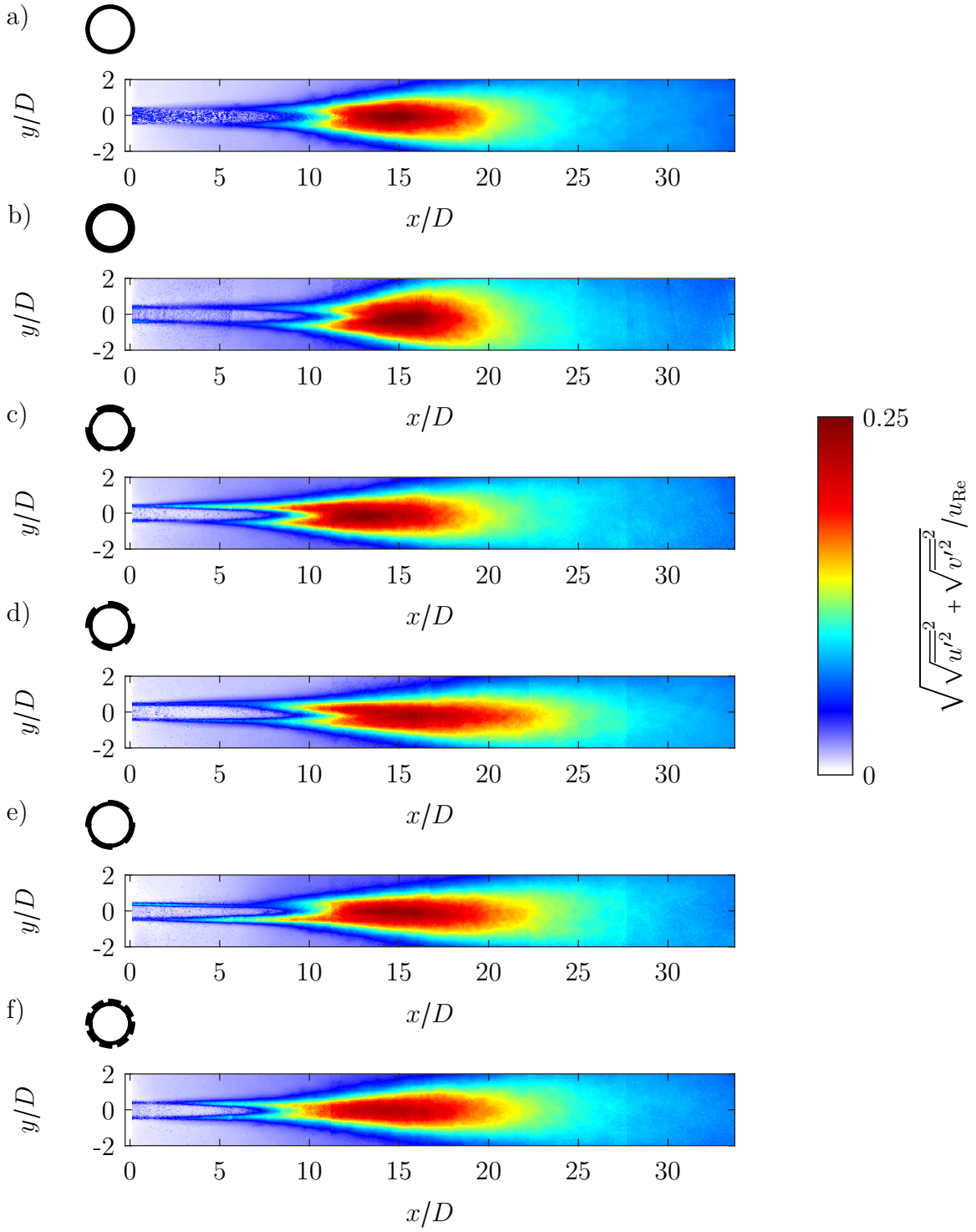

Figure 5.62: Comparison of the normalized, ensemble-averaged velocity fluctuation fields in the free jet behind the different trailing edges with passive flow control structures. a) standard orifice; b) orifice with circumferential conical expansion; c) orifice with three notches; d) orifice with four large angle notches; e) orifice with four small angle notches; f) orifice with eight notches.

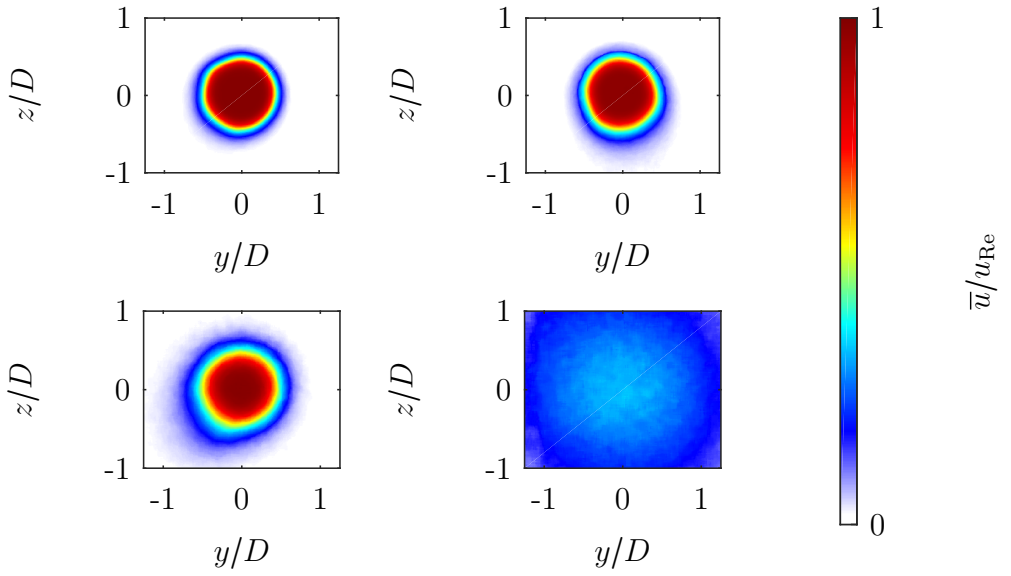

Figure 5.63: Development of the jet shape behind the original trailing edge over the length (x/D = 2.5, x/D = 5, x/D = 10 and x/D = 20) at a Reynolds number of Re = 2000.

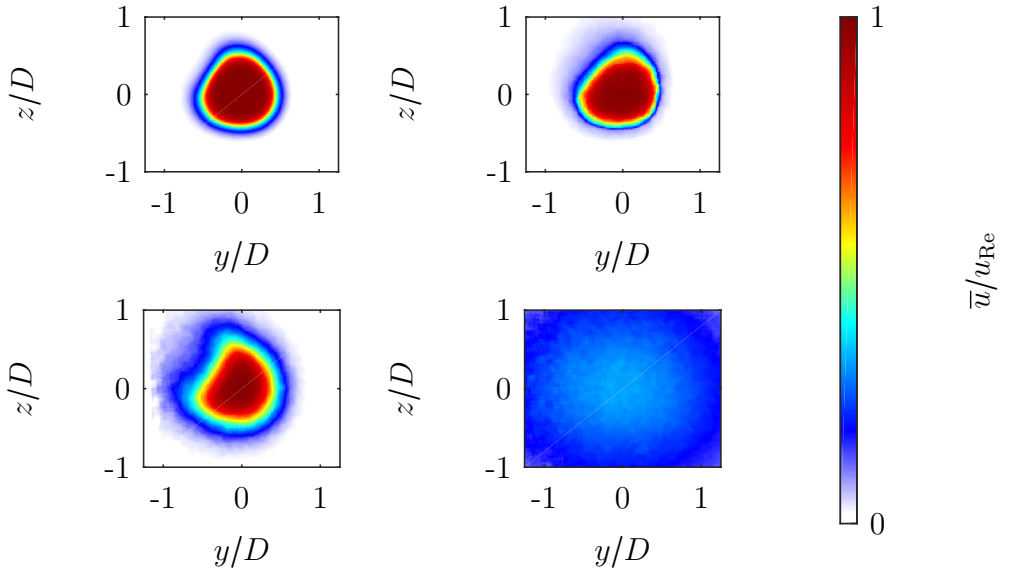

Figure 5.64: Development of the jet shape behind the orifice with three notches on the trailing edge over the length (x/D = 2.5, x/D = 5, x/D = 10 and x/D = 20) at a Reynolds number of Re = 2000.

Behind the orifice with eight recesses, no octagonal free jet can be seen, as would be expected from the other results. This may be due to the fact that with eight recesses, the structures may be too close to each other, so that no clear correlation between the free jet cross-section shape and the orifice's trailing edge can be recognized.

These results show that the orifice rear edge, i.e. the number and size of the recesses, can have a significant influence on the free jet flow. The results explain the previously varying degrees and shapes of free jet shear layers.

The free jet cross-sectional velocity fields at the higher Reynolds number Re = 5700 are shown in Figure 5.66. It can be seen that the free jet shape is largely round for all the investigated orifice trailing edges and no influence of the passive flow control structures on the velocity field can be detected. This impression is also visible in the 2D velocity fields shown in Figure 5.67.

These results indicate that at the higher Reynolds number and the associated higher flow velocity, the flow detaches at the trailing edge of the orifice or at the conical flare, if present, and does not follow the orifice contour. Accordingly, the shear layer is not affected by the orifice trailing edges or the passive flow control devices. The problem of flow separation when using conical flares is significantly increased compared to the tabs widely used in the literature ((Samimy et al., 1993) (Zaman et al., 1994) (Mi et al., 2007)) and reduces the effect of passive flow control. The reason for using flares instead of tabs was that the pressure drop should not be increased by the additional blocking, because this would counteract the increase in turbulence intensity at lower pressure drop or lower Reynolds number. The flow can also detach behind the tabs, but this causes mixing of the flow field. In addition, the flow must first follow the blocking by the tabs, so that a mixing of the flow or the boundary layer inevitably occurs.

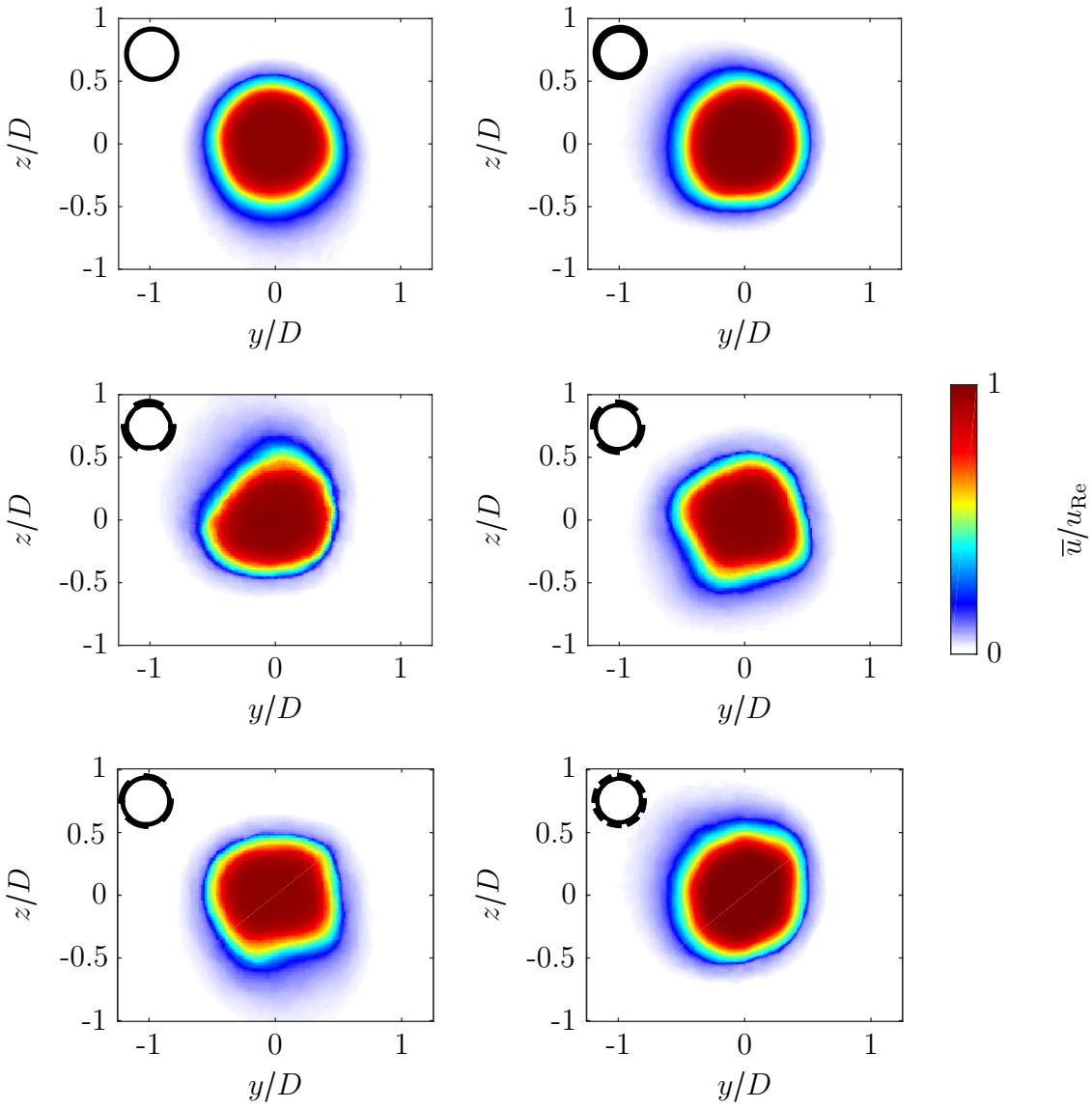

Figure 5.65: Comparison of the jet shapes after the different trailing edges at a Reynolds number of $Re = 2000$ and at the x-Position $x/D = 5$.

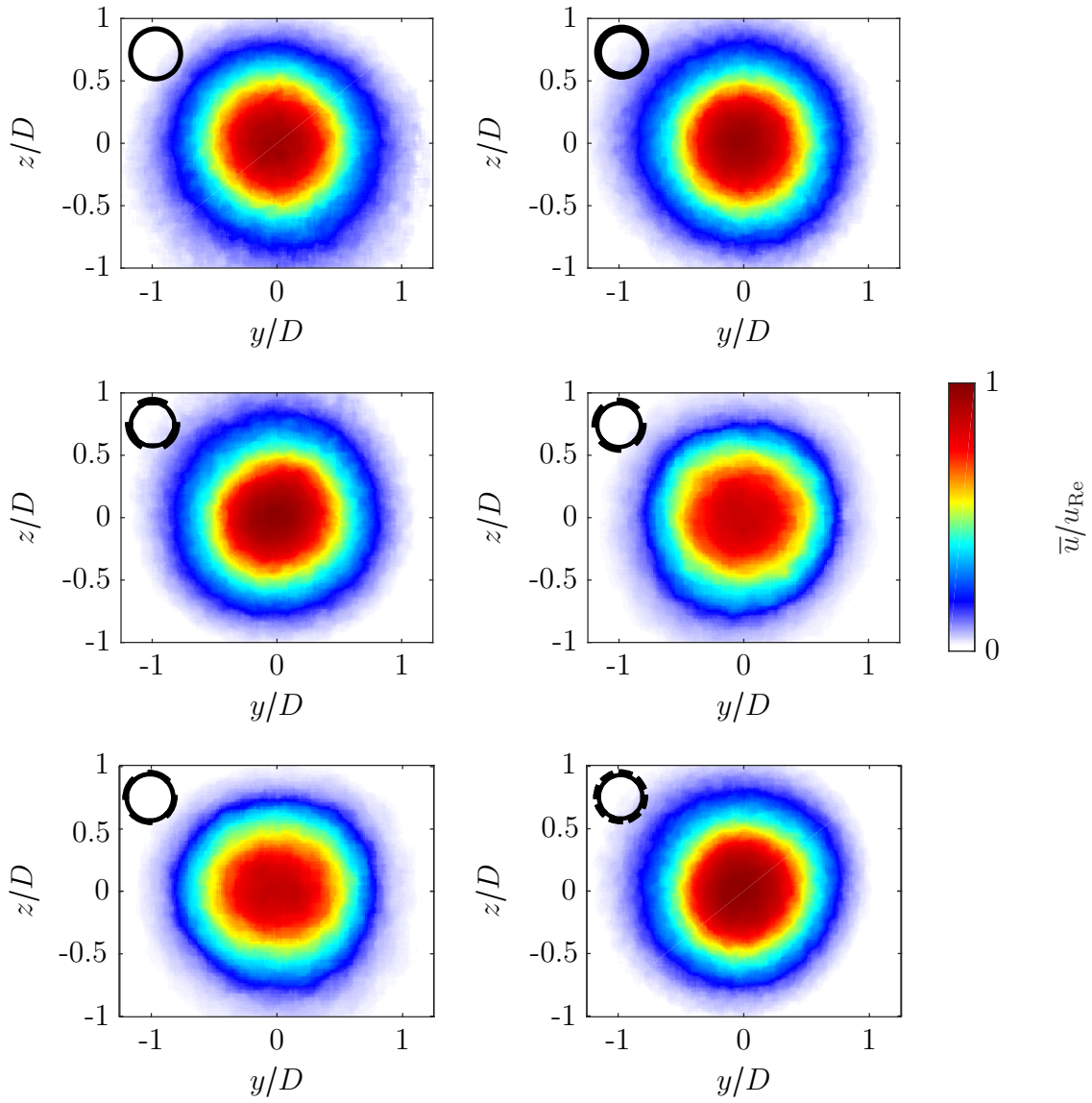

Figure 5.66: Comparison of the jet shapes after the different trailing edges at a Reynolds number of $Re = 5700$ and at the x-Position $x/D = 5$.

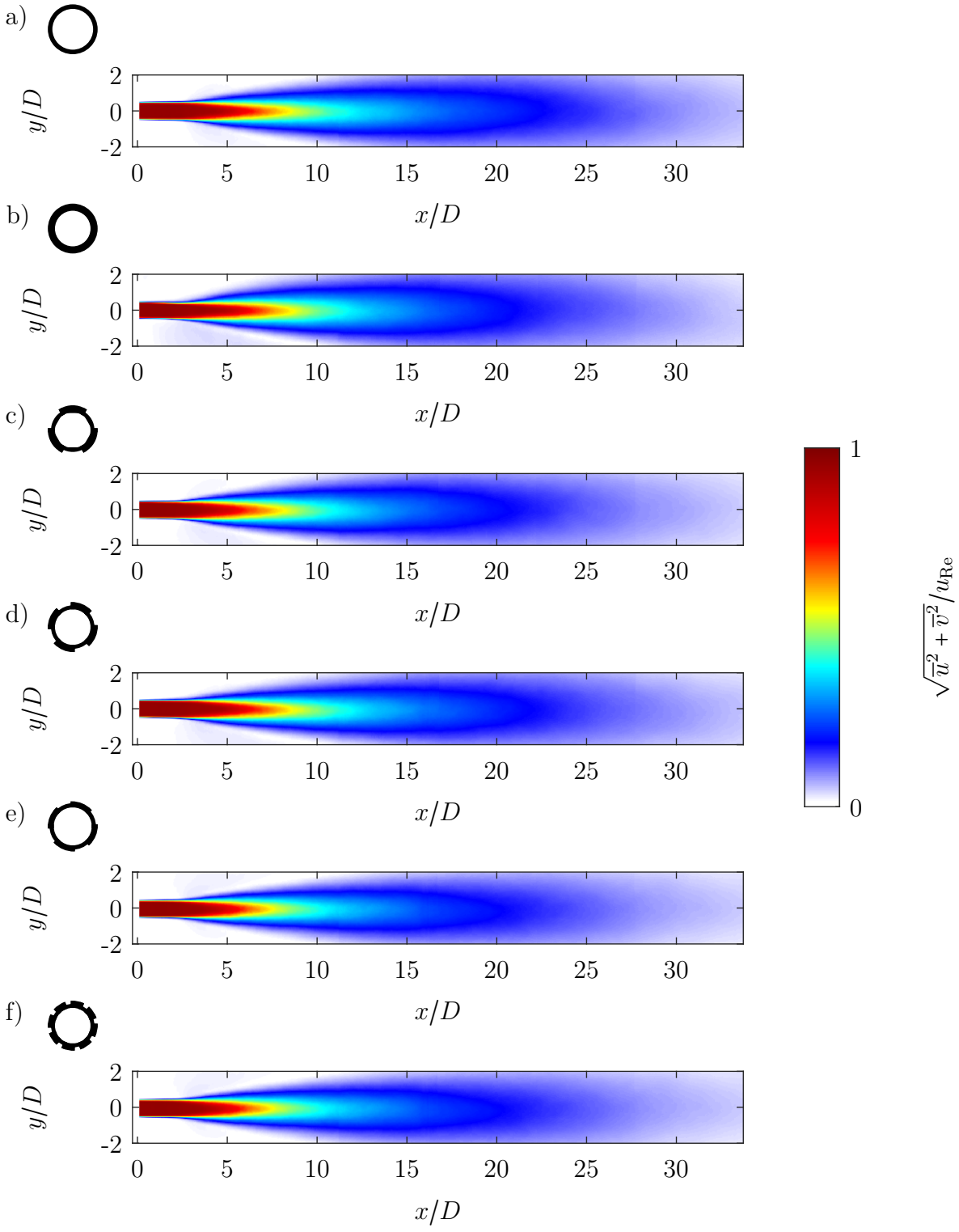

Figure 5.67: Comparison of the normalized, ensemble-averaged velocity fields in the free jet behind the six free jet trailing edges investigated for flow control. a) standard orifice; b) orifice with circumferential conical expansion; c) orifice with three notches; d) orifice with four large angle notches; e) orifice with four small angle notches; f) orifice with eight notches.

6

Conclusion and outlook

An experimental setup was designed and built to investigate droplet breakup during transient conditions in the high-pressure homogenization process with an orifice as disintegration unit. The experimental plant has an optically very highly accessible measuring section consisting of an inflow channel to the orifice made of glass. The orifice unit itself, which is made of acrylic glass, and the low-pressure trailing channel made of glass. The experimental unit can be operated stationary at an adjustable Reynolds number. The pressure drop required for the set Reynolds number is regulated by a frequency controlled pump and a selfmade Labview program for process automation. The temperature is controlled manually via valves and a heat exchanger. The experimental plant is designed according to a scaling concept so that the measuring section is enlarged by a scaling factor of 50, geometrically similar to an original plant, investigated at a project partner. To ensure that the test results are comparable between the scales, the material parameters density and viscosity of the two phases and the interfacial tension between the phases were also adjusted according to the scaling concept. The operating parameters pressure difference and primary droplet diameter were adjusted as well. As a result, the homogenizing pressure is greatly reduced for comparable Reynolds numbers, so that the experimental glass plant is pressure-stable. In addition to the strictly scaled material system, two other systems or two other disperse phases were used, so that the influence of the viscosity ratio on droplet breakup in turbulent flows can be investigated.

To investigate the drop breakup in the experimental setup, the shadowgraphy method was modified so that the contrast between the drop and the background, or rather the visualization of the drop, could be significantly improved. For this purpose, a background pattern was added, by which not the shadowing per se, but the distortion of the background pattern by the light diffraction at the interphase provides a clear contrast. In addition to the illumination intensity, the orientation of the background pattern is also important for the evaluation of the experiments. It has been shown that an angle of about 45° between the axes of the background pattern and the main flow direction is most suitable for visualization. Based on the recorded images, droplet masks were created using a Matlab algorithm so that the droplet trajectory can be evaluated automatically. These masks are the basis for the reconstruction of the drop volume in the performed 3D drop reconstructions, also done with a Matlab algorithm.

For the studies on drop breakup, first the velocity fields in the test plant were measured and analyzed using PIV. It is shown that the flow at the orifice inlet is characterized by a strong elongational flow and, in the wall region, also by a strong shear flow. The normalized velocity profile in this region is independent of the Reynolds number. Behind the orifice a free jet is formed, which is surrounded by a recirculation region. The free jet is very symmetrical in the time average and does not attach to a wall even with decreasing trailing channel diameters, but spreads out symmetrically. Due to the increase in wall effects with smaller trailing channels, the free jet shortens in these cases and the velocity dissipates faster.

An increase of the Reynolds number from Re = 2000 which has been investigated in most cases in this work to Re = 5700 leads to a shortening of the free jet. This means that the nearly laminar free jet core exiting the orifice and surrounded by a thin shear layer decays earlier and breaks down into a turbulent and fluctuating free jet. The reason for this may be the much stronger velocity gradient in the shear layer, which causes the instabilities, i.e. the Kelvin-Helmholtz instabilities, to grow stronger and faster, leading to a faster decay of the stable free jet. The decaying free jet leads to a very strong turbulent region with high temporal and spatial velocity fluctuations. The vortex size can be determined from instantaneous velocity fields. In addition, it is possible to calculate it from simplifications of the Kolmogorov-Hinze theory. However, the calculation leads to a slight overestimation of the size compared to the measured vortex sizes.

Based on the velocity field measurements, time-resolved high-speed recordings of the droplet deformation and breakup process were taken. The images from the orifice region show the deformation process of the droplet due to the elongation and shear flow in the inlet region of the orifice. The measurements show that the droplet deformation strongly depends on the local flow conditions around the droplet. Due to the droplet expansion, which increases as a result of the deformation process, the droplet extends simultaneously over a wide range in the flow direction, so that the integral length change results from locally distinctly different stresses. On the one hand, the drop front and the drop end can be stressed differently at the same time, and on the other hand, the drop front and the drop end are stressed differently when passing the same point, since the filament diameter decreases due to the steady elongation of the drop and is different between the drop front and the drop end. Higher Reynolds numbers result in more deformation, i.e. longer droplet filaments than lower Reynolds numbers. Changes in viscosity ratio have a significant effect on droplet elongation. A reduction of the viscosity ratio leads to a significantly stronger elongation. In addition, it can be observed in the region behind the orifice that the drop shape is slightly different for the three viscosity ratios investigated. The droplet of the low viscosity ratio has a tapered droplet end and a spherical droplet front, while the two higher viscosity ratios are almost cylindrical filaments with rounded ends. The influence of primary droplet size was also investigated, with longer filaments forming with larger primary droplet diameter. The deformation process appears to be similar regardless of the size of the primary droplet, but because of the difference in scale and size, the final elongation is different. In all cases investigated, the deformation takes place along the streamlines, so that the droplets leave the orifice as a straight stretched filament even if

the deformation was not symmetrical beforehand, which is the case, for example, if the droplets originated from a position radially deviating from the symmetry axis. With increasing radial position, the elongation of the droplets can reach very high values, so that the droplet front behind the orifice disintegrates in the free jet area, while the rear part is still in the orifice, where it may be further deformed.

According to the velocity fields described, there are different zones behind the orifice in which the drop is subjected to different stresses. In the free jet core zone, the droplet stretched by the orifice inlet flow experiences hardly any external stresses, so that relaxation of the droplet can occur. This can be observed in particular with highly viscous droplets and a low Reynolds number, which flow through the orifice along the axis of symmetry, since on the one hand the elongation of the droplets is very low, and on the other hand the free jet core region is very long, so that the time for relaxation is greatest. Droplets moving at the edge experience constant shear behind the orifice in the shear layer surrounding the free jet core region. Above a certain length and radial position, they can also be caught by the Kelvin-Helmholtz vortices and become swirled. This droplet-vortex interaction leads to a very strong additional elongation of the filaments mostly to below the resolution limit. The Kelvin-Helmholtz instability also leads to the decay of the free jet core region, so that droplets flowing centrally through the orifice start to meander with the free jet at a certain position and are then strongly deformed three-dimensionally by vortices. This turbulent deformation process itself occurs independently of the viscosity ratio and leads to such strong deformation that the droplet filaments can no longer be clearly identified due to the three-dimensional deformation and superposition. The start of this deformation process, however, is influenced by the viscosity ratio, since, as already described, in the case of highly viscous droplets, due to the lower elongation in the orifice and the more progressed relaxation, initially no filaments interact with the turbulent velocity field and the vortices contained therein, but almost completely relaxed primary droplets. These are again stretched to filaments by the vortices. The transition of the linearly stretched droplet filament to the three-dimensionally deformed filament or film like structure was investigated using 3D reconstruction of the droplet volume. In addition, simultaneous 2D2C-PIV velocity measurements and shadowgraphs of the deformation process were performed. Due to the droplet extent and deformation in depth direction as well as the lack of three-dimensional and too low spatial resolution, no force estimates could be performed on the droplet deformation.

Corresponding to the shift of the velocity field with the increase of the Reynolds number, the droplet deformation and breakup zones also shift. The free jet core area becomes shorter and the time of the droplet in this area becomes shorter due to the higher flow velocity, so that no relaxation of the droplet can be observed. The high-turbulence zone also shifts forward towards the orifice. Although the turbulence intensity normalized by the theoretical orifice velocity is similar for the two Reynolds numbers investigated, and the extent of the highly turbulent zone is also similar, the absolute turbulence intensity is significantly greater, so that droplet deformation occurs more rapidly. This is also reflected in the more compact filament structure, although the individual filament segments cannot be visualized more precisely. At the lower Reynolds number, large- and small-scale vortices overlap, so that there is a higher spa-

tial expansion of the filament structures than at the higher Reynolds number, where the small-scale vortices predominate, or are at least intense enough to deform the droplet very quickly to below the visualization limit.

The investigation of the drop breakup can be statistically correlated with the ensemble-averaged velocity fields, but for the individual drop the local and instantaneous velocity gradients and vortex fields are decisive. Due to the sometimes very large spatial extent of the droplets or droplet filaments, a large number of independent deformation processes distributed over the entire droplet can occur simultaneously, so that the breakup of the droplet is not a single event, but occurs at several points and at different times starting from a primary droplet. The exact disintegration process in turbulently deformed droplet filaments, i.e. the separation of the individual secondary droplets from the droplet filament, which may be highly three-dimensionally twisted and folded, cannot be observed accurately in most cases despite enlargement of the test facility by a scale factor of 50, because the spatial resolution is not given. Only in individual less stressed cases can the process be observed with comparatively coarse drops. This observation makes it seem unlikely that droplet breakup in the free jet region behind the orifice is a stepwise process in which one disintegration step follows the next or that it is an instability driven process where breakup happens simultaneously across the whole filament like it would be driven by the Plateau-Rayleigh instability with capillary waves; instead, the disintegration appears to take place in particularly strongly deformed filament segments. Segments that have been less strongly stressed up to this point can be further deformed or, when the external stresses decrease, i.e. when they leave the highly active turbulent zone, relax to form larger secondary droplets. During this relaxation process, filament segments can break up at relatively thin parts, so that a less stressed filament segment does not necessarily relax as a whole to form a secondary droplet. The secondary drops arising from a filament segment mainly form at somewhat less deformed points such as junctions, loops or end points.

Due to the low volume concentration of the disperse phase, which is necessary for the investigation of the single droplet breakup processes, it is unfortunately not possible to perform droplet size analyses. This would allow a clear correlation between the observed differences in the breakup processes and the resulting droplet size or droplet size distribution. At this point, reference must be made to the investigations carried out in the original scale or the experiments carried out in the experimental plant enlarged to a scale of 5, in which droplet size analyses could be carried out (Mutsch et al., 2021a). Due to the similarity in the determined velocity fields (Preiss et al., 2021) and the similarity of the observed droplet deformation processes (Mutsch et al., 2021a), the breakup processes in total should be comparable.

When injecting droplets into the free jet area behind the orifice, as used in the SHM process, basically similar breakup mechanisms occur. The investigations on this process design show that if the droplets are injected early enough behind the orifice into the free jet, they are deformed and break up very quickly and without pre-expansion within the orifice due to the interaction with the shear layer and the resulting turbulent layer or vortex zone. No influence of the viscosity ratio on this process could be observed. Mainly, the investigated single droplet breakup processes differ in the fact that local and instantaneous velocity fields or turbulence intensities are not constant, so that

the single droplet investigations can only be compared statistically, and the number of experiments is too small to make clear statistical statements about the forces. However, the individual processes can be observed very well. As long as the droplets enter the shear layer or are injected directly into the highly active zone of the turbulent decaying free jet, a sometimes very pronounced deformation process takes place until the droplets break up. If the droplets are placed outside these zones, there is a possibility that the droplets will be carried along by the recirculation flow or by the edges of the main flow and will be transported past the highly active zone. This can also lead to droplet disintegration, but in these cases the disintegration appears to be much slower and, above all, less intense, since the external stresses decrease with increasing distance from the orifice, so that only coarse secondary droplets are formed. Therefore, it seems to be important for the industrial application of the SHM process and the line routing in which the disperse primary droplets are injected into the free jet only after the orifice to ensure that the droplets do not flow past the free jet or the high-turbulence zone.

Since no droplet size analyses could be performed in the studies on this process design either, it is not possible to explain the exact mechanisms of droplet breakup below the visualization limit as well as the differences with respect to the optimal dosing point compared to the literature (Köhler et al., 2007).

The results for the injection of primary droplets into the free jet can, in addition to the application for the SHM process, provide an explanation for the operating principle of the turbulent mixing chamber as used, for example, by Kolb (2001). Secondary droplets, which are not completely broken up by droplet-vortex interactions after passing through the orifice and the free jet, because they may have randomly passed through less stressed zones, could interact again with the free jet or the shear layer and the vortices through the backflow region or the mixed flow in the turbulence chamber and thus be broken up more finely. The entrainment takes place mainly in the area of the shear layer surrounding the free jet, so that the droplets should be strongly deformed and efficiently broken up according to the previously shown findings. A small mixing chamber, i.e. a short distance between two orifices, increases the probability that droplets interact several times with the free jet or the vortices. If the distance between the orifices is too large and the free jet has expanded to the wall in the time average, a backflow of the droplet is less likely and thus the secondary disintegration process. However, care should be taken that the second orifice stage is not too close to the first orifice stage, or at least that the free jet cannot simply flow straight through the second orifice (see (Finke et al., 2014)), as this will also not create an efficient mixing chamber. Orifices with inclined bores (Aguilar et al., 2004) or offset, eccentric orifice bores (Kolb, 2001) or possibly other geometries seem to be very interesting for this process design since a strong mixing chamber can be created as in the case of the excentric jet investigated by Kolb (2001).

An increase in turbulence through the use of passive flow control devices with more precise conical recesses at the trailing edge of the orifice was also investigated by velocity field measurements using PIV and PTV. The results show that the influence of the free jet and a shift of the turbulence zones is possible, but this influence depends on the Reynolds number. At the higher Reynolds number, flow separation occurs at the conical expansions, so that the influence ceases to exist. Passive flow control elements

which, in contrast to the elements investigated, lead to blocking of the channel, such as tabs have been used in particular for gas flows (Zaman et al., 1994) but also liquid flows (Lemenand et al., 2005) and seem to be more efficient, since no detachment occurs or detachment at the trailing edge of the tabs does not cause any disadvantage, so that the overall mixing is improved.

Based on the studies on droplet breakup and the precise knowledge of the velocity fields, it is possible to determine the flow conditions relevant for turbulent droplet breakup and, based on this, to draw conclusions for an efficient homogenizing unit. The shear layer and the highly turbulent region of the decaying free jet seem to be especially relevant. Particularly interesting, therefore, seem to be orifices with rectangular orifice shapes, since they have a high circumference-to-area ratio. In this context, a systematic study on the influence of the aspect ratio would be interesting, since the disintegration efficiency could possibly prove to be independent of the aspect ratio and depend only on the gap width. Thus, it might be possible to flexibly adjust the production flow to the production volume requirements by changing the gap length without altering the disintegration processes and the efficiency, since the characteristic variable – the gap width – remains constant. Only the contraction ratio would be changed one-dimensionally by simply adjusting the gap length.

References

Aguilar, F., Köhler, K., Schubert, H., and Schuchmann, H. (2008). "Herstellen von Emulsionen in einfachen und modifizierten Lochblenden: Einfluss der Geometrie auf die Effizienz der Zerkleinerung und Folgen für die Maßstabsvergrößerung". In: Chemie Ingenieur Technik 80.5, pp. 607–613.

Aguilar, F., Freudig, B., and Schuchmann, H. (2004). "Herstellen von Emulsionen in Hochdruckhomogenisatoren mit modifizierten Lochblenden". In: Chemie Ingenieur Technik 76.4, pp. 396–399.

Andersson, R. and Andersson, B. (2006). "On the breakup of fluid particles in turbulent flows". In: AIChE Journal 52.6, pp. 2020–2030.

Angeli, P. and Hewitt, G. F. (2000). "Drop size distributions in horizontal oil-water dispersed flows". In: Chemical Engineering Science 55.16, pp. 3133–3143.

Bentley, B. J. and Leal, L. G. (1986). "An experimental investigation of drop deformation and breakup in steady, two-dimensional linear flows". In: Journal of Fluid Mechanics 167, pp. 241–283.

Binks, B. (1998). "Modern aspects of emulsion science". In: ed. by B. Binks. The Royal Society of Chemistry. Chap. 1 Emulsions - Recent Advances in Understanding, pp. 1–55.

Blonski, S., Korczyk, P. M., and Kowalewski, T. A. (2007). "Analysis of turbulence in a micro-channel emulsifier". In: International Journal of Thermal Sciences 46.11. Nano, Micro and Mini Channels, pp. 1126–1141.

Bolgar, I., Scharnowski, S., and Kähler, C. J. (2019). "Passive Flow Control for Reduced Load Dynamics Aft of a Backward-Facing Step". In: AIAA Journal 57.1, pp. 120–131.

Bradbury, L. J. S. and Khadem, A. H. (1975). "The distortion of a jet by tabs". In: Journal of Fluid Mechanics 70.4, pp. 801–813.

Budde, C., Schaffner, D., and Walzel, P. (2002). "Modellversuche zum Tropfenzerfall an Blenden in Flüssig/Flüssig/Dispersionen". In: Chemie Ingenieur Technik 74.1-2, pp. 101–104.

Calabrese, R. V., Chang, T. P. K., and Dang, P. T. (1986). "Drop breakup in turbulent stirred-tank contactors. Part I: Effect of dispersed-phase viscosity". In: AIChE Journal 32.4, pp. 657–666.

Cristini, V., Bławzdziewicz, J., Loewenberg, M., and Collins, L. R. (2003). "Breakup in stochastic Stokes flows: sub-Kolmogorov drops in isotropic turbulence". In: Journal of Fluid Mechanics 492, pp. 231–250.

Davies, J. (1985). "Drop sizes of emulsions related to turbulent energy dissipation rates". In: Chemical Engineering Science 40.5, pp. 839–842.

Eastwood, C. D., Armi, L., and Lasheras, J. (2004). "The breakup of immiscible fluids in turbulent flows". In: Journal of Fluid Mechanics 502, p. 309.

Elemans, P., Bos, H., Janssen, J., and Meijer, H. (1993). “Transient phenomena in dispersive mixing”. In: Chemical Engineering Science 48.2, pp. 267–276.

Finke, J. H., Niemann, S., Richter, C., Gothsch, T., Kwade, A., Büttgenbach, S., and Müller-Goymann, C. C. (2014). “Multiple orifices in customized microsystem high-pressure emulsification: The impact of design and counter pressure on homogenization efficiency”. In: Chemical Engineering Journal 248, pp. 107–121.

Floury, J., Desrumaux, A., and Lardières, J. (2000). “Effect of high-pressure homogenization on droplet size distributions and rheological properties of model oil-in-water emulsions”. In: Innovative Food Science & Emerging Technologies 1.2, pp. 127–134.

Foss, J. K. and Zaman, K. B. M. Q. (1999). “Large- and small-scale vortical motions in a shear layer perturbed by tabs”. In: Journal of Fluid Mechanics 382, pp. 307–329.

Freudig, B., Tesch, S., and Schubert, H. (2003). “Production of Emulsions in High-Pressure Homogenizers – Part II: Influence of Cavitation on Droplet Breakup”. In: Engineering in Life Sciences 3.6, pp. 266–270.

Galinat, S., Masbernat, O., Guiraud, P., Dalmazzone, C., and Noı¨k, C. (2005). “Drop break-up in turbulent pipe flow downstream of a restriction”. In: Chemical Engineering Science 60.23, pp. 6511–6528.

Galinat, S., Risso, F., Masbernat, O., and Guiraud, P. (2007). “Dynamics of drop breakup in inhomogeneous turbulence at various volume fractions”. In: Journal of Fluid Mechanics 578, pp. 85–94.

Galinat, S., Torres, L. G., Masbernat, O., Guiraud, P., Risso, F., Dalmazzone, C., and Noik, C. (2006). “Breakup of a drop in a liquid–liquid pipe flow through an orifice”. In: AIChE Journal 53.1, pp. 56–68.

Gothsch, T., Richter, C., Beinert, S., Schilcher, C., Schilde, C., Büttgenbach, S., and Kwade, A. (2016). “Effect of cavitation on dispersion and emulsification process in high-pressure microsystems (HPMS)”. In: Chemical Engineering Science 144, pp. 239–248.

Gothsch, T., Schilcher, C., Richter, C., Beinert, S., Dietzel, A., Büttgenbach, S., and Kwade, A. (2015). “High-pressure microfluidic systems (HPMS): flow and cavitation measurements in supported silicon microsystems”. In: Microfluidics and Nanofluidics 18.1, pp. 121–130.

Grace, H. P. (1982). “Dispersion Phenomena in High Viscosity Immiscible Fluid Systems and Applications of Static Mixers as Dispersion Device in Such Systems”. In: Chemical Engineering Communications 14.3-6, pp. 225–277.

Graftieaux, L., Michard, M., and Grosjean, N. (2001). “Combining PIV, POD and vortex identification algorithms for the study of unsteady turbulent swirling flows”. In: Measurement Science and Technology 12.9, pp. 1422–1429.

Håkansson, A. (2015). “Engineering Aspects of Food Emulsification and Homogenization”. In: ed. by M. Rayner and P. Dejmek. CRC PR INC. Chap. 5 Droplet Breakup in High-Pressure Homogenizers, pp. 125–148.

Håkansson, A. (2019). “Emulsion Formation by Homogenization: Current Understanding and Future Perspectives”. In: Annual Review of Food Science and Technology 10.1, pp. 239–258.

Håkansson, A., Fuchs, L., Innings, F., Revstedt, J., Bergenståhl, B., and Trägårdh, C. (2010). “Visual observations and acoustic measurements of cavitation in an ex-

perimental model of a high-pressure homogenizer". In: Journal of Food Engineering 100.3, pp. 504–513.

Håkansson, A., Fuchs, L., Innings, F., Revstedt, J., Trägårdh, C., and Bergenståhl, B. (2011a). "High resolution experimental measurement of turbulent flow field in a high pressure homogenizer model and its implications on turbulent drop fragmentation". In: Chemical Engineering Science 66.8, pp. 1790–1801.

Håkansson, A., Fuchs, L., Innings, F., Revstedt, J., Trägårdh, C., and Bergenståhl, B. (2011b). "On flow-fields in a high pressure homogenizer and its implication on drop fragmentation". In: Procedia Food Science 1. 11th International Congress on Engineering and Food (ICEF11), pp. 1353–1358.

Hecht, L. L., Merkel, T., Schoth, A., Wagner, C., Köhler, K., Muñoz-Espí, R., Landfester, K., and Schuchmann, H. P. (2013). "Emulsification of particle loaded droplets with regard to miniemulsion polymerization". In: Chemical Engineering Journal 229, pp. 206–216.

Hesketh, R. P., Etchells, A. W., and Russell, T. F. (1991). "Experimental observations of bubble breakage in turbulent flow". In: Industrial & engineering chemistry research 30.5, pp. 835–841.

Hinze, J. O. (1955). "Fundamentals of the hydrodynamic mechanism of splitting in dispersion processes". In: AIChE Journal 1.3, pp. 289–295.

Innings, F. and Trägårdh, C. (2005). "Visualization of the Drop Deformation and Break-Up Process in a High Pressure Homogenizer". In: Chemical Engineering & Technology 28.8, pp. 882–891.

Innings, F. and Trägårdh, C. (2007). "Analysis of the flow field in a high-pressure homogenizer". In: Experimental Thermal and Fluid Science 32.2, pp. 345–354.

Island, T. C., Urban, W. D., and Mungal, M. G. (1998). "Mixing enhancement in compressible shear layers via sub-boundary layer disturbances". In: Physics of Fluids 10.4, pp. 1008–1020.

Isomoto, K. and Honami, S. (1989). "The Effect of Inlet Turbulence Intensity on the Reattachment Process Over a Backward-Facing Step". In: Journal of Fluids Engineering 111.1, pp. 87–92.

Jahnke, S. (1998). "Emulsions and nanosuspensions for the formulation of poorly soluble drugs". In: ed. by R. H. Müller, S. Benita, and B. Bohm. CRC Press. Chap. The theory of high-pressure homogenization, pp. 177–200.

Janssen, J. and Meijer, H. (1993). "Droplet breakup mechanisms: Stepwise equilibrium versus transient dispersion". In: Journal of Rheology 37.4, pp. 597–608.

Janssen, J., Peters, G., and Meijer, H. (1993). "An opposed jets device for studying the breakup of dispersed liquid drops". In: Chemical Engineering Science 48.2, pp. 255–265.

Kang, S. and Choi, H. (2002). "Suboptimal feedback control of turbulent flow over a backward-facing step". In: Journal of Fluid Mechanics 463, pp. 201–227.

Karasch, S. and Kulozik, U. (2008). "Hochdruckhomogenisierung von Milch mit modifizierten Lochblenden im Vergleich zu konventionellen Flachventilen". In: Chemie Ingenieur Technik 80.8, pp. 1117–1124.

Karbstein, H. and Schubert, H. (1995). "Developments in the continuous mechanical production of oil-in-water macro-emulsions". In: Chemical Engineering and Processing: Process Intensification 34.3, pp. 205–211.

Kelemen, K. (2014). “Inline-Messung des Tropfenaufbruchs in Hochdruckblenden: Möglichkeiten und Limitierungen der uPIV”. PhD thesis. Karlsruher Institut für Technologie.

Kelemen, K., Gepperth, S., Koch, R., Bauer, H.-J., and Schuchmann, H. (2015). “On the visualization of droplet deformation and breakup during high-pressure homogenization”. In: Microfluidics and Nanofluidics 19.5, pp. 1139–1158.

Kelemen, K., Schuch, A., and Schuchmann, H. (2014a). “Influence of Flow Conditions in High-Pressure Orifices on Droplet Disruption of Oil-in-Water Emulsions”. In: Chemical Engineering & Technology 37.7, pp. 1227–1234.

Kelemen, K., Crowther, F., Cierpka, C., Hecht, L., Kähler, C., and Schuchmann, H. (2014b). “Investigations on the characterization of laminar and transitional flow conditions after high pressure homogenization orifices”. In: Microfluidics and Nanofluidics 18.4, pp. 599–612.

Kempa, L., Schuchmann, H. P., and Schubert, H. (2006). “Tropfenzerkleinerung und Tropfenkoaleszenz beim mechanischen Emulgieren mit Hochdruckhomogenisatoren”. In: Chemie Ingenieur Technik 78.6, pp. 765–768.

Kim, J.-H. and Samimy, M. (1999). “Mixing enhancement via nozzle trailing edge modifications in a high speed rectangular jet”. In: Physics of Fluids 11.9, pp. 2731–2742.

Köhler, K., Aguilar, F. A., Hensel, A., Schubert, K., Schubert, H., and Schuchmann, H. P. (2009). “Design of a Micro-Structured System for the Homogenization of Dairy Products at High Fat Content - Part III: Influence of Geometric Parameters”. In: Chemical Engineering & Technology 32.7, pp. 1120–1126.

Köhler, K., Aguilar, F., Hensel, A., Schubert, K., Schubert, H., and Schuchmann, H. P. (2007). “Design of a Microstructured System for Homogenization of Dairy Products with High Fat Content”. In: Chemical Engineering & Technology 30.11, pp. 1590–1595.

Köhler, K., Santana, A. S., Braisch, B., Preis, R., and Schuchmann, H. (2010). “High pressure emulsification with nano-particles as stabilizing agents”. In: Chemical Engineering Science 65.10, pp. 2957–2964.

Köhler, K. and Schuchmann, H. (2015). “Engineering Aspects of Food Emulsification and Homogenization”. In: ed. by R. Marilyn and D. Petr. CRC PR INC. Chap. 7 High-Pressure Homogenization with Microstructured Systems, pp. 169–193.

Köhler, K. and Schuchmann, H. (2012). “Simultanes Emulgieren und Mischen”. In: Chemie Ingenieur Technik 84.9, pp. 1538–1544.

Kolb, G. (2001). “Zur Emulsionsherstellung in Blendensystemen”. PhD thesis. Universität Bremen.

Kollhoff, R. T., Kelemen, K., and Schuchmann, H. P. (2015). “Local Multiphase Flow Characterization with Micro Particle Image Velocimetry Using Refractive Index Matching”. In: Chemical Engineering & Technology 38.10, pp. 1774–1782.

Kolmogorov, A. N. (1941). “The local structure of turbulence in incompressible viscous fluid for very large Reynolds numbers”. In: C. R. Acad. Sci. URSS 30, pp. 301–305.

Kolmogorov, A. N. (1949). “On the breakage of drops in a turbulent flow”. In: Dokl. Akad. Navk. SSSR 66, pp. 825–828.

Komrakova, A. E. (2019). “Single drop breakup in turbulent flow”. In: The Canadian Journal of Chemical Engineering 97.10, pp. 2727–2739.

Kurzhals, H. (1977). “Untersuchungen über die physikalisch-technischen Vorgänge beim Homogenisieren von Milch”. PhD thesis. Technische Universitaet, Hannover.

Lemenand, T., Dupont, P., Valle, D. D., and Peerhossaini, H. (2005). “Turbulent Mixing of Two Immiscible Fluids”. In: Journal of Fluids Engineering 127.6, pp. 1132–1139.

Lemenand, T., Valle, D. D., Dupont, P., and Peerhossaini, H. (2017). “Turbulent spectrum model for drop-breakup mechanisms in an inhomogeneous turbulent flow”. In: Chemical Engineering Science 158, pp. 41–49.

Maniero, R., Masbernat, O., Climent, E., and Risso, F. (2012). “Modeling and simulation of inertial drop break-up in a turbulent pipe flow downstream of a restriction”. In: International Journal of Multiphase Flow 42, pp. 1–8.

Martínez-Bazán, C., Montañés, J. L., and Lasheras, J. C. (1999a). “On the breakup of an air bubble injected into a fully developed turbulent flow. Part 1. Breakup frequency”. In: Journal of Fluid Mechanics 401, pp. 157–182.

Martínez-Bazán, C., Montañés, J. L., and Lasheras, J. C. (1999b). “On the breakup of an air bubble injected into a fully developed turbulent flow. Part 2. Size PDF of the resulting daughter bubbles”. In: Journal of Fluid Mechanics 401, pp. 183–207.

McCormick, D. C. and Bennett, J. C. (1994). “Vortical and turbulent structure of a lobed mixer free shear layer”. In: AIAA Journal 32.9, pp. 1852–1859.

Mengle, V. G. (2005). “Jet Noise Characteristics of Chevrons in Internally Mixed Nozzles”. In: 11th AiAA/CEAS Aeroaucustics Conference.

Mi, J., Kalt, P., Nathan, G. J., and Wong, C. Y. (2007). “PIV measurements of a turbulent jet issuing from round sharp-edged plate”. In: Experiments in Fluids 42.4, pp. 625–637.

Mishra, C. and Peles, Y. (2005). “Cavitation in flow through a micro-orifice inside a silicon microchannel”. In: Physics of Fluids 17.1, p. 013601.

Mohr, K.-H. (1987). “High-pressure homogenization. Part II. The influence of cavitation on liquid-liquid dispersion in turbulence fields of high energy density”. In: Journal of Food Engineering 6.4, pp. 311–324.

Mutsch, B., Preiss, F. J., Dagenbach, T., Karbstein, H. P., and Kähler, C. J. (2021a). “Scaling of Droplet Breakup in High-Pressure Homogenizer Orifices. Part II: Visualization of the Turbulent Droplet Breakup”. In: ChemEngineering 5.2, p. 31.

Mutsch, B., Walzel, P., and Kähler, C. J. (2021b). “Comparison of Experimental and Numerical Transient Drop Deformation during Transition through Orifices in High-Pressure Homogenizers”. In: ChemEngineering 5.3, p. 32.

Neumann, J. and Wengle, H. (2004). “Coherent structures in controlled separated flow over sharp-edged and rounded steps”. In: Journal of Turbulence 5.

Park, H., Jeon, W.-P., Choi, H., and Yoo, J. Y. (2007). “Mixing enhancement behind a backward-facing step using tabs”. In: Physics of Fluids 19.10, p. 105103.

Phipps, L. W. (1974). “Cavitation and separated flow in a simple homogenizing valve and their influence on the break-up of fat globules in milk”. In: Journal of Dairy Research 41.1, pp. 1–8.

Preiss, F. J., Mutsch, B., Kähler, C. J., and Karbstein, H. P. (2021). “Scaling of Droplet Breakup in High-Pressure Homogenizer Orifices. Part I: Comparison of Velocity Profiles in Scaled Coaxial Orifices”. In: ChemEngineering 5.1, p. 7.

Raffel, M., Willert, C. E., Scarano, F., Kähler, C. J., Wereley, S. T., and Kompenhans, J. (2018). Particle Image Velocimetry. Springer International Publishing.

Rähse, W. and Dicoi, O. (2009). “Produktdesign disperser Stoffe: Emulsionen für die kosmetische Industrie”. In: Chemie Ingenieur Technik 81.9, pp. 1369–1383.

Raikar, N. B., Bhatia, S. R., Malone, M. F., and Henson, M. A. (2009). “Experimental studies and population balance equation models for breakage prediction of emulsion drop size distributions”. In: Chemical Engineering Science 64.10, pp. 2433–2447.

Rayner, M. (2015). “Engineering Aspects of Food Emulsification and Homogenization”. In: ed. by M. Rayner and P. Dejmek. CRC PR INC. Chap. 1 Scales and Forces in Emulsification, pp. 3–32.

Samimy, M., Zaman, K. B. M. Q., and Reeder, M. F. (1993). “Effect of tabs on the flow and noise field of an axisymmetric jet”. In: AIAA Journal 31.4, pp. 609–619.

Sauter, C. and Schuchmann, H. (2008). “Materialschonendes Hochdruckdispergieren mit dem High Pressure Post Feeding (HPPF)-System”. In: Chemie Ingenieur Technik 80.3, pp. 365–372.

Schlender, M., Minke, K., Spiegel, B., and Schuchmann, H. P. (2015a). “High-pressure double stage homogenization processes: Influences of plant setup on oil droplet size”. In: Chemical Engineering Science 131, pp. 162–171.

Schlender, M., Spengler, A., and Schuchmann, H. P. (2015b). “High-pressure emulsion formation in cylindrical coaxial orifices: Influence of cavitation induced pattern on oil drop size”. In: International Journal of Multiphase Flow 74, pp. 84–95.

Schrijer, F., Sciaccitano, A., and Scarano, F. (2010). “Experimental investigation of flow control devices for the reduction of transonic buffeting on rocket afterbodies”. In: 15th Int Symp on Applications of Laser Techniques to Fluid Mechanics.

Schubert, H. and Engel, R. (2004). “Product and Formulation Engineering of Emulsions”. In: Chemical Engineering Research and Design 82.9. In Honour of Professor Alvin W. Nienow, pp. 1137–1143.

Schubert, H. and Armbruster, H. (1989). “Prinzipien der Herstellung und Stabilität von Emulsionen”. In: Chemie Ingenieur Technik 61.9, pp. 701–711.

Schultz, S., Wagner, G., and Ulrich, J. (2002). “Hochdruckhomogenisation als ein Verfahren zur Emulsionsherstellung”. In: Chemie Ingenieur Technik 74.7, pp. 901–909.

Schultz, S., Wagner, G., Urban, K., and Ulrich, J. (2004). “High-Pressure Homogenization as a Process for Emulsion Formation”. In: Chemical Engineering & Technology 27.4, pp. 361–368.

Seiferth, H. (1946). Vorausberechnung und Beseitigung der Schwingungen von Freistahl-Windkanälen. Tech. rep. Aerodynamische Versuchsanstalt.

Stang, M., Schuchmann, H., and Schubert, H. (2001). “Emulsification in High-Pressure Homogenizers”. In: Engineering in Life Sciences 1.4, pp. 151–157.

Stevenson, M. J. and Chen, X. D. (1997). “Visualization of the flow patterns in a high-pressure homogenizing valve using a CFD package”. In: Journal of Food Engineering 33.1, pp. 151–165.

Stone, H. A., Bentley, B. J., and Leal, L. G. (1986). “An experimental study of transient effects in the breakup of viscous drops”. In: Journal of Fluid Mechanics 173, pp. 131–158.

Swartz, J. E. and Kessler, D. P. (1970). “Single drop breakup in developing turbulent pipe flow”. In: AIChE Journal 16.2, pp. 254–260.

Taylor, G. I. (1934). “The formation of emulsions in definable fields of flow”. In: Proceedings of the Royal Society of London. Series A, Containing Papers of a Mathematical and Physical Character 146.858, pp. 501–523.

Tesch, S., Freudig, B., and Schubert, H. (2003). “Production of Emulsions in High-Pressure Homogenizers – part I: Disruption and Stabilization of Droplets”. In: Chemical Engineering & Technology 26.5, pp. 569–573.

Tjahjadi, M. and Ottino, J. M. (1991). “Stretching and breakup of droplets in chaotic flows”. In: Journal of Fluid Mechanics 232.-1, p. 191.

Umbanhowar, P. B., Prasad, V., and Weitz, D. A. (2000). “Monodisperse Emulsion Generation via Drop Break Off in a Coflowing Stream”. In: Langmuir 16.2, pp. 347–351.

Urban, K., Wagner, G., Schaffner, D., and Ulrich, J. (2006). “Dispergierscheiben, die bessere Alternative zum Hochdruck beim Emulgieren?” In: Chemie Ingenieur Technik 78.8, pp. 1069–1077.

Vankova, N., Tcholakova, S., Denkov, N. D., Ivanov, I. B., Vulchev, V. D., and Danner, T. (2007). “Emulsification in turbulent flow: 1. Mean and maximum drop diameters in inertial and viscous regimes”. In: Journal of Colloid and Interface Science 312.2, pp. 363–380.

Velmula, M., Pavuluri, P., Rajashekar, S., and Rao, V. U. M. (2015). “Nanosuspension technology for poorly soluble drugs-a review”. In: World Journal of Pharmacy and Pharmaceutical Sciences 4.7, pp. 1612–1625.

Walstra, P. (1983). “Encyclopedia of Emulsion Technology”. In: ed. by P. Becher. M. Dekker. Chap. Formation of Emulsions.

Walstra, P. and Smulders, P. E. (1998). “Modern aspects of emulsion science”. In: ed. by B. Binks. The Royal Society of Chemistry. Chap. 2 Emulsion Formation, pp. 56–99.

Wieth, L., Kelemen, K., Braun, S., Koch, R., Bauer, H.-J., and Schuchmann, H. P. (2016). “Smoothed Particle Hydrodynamics (SPH) simulation of a high-pressure homogenization process”. In: Microfluidics and Nanofluidics 20.2.

Windhab, E., Dressler, M., Feigl, K., Fischer, P., and Megias-Alguacil, D. (2005). “Emulsion processing—from single-drop deformation to design of complex processes and products”. In: Chemical Engineering Science 60.8. 5th International Symposium on Mixing in Industrial Processes (ISMIP5), pp. 2101–2113.

Zaman, K. B. M. Q., Reeder, M. F., and Samimy, M. (1994). “Control of an axisymmetric jet using vortex generators”. In: Physics of Fluids 6.2, pp. 778–793.

Zhao, X. (2007). “Drop breakup in dilute Newtonian emulsions in simple shear flow: New drop breakup mechanisms”. In: Journal of Rheology 51.3, pp. 367–392.

Nomenclature

Latin symbols

x, y, z	coordinate system	m
u, v, w	velocity components	m/s
A_i	droplet area at a point in time	m^2
A_o	droplet area after the orifice	m^2
A_{inlet}	inlet channel cross sectional area	m^2
$A_{orifice}$	orifice cross sectional area	m^2
b	constant	-
c	constant	-
D	diameter of the orifice	m
D_i	diameter of the inlet channel	m
D_o	diameter of the outlet channel	m
d	droplet diameter	m
d_P	primary droplet diameter	m
d_{max}	maximum droplet diameter	m
d_{jet}	jet diameter	m
d_{vortex}	measured vortex diameter	m
E_V	volumetric energy density	J/m^3
f	dissipated velocity fraction	-
H	image heigth	px
h	gap width	m
I	camera image intensity	-
$I_{Cam.max}$	maximum camera image intensity	-
i	frame number	-
L	orifice length	m
l	droplet filament length	m
l_K	Kolmogorov length	m
l_0	diameter of the largest vortex	m
n	refractive index	-
P_{diss}	dissipated power	W
Δp	pressure difference	Pa
p_{La}	Laplace pressure	Pa
p_1	pressure in front of the homogenization unit	Pa
p_2	pressure in behind the homogenization unit	Pa
R	radius of curvature	m
r	radius	m
r_{in}	radial droplet injection location	m
t	time	s
u_{Re}	theoretical orifice velocity	m/s

$u_{\mathrm{Re,in}}$	theoretical inlet channel velocity	m/s
$\dot{V}$	volumetric flow rate	m^3/s
V_{diss}	dissipation volume	m^3
W	image width	px
$x_{3,2}$	Sauter diameter	m

Greek symbols

α	conical inlet angle	°
γ	interfacial tension	N/m
ϵ	turbulent kinetic energy	m^2/s^2
η	viscosity	mPas
η_{c}	viscosity of the continuous phase	mPas
η_{d}	viscosity of the disperse phase	mPas
ρ	density	kg/m^3
ρ_{c}	density of the continuous phase	kg/m^3
ρ_{d}	density of the disperse phase	kg/m^3
σ	external stresses	Pa
τ_{visc}	viscous shear stress	Pa
τ_{ext}	external shear stress	Pa
τ_{TI}	turbulent inert stress	Pa

Indexes

i	point in time or recorded time-step	-

Dimensionless numbers

A^*	area ratio	-
Ca	Capillary number	-
Ca_{crit}	critical Capillary number	-
D^*_{O}	outlet channel size ratio	-
d^*_{P}	drop size ratio	-
η^*	viscosity ratio	-
Re	Reynolds number	-
r^*	dimensionless radial droplet injection location	-
S	solidity	-
Th	Thoma number	-
We	Weber number	-

A

Appendices

A.1. Droplet breakup after passing the orifice

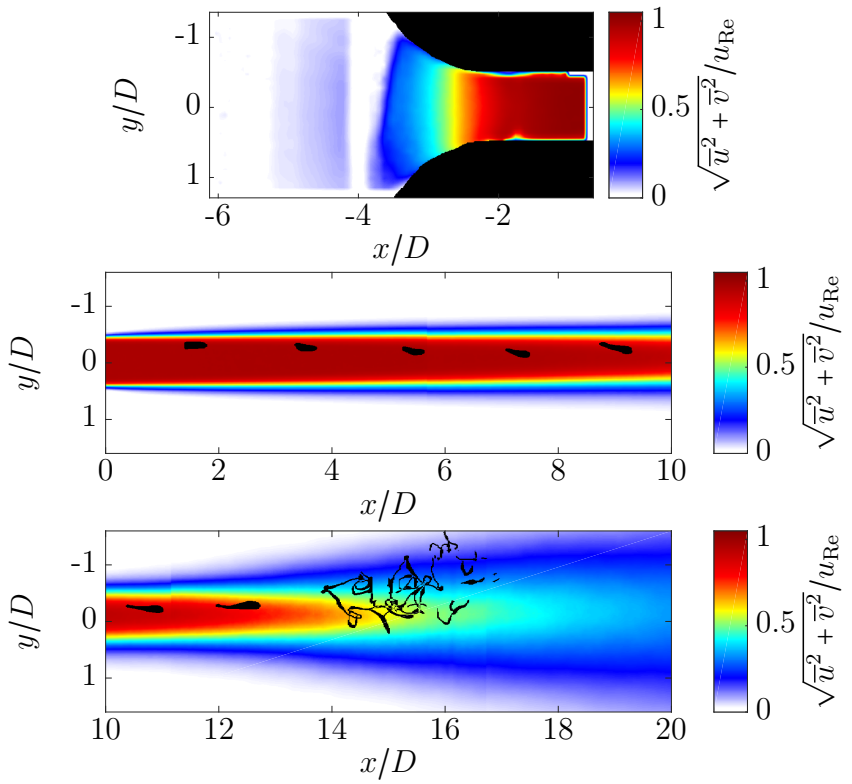

Figure A.1: Representation of the temporal and spatial drop breakup in the free jet behind the orifice for a drop with viscosity ratio η^* = 10.8 at a Reynolds number of Re = 2000. The time-averaged velocity field is shown in the background. The dimensionless dosing point of the primary drop is r^* = 0.8.

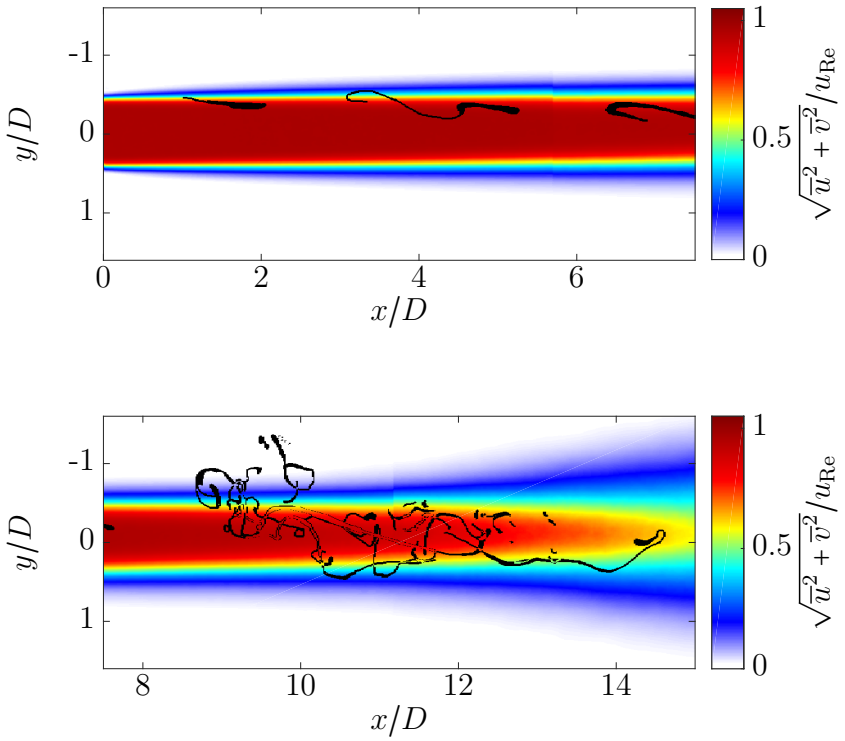

Figure A.2: Representation of the temporal and spatial drop breakup in the free jet behind the orifice for a drop with viscosity ratio η^* = 10.8 at a Reynolds number of Re = 2000. The time-averaged velocity field is shown in the background. The dimensionless dosing point of the primary drop is r^* = 0.9.

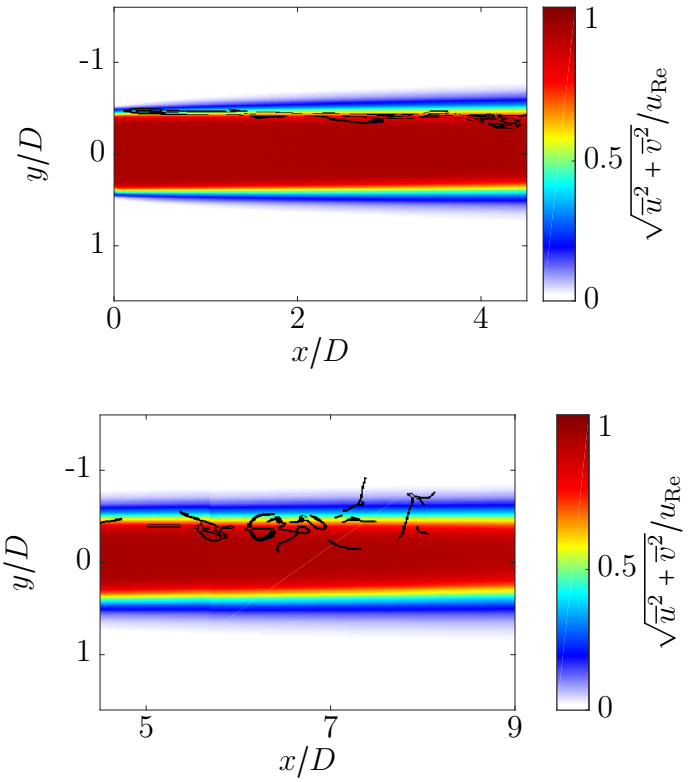

Figure A.3: Representation of the temporal and spatial drop breakup in the free jet behind the orifice for a drop with viscosity ratio η^* = 10.8 at a Reynolds number of Re = 2000. The time-averaged velocity field is shown in the background. The dimensionless dosing point of the primary drop is r^* = 1.

A.2. Droplet breakup without passing the orifice

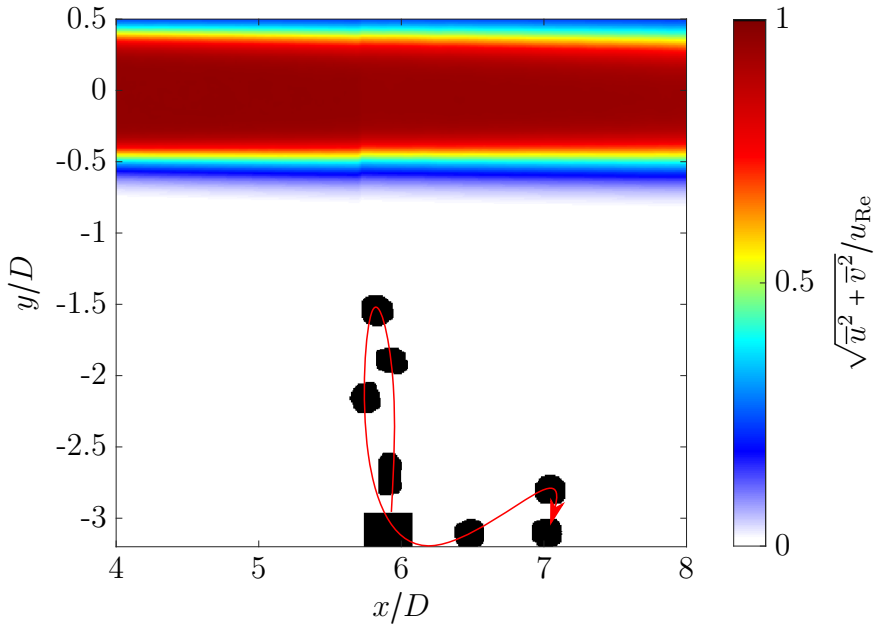

Figure A.4: Example of a droplet injected in the near region of the jet that is deflected by the recirculation flow or reflected by the free jet, shown as a black mask with the normalized, time-averaged velocity field of the free jet as background. The drop path is marked by a red arrow.